



HAL
open science

Search for SUSY Electroweak production at LHC Run 2 and study of CMOS sensor for ITk replacement in second-half of HL-LHC

Ngoc Khanh Vu

► **To cite this version:**

Ngoc Khanh Vu. Search for SUSY Electroweak production at LHC Run 2 and study of CMOS sensor for ITk replacement in second-half of HL-LHC. Physics [physics]. AMU - Aix Marseille Université, 2021. English. NNT: . tel-03551191

HAL Id: tel-03551191

<https://amu.hal.science/tel-03551191>

Submitted on 1 Feb 2022

HAL is a multi-disciplinary open access archive for the deposit and dissemination of scientific research documents, whether they are published or not. The documents may come from teaching and research institutions in France or abroad, or from public or private research centers.

L'archive ouverte pluridisciplinaire **HAL**, est destinée au dépôt et à la diffusion de documents scientifiques de niveau recherche, publiés ou non, émanant des établissements d'enseignement et de recherche français ou étrangers, des laboratoires publics ou privés.

THÈSE DE DOCTORAT

Soutenue le 17/12/2021 par

VU Ngoc Khanh

Titre de la thèse:

Search for SUSY Electroweak production at LHC Run 2 and study of CMOS sensor for ITk replacement in second-half of HL-LHC

Discipline

Physique et Sciences de la Matière

Spécialité

Physique des Particules et Astroparticules

École doctorale 352

Physique et Sciences de la Matière

Laboratoire/Partenaires de recherche

Centre de Physique des Particules de
Marseille (CPPM) UMR 7346
Aix-Marseille Université

Composition du jury

Marie-Hélène GENEST
LSPC, Grenoble, France

Rapporteuse

Freya BLEKMAN
Vrije Universiteit Brussel, Belgium

Rapporteuse

Cinzia DA VIA
Manchester University, United Kingdom

Examinatrice

Benjamin FUKS
LPTHE, Paris, France

Examineur

Cristinel DIACONU
CPPM, Marseille, France

Président du jury

Steve MUANZA
CPPM, Marseille, France

Directeur de thèse

Farès DJAMA
CPPM, Marseille, France

Co-Directeur de thèse

Acknowledgements

First of all, I would like to express my gratitude to my supervisor Steve Muanza and my co-supervisor Farès Djama for giving the opportunity to perform my doctorate study with the CPPM ATLAS group. I would like to thank for your supports and for the patience you had during this thesis. Also thank you for your time, guidance and instructive comments in the past three years.

I am deeply grateful to Da Xu, Valentina Tudorache, Eric Schanet, Alberto Cervelli and all the other members in the SUSY 1L team for your guidance, your valuable inputs and continuous feedback in the analysis. I would also like to thank Juanan Garcia for helping me to complete my ATLAS qualification task and thank Thomas Strebler and Arnaud Duperrin for investing your time in my CMOS study. It was a great honor and privilege working with all of you. I am also grateful to Brigitte Pantat for your kindness. Without you, I would never be able to complete my paperwork.

I would like to express my gratitude to the reviewers of this manuscript, Marie-Hélène Genest and Freya Blekman, as well as the other jury members, Cinzia DaVia, Benjamin Fuks and Cristinel Diaconu. Thank you for taking the time to read my work and attend my defense. Thank you as well for all of your incoming questions and comments.

I would like to thank all my colleagues and friends at CPPM: Giovanni, Jacopo, Gaia, Rima, Neelam, Marie, Sylvain and many more for your professional and personal supports. I am very grateful to Nghia for your professional and personal help and for being a great senior that I could ever have. Simultaneously, I would like to thank all of my Vietnamese friends, especially Minh, Quyen, Nhan, Nguyen, Viet, Nam, Hoa for all the wonderful moments that we spent together. You all made my time in France great.

Finally, I would like to express my deepest gratitude to my grand family, my parents(-in-law), my brothers(-in-law) and especially my wife Cam Suong for your endless love, continuous support and encouragement during these years. Thank you for always standing with me during the most difficult periods. This accomplishment would not have been possible without you.

Résumé

Le Modèle Standard (MS) est une théorie remarquablement efficace jusqu'à présent. Cependant, il ne constitue pas une description complète de la nature. La découverte du boson de Higgs en 2012 par les expériences ATLAS et CMS a confirmé le mécanisme de la brisure de la symétrie électrofaible et a également mis en lumière le problème de hiérarchie dû à un ajustement fin, non naturel, de la masse du boson de Higgs. La supersymétrie (SUSY) est une extension théorique du MS qui résout le problème de hiérarchie en postulant d'un partenaire SUSY pour chaque particule du MS. De plus, la SUSY fournit une explication à de nombreuses autres questions ouvertes telles que l'origine de la Matière Noire et l'unification des interactions fondamentales à haute énergie. Cette thèse concerne une analyse visant à rechercher une production SUSY électrofaible d'une paire de charginos ($\tilde{\chi}_1^\pm \tilde{\chi}_1^\pm$) ou d'une paire chargino-neutralino ($\tilde{\chi}_1^\pm \tilde{\chi}_2^0$) dans le contexte de Modèles Simplifiés incluant la conservation de la R -parité dans lesquels le chargino ($\tilde{\chi}_1^\pm$) se désintègre dans le neutralino le plus léger ($\tilde{\chi}_1^0$) en émettant un boson W et le neutralino ($\tilde{\chi}_2^0$) se désintègre dans le neutralino le plus léger en émettant un boson Z . L'analyse sélectionne des événements compatibles avec une topologie caractérisée par la présence d'un lepton (électron ou muon) isolé, accompagné de jets et d'impulsion transverse manquante. Elle est effectuée pour la première fois au LHC sur un échantillon de données d'une luminosité intégrée de 139 fb^{-1} , ce qui correspond à l'intégralité des collisions pp collectées par le détecteur ATLAS au cours du Run 2. Cette analyse exploite les jets à grand rayon pour augmenter sa sensibilité au signal. Les incertitudes systématiques expérimentales et théoriques sont incluses dans les résultats présentés. Le taux d'événements observés est compatible avec le taux d'événements prédits. L'analyse établit une limite attendue excluant à 95% niveau de confiance une masse de chargino/neutralino ($\tilde{\chi}_1^\pm / \tilde{\chi}_2^0$) inférieure à 680 (720) GeV pour un neutralino le plus léger de masse nulle dans la recherche $\tilde{\chi}_1^\pm \tilde{\chi}_1^\mp$ ($\tilde{\chi}_1^\pm \tilde{\chi}_2^0$).

Lors de la phase de Haute Luminosité du LHC (HL-LHC) débutant en 2027, le détecteur interne d'ATLAS va être complètement remplacé par un détecteur entièrement en silicium, le trajectographe interne ITk. Pendant toute la durée du HL-LHC, les couches les plus internes de l'ITk seront exposées à une radiation d'un flux de $2 \times 10^{16} \text{ n}_{\text{eq}}/\text{cm}^2$. Toutefois, les senseurs à pixels de l'ITk ne peuvent résister qu'à un flux maximum de $10^{16} \text{ n}_{\text{eq}}/\text{cm}^2$, impliquant que les couches les plus internes devraient être remplacées au milieu du HL-LHC. Si la technologie des senseurs CMOS est prête à résister à un flux de $1.6 \times 10^{16} \text{ n}_{\text{eq}}/\text{cm}^2$ au moment du HL-LHC, alors cette technologie pourrait être la plus prometteuse pour remplacer les traditionnels senseurs planaires en 3D. Dans cette thèse, une nouvelle conception du détecteur à pixels ITk constitué

par des senseurs CMOS épais de $50 \mu\text{m}$ et d'une taille de $25 \times 25 \mu\text{m}^2$ est simulée par les couches les plus internes. Cette simulation montre les avantages que donnerait des senseurs CMOS par une réduction du ToT et de la largeur des agrégats, ainsi qu'une précision accrue pour le paramètre d'impact transverse des traces reconstruites pour un échantillon de muons de $p_T = 100 \text{ GeV}$.

La mesure du courant de fuite est l'une des principales méthodes pour suivre les dommages dûs aux radiations dans le silicium. Ce courant de fuite peut être mesuré avec précision au niveau d'un module, en utilisant l'alimentation. Par contre, au niveau d'un pixel, il est difficile de mesurer précisément le courant de fuite. Dans cette thèse, le mécanisme de MonLeak (suivi du courant de fuite) est utilisé pour mesurer le courant de fuite au niveau des pixels des modules de l'IBL, c'est-à-dire des couches de pixels dites "B-Layer", "Layer 1", "Layer 2" et disques. Les mesures effectuées en 2019 lors d'un échantillonnage du MonLeak dans les couches de pixels et dans les disques, étant environ deux fois plus élevées que les mesures des alimentations collectées par le système de contrôle du détecteur (DCS), révèlent un important désaccord. Ce désaccord atteint même un ordre de grandeur dans l'IBL.

Aux hautes luminosités du LHC, plusieurs sources d'inefficacité contribuent à la perte de point d'impact dans la lecture du détecteur à pixels. Les taux de pertes associés à ces sources ne sont pas encore simulés, seuls une fraction ad-hoc de 0.9% de points d'impact du Monte-Carlo (MC) sont retirés aléatoirement pour en tenir compte dans la simulation. Cette méthode était bien adaptée au Run 1, mais ne fonctionne plus au Run 2. Dans cette thèse, de nouvelles méthodes sont développées en utilisant des données pour estimer plus précisément le taux de perte des doubles points d'impact (DH), due à la perte d'un point d'impact survenant quand le pixel est encore occupé par un point d'impact précédent, ainsi que le taux de perte dues à des copies tardives (LC) de points d'impact survenant plus tard que le temps de latence du déclenchement. Un taux préliminaire de perte DH de 0.96% est obtenu pour la couche "B-Layer" avec la nouvelle méthode est peut être considéré comme la limite inférieure sur le taux de perte de cette couche.

Synthèse en français

De quoi sommes-nous faits ? Ou quels sont les éléments constitutifs fondamentaux de la matière ? Ou encore, quelle est la description de la nature ? Ce sont les questions fondamentales qui fascinent les humains depuis des siècles. Le modèle standard (MS) de la physique des particules a été développé depuis le 20^e siècle afin de trouver la réponse à ces questions. Il s'agit d'un modèle théorique qui utilise un formalisme mathématique pour décrire les propriétés des particules élémentaires et leurs interactions fondamentales. Jusqu'à présent, le MS est devenu une théorie remarquablement réussie avec de nombreux tests précis confirmant sa validité et son pouvoir de prédiction. Malgré ses succès, le MS n'est toujours pas une description complète de la nature. Diverses observations expérimentales impliquent qu'il doit y avoir de la physique au-delà. L'existence de la matière noire qui est nécessaire pour expliquer de nombreuses observations astrophysiques et cosmologiques, la masse des neutrinos requise pour les oscillations observées des neutrinos et la tension entre le moment magnétique anormal des muons prédit par le MS et observé expérimentalement sont des exemples de tels phénomènes qui ne peuvent être compris dans le cadre du MS. En outre, bien que ne contredisant pas directement le MS, de nombreuses difficultés théoriques apparues dans le cadre de nos connaissances actuelles de la physique fondamentale, telles que le problème de la hiérarchie ou l'unification des constantes de couplage de jauge, suggèrent la nécessité d'une nouvelle physique.

La découverte d'une particule semblable au boson de Higgs avec une masse de ~ 125 GeV en 2012 aux expériences ATLAS et CMS du Grand collisionneur de hadrons (LHC) a confirmé le mécanisme Brout-Englert-Higgs de la brisure de symétrie électrofaible dans le MS, mais a également souligné le problème de hiérarchie dans la masse du boson de Higgs. Parmi les diverses théories au-delà du MS, la *Supersymétrie* (SUSY), une extension du MS, devient plus favorable en raison de son élégance et de sa relative simplicité. Cette théorie postule l'existence d'un nouveau partenaire supersymétrique fermion (boson) pour chaque boson (fermion) dans le MS et aborde donc directement le problème de la hiérarchie. En outre, dans le cas d'une symétrie Z_2 supplémentaire supposée, connue sous le nom de conservation de la parité R , la particule supersymétrique (LSP) la plus légère doit être stable, en faible interaction et peut donc être un candidat viable pour la matière noire. SUSY offre également une possibilité d'unification de l'interaction forte et de l'interaction électrofaible à haute échelle d'énergie. Dans les scénarios SUSY, les partenaires du boson de Higgs MS (h) et des bosons de jauge, connus sous le nom de higgsinos, winos, et bino sont collectivement appelés électrojauginos. Les charginos $\tilde{\chi}_i^\pm$ ($i = 1, 2$) et les neutralinos $\tilde{\chi}_j^0$ ($j = 1, 2, 3, 4$) sont les états propres de masse des électroweakinos qui sont des

superpositions linéaires de higgsinos, winos, et bino. Les considérations de naturalité suggèrent que les plus légers des électroweakinos ont des masses proches de l'échelle électrofaible. Dans les scénarios où les particules SUSY fortement produites sont plus lourdes que quelques TeV, la production directe d'électroweakinos pourrait être le mécanisme de production SUSY dominant au LHC. Le chargino le plus léger et le neutralino le plus proche du plus léger peuvent se désintégrer via $\tilde{\chi}_1^\pm \rightarrow W \tilde{\chi}_1^0$ et $\tilde{\chi}_2^0 \rightarrow h/Z \tilde{\chi}_1^0$ respectivement dans les scénarios où les superpartenaires leptoniques sont plus lourds que les électroweakinos. Les scénarios avec des électroweakinos légers fournissent également une explication possible de la divergence entre la mesure du moment magnétique anormal $g - 2$ du muon et les prédictions du SM.

Le LHC est actuellement le collisionneur de particules le plus grand et le plus énergétique du monde. Cette machine fait entrer en collision des protons à une énergie de centre de masse allant jusqu'à 14 TeV dans le tunnel de 27 km situé à 100 m sous terre au CERN, à Genève. Le détecteur ATLAS, installé autour de l'un des quatre points d'interaction où les faisceaux de protons entrent en collision dans l'anneau du LHC, est le plus grand détecteur polyvalent jamais construit. Il exploite les informations des collisions pp pour tester les prédictions du SM et rechercher le signe d'une nouvelle physique à l'échelle du TeV également. Le sous-système le plus interne d'ATLAS est le détecteur de pixels qui contient trois couches de barils : la couche B, la couche 1 et la couche 2 placées à des rayons de 50,5 mm, 88,5 mm et 122,5 mm de l'axe du faisceau, respectivement, et deux embouts avec trois disques chacun. Le détecteur de pixels utilise au total 1744 modules de pixels en silicium, chaque module étant constitué d'une dalle de senseur planaire en silicium $n^+ - in - n$ qui est liée à 16 puces électroniques frontales de 2880 pixels chacune. La taille nominale des pixels est de $50 \times 400 \mu\text{m}^2$. Pendant l'arrêt prolongé 1 (2013-2015), une nouvelle couche de pixels, la couche B insérable (IBL), a été ajoutée au détecteur de pixels, à un rayon de 33,5 mm de l'axe du faisceau. À la différence des autres couches de pixels, cette couche supplémentaire utilise des senseurs en silicium basés sur les technologies hybride planaire et 3D, avec une taille de pixel de $50 \times 250 \mu\text{m}^2$. Cette conception permet au détecteur de pixels de fournir une grande qualité de mesures de la piste et du vertex dans l'extrême proximité du tube du faisceau où le dispositif subit une grande quantité de dommages dus au rayonnement. En outre, elle est également bénéfique dans la reconstruction des vertex secondaires associés aux particules à longue durée de vie, telles que les hadrons b , et améliore ainsi les performances de marquage des saveurs.

Le LHC prévoit d'entrer dans une phase de haute luminosité (HL-LHC) en 2027 pour atteindre une précision et une puissance statistique encore plus élevées. Dans cette phase, la luminosité instantanée devrait atteindre jusqu'à $7,5 \times 10^{34} \text{ cm}^{-2}\text{s}^{-1}$, soit une luminosité supérieure d'un facteur 5 environ à la luminosité typique du Run 2. Cela se traduira par une moyenne de 200 collisions inélastiques pp par croisement de faisceaux et générera donc un environnement beaucoup plus dur pour le détecteur ATLAS avec des niveaux de radiations beaucoup plus élevés par rapport au Run 3 (2022-2024). Afin de permettre à ATLAS de poursuivre son étude du spectre de la physique des hautes énergies avec des performances équivalentes ou même supérieures à celles

du détecteur actuel, ses sous-systèmes subiront quelques mises à niveau pour faire face au niveau de radiation élevé du HL-LHC. Un nouveau détecteur de temps à haute granularité (HGTD) sera ajouté et, en particulier, le détecteur interne d'ATLAS (INDET) sera entièrement remplacé par un nouveau détecteur interne entièrement en silicium (ITk). Le détecteur ITk se compose d'un sous-système de détecteur de pixels en silicium (le détecteur de pixels ITk) dans la région la plus proche du tuyau de faisceau et d'un sous-système de détecteur à micropistes en silicium (le détecteur de pistes ITk) à des rayons plus élevés du tuyau de faisceau. Grâce à cette séparation, la granularité du détecteur est optimisée pour distinguer les pistes proches tout en minimisant le nombre de canaux de lecture et le coût du système. Comme dans le cas de l'INDET, chaque sous-détecteur est divisé en une région de tonneau avec plusieurs couches concentriques autour de la direction du faisceau et deux bouchons d'extrémité composés de disques (pour le détecteur à piste) ou d'anneaux (pour le détecteur à pixels) placés perpendiculairement à la ligne du faisceau, couvrant les régions avant.

Les trois parties principales abordées dans cette thèse sont décrites dans ce qui suit.

Mesures instrumentales sur le détecteur de pixels pendant le Run 2

En tant que partie la plus proche du tube du faisceau, le détecteur de pixels d'ATLAS subit une grande quantité de dommages dus au rayonnement, ce qui altère les performances du détecteur. L'une des méthodes les mieux caractérisées pour surveiller les dommages causés par les rayonnements sur le silicium consiste à mesurer le courant de fuite du détecteur, qui augmente linéairement avec la fluence d'irradiation. Dans le détecteur de pixels, alors que le courant de fuite peut être mesuré précisément au niveau de la granularité du module en utilisant le sous-système d'alimentation, il est beaucoup plus difficile d'obtenir des mesures précises au niveau de la granularité du pixel pour le courant de fuite. Pour cette étude, le mécanisme MonLeak (surveillance du courant de fuite) est utilisé pour surveiller le courant de fuite pixel par pixel pour l'IBL, les couches de pixels (couche B, couche 1, couche 2) et les disques. Dans les couches de pixels et les disques, les balayages MonLeak peuvent uniquement mesurer le courant de fuite au niveau du pixel en combinaison avec le courant de retour du préamplificateur mis en œuvre dans chaque pixel des puces FE-I3. Trois scans MonLeak (un en 2015 et deux en 2019) ont été effectués pour mesurer le courant de fuite au niveau du pixel des modules dans les couches et les disques Pixel. Les mesures MonLeak présentent des divergences avec les mesures d'alimentation enregistrées par le système de contrôle des détecteurs (DCS), étant plus élevées d'un facteur d'environ 2 en 2019. Cependant, on observe toujours une tendance raisonnable pour les courants de fuite dans ces balayages MonLeak, étant cohérente avec la quantité de dommages de rayonnement que chacune des couches de pixels a subi. Dans l'IBL, les scans MonLeak mesurent le courant de fuite par pixel à l'aide du convertisseur

analogique-numérique 10 bits d'usage général (GADC) mis en œuvre sur chaque puce FE-I4B. Deux scans ont été effectués en 2019. Leurs mesures montrent un énorme écart avec les données du DCS (plus élevé d'un facteur d'un ordre de grandeur). Par conséquent, les mesures de MonLeak pour l'IBL ne sont pas fiables et le GADC doit être calibré davantage. L'étude des mesures de courant de fuite au niveau du pixel était ma tâche de qualification pour être intégré à la liste d'auteurs ATLAS et est décrite en détail dans la section 5.1.

Un autre défi qui se pose pour le détecteur de pixels est le fait que les données de hit de pixel peuvent être perdues pendant le mécanisme de lecture en raison du taux élevé de hits du détecteur aux hautes luminosités du LHC. Plusieurs sources contribuent à cette inefficacité. Jusqu'à présent, les pertes de pixel-hit provenant de ces sources n'ont pas encore été simulées. Au lieu de cela, seule une fraction ad-hoc de 0,9% a été appliquée aux échantillons Monte Carlo (MC). Cette hypothèse était bonne pour le Run 1, mais ne convient plus pour le Run 2. Dans cette thèse, de nouvelles méthodes sont développées afin d'estimer plus précisément les taux de perte de pixel-hits de la source d'inefficacité Double-hit (DH), qui est due à la perte d'un hit arrivant sur un pixel alors que ce pixel est encore occupé par le hit précédent, et de la source d'inefficacité Late Copying (LC), qui est due à la perte de hits arrivant sur des tampons Double-Columns après la latence de déclenchement. Les taux de perte de ces deux sources peuvent être calculés pour chacune des couches de pixels et des bouchons d'extrémité en utilisant la distribution pixel-ToT de la couche. Le taux de perte DH préliminaire pour la couche B, obtenu avec la nouvelle méthode en utilisant les données de l'exécution 362776, est de 0,96%, déjà supérieur à la fraction ad-hoc de 0,9% appliquée pour la simulation MC. Ce nouveau taux de perte DH doit être considéré comme une limite inférieure pour le taux de perte dans la couche B. Les nouvelles méthodes d'estimation développées dans cette étude seront également utilisées pour calculer les taux de perte avec les données des autres séries pour une validation supplémentaire ainsi que pour étudier comment les taux de perte s'échelonnent avec la luminosité. La discussion détaillée de l'estimation du taux de perte par pixel à l'aide de données réelles est donnée dans la section 5.2.

Senseur CMOS pour le remplacement de l'ITk dans la seconde partie du HL-LHC

Pendant toute la durée de vie du HL-LHC, une luminosité intégrée attendue allant jusqu'à 4000 fb^{-1} sera délivrée au détecteur ATLAS, ce qui correspond à une fluence de rayonnement accumulée allant jusqu'à $2 \times 10^{16} \text{ n}_{\text{eq}}/\text{cm}^2$ à laquelle les couches de pixels ITk les plus internes devront être exposées. Cependant, les senseurs de pixels ITk ne peuvent résister qu'à une fluence maximale d'environ $10^{16} \text{ n}_{\text{eq}}/\text{cm}^2$ et, par conséquent, ces couches devraient être remplacées après avoir intégré la moitié de la luminosité attendue, c'est-à-dire à la demi-vie du HL-LHC. Pour ce remplacement, les senseurs de pixels CMOS, qui sont produits en exploitant la technologie CMOS,

sont particulièrement intéressants pour remplacer les senseurs de pixels traditionnels. Les senseurs CMOS sont largement utilisés dans l'industrie des puces depuis 20 ans. Ils peuvent être exploités efficacement avec une épaisseur réduite et une taille de pas de pixel réduite, améliorant ainsi la granularité et diminuant le budget matériel du détecteur de pixel ITk. L'utilisation des senseurs CMOS pour les couches ITk les plus internes profiterait aussi directement aux étiquetages b et τ . En outre, le module de pixels CMOS peut avoir une conception monolithique avec le senseur et l'électronique logés dans le même bloc de silicium. Par conséquent, son processus de production est plus simple, ce qui permet un approvisionnement rapide avec un temps de réaction rapide. En outre, moins de matériau est nécessaire, ce qui entraîne un coût de détecteur beaucoup plus faible et une réduction de l'effet de diffusion multiple. Dans cette thèse, la disposition du détecteur à pixel ITk avec les senseurs CMOS de $50 \mu\text{m}$ d'épaisseur et $25 \times 25 \mu\text{m}^2$ de pas de pixel utilisés dans les couches les plus internes est simulée en utilisant Geant 4 et un échantillon de 250000 muons uniques avec $p_T = 100 \text{ GeV}$. La simulation a démontré les avantages obtenus en utilisant les senseurs CMOS avec une réduction du ToT et de la largeur du cluster et une meilleure précision dans la reconstruction du paramètre transversal de la trace d_0 . Dans les prochaines étapes, ces avantages seront quantifiés pour des échantillons de muons avec différents p_T . À l'avenir, cette nouvelle disposition du détecteur avec les senseurs CMOS utilisés sera simulée avec des échantillons de jets de saveur lourde afin d'estimer le gain en performance de marquage b , en particulier à des p_T élevés. L'étude détaillée du senseur CMOS pour le remplacement de l'ITk dans la seconde partie du HL-LHC est présentée dans la section 6.3.

Recherche de la production électrofaible de charginos et neutralinos dans les états finaux avec un lepton, des jets et un moment transversal manquant

Cette thèse se concentre sur une analyse ciblant deux recherches SUSY dédiées à la production électrofaible de charginos et de neutralinos. L'une des recherches, nommée C1C1-WW, vise la production directe d'une paire de charginos les plus légers ($\tilde{\chi}_1^\pm \tilde{\chi}_1^\mp$) où chaque $\tilde{\chi}_1^\pm$ se désintègre ensuite en un boson W et un neutralino le plus léger ($\tilde{\chi}_1^0$). Cette recherche se concentre sur un scénario où l'un des bosons W se désintègre de manière hadronique et l'autre se désintègre de manière leptonique à travers un lepton léger (électron ou muon) et un neutrino. L'autre recherche, appelée C1N2-WZ, porte sur la production directe d'une paire composée d'un chargino le plus léger et d'un neutralino presque aussi léger ($\tilde{\chi}_1^\pm \tilde{\chi}_2^0$), où le $\tilde{\chi}_2^0$ se désintègre ensuite en un boson Z et un $\tilde{\chi}_1^0$, tandis que le $\tilde{\chi}_1^\pm$ se désintègre en un boson W et un $\tilde{\chi}_1^0$. Cette recherche cible un scénario dans lequel le boson Z se désintègre de manière hadronique et le boson W se désintègre de manière leptonique à travers un lepton chargé (électron ou

muon) et un neutrino. Les modèles de signaux considérés dans ces deux recherches s'inscrivent dans le contexte du modèle simplifié conservant la parité R , dans lequel le $\tilde{\chi}_1^0$ est la particule supersymétrique la plus légère (LSP), étant stable, en faible interaction et donc invisible pour le détecteur; le $\tilde{\chi}_1^\pm$ et le $\tilde{\chi}_2^0$ sont dégénérés en masse; les rapports d'embranchement du $\tilde{\chi}_1^\pm \rightarrow W\tilde{\chi}_1^0$ et du $\tilde{\chi}_2^0 \rightarrow Z\tilde{\chi}_1^0$ sont supposés être de 100%, tandis que les rapports d'embranchement des désintégrations des bosons W et Z sont considérés comme ceux du SM. L'état final est alors caractérisé par la présence d'exactly un lepton chargé (électron ou muon) accompagné de jets et de moment transversal manquant provenant des LSP et du neutrino. Les recherches C1C1-WW et C1N2-WZ via ce canal d'état final à un lepton sont effectuées pour la première fois dans ATLAS et cette analyse vise une luminosité intégrée de 139 fb^{-1} , correspondant aux données complètes du Run 2 collectées par le détecteur ATLAS. L'analyse exploite les jets large- R reconstruits pour améliorer la sensibilité de l'analyse. Deux types de région de signal (SR), la SR boostée et la SR résolue, sont définis. La SR boostée vise un scénario dans lequel les jets provenant de la désintégration du boson hadronique W/Z sont colinéaires et fusionnent éventuellement les uns avec les autres pour former des jets de grande taille R . Par conséquent, dans la SR boostée, au moins un jet de grande taille R observé dans l'événement est requis. Cette SR vise des signaux avec une division de masse élevée entre le $\tilde{\chi}_1^\pm/\tilde{\chi}_2^0$ et le $\tilde{\chi}_1^0$. En revanche, la SR résolue se concentre sur un autre scénario où les jets provenant de la désintégration du boson W/Z sont séparés les uns des autres et donc aucun jets de grande taille R observé dans l'événement n'est requis dans cette SR. La SR résolue vise des signaux avec une faible division de masse entre le $\tilde{\chi}_1^\pm/\tilde{\chi}_2^0$ et le $\tilde{\chi}_1^0$. Outre le nombre de jets de grande taille, d'autres variables cinématiques discriminantes sont également utilisées pour définir les SR boostés et résolus. Un balayage multidimensionnel des coupures ainsi que des graphiques $N-1$ sont utilisés pour optimiser les coupures sur ces variables. À ce stade, les SR boostées et résolues sont divisées en intervalles orthogonaux dans la masse transvers m_T afin d'optimiser la sensibilité pour toutes les régions de l'espace de phase de la grille de signal. Des régions de contrôle (CRs) dédiées sont définies pour l'estimation des rendements attendus des fonds dominants (W +jets, diboson, $t\bar{t}$) dans les SRs. Ces CRs sont conçues pour être orthogonales les unes aux autres et ne pas se chevaucher avec les SRs. La contribution des sous-processus avec au moins deux leptons dans l'état final du fond de diboson (DB2L) est estimée à l'aide d'une CR séparée qui requiert exactement deux leptons observés dans l'événement. Cette CR est également conçue pour minimiser le chevauchement avec les SRs d'analyse 2L2J. D'autre part, les rendements attendus de dibosons provenant de sous-processus n'ayant qu'un lepton dans l'état final (DB1L) sont déterminés à l'aide des mêmes CRs qui sont conçus pour l'estimation de W +jets. Ces CRs sont définis séparément pour les scénarios boostés et résolus. De même, l'estimation de $t\bar{t}$ repose sur des CRs qui sont également distinctes pour les régimes résolu et boosté. Les autres fonds qui sont mineurs dans cette analyse sont déterminés directement à partir de la simulation. Des régions de validation (VRs) correspondantes, orthogonales les unes aux autres et ne se chevauchant pas avec les SRs et les CRs, sont conçues entre les

SRs et les CRs afin de vérifier l'extrapolation de l'estimation du fond des CRs dans les SRs. Les incertitudes systématiques expérimentales et théoriques sont incluses dans l'analyse. Pour les fonds majeurs avec des CRs dédiés, ces incertitudes sont calculées en utilisant l'approche du facteur de transfert, tandis que pour les fonds mineurs estimés directement à partir de la simulation, elles sont calculées en utilisant directement les rendements attendus. Les résultats obtenus dans cette analyse ont montré une compatibilité des rendements observés et attendus des événements dans les CRs et les VRs. La limite d'exclusion dépendant du modèle à 95% CL s'étend jusqu'à 680 (720) GeV dans $m_{\tilde{\chi}_1^\pm/\tilde{\chi}_2^0}$ pour $\tilde{\chi}_1^0$ sans masse dans la recherche C1C1-WW (C1N2-WZ). Les points principaux de la stratégie d'analyse et le résultat important du présent travail sont illustrés dans le chapitre 7.

Abstract

The Standard Model (SM) has been a remarkably successful theory so far. However, it is still far from being a complete description of nature. The discovery of the SM Higgs boson by ATLAS and CMS experiments in 2012 has confirmed the electroweak symmetry breaking mechanism and also highlighted the hierarchy problem due to the unnatural fine-tuning in the Higgs boson mass. Supersymmetry (SUSY), a theoretical extension to the SM, directly resolves the hierarchy problem by postulating the existence of a new supersymmetric partner for each particle in the SM. In addition, SUSY also provides an explanation for many other open questions such as the Dark Matter origin and the unification of fundamental interactions at high energy scale. This thesis concentrates on an analysis targeting SUSY searches for electroweak production of chargino-chargino ($\tilde{\chi}_1^\pm \tilde{\chi}_1^\mp$) or chargino-neutralino ($\tilde{\chi}_1^\pm \tilde{\chi}_2^0$) pairs in the context of R -parity conserving simplified models in which the lightest chargino ($\tilde{\chi}_1^\pm$) decays into a W boson and the lightest neutralino ($\tilde{\chi}_1^0$), while the next-to-lightest neutralino ($\tilde{\chi}_2^0$) into a Z boson and the lightest neutralino. The analysis focuses on final states characterized by the presence of one isolated lepton (either electron or muon) accompanied by jets and missing transverse momentum. It is performed for the first time at the LHC and targets an integrated luminosity of 139 fb^{-1} corresponding to the full Run 2 pp collision data recorded by the ATLAS detector. This analysis exploits large- R jets to enhance the search sensitivities. Due to the fact that the analysis is not approved at the time of writing, the analysis results presented in this thesis are obtained with observed data still being blind in Signal Regions and with both the experimental and theoretical systematic uncertainties included. A compatibility of the observed and expected event yields can be observed in Control Regions and Validation Regions. The expected exclusion limit at 95% CL extends up to 680 (720) GeV in the $\tilde{\chi}_1^\pm / \tilde{\chi}_2^0$ mass for the massless $\tilde{\chi}_1^0$ in the $\tilde{\chi}_1^\pm \tilde{\chi}_1^\mp$ ($\tilde{\chi}_1^\pm \tilde{\chi}_2^0$) search.

In the High Luminosity LHC phase starting from 2027, the current ATLAS Inner Detector will fully be replaced by a new all-silicon detector, the Inner Tracker (ITk). During the entire HL-LHC lifetime, the innermost ITk layers will be exposed to an expected integrated radiation fluence of up to $2 \times 10^{16} \text{ n}_{\text{eq}}/\text{cm}^2$. However, the ITk pixel sensors can only withstand the maximum fluence of roughly $10^{16} \text{ n}_{\text{eq}}/\text{cm}^2$, implying that these innermost layers should be replaced by the half-life of the HL-LHC. For this replacement, if the CMOS sensor technology is ready to withstand a fluence of up to $1.6 \times 10^{16} \text{ n}_{\text{eq}}/\text{cm}^2$ by then, the CMOS sensors could become the most promising candidates to replace the tradition planar and 3D sensors. In this thesis, a new ITk Pixel detector layout with the CMOS sensors of $50 \mu\text{m}$ thick and $25 \times 25 \mu\text{m}^2$ pixel size used in the innermost layers is simulated. The simulation has shown

the advantages achieved using the CMOS sensors with a reduction in the cluster Time-over-Threshold (ToT), width and an improved precision in the track transverse parameter reconstruction for a sample of $p_T = 100$ GeV muons.

Measuring leakage current is one of the most characterised methods to monitor the silicon radiation damage. While the leakage current at the module granularity level can be measured precisely using the power supply sub-system, it is difficult to achieve the precise measurements for the pixel-level leakage current. In this thesis, the MonLeak (monitoring of the leakage current) mechanism is used to measure the pixel-level leakage current of modules in the IBL, the Pixel layers (B-Layer, Layer 1, Layer 2) and disks. Measurements obtained from the MonLeak scans in 2019 show discrepancies with the power supply measurements recorded by the Detector Control System (DCS), being higher by a factor of about 2 in the Pixel layers and disks, while extremely higher by a factor of around one order of magnitude in the IBL.

At the high luminosities of the LHC, there are several inefficiency sources contributing to the loss of hit data during the readout mechanism. The loss rates of these sources have not been simulated yet, but only an ad-hoc fraction of 0.9% of Monte-Carlo (MC) hits was discarded randomly to account for these inefficiencies in simulation. This assumption was fine for Run 1 but no longer suitable for Run 2. In this thesis, new methods are developed, using real data to estimate more precisely the Double-hit (DH) loss rate due to the loss of a hit arriving at a pixel while this pixel is still busy with the previous hit and the Late copying (LC) loss rate corresponding the loss of hits arriving at Double-Columns buffers later than the trigger latency. The preliminary DH loss rate of 0.96% for B-Layer is obtained from the new method and can be considered as a lower limit for the loss rate in this layer.

Contents

Acknowledgements	2
Résumé	3
Synthèse en français	5
Abstract	12
Contents	14
List of Figures	17
List of Tables	24
Introduction	26
1 The Standard Model in Particle Physics	30
1.1 Elementary particles in the Standard Model	31
1.2 The gauge theory in the Standard Model	31
1.3 The strong interaction	33
1.4 The electroweak interaction	34
1.5 The electroweak spontaneous symmetry breaking	36
1.6 Higgs boson measurements	38
1.7 Successes and limitations of the Standard Model	41
2 Supersymmetry	45
2.1 Basics of Supersymmetry	46
2.2 The Minimal Supersymmetric Standard Model	47
2.2.1 Lagrangian of chiral supermultiplets	47
2.2.2 Lagrangian of gauge supermultiplets	48
2.2.3 Lagrangian of soft SUSY breaking in the MSSM	49
2.2.4 R-parity	50
2.2.5 Neutralinos and charginos sector	51
2.3 Supersymmetric models	53
2.3.1 mSUGRA	53
2.3.2 GMSB	54
2.3.3 pMSSM	54

2.3.4	Simplified models	55
2.4	Search for SUSY electroweak production at the LHC	55
3	The Large Hadron Collider and the ATLAS detector	58
3.1	The Large Hadron Collider	58
3.1.1	The accelerator complex and injection chain	59
3.1.2	Luminosity and pile-up	61
3.2	The ATLAS detector	64
3.2.1	The ATLAS coordinate system	65
3.2.2	The Inner Detector	66
3.2.3	Calorimeters	68
3.2.4	Muon Spectrometer	72
3.2.5	Trigger and Data Acquisition	74
3.3	Physics object reconstruction in the ATLAS detector	76
3.3.1	Tracks	76
3.3.2	Primary vertices	78
3.3.3	Electrons and photons	80
3.3.4	Muons	81
3.3.5	Jets	84
3.3.6	Missing Transverse Momentum	90
3.4	Monte Carlo event simulation	91
3.4.1	Event generation	92
3.4.2	Detector simulation	93
3.4.3	Digitisation and reconstruction	94
3.4.4	Production campaign	94
4	The ATLAS pixel detector	95
4.1	General layout	95
4.2	Sensors	97
4.2.1	Planar sensor	99
4.2.2	3D sensor	100
4.3	Readout electronic chips	103
5	Instrumental measurements on the Pixel Detector during Run 2	105
5.1	Pixel-level leakage current measurements	105
5.1.1	Pixel-level leakage current measurements in the Pixel layers and disks	108
5.1.2	Pixel-level leakage current measurements in the IBL	118
5.1.3	Summary	125
5.2	Estimation of pixel-hit loss rate using real data	125
6	ATLAS during the High Luminosity LHC	134
6.1	The High-Luminosity LHC	135
6.2	The ATLAS Inner Tracker	137

6.2.1	The ITk Pixel detector	137
6.2.2	The ITk Strip detector	140
6.3	CMOS sensor for ITk replacement in second-half of HL-LHC	141
7	Search for electroweak production of charginos and neutralinos in final states with one lepton, jets and missing transverse momentum	150
7.1	Data and simulated samples	152
7.1.1	Dataset	152
7.1.2	Simulated samples	152
7.2	Reconstructed objects and triggers	154
7.2.1	Object definition	154
7.2.2	Overlap removal	156
7.2.3	Triggers	157
7.3	Event selection	158
7.3.1	Discriminating variables	158
7.3.2	Event preselection	159
7.3.3	Signal region optimization for C1C1-WW search	161
7.3.4	Signal region optimization for C1N2-WZ search	162
7.4	Background estimation	168
7.4.1	Diboson 2L estimation	168
7.4.2	W+jets and diboson 1L estimation	168
7.4.3	ttbar estimation	170
7.5	Systematic uncertainties	172
7.5.1	Experimental uncertainties	172
7.5.2	Theoretical uncertainties	173
7.6	Results	174
7.6.1	Background-only fit	174
7.6.2	Model-dependent fit	175
	Conclusion	179
	Bibliography	183

List of Figures

1.1	An illustration of the Higgs potential with $\mu^2, \lambda > 0$. For $\mu^2 > 0$, the minimum is at $ \phi _{\min} = \sqrt{\frac{2\mu^2}{\lambda}}$ formed by a degenerate ring of vacuum states. Choosing any point in the ring of minima breaks spontaneously the $SU(2)_L \times U(1)_Y$ symmetry [17].	37
1.2	Invariant mass distribution of di-photon candidates measured by the ATLAS experiment [20].	39
1.3	A summary of the current Higgs boson mass measurements in individual and combined analyses. The combined ATLAS and CMS result in Run 1 is added for comparison [22].	40
1.4	The best fit result on the signal strength for ggF, VBF, VH and $t\bar{t}H + tH$ production modes in each relevant decay channels of the Higgs boson [30].	41
1.5	Reduced coupling-strength modifiers $\kappa_F \frac{m_F}{v}$ for fermions ($F = t, b, \tau, \mu$) and $\sqrt{\kappa_V} \frac{m_V}{v}$ for weak gauge bosons ($V = W^\pm, Z$) as a function of their masses m_F and m_V , respectively, and the vacuum expectation value of the Higgs field $v = 246$ GeV. The SM prediction for both cases is also shown (dotted line). The black error bars represent 68% confidence level (CL) intervals for the measured parameters. For κ_μ the light error bars indicate the 95% CL interval. The coupling modifiers κ_F and κ_V are measured assuming no BSM contributions to the Higgs boson decays, and the SM structure of loop processes such as $gg \rightarrow H, H \rightarrow \gamma\gamma$ and $H \rightarrow gg$. The lower inset shows the ratios of the values to their SM predictions [30].	42
1.6	A summary on the test statistic for the spin-0 SM Higgs boson and the alternative spin-1 and spin-2 hypotheses based on the combined analysis $H \rightarrow ZZ$ and $H \rightarrow WW$ [31].	43
2.1	One-loop radiative corrections to the Higgs boson mass, due to (left) a fermion and (right) a scalar boson.	45
2.2	Cross section for the production of sparticles at LHC at 13 TeV center-of-mass energy as a function of the average mass of the pair produced [65].	56
2.3	The 95% CL exclusion limits on $\tilde{\chi}_1^\pm \tilde{\chi}_1^\mp$ and $\tilde{\chi}_1^\pm \tilde{\chi}_2^0$ production with SM-boson-mediated decays, as a function of the $\tilde{\chi}_1^\pm / \tilde{\chi}_2^0$ and $\tilde{\chi}_1^0$ masses. The production cross-section is for pure wino $\tilde{\chi}_1^\pm$ and $\tilde{\chi}_2^0$. Each individual exclusion contour represents a union of the excluded regions of one or more analyses [66].	57

3.1	A representation of the CERN accelerator complex	60
3.2	3.2a Peak instantaneous luminosity delivered to ATLAS as a function of time for the 2018 data-taking period. 3.2b Cumulative luminosity versus time delivered to ATLAS (green), recorded by ATLAS (yellow) and certified to be good quality data (blue) during stable beams for pp collisions at 13 GeV center-of-mass energy in 2015-2018 [82].	62
3.3	Distribution of the mean number of interactions per bunch-crossing for each year of Run 2 data at 13 TeV center-of-mass energy [82].	64
3.4	A schematic view of the ATLAS detector [68].	65
3.5	3.5a Cut-away view of the ATLAS Inner Detector. 3.5b Transverse section of the ATLAS Inner Detector with structural elements [68].	67
3.6	A cut-away view of the ATLAS calorimeter system [68].	69
3.7	3.7a View of the accordion geometry of the ECAL. 3.7b Schematic showing of a tile calorimeter module. The various components of the optical read-out, namely the tiles, the fibres and the photomultipliers, are shown [68].	71
3.8	A cut-away view of the ATLAS Muon Spectrometer [68].	73
3.9	Schematic illustration of the ATLAS Run 2 Trigger and Data Acquisition system [94].	75
3.10	Transverse view of an ATLAS detector segment with a representation of the interaction of different types of particles in the different sub-detectors [95]. The solid curves display the tracks of charged particles while the dashed ones correspond to neutral particles. The muon emerging from the interaction region traverses all detector layers and its track is determined by measurements from both the Inner Detector and Muon Spectrometer. The electron and photon are mainly stopped in the Electromagnetic calorimeter and are distinguished from one another by the presence or absence, respectively, of a track matching the corresponding energy deposit in the calorimeter. The proton and neutron are predominantly captured by the hadronic calorimeter with the former additionally leaving a track in the Inner Detector. Lastly, the neutrino goes through the whole detector without leaving any signature.	76
3.11	Sketch of the flow of tracks through the ambiguity solver [96].	78
3.12	The 3.12a transverse and 3.12b longitudinal impact parameter resolutions as functions of p_T in 2015 (with IBL) and 2012 (without IBL) [99]. Tracks were required to pass the Loose selection as discussed.	78
3.13	Vertex reconstruction efficiency as a function of the number of tracks in low- μ data compared to Monte Carlo simulation (Pythia 8 A2:MSTW2008LO). This measurement uses data corresponding to an integrated luminosity of $216.9 \mu\text{b}^{-1}$ [102].	79
3.14	3.14a Prompt electron identification efficiency obtained in simulated $Z \rightarrow ee$ events. 3.14b Fake electron misidentification efficiency obtained from a simulated multijet sample [105].	81

3.15	Reconstruction efficiency of muon candidates as a function of η for 3.15a Loose, Medium, 3.15b Tight and 3.15c High- p_T identification selection measured in $Z \rightarrow \mu\mu$ events [108].	83
3.16	Sketch of pp collision and resulting collimated spray of particles, a jet [111].	84
3.17	A visualization of a secondary vertex characterized by the distance displaced from the primary vertex in the transverse plane L_{xy} and the impact parameter of a track denoted as d_0 which is used for the SV reconstruction [112]	85
3.18	3.18a The set of b -tagging algorithms currently in use in the ATLAS experiment. 3.18b Diagram of the RNNIP tagger from input (left) to output (right) [113].	86
3.19	3.19a The light-flavour jet and 3.19b the c-jet rejections versus the b -jet tagging efficiency for the IP3D, SV1, JetFitter, MV2 and DL1 b -tagging algorithms evaluated on the baseline $t\bar{t}$ events [124].	88
3.20	Calibration stages for EM-scale jets [125].	89
3.21	ATLAS Monte Carlo simulation flow [127].	91
3.22	Schematic overview of a pp collision event generation emphasizing the different steps involved [129].	92
4.1	A schematic view of the IBL stave [143].	96
4.2	Section of the IBL barrel, the beam pipe and the services in r - ϕ [143].	96
4.3	Material budget distribution along η in units of radiation length X_0 of (4.3a) the IBL [143] and (4.3b) the pixel detector [142].	97
4.4	The present pixel module displaying a sensor [146].	99
4.5	Comparison of depletion zones in n^+ -in- n pixel sensors before (4.5a) and after (4.5b) type inversion [142].	100
4.6	Comparison of the edge designs of (4.6a) the ATLAS Pixel detector sensor and (4.6b) the planar IBL pixel sensor [143].	101
4.7	A schematic view of (left) the planar n^+ -in- n sensor and (right) the 3D n^+ -in- p sensor. The n^+ electrodes are illustrated in green, while the p^+ electrodes are coloured in red. d_c denotes the charge collection distance. [149].	102
4.8	Design of the columns of (left) FBK and (right) CNM 3D sensors [143].	102
4.9	Block diagram for the system architecture of B-Layer [142].	104
5.1	5.1a Feedback circuit [164]. 5.1b ADC map for the module L0_B04_S2_-A7_M1A.	108

5.2	The total leakage currents measured by SCAN_S000051508 (in blue) or the power supply (in red) of some module groups, each supplied by a common power supply unit, in (5.2a) B-Layer, (5.2b) Layer 1, (5.2c) Layer 2 and (5.2d) disks. The lower pads show the ratios of the MonLeak measurements to the power supply measurements. The power supply data were recorded by DCS during the time period when the scan took place. The unit is [mA].	111
5.3	The total leakage currents measured by SCAN_S000074820 (in blue) or the power supply (in red) of some module groups, each supplied by a common power supply unit, in (5.3a) B-Layer, (5.3b) Layer 1, (5.3c) Layer 2 and (5.3d) disks. The lower pads show the ratios of the MonLeak measurements to the power supply measurements. The power supply data were recorded by DCS during the time period when the scan took place. The unit is [mA].	112
5.4	The total leakage currents measured by SCAN_S000075304 (in blue) or the power supply (in red) of some module groups, each supplied by a common power supply unit, in (5.4a) B-Layer, (5.4b) Layer 1, (5.4c) Layer 2 and (5.4d) disks. The lower pads show the ratios of the MonLeak measurements to the power supply measurements. The power supply data were recorded by DCS during the time period when the scan took place. The unit is [mA].	113
5.5	The leakage currents in [mA] of the modules in (5.5a) B-Layer, (5.5b) Layer 1 and (5.5c) Layer 2 obtained from the MonLeak scan SCAN_S000051508. The blank cells represent the modules deactivated during the scan.	114
5.6	The leakage currents in [mA] of the modules in (5.6a) B-Layer, (5.6b) Layer 1 and (5.6c) Layer 2 obtained from the MonLeak scan SCAN_S000074820. The blank cells represent the modules deactivated during the scan.	115
5.7	The leakage currents in [mA] of the modules in (5.7a) B-Layer, (5.7b) Layer 1 and (5.7c) Layer 2 obtained from the MonLeak scan SCAN_S000075304. The blank cells represent the modules deactivated during the scan.	116
5.8	The z -dependence of the leakage current for B-Layer (black), Layer 1 (blue) and Layer 2 (red) in (5.8a) SCAN_S000051508, (5.8b) SCAN_S000074820 and (5.8c) SCAN_S000075304.	117
5.9	Block diagram of the GADC [144].	118
5.10	GADC as a function of pulser DAC, scanned by a Rx channel.	119
5.11	5.11a The GADC-versus-pulserDAC scans of the two Rx channels connected to the two FE-I4B chips of the module LI_S05_A_M1_A1, fitted with the linear function in Equation 5.6. 5.11b The leakage current map (in [μ A]) obtained from a MonLeak scan for the module LI_S05_A_M1_A1.	120

5.12	The total leakage currents of some module groups in the IBL, measured from (5.12a) SCAN_S000074783 or (5.12b) SCAN_S000075396 (in blue) with the data recorded by DCS (in red) during the same time periods when the two scans took place. The lower pads show the ratios of the MonLeak measurements to the DCS data. The unit is [mA].	122
5.13	The leakage currents in [mA] of the modules in the IBL obtained from the MonLeak scans (5.13a) SCAN_S000074783 and (5.13b) SCAN_S000075396.	123
5.14	The z -dependence of the leakage current for the IBL in (5.14a) SCAN_S000074783 and (5.14b) SCAN_S000075396.	124
5.15	The ToT distribution of Layer 1. An unnatural decrease of the number of hits can be observed in the high-ToT region (ToT > 250 BC).	126
5.16	Occupancy maps of the barrel layers and end-caps in the run 362776.	129
5.17	ToT distributions of the barrel layers and end-caps in the run 362776.	130
5.18	ToT distributions at high-ToT region of the Pixel barrel layers and end-caps in the run 362776. The exponential function in Equation 5.12 is fitted with several ToT bins just before the LC point.	132
6.1	The LHC baseline program including the HL-LHC [165].	134
6.2	Comparison of physics reach expected at the end of lifetime of the LHC and at the end of lifetime of the HL-LHC. The left plot shows uncertainty in the Higgs boson signal strengths. The right plot shows discovery reach (solid lines) and exclusion limits (dashed lined) for charginos and neutralinos in $\tilde{\chi}_1^\pm \tilde{\chi}_2^0 \rightarrow W^{(*)} \tilde{\chi}_1^0 Z^{(*)} \tilde{\chi}_1^0$ decays. Both taken from [169].	136
6.3	(6.3a) Display of the Inner Tracker layout for the HL-LHC phase of ATLAS. (6.3b) Schematic layout of the ITk with Strip (blue) and Pixel (red) detectors showing only one quadrant and only active detector elements; the horizontal axis is along the beam line with zero being the interaction point and the vertical axis is the radius measured from the interaction region [172].	138
6.4	Muon energy loss distribution for the CMOS layout (in red) and for the ITk layout 23-00-03 (in blue).	143
6.5	ToT distributions after digitization and clusterization using CMOS layout with Digital Clustering (in red) or ITk layout with Digital Clustering (in blue) or ITk layout with Analogue Clustering (in green) in (6.5a) L0, (6.5b) R0, (6.5c) L1, (6.5d) R0.5 and R1.	144
6.6	Cluster transverse width distributions after digitization and clusterization using CMOS layout with Digital Clustering (in red) or ITk layout with Digital Clustering (in blue) or ITk layout with Analogue Clustering (in green) in (6.6a) L0, (6.6b) R0, (6.6c) R0.5 and R1.	145

6.7	Cluster z -width distributions after digitization and clusterization using CMOS layout with Digital Clustering (in red) or ITk layout with Digital Clustering (in blue) or ITk layout with Analogue Clustering (in green) in (6.7a) L0, (6.7b) R0, (6.7c) L1, (6.7d) R0.5 and R1.	146
6.8	Distributions of the reconstructed track (6.8a) p_T , (6.8b) η , (6.8c) ϕ and (6.8d) transverse parameter d_0 , obtained using CMOS + Digital Clustering (in red), or ITk + Digital Clustering (in blue), or ITk + Analogue Clustering (in green).	147
6.9	The transverse impact parameter resolution σ_{d_0} (left plots) and the longitudinal impact parameter resolution σ_{z_0} (right plots) as functions of η for the three configurations: CMOS + Digital Clustering (in red), ITk + Digital Clustering (in blue) and ITk + Analogue Clustering (in green). From top to bottom, the plots are shown for the simulations using the $p_T = 100$ GeV, $p_T = 10$ GeV and $p_T = 1$ GeV muon samples.	148
7.1	Feynman diagram for electroweakino (7.1a) $\tilde{\chi}_1^\pm \tilde{\chi}_1^\mp$ and (7.1b) $\tilde{\chi}_1^\pm \tilde{\chi}_2^0$ pair production. One $\tilde{\chi}_1^\pm$ subsequently decays to a $\tilde{\chi}_1^0$ and a W boson which further decays leptonically. The other $\tilde{\chi}_1^\pm$ or $\tilde{\chi}_2^0$ subsequently decays to a $\tilde{\chi}_1^0$ and a W or Z boson which further decays hadronically.	151
7.2	The jet mass window cuts for (7.2a) the W -tagger and (7.2b) the Z -tagger at the 50% signal efficiency working point and (7.2c) the Higgs-tagger at the 68% signal efficiency working point.	156
7.3	Data/MC comparisons for discriminating variables used in the analysis. Only statistical uncertainties are considered in the error band.	160
7.4	Data/MC comparisons for discriminating variables used in the analysis. Only statistical uncertainties are considered in the error band.	161
7.5	$N - 1$ plots for the boosted SR of the C1C1-WW search, with exemplary signal points and all m_T bins included. In all figures except 7.5f, the significance in the lower pad is obtained by summing up all the events in the direction of the cut arrow and includes 30% uncertainty as well as MC statistical uncertainty. In 7.5f the significance is only computed on a bin-by-bin basis, i.e. not summing up all events in the direction of the cut arrow. Only statistical uncertainties are considered in the error band.	164
7.6	$N - 1$ plots for the resolved SR of the C1C1-WW search, with exemplary signal points and all m_T bins included. In all figures except 7.6f, the significance in the lower pad is obtained by summing up all the events in the direction of the cut arrow and includes 30% uncertainty as well as MC statistical uncertainty. In 7.6f the significance is only computed on a bin-by-bin basis, i.e. not summing up all events in the direction of the cut arrow. Only statistical uncertainties are considered in the error band.	165

7.7	$N - 1$ plots for the boosted SR of the C1N2-WZ search, with exemplary signal points and all m_T bins included. In all figures except 7.7f, the significance in the lower pad is obtained by summing up all the events in the direction of the cut arrow and includes 30% uncertainty as well as MC statistical uncertainty. In 7.7f the significance is only computed on a bin-by-bin basis, i.e. not summing up all events in the direction of the cut arrow. Only statistical uncertainties are considered in the error band.	166
7.8	$N - 1$ plots for the resolved SR of the C1N2-WZ search, with exemplary signal points and all m_T bins included. In all figures except 7.8f, the significance in the lower pad is obtained by summing up all the events in the direction of the cut arrow and includes 30% uncertainty as well as MC statistical uncertainty. In 7.8f the significance is only computed on a bin-by-bin basis, i.e. not summing up all events in the direction of the cut arrow. Only statistical uncertainties are considered in the error band.	167
7.9	The pulls between the number of events observed and the total background expected after-fit in control, validation and signal regions. . .	175
7.10	Correlation matrix of the background-only fit.	176
7.11	Values of the normalization factors and of the nuisance parameters after the background-only fit.	177
7.12	Expected exclusion limits at 95% for the C1C1-WW search.	178
7.13	Expected exclusion limits at 95% for the C1N2-WZ search.	178

List of Tables

1.1	Summary of fermions and their basic properties. In the SM, neutrinos are considered as massless particles. However, neutrino oscillation observations [12] provided evidence showing that neutrinos should have mass.	32
1.2	Summary of the characteristics of interacting bosons in the Standard Model.	32
1.3	Summary of the three quantum numbers including the weak isospin I_3 , the weak hypercharge Y , and the electric charge Q for fermions in the SM.	35
2.1	Chiral supermultiplets in the MSSM. The spin-0 fields are complex scalars, the spin-1/2 fields are left-handed Weyl spinors [43].	47
2.2	Gauge supermultiplets in the MSSM [43].	48
4.1	The mean radius, the number of staves and the number of modules in each stave for the barrel pixel layers.	97
4.2	The active area, the pixel size, the sensor thickness and the pixel array per FE for the barrel pixel layers.	98
4.3	The mean z , the number of sectors and the number of modules in each sector for the end-cap disks.	98
4.4	The active area, the pixel size, the sensor thickness and the pixel array per FE for the end-cap disks.	98
5.1	Selection of GADC inputs [144].	119
5.2	The average occupancy and the DH loss rate computed for each of barrel layers and end-caps using data of the run 362776.	128
5.3	The number of lost hits and the LC loss rate computed for each of Pixel layers and end-caps using data of the run 362776.	131
6.1	Parameters for the ITk pixel flat barrel and inclined rings, taken from [172]. The number of sensors per row refers to a complete stave in the central, flat part of the barrel where sensors are placed parallel to the beam line. The number of inclined rings refers to both sides of the detector. . . .	139
6.2	Parameters for the ITk pixel end-caps, taken from [172]. The radii refer to the innermost point of the modules on a ring. The number of rings refers to both sides of the detector.	139

7.1	The SM background MC simulation samples used in this analysis. The generators, the parton showers, tunes used for the underlying event, PDF sets and order in α_s of cross-section calculations used for yield normalisation are shown.	153
7.2	The single-electron triggers which are used in the analysis.	157
7.3	The single-muon triggers which are used in the analysis.	157
7.4	Definition of the resolved and boosted SRs for C1C1-WW search, obtained from the optimization procedure.	163
7.5	Definition of the resolved and boosted SRs for C1N2-WZ search, obtained from the optimization procedure.	163
7.6	Summary of the selection requirements for both DB2L CR and VR. . .	169
7.7	Summary of the selection requirements for WDB1L boost CR, VR1 and VR2.	169
7.8	Summary of the selection requirements for WDB1L resolved control and validation regions.	170
7.9	Summary of the selection requirements for Top boost CR, VR1 and VR2. .	171
7.10	Summary of the selection requirements for Top resolved control and validation regions.	171

Introduction

What are we made of? Or what are the fundamental constitutive elements of matter? Or what is the description of nature? These are the fundamental questions that have fascinated humans for centuries. The Standard Model (SM) of particle physics has been developed since the 20th century in order to find out the answer for these questions. It is a theoretical model that uses mathematical formalism to describe properties of the elementary particles and their fundamental interactions. So far the SM has become a remarkably successful theory with many precise tests confirming its validity and predictive power. Despite its successes, the SM is still not a complete description of nature. There are various experimental observations implying that there must be physics beyond it. The existence of Dark Matter which is required to explain numerous astrophysical and cosmological observations, the neutrino mass required for the observed neutrino oscillations and the strain between the SM predicted and experimentally observed muon anomalous magnetic moment are examples of such phenomena that are not able to be understood in the framework of the SM. Additionally, although not directly contradicting the SM, many theoretical difficulties that have arisen within our present knowledge of fundamental physics, such as the hierarchy problem or the unification of gauge coupling constants, suggest the need of new physics.

The discovery of a Higgs-boson-like particle with a mass of ~ 125 GeV in 2012 at the ATLAS and CMS experiments of the Large Hadron Collider (LHC) has confirmed the impressive success of the SM, but also emphasized the hierarchy problem in the Higgs boson mass. Among various theories beyond the SM (BSM), *Supersymmetry* (SUSY), an extension to the SM, becomes more favorable because of its elegance and relative simplicity. This theory postulates the existence of a new fermion (boson) supersymmetric partner for each boson (fermion) in the SM and therefore address directly the hierarchy problem. Furthermore, in the case of an additional supposed Z_2 symmetry, known as the R -parity conservation, the lightest supersymmetric particle (LSP) must be stable, weakly interacting and thus can be a viable candidate for Dark Matter. SUSY also provides a possibility for a unification of the strong and electroweak interaction at high energy scale.

The LHC is currently the largest and most energetic particle collider in the world. This machine collides protons at a center-of-mass energy of 13 TeV in the 27 km tunnel located 100 m underground at CERN, Geneva. The ATLAS detector, installed around one of the four interaction points where protons beams are collided in the LHC ring, is the largest general-purpose detector ever built. It exploits information from pp collisions to test the SM predictions and search for the sign of new physics

at TeV scale as well. The innermost sub-system of ATLAS is the pixel detector which contains modules each composed of a silicon sensor and readout chips. The sensor is segmented into small pixel cells that are interconnected to readout cells of the chips via bump balls. This design brings the pixel detector a fine granularity, being beneficial for the detector tracking performance, especially the vertex reconstruction. As the part closest to the beam pipe, the pixel detector suffers a large amount of radiation damage, which spoils the detector performance. One of the most characterized method to monitor the silicon radiation damage is measuring the leakage current. For the pixel detector, the leakage current can be measured either at module granularity level using the power supply sub-system or at the pixel granularity level using the MonLeak mechanism. This thesis focuses on the latter and my work involving this, as of my qualification task for the ATLAS authorship, is making use of outputs of the MonLeak scans to retrieve and study the pixel-level leakage current in the pixel modules. Another challenge arising for the pixel detector is the fact that pixel hit data can be lost during the readout mechanism due to the high rate of hits from the detector at the high luminosities of the LHC. So far only an ad-hoc fraction of 0.9% has been applied to simulation in order to account for the inefficiency and this was found to be no longer consistent with the actual data in the LHC Run 2 (a data taking period between 2015-2018). For the work related to this challenge, I have contributed to develop new methods using real data to provide a more precise estimation of the hit loss rate which will then be used to replace the canonical 0.9% in Monte-Carlo simulation.

The LHC is planning to enter a high luminosity phase (HL-LHC) in 2027 to achieve an even higher precision and statistical power. In this phase, the instantaneous luminosity is expected to reach up to $7.5 \times 10^{34} \text{ cm}^{-2}\text{s}^{-1}$, higher than the typical luminosity of Run 2 by approximately a factor of 5. This will result in an average of 200 inelastic pp collisions per bunch crossing and thus will generate a much harsher environment for the ATLAS detector with much higher radiation levels compared to Run 3 (2022-2024). In order to allow ATLAS to continue its investigation of the high energy physics spectrum with equivalent or even greater physics performance compared to the current detector, its sub-systems will undergo some upgrades to cope with the high radiation level of the HL-LHC. A new High Granularity Timing Detector (HGTD) will be added and, particularly, the ATLAS Inner Detector will be fully replaced by a new all-silicon Inner Tracker (ITk). During the entire HL-LHC lifetime, an expected integrated luminosity of up to 4000 fb^{-1} will be delivered to the ATLAS detector, corresponding to an accumulated radiation fluence of up to $2 \times 10^{16} \text{ n}_{\text{eq}}/\text{cm}^2$ to which the innermost ITk layers will have to be exposed. However, the ITk pixel sensors can only withstand the maximum fluence of roughly $10^{16} \text{ n}_{\text{eq}}/\text{cm}^2$ and therefore these layer are expected to be exchanged after having integrated half of the expected luminosity i.e by the HL-LHC half-life. For this replacement, CMOS sensors could be the most promising candidates to replace the traditional pixel sensors. The CMOS technology is commercially mature and can bring many advantages to the ITk detector. The CMOS sensors can work efficiently with a smaller thickness and

pixel size, improving the detector granularity and consequently improving the flavour taggings. The achievable monolithic design of CMOS can also reduce the detector cost as well as the multiple scattering effect. My involvement in this topic is simulating a new ITk detector layout with the CMOS sensors of $50 \mu\text{m}$ thick and $25 \times 25 \mu\text{m}^2$ pixel size used in the innermost layers. The simulation has been done for both the new layout and the baseline layout using $p_T = 100 \text{ GeV}$, $p_T = 10 \text{ GeV}$ and $p_T = 1 \text{ GeV}$ single muon samples in order to evaluate the use of CMOS sensors and their advantages.

Beside the work regarding the detector instrumentation, my main work in this thesis involves an analysis targeting SUSY searches for electroweak production of charginos and neutralinos at the ATLAS detector. Charginos $\tilde{\chi}_i^\pm$ ($i = 1, 2$) and neutralinos $\tilde{\chi}_j^0$ ($j = 1, 2, 3, 4$) are the mass eigenstates which are linear superpositions of supersymmetric partners of Higgs and the gauge bosons. They are suggested to have masses near the electroweak scale. In scenarios where the strongly produced SUSY particles are heavier than a few TeV, the direct production of these electroweak SUSY particles may be the dominant SUSY production mechanism at the LHC. The searches are conducted in the context of R -parity conserving model with the lightest neutralino ($\tilde{\chi}_1^0$) being a LSP, while the lightest chargino ($\tilde{\chi}_1^\pm$) and next-to-lightest neutralino ($\tilde{\chi}_2^0$) being nearly mass degenerate. The analysis presented in this document focuses on the case in which the $\tilde{\chi}_1^\pm$ decays into a W boson and a $\tilde{\chi}_1^0$, while the $\tilde{\chi}_2^0$ into a Z boson and a $\tilde{\chi}_1^0$. The signature is characterised by the presence of exactly one light lepton (electron or muon), jets and missing transverse momentum from the $\tilde{\chi}_1^0$ s and neutrinos. This analysis is performed for the first time at ATLAS and targets an integrated luminosity of 139 fb^{-1} corresponding to the full Run 2 pp collision data recorded by ATLAS. It employs the recent ATLAS large-R jet reconstruction technique, the Particle Flow jets and a strategy that was well developed in the previous $Wh1lbb$ search [1] to enhance the search sensitivities. The analysis is being carried out by the ATLAS SUSY one-lepton team and I am one of the main contributors in this analysis. Specifically, I have contributed mostly in developing the one-lepton framework, launching the production, optimising the analysis sensitivity, estimating the theoretical systematic uncertainties and carrying out the fit and statistical interpretation of the results.

The present thesis manuscript is organised as follows:

- Chapter 1 summarizes the fundamental concepts of the Standard Model in Particle Physics.
- Chapter 2 presents the basics of Supersymmetry, in particular the Minimal Supersymmetric Standard Model (MSSM) as well as the charginos and neutralinos sector with searches for their production in the context of simplified models at the LHC.
- Chapter 3 provides an overview of the Large Hadron Collider and the ATLAS detector. This is then followed by a description of the physics object reconstruction and the Monte Carlo event simulation procedure in the ATLAS detector.

- Chapter 4 describes in details the layout, the sensor technology and the readout electronic chips used in the present ATLAS Pixel Detector.
- Chapter 5 discusses my work involving the Pixel Detector. This chapter begins with the study of the pixel-level leakage current measurements and then demonstrates the study for the pixel-hit loss rate estimation using real data.
- Chapter 6 summarizes the plan and physics motivation of the HL-LHC phase. In addition, an overview of the ATLAS upgrades and a description of the ITk detector in the HL-LHC are also given in this chapter. The last section of this chapter, Section 6.3 presents my work related to the simulation of CMOS sensors for the ITk replacement in the second-half of the HL-LHC.
- Chapter 7 illustrates the analysis conducted to search for SUSY electroweak production at the LHC Run 2 (as mentioned above). It includes the main points of the analysis strategy and the important outcome of the present work.

1 The Standard Model in Particle Physics

With several predictions being experimentally tested at an impressive level of precision, the Standard Model (SM) has been a remarkably successful theory in describing the most fundamental properties and interactions of elementary particles that compose the natural world. The SM is a Quantum Field Theory (QFT), a framework mixing quantum mechanics and special relativity, and describes three out of the four fundamental interactions: electromagnetic, weak, and strong interactions. The remaining interaction, gravity, is currently described in the domain of classical physics with General Relativity. Its description in the SM has been a long standing theoretical problem, due to the fact that there has not been a consistent QFT description for gravity so far. Fortunately, in the field of particle physics, the gravitational interaction is often ignored due to its negligible effect.

In the context of QFT, fundamental particles are described by *quantum fields* which are operator functions on the quantum mechanical Hilbert space of the particle states. Three specific categories of fields corresponding to three classes of particles are defined. The first one is scalar fields ϕ which describes spin-0 particles, while the second one is vector fields A_μ ($\mu = 0, 1, 2, 3$) describing spin-1 particles and the last one is spinor fields ψ describing spin-1/2 particles. The mathematical expression of the SM is inspired from the Lagrangian formalism of the classical mechanics. The SM Lagrangian \mathcal{L}_{SM} is expressed as a function of fields and their partial derivatives with respect to the space-time coordinates.

The dynamics and kinematics of a system are controlled by its Lagrangian under imposed transformations which leave the Lagrangian invariant. These are known as *symmetries*. In the case of the SM, the Lagrangian is required to be invariant under the Lorentz symmetry and the following gauge symmetry group:

$$SU(3) \times SU(2) \times U(1). \tag{1.1}$$

The $SU(3)$ group is the symmetry group of *Quantum chromodynamics* (QCD) [2, 3, 4] which is a gauge theory describing the strong interaction between colour charged particles. This theory was developed in the second-half of the 20th century in order to provide an explanation for the structure and interaction of the newly discovered hadron [5]. The QCD was constructed based on the success of an earlier theory that describes the electromagnetic interaction between electrically charged particles based on $U(1)$ gauge group. This is known as *Quantum electrodynamics* (QED) [6]. Few years

before the establishment of the QCD, Sheldon Glashow, Abdus Salam and Steven Weinberg suggested an idea for the *electroweak* theory, which is a common framework of the electromagnetic and weak interactions based on a $SU(2) \times U(1)$ group [7, 8]. In addition, a mechanism of spontaneous symmetry breaking [9, 10, 11] was introduced at around the same period to generate SM particles' masses while maintaining the gauge invariance of the electroweak Lagrangian.

1.1 Elementary particles in the Standard Model

Depending on the spin number, elementary particles in the SM are classified into *fermions* or *bosons*. The former are particles with spin of 1/2 while the latter are particles whose spin is an integer number ($s = 0, 1$). For each particle, there exists an associated anti-particle which has the same mass but opposite *additive quantum numbers*¹.

Fermions are further separated into two categories based on whether they interact strongly. Fermions which also act through the strong force and hence carry a colour charge are called *quarks*. There are six quark types (or flavours) organised in three generations with increasing mass. In contrast, fermions which do not "feel" the strong force and thus do not carry a colour charge are known as *leptons*. Similarly to quarks, there are also six lepton types categorized into three generations of increasing mass. Table 1.1 summarizes the basic properties of fermions (quarks and leptons). Fermions are often considered as the building block of matter as they are main ingredients in the formation of nuclei, and subsequently, atoms.

On the other hand, spin-1 bosons are the mediators of the three fundamental interactions in the SM. The last particle in the SM, the Higgs boson, is a scalar (spin-0) boson and is responsible for the mechanism of the spontaneous electroweak symmetry breaking. The characteristics of bosons and the corresponding interaction that they carry are shown in Table 1.2.

1.2 The gauge theory in the Standard Model

A gauge theory is established by requiring the Lagrangian of a free system to be invariant under the local gauge transformation in which the spinor (fermion) fields transform as follows:

$$\psi \rightarrow \exp\left(i \sum_{a=1}^n \alpha^a(x^\mu) T_a\right) \psi, \quad (1.2)$$

where $\alpha^a(x^\mu)$ denotes the local phase as a function of the space-time, while T_a ($a = 1, \dots, n$) denote the generators of the gauge group and are chosen depending on the representation of the fields. In the case of the SM, one considers the $U(1)$, $SU(2)$ and $SU(3)$ groups. Based on the Lie algebra, the generators hold the commutation relation

¹Additive quantum numbers are those related to continuous symmetries, e.g electric charge.

Fermion type	Generation	Flavour	Charge	Mass [GeV]
Lepton	1 st	ν_e (e neutrino)	0	-
		e (electron)	-1	511×10^{-6}
	2 nd	ν_μ (μ neutrino)	0	-
		μ (muon)	-1	106×10^{-3}
	3 rd	ν_τ (τ neutrino)	0	-
		τ (tau)	-1	1.777
Quark	1 st	u (up)	2/3	2.2×10^{-3}
		d (down)	-1/3	4.7×10^{-3}
	2 nd	c (charm)	2/3	1.28
		s (strange)	-1/3	0.096
	3 rd	t (top)	2/3	173.1
		b (bottom)	-1/3	4.18

Table 1.1: Summary of fermions and their basic properties. In the SM, neutrinos are considered as massless particles. However, neutrino oscillation observations [12] provided evidence showing that neutrinos should have mass.

Boson	Spin	Charge	Mass [GeV]	Interaction
γ (photon)	1	0	0	Electromagnetic
W^\pm	1	± 1	80.4	Weak
Z	1	± 0	91.2	
g (gluon)	1	0	0	Strong
H (Higgs)	0	0	125.09	-

Table 1.2: Summary of the characteristics of interacting bosons in the Standard Model.

given as:

$$[T_a, T_b] = i f_{abc} T_c, \quad (1.3)$$

where f_{abc} is a real number and is known as the structure constant of the symmetry group.

In addition, the gauge vector field W_μ^a needs to transform as:

$$W_\mu^a \rightarrow W_\mu^a + \frac{1}{g} \partial_\mu \alpha^a(x) + f_{abc} W_\mu^b \alpha^c(x), \quad (1.4)$$

where g is the coupling constant of the interaction. The gauge invariance of the Lagrangian of the theory is protected by replacing the partial derivative ∂_μ with a covariant derivative D_μ :

$$\partial_\mu \rightarrow D_\mu = \partial_\mu - i g T_a W_\mu^a. \quad (1.5)$$

The kinetic term $\mathcal{L}_{W,kinetic}$ of the gauge field W_μ^a is expressed in terms of the field

strength tensors $F_{\mu\nu}^a$:

$$\mathcal{L}_{W,kinetic} = -\frac{1}{4}F_{\mu\nu}^a F_a^{\mu\nu}, \quad (1.6)$$

where

$$F_{\mu\nu}^a = \partial_\mu W_\nu^a - \partial_\nu W_\mu^a + g f_{abc} W_\mu^b W_\nu^c. \quad (1.7)$$

The locally gauge invariant Lagrangian describing massless fermions and gauge bosons in the SM is generally defined as:

$$\mathcal{L} = -\frac{1}{4}F_{\mu\nu}^a F_a^{\mu\nu} + \bar{\psi} i \gamma^\mu D_\mu \psi, \quad (1.8)$$

where γ^μ are the Dirac gamma matrices.

1.3 The strong interaction

As already mentioned, the strong interaction is described by QCD which is the gauge theory formulated based on the $SU(3)_C$ symmetry group where C is the colour charge. Quarks are the only fermions participating in the strong interaction and carrying a colour charge that can be one of either the three colours (red, green and blue) or the three anti-colours (anti-red, -green and -blue). In QCD, quarks are characterized by triplets of the spinor fields Ψ_f for each quark flavour ($f = u, d, c, s, t, b$). The covariant derivative can be then derived in the following form according to the formalism of the $SU(3)_C$ gauge theory group:

$$D_\mu = \partial_\mu - i g_s \frac{\lambda_a}{2} G_\mu^a, \quad (1.9)$$

where $\lambda_a/2$ ($a = 1, \dots, 8$) are the eight generators of the $SU(3)_C$ group and they are defined as the eight Gell-Mann matrices, g_s denotes the strong coupling constant, while G_μ^a are eight gauge vector fields describing gluons, mediators of the strong force. The field strengths of gluons are expressed as follows:

$$G_{\mu\nu}^a = \partial_\mu G_\nu^a - \partial_\nu G_\mu^a + g_s f_{abc} G_\mu^b G_\nu^c. \quad (1.10)$$

Gluons also carry a colour charge themselves (a colour or an anti-colour) and the self-interaction among them allows for colour exchanges between quarks.

The strong interactions of quarks and gluons are described with the following QCD Lagrangian:

$$\mathcal{L}_{\text{QCD}} = \sum_f \bar{\Psi}_f i \gamma^\mu D_\mu \Psi_f - \frac{1}{4} G_{\mu\nu}^a G_a^{\mu\nu}. \quad (1.11)$$

An important property of the strong interaction is that its running coupling constant α_s becomes smaller with respect to increasing energy scale of the interaction process,

as shown in the following expression at one-loop level [13]:

$$\alpha_s(Q^2) = \frac{1}{\beta_0 \ln\left(\frac{Q^2}{\Lambda^2}\right)}, \quad (1.12)$$

where Q^2 is the energy scale, Λ denotes the fundamental energy scale of the strong interactions and β_0 is a constant calculated by Gross, Wilczek and Politzer [14, 15]. At short distances (high energy scales) the running coupling constant of strong interactions becomes small and therefore quarks and gluons interact very weakly. This is called the *asymptotic freedom* of quarks and gluons. However, the strong coupling constant becomes very large at large distances (low energy scales). Therefore, if quarks get separated, the potential energy between them increases up to a given threshold at which it is energetically more favorable that quark–anti-quark pairs are created. For this reason quarks cannot be observed in isolation, instead they cluster to colour neutral groups of quarks, the hadrons. This phenomenon is known as *colour confinement*, the process of the creation of quark–anti-quark pairs and clustering to hadrons are denoted as *hadronisation* or *fragmentation*. The resulting hadrons do not solely consist of the valence quarks that built up the hadron. In addition, there is an indefinite number of sea (anti-)quarks and gluons that carry parts of the momentum of the hadron and constantly exchange colour charge among themselves.

1.4 The electroweak interaction

The electroweak model is a common theory of the electromagnetic and weak interactions, proposed by Glashow, Salam and Weinberg [7, 8]. This theory is formulated based on the local gauge symmetry group of $SU(2)_L \times U(1)_Y$. $SU(2)_L$ is the local gauge symmetry group of the weak isospin and the L index means that only left-handed components of fermions participate in the weak interaction, i.e coupling to the gauge fields of the $SU(2)_L$ group, while right-handed ones do not undergo the weak interaction, i.e no coupling to the $SU(2)_L$ gauge fields. This reflects the parity violation observed in Wu's experiment in 1957 [16]. The Y index denotes the weak hypercharge and $U(1)_Y$ is the local gauge symmetry group of the weak hypercharge.

According to this, the spinor fields of fermions are grouped into left-handed doublets and right-handed singlets, as follows:

$$L_i = \begin{pmatrix} \nu_i \\ l_i \end{pmatrix}_L, \quad l_{i,R}, \quad Q_i = \begin{pmatrix} u_i \\ d_i \end{pmatrix}_L, \quad u_{i,R}, \quad d_{i,R}. \quad (1.13)$$

In Equation 1.13, $i = 1, 2, 3$ is the index of the three fermion generations. It should be noted that only left-handed neutrinos exist within the SM framework. Beside the mass, the fermion fields are also characterized by the third component of the weak isospin I_3 , the weak hypercharge Y and the electric charge Q . The relation between these three quantum numbers is expressed by the following Gell-Mann-Nishijima

Fermion type	Representation in $SU(2)_L \times U(1)_Y$			I_3	Y	Q
Lepton	$\begin{pmatrix} \nu_e \\ e \end{pmatrix}_L$	$\begin{pmatrix} \nu_\mu \\ \mu \end{pmatrix}_L$	$\begin{pmatrix} \nu_\tau \\ \tau \end{pmatrix}_L$	$+\frac{1}{2}$	-1	0
	e_R	μ_R	τ_R	$-\frac{1}{2}$	-1	-1
				0	-2	-1
Quark	$\begin{pmatrix} u \\ d \end{pmatrix}_L$	$\begin{pmatrix} c \\ s \end{pmatrix}_L$	$\begin{pmatrix} t \\ b \end{pmatrix}_L$	$+\frac{1}{2}$	$+\frac{1}{3}$	$+\frac{2}{3}$
	u_R	c_R	t_R	$-\frac{1}{2}$	$+\frac{1}{3}$	$-\frac{1}{3}$
	d_R	s_R	b_R	0	$+\frac{4}{3}$	$+\frac{2}{3}$
			0	$-\frac{2}{3}$	$-\frac{1}{3}$	

Table 1.3: Summary of the three quantum numbers including the weak isospin I_3 , the weak hypercharge Y , and the electric charge Q for fermions in the SM.

formula:

$$Q = I_3 + \frac{Y}{2}. \quad (1.14)$$

Table 1.3 summarizes the values of the three quantum numbers for all fermions.

There are four generators in the $SU(2)_L \times U(1)_Y$ gauge group, three are from $SU(2)_L$ and correspond to three gauge vector fields W_μ^a ($a = 1, 2, 3$), while the remaining one is from $U(1)_Y$ and corresponds to an additional boson field B_μ . The Lagrangian \mathcal{L}_{EW} of the electroweak theory is then derived based on the principles of constructing a gauge-invariant field theory for the electroweak interaction as follows:

$$\begin{aligned} \mathcal{L}_{EW} = & \sum_{j=1}^3 i(\bar{L}_j \gamma^\mu D_\mu L_j + \bar{Q}_j \gamma^\mu D_\mu Q_j + \bar{l}_{j,R} \gamma^\mu D_\mu l_{j,R} + \bar{u}_{j,R} \gamma^\mu D_\mu u_{j,R} + \bar{d}_{j,R} \gamma^\mu D_\mu d_{j,R}) \\ & - \frac{1}{4} W_{\mu\nu}^a W_a^{\mu\nu} - \frac{1}{4} B_{\mu\nu} B^{\mu\nu}. \end{aligned} \quad (1.15)$$

In Equation 1.15, D_μ is the covariant derivative and is expressed as:

$$D_\mu = \begin{cases} \partial_\mu - \frac{1}{2} i g_W \sigma_a W_\mu^a - \frac{1}{2} i g_Y Y B_\mu & \text{for left-handed fields} \\ \partial_\mu - \frac{1}{2} i g_Y Y B_\mu & \text{for right-handed fields} \end{cases}, \quad (1.16)$$

where σ_a denote the Pauli matrices, g_W and g_Y determine the coupling strengths of the fermions to the gauge bosons W_μ^a and B_μ respectively. The field strength tensors of these gauge vector fields are:

$$\begin{aligned} W_{\mu\nu}^a &= \partial_\mu W_\nu^a - \partial_\nu W_\mu^a + g_W \epsilon_{abc} W_\mu^b W_\nu^c, \\ B_{\mu\nu} &= \partial_\mu B_\nu - \partial_\nu B_\mu, \end{aligned} \quad (1.17)$$

with ϵ_{abc} is the Levi-Civita tensor, representing the structure constant of the $SU(2)_L$

group. The W_μ^1 and W_μ^2 mix together to give the charged W^\pm vector bosons as follows:

$$W_\mu^\pm = \frac{1}{\sqrt{2}}(W_\mu^1 \mp iW_\mu^2), \quad (1.18)$$

whereas the rotation of W_μ^3 and B_μ in the (I_3, Y) plane results in the neutral Z and photon vector bosons, as:

$$\begin{pmatrix} Z_\mu \\ A_\mu \end{pmatrix} = \begin{pmatrix} \cos \theta_W & \sin \theta_W \\ -\sin \theta_W & \cos \theta_W \end{pmatrix} \begin{pmatrix} W_\mu^3 \\ B_\mu \end{pmatrix}, \quad (1.19)$$

where θ_W is the mixing angle and is determined by

$$\cos \theta_W = \frac{g_W}{\sqrt{g_W^2 + g_Y^2}}. \quad (1.20)$$

1.5 The electroweak spontaneous symmetry breaking

The electroweak Lagrangian, as constructed in Section 1.4, does not include any mass terms for the gauge bosons and fermions as they are prohibited by the Lagrangian invariance under the $SU(2)_L \times U(1)_Y$ group transformations. This does not reflect the experimental observations which confirm that these particles are massive and therefore necessitate a mechanism which can generate masses for these particles without breaking the gauge invariance of the theory. The Brout-Englert-Higgs (BEH) mechanism (also referred to as the Higgs mechanism) for the spontaneous breaking of the $SU(2)_L \times U(1)_Y$ symmetry was proposed in 1964 in order to serve this end.

This mechanism starts with introducing a complex scalar field ϕ , the Higgs field, which has an isospin doublet structure as follows:

$$\phi = \begin{pmatrix} \phi^+ \\ \phi^0 \end{pmatrix} = \frac{1}{\sqrt{2}} \begin{pmatrix} \phi_1 + i\phi_2 \\ \phi_3 + i\phi_4 \end{pmatrix}. \quad (1.21)$$

This field carries the electroweak quantum numbers of $I_3 = \pm \frac{1}{2}$ and $Y = 1$ and is described by the Lagrangian given as:

$$\mathcal{L}_{\text{Higgs}} = (D_\mu \phi)^\dagger (D^\mu \phi) - V(\phi). \quad (1.22)$$

In this equation, the covariant derivative D_μ is the same as the one defined in Equation 1.16 with $Y = 1$, $V(\phi)$ is the potential term of the Higgs Lagrangian and has the following form:

$$V(\phi) = -\mu^2 \phi^\dagger \phi + \frac{\lambda}{4} (\phi^\dagger \phi)^2, \quad (1.23)$$

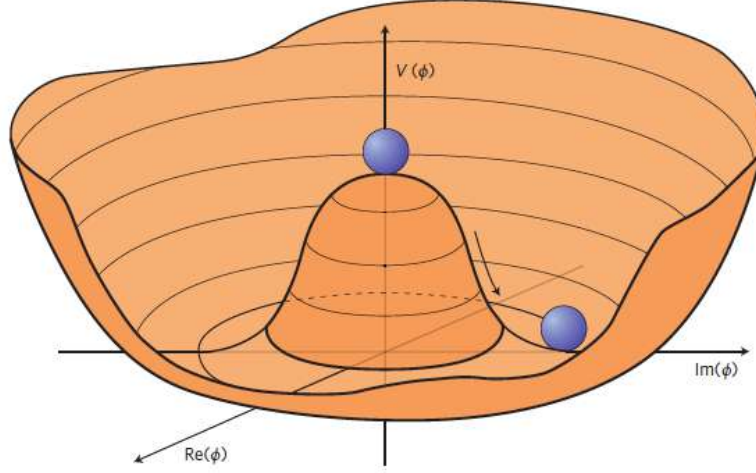


Figure 1.1: An illustration of the Higgs potential with $\mu^2, \lambda > 0$. For $\mu^2 > 0$, the minimum is at $|\phi|_{\min} = \sqrt{\frac{2\mu^2}{\lambda}}$ formed by a degenerate ring of vacuum states. Choosing any point in the ring of minima breaks spontaneously the $SU(2)_L \times U(1)_Y$ symmetry [17].

where λ represents the self-coupling parameter and μ is the parameter associated to the Higgs field mass. To have a stable vacuum, i.e a finite minimal value of the potential, the condition $\lambda > 0$ is required; the Higgs field configuration at the minimum potential is referred to as the vacuum or ground state with its absolute value known as the *vacuum expectation value* (vev). In addition, $\mu^2 > 0$ is required in order for the potential to have a “Mexican hat” shape, as illustrated in Figure 1.1. The vev of the Higgs potential under these conditions is:

$$\langle 0|\phi|0\rangle = \frac{1}{\sqrt{2}} \begin{pmatrix} 0 \\ v \end{pmatrix} \quad \text{with} \quad v = \frac{2\mu}{\sqrt{\lambda}}. \quad (1.24)$$

The ground state is *selected* such that the neutral component ϕ^0 of the Higgs doublet has the vacuum expectation value. Although the Lagrangian is still invariant under the $SU(2)_L \times U(1)_Y$ group, this ground state does not remain symmetric under this group transformation anymore. It is however invariant under the $U(1)_{em}$ local gauge symmetry group which allows to preserve the electromagnetic gauge symmetry. This is known as the *electroweak spontaneous symmetry breaking*. One can rewrite the Higgs doublet ϕ in a simple form by expanding ϕ around its vev and using the unitary gauge, as follows:

$$\phi = \frac{1}{\sqrt{2}} \begin{pmatrix} 0 \\ v + H \end{pmatrix}, \quad (1.25)$$

where H is a real scalar field representing a neutral scalar particle which is so-called Higgs boson with mass $m_H = \mu\sqrt{2}$. By inserting Equation 1.25 into the kinetic part of

the Higgs Lagrangian in Equation 1.22 and reforming the gauge bosons W_μ^a ($a = 1, 2, 3$) and B_μ as in Equations 1.18 and 1.19, one can obtain the masses of the physical gauge bosons W_μ^\pm , Z_μ and A_μ :

$$m_{W^\pm} = \frac{v}{2} g_W. \quad m_Z = \frac{v}{2} \sqrt{g_W^2 + g_Y^2}, \quad m_A = 0. \quad (1.26)$$

It can be seen that, after the electroweak spontaneous symmetry breaking following the EBH mechanism, the masses of the weak interaction mediators, W^\pm and Z , are generated, while photon remains massless.

The masses of charged fermions can be generated by their interaction with the Higgs field which is so-called the Yukawa interaction. It is described using the Yukawa Lagrangian given by:

$$\mathcal{L}_{\text{Yukawa}} = -y_{i,l}(\bar{L}_i\phi)l_{i,R} - y_{i,u}(\bar{Q}_i\phi^c)u_{i,R} - y_{i,d}(\bar{Q}_i\phi)d_{i,R} + h.c., \quad (1.27)$$

where $i = 1, 2, 3$ is the index of the fermion generation, $y_{i,l}$ is the Yukawa coupling of charged lepton, $y_{i,u}$ is the Yukawa coupling of up-type quark, $y_{i,d}$ is the Yukawa coupling of down-type quark, and $\phi^c = i\sigma_2\phi^*$ is the charge-conjugate of the Higgs field with σ_2 being the second Pauli matrix. By implementing the Higgs field in the form of Equation 1.25 into the Yukawa Lagrangian, the charged fermion's mass terms are created and their masses are found to be proportional to the corresponding Yukawa couplings, as follows:

$$m_{i,l} = \frac{v}{\sqrt{2}}y_{i,l}, \quad m_{i,u} = \frac{v}{\sqrt{2}}y_{i,u}, \quad m_{i,d} = \frac{v}{\sqrt{2}}y_{i,d}. \quad (1.28)$$

The entire picture for the SM Lagrangian under the $SU(3)_C \times SU(2)_L \times U(1)_Y$ symmetry can be derived as:

$$\mathcal{L}_{SM} = \mathcal{L}_{QCD} + \mathcal{L}_{EW} + \mathcal{L}_{Higgs} + \mathcal{L}_{Yukawa} \quad (1.29)$$

This encapsulates all the fundamental interactions of the elementary particles. However, there are 18 free parameters in the SM Lagrangian. They comprise three gauge couplings, three lepton masses, six quark masses, four parameters in the mass mixing matrix for quarks, which is known as the Cabibbo-Kobayashi-Maskawa (CKM) matrix [18, 19], and two parameters in the Higgs sector (m_H and λ) as well.

1.6 Higgs boson measurements

The ATLAS and CMS experiments at the Large Hadron Collider (LHC) (see Chapter 3) found the Higgs boson in 2012 [20, 21], and they remain the world's only physics experiments capable of producing and studying the Higgs boson's characteristics to this day. The discovery of the Higgs boson is immediately represented in the

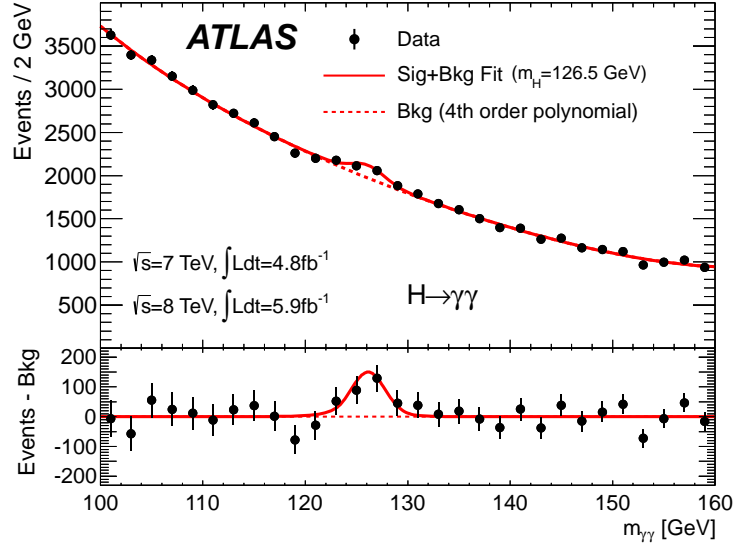


Figure 1.2: Invariant mass distribution of di-photon candidates measured by the ATLAS experiment [20].

appearance of a peak resonance in the di-photon invariant mass distribution, as shown in Figure 1.2. The two experiments have conducted several analyses of its properties in order to confirm that this mass resonance at around 125 GeV is the Higgs boson of the SM. These analyses include measurements of massive particles' couplings to the Higgs boson and investigation of the spin-CP state of the Higgs boson.

Higgs boson mass measurements The Higgs boson mass is often measured via clean channels of the Higgs boson decays including $H \rightarrow \gamma\gamma$ and $H \rightarrow ZZ^* \rightarrow 4l$. The Higgs mass can be well reconstructed exploiting the high resolution of the lepton and photon reconstruction. Figure 1.3 summarizes the recent results of various analyses which have been performed to measure the Higgs boson mass at the ATLAS experiment. The measurement using the combined Run 1 and a part of Run 2 data recorded by ATLAS has shown that the Higgs mass is $m_H = 124.97 \pm 0.24$ GeV [22].

Couplings measurements The couplings of massive bosons and fermions with the Higgs boson in the SM are given by:

$$g_V \sim 2 \frac{m_V^2}{v}, \quad y_f = \sqrt{2} \frac{m_f}{v}, \quad (1.30)$$

where V indicates the weak interaction mediators, W^\pm and Z bosons, while f stands for the charged leptons and quarks. The information of the coupling constants can be extracted from the measurement of the cross-section (σ) of different Higgs production modes together with the branching ratio (Br) of the Higgs boson decay channels.

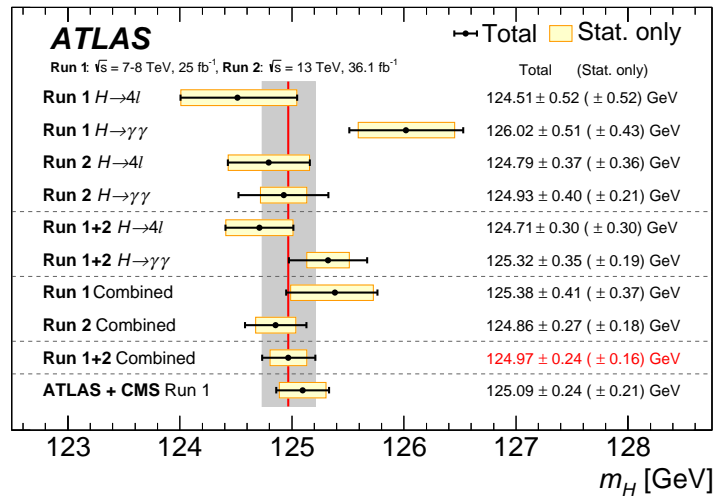


Figure 1.3: A summary of the current Higgs boson mass measurements in individual and combined analyses. The combined ATLAS and CMS result in Run 1 is added for comparison [22].

The signal strength μ is often used to represent the result of the measurement. This quantity is defined as the ratio of $(\sigma \times \text{Br})_{\text{obs}}$ observed from the measurement to $(\sigma \times \text{Br})_{\text{exp}}$ predicted by the SM. Figure 1.4 illustrates the signal strength measurements using up to 80 fb^{-1} of data recorded by ATLAS in Run 2, whereas Figure 1.5 represents the coupling constant of massive particles with the Higgs boson. The couplings of the third generation fermions with the Higgs boson are measured in both ATLAS and CMS exploiting the large amount of Run 2 data [23, 24, 25, 26, 27, 28, 29]. A good agreement with the SM predictions can be observed from the measurement results.

Spin and parity measurements The SM Higgs boson is assumed to be a particle with spin of 0 and even CP, carrying the quantum number $J^P = 0^+$. This assumption can be tested against different spin-parity scenarios through experimental measurements of di-photon and di-boson decay channels of the Higgs boson. From $\sqrt{s} = 8$ TeV data, ATLAS and CMS have excluded the spin-1 hypothesis at 99.7% confidence level (CL) and the spin-2 hypothesis at 99.9% CL. The expected separations from the distributions of the test statistic for all the scenarios of interest are summarized in Figure 1.6. The spin-0 nature of Higgs can be confirmed from the results obtained, being in agreement with the SM and the Higgs boson also favors the even parity scenario predicted by the SM.

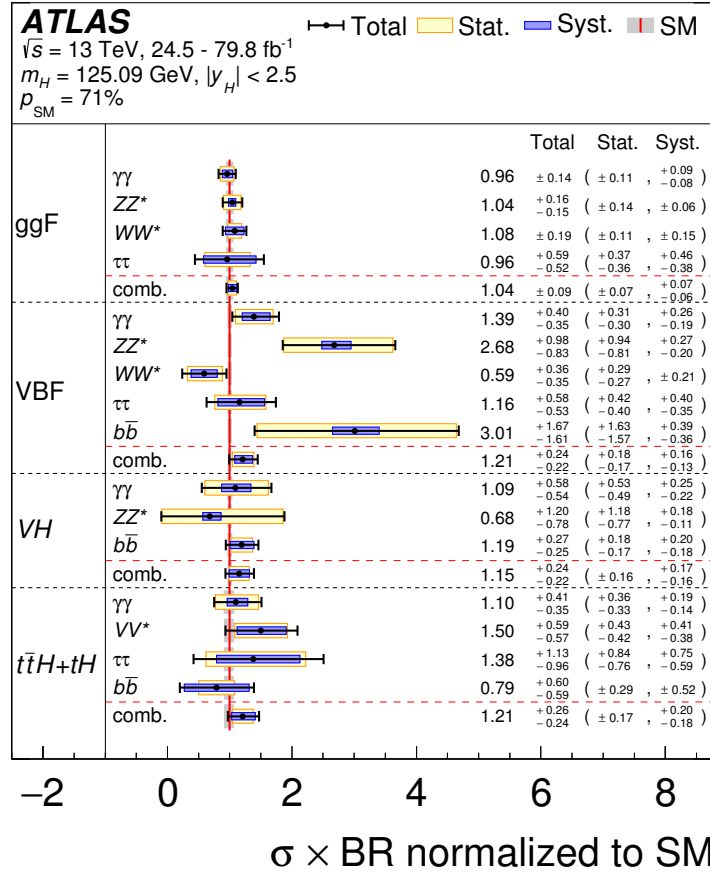


Figure 1.4: The best fit result on the signal strength for ggF , VBF , VH and $t\bar{t}H + tH$ production modes in each relevant decay channels of the Higgs boson [30].

1.7 Successes and limitations of the Standard Model

The SM has been the most successful particle physics theory to date. The weak interaction mediators, Z and W^\pm gauge boson were discovered for the first time at CERN in 1983 [32, 33]. The top quark, the heaviest fermion, was later found in 1995 at Fermilab by the CDF and D0 experiments [34, 35]. Soon thereafter, in 2000, the DONUT experiment gave the first direct proof for the existence of tau neutrino (ν_τ), the last fermion identified in the SM [36]. Then, in 2012, the Higgs boson, the last missing component of the SM, was discovered [20, 21].

Despite its remarkable accomplishment in accurately explaining particles, their production mechanism and interactions, the SM is still far from a comprehensive theory as it still presents several shortcomings. The SM has not yet addressed the

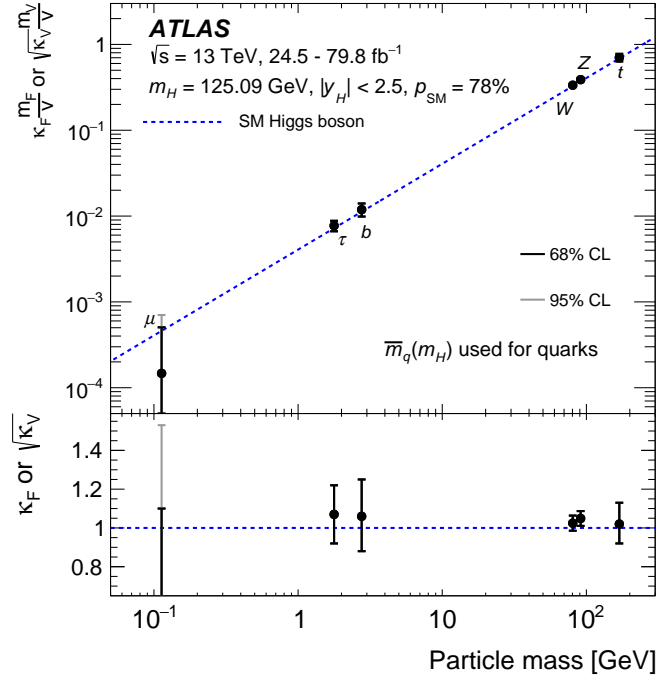


Figure 1.5: Reduced coupling-strength modifiers $\kappa_F \frac{m_F}{v}$ for fermions ($F = t, b, \tau, \mu$) and $\sqrt{\kappa_V} \frac{m_V}{v}$ for weak gauge bosons ($V = W^\pm, Z$) as a function of their masses m_F and m_V , respectively, and the vacuum expectation value of the Higgs field $v = 246$ GeV. The SM prediction for both cases is also shown (dotted line). The black error bars represent 68% confidence level (CL) intervals for the measured parameters. For κ_μ the light error bars indicate the 95% CL interval. The coupling modifiers κ_F and κ_V are measured assuming no BSM contributions to the Higgs boson decays, and the SM structure of loop processes such as $gg \rightarrow H$, $H \rightarrow \gamma\gamma$ and $H \rightarrow gg$. The lower inset shows the ratios of the values to their SM predictions [30].

following questions:

- Gravity: The SM does not contain a quantum field theory description of gravitational interaction.
- Neutrino mass: Neutrinos are considered massless particles in the perspective of SM. However, neutrinos are predicted to be massive based on studies of neutrino oscillations [37].
- Existence of Dark Matter: Persuasive astrophysical data [38, 39, 40] indicate that the particles predicted by the Standard Model are insufficient to account for the matter composition of certain galaxies, implying the presence of a new kind

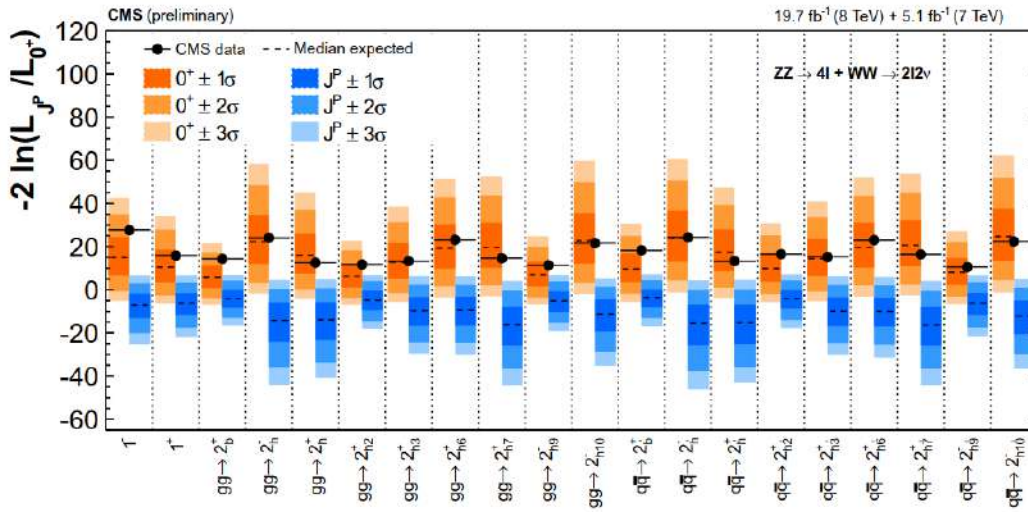


Figure 1.6: A summary on the test statistic for the spin-0 SM Higgs boson and the alternative spin-1 and spin-2 hypotheses based on the combined analysis $H \rightarrow ZZ$ and $H \rightarrow WW$ [31].

of matter termed *Dark Matter*. Dark Matter has previously been shown to have gravitational effects (lensing effect). A theory other than the Standard Model is needed to characterize its nature and characteristics.

- Existence of Dark Energy: Cosmological evidence of the universe's accelerating expansion suggests the existence of another component of our universe, *Dark Energy*, that is responsible for this phenomena. It's nature is still a mystery to us.
- Matter-antimatter asymmetry: The observable universe is nearly entirely composed of matter, and the Standard Model does not explain why matter and anti-matter should not exist in equal quantities. This imbalance cannot be explained only by the observed CP violation in weak interactions [41, 42].
- Interaction unification: The unification of electromagnetic and weak interactions into the electroweak interaction inspired the possibility to combine the strong and electroweak forces together at even higher energies. The ultimate aim would then be to unify this with gravity and have one fundamental unified interaction.
- Hierarchy problem: Like any massive particles in the SM, the Higgs boson mass receives radiative corrections from quantum loop processes via the coupling with other elementary particles. As an example, the correction contribution

Δm_H^2 from a fermion f to the Higgs mass can be written as

$$\Delta m_H^2 = -\frac{|y_f|^2}{8\pi^2} \Lambda_{\text{UV}}^2 + \dots, \quad (1.31)$$

where y_f is the Yukawa coupling of the fermion f to the Higgs boson and is directly proportional to the fermion mass, Λ_{UV} is the ultraviolet momentum cut-off used to regulate the loop integral. The cut-off can be assumed as $\Lambda_{\text{UV}} \sim 10^{19}$ GeV of the Planck scale, because the SM does not predict the physics higher than this scale where quantum effects of gravity become significant. Since the physical Higgs mass is proportional to the quadratic sum of the Higgs bare mass and its radiative correction, this requires the bare mass to unnaturally *fine-tune* to cancel the enormous cut-off and give a value of 125 GeV. This theoretical issue is referred to as the *hierarchy problem* due to the unpleasant fine-tuning up to 17 order of magnitude.

The need for a theory beyond the SM (BSM) arises in order to find out answers for these open questions. One of the BSM models, Supersymmetry (SUSY), which directly addresses the hierarchy problem will be discussed in the next chapter.

2 Supersymmetry

The concept of Supersymmetry (SUSY) [43] was introduced in early 1970s [44, 45, 46] and it has been found to provide answers to some of the major limitations of the SM mentioned in Section 1.7.

One of the SM limitations is the hierarchy problem arising from the radiative corrections of the Higgs boson mass from quantum loop processes. Figure 2.1 shows two example Feynman diagrams contributing to the Higgs mass. The correction from the fermion loop (Figure 2.1 left) has already been discussed in Equation 1.31. The equivalent expression for the correction from the quantum loop of a scalar boson S with mass m_S (Figure 2.1 right) is:

$$\Delta m_H^2 = \frac{\lambda_S}{16\pi^2} \left[\Lambda_{UV}^2 - 2m_S^2 \log\left(\frac{\Lambda_{UV}}{m_S}\right) + \dots \right], \quad (2.1)$$

where λ_S is the coupling strength between Higgs and the scalar boson S . Comparing Equations 1.31 and 2.1, in particular, the opposite sign of the quadratically diverging terms, it is clear that the divergent contribution from a fermion in the Higgs mass can be neatly cancelled if this fermion is accompanied by two complex scalar bosons with $\lambda_S = |y_f|^2$. This is the primary idea of SUSY as will be shown in this section. The remaining radiative corrections are only the logarithmic terms. In order to obtain the observed Higgs boson mass without large fine-tuning, the scalar boson mass m_S should be at the TeV scale.

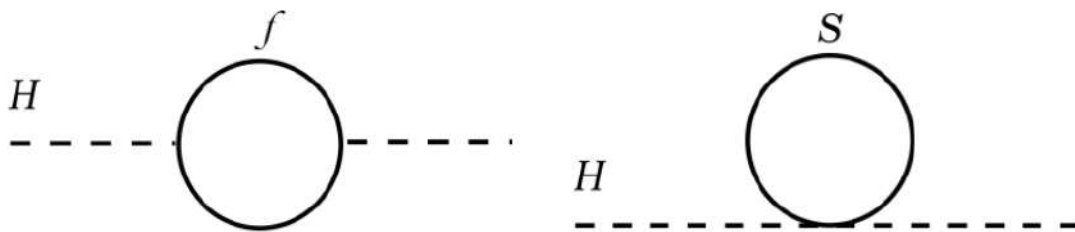


Figure 2.1: One-loop radiative corrections to the Higgs boson mass, due to (left) a fermion and (right) a scalar boson.

Beside addressing directly the hierarchy problem, SUSY also provides a possibility for the unification of the strong and electroweak gauge couplings at the scale of $M_{GUT} \sim 10^{16}$ GeV [47]. Furthermore, SUSY proposes a natural candidate for Dark Matter [48] in R-parity conserving scenario (see Section 2.2.4) or, could give reason of

the Baryon Asymmetry of the universe [49] if R-parity is not conserved. Since none of the superpartners predicted by SUSY have been observed yet, it must be a broken symmetry and the corresponding SUSY-breaking mass parameters are not larger than a few TeV due to the *naturalness considerations* [50, 51].

2.1 Basics of Supersymmetry

Supersymmetry (SUSY) is a symmetry relating fermions and bosons, and vice versa. A SUSY transformation is initiated by a generator Q that shifts, upwards or downwards, the spin S by half a unit of \hbar as:

$$\begin{aligned} Q|S\rangle &= |S \pm 1/2\rangle, \\ Q|\text{boson}\rangle &= |\text{fermion}\rangle, \\ Q|\text{fermion}\rangle &= |\text{boson}\rangle. \end{aligned} \tag{2.2}$$

In the simplest scenario, there are only one fermionic generator Q and its hermitian conjugate Q^\dagger . They can be expressed in terms of two Weyl spinors. The anti-commutation relations between Q and Q^\dagger are presented as follows:

$$\{Q, Q^\dagger\} \propto P^\mu, \tag{2.3}$$

$$\{Q, Q\} = \{Q^\dagger, Q^\dagger\} = 0, \tag{2.4}$$

$$\{P^\mu, Q\} = \{P^\mu, Q^\dagger\} = 0, \tag{2.5}$$

where P^μ denotes the four-momentum generator of the space-time translations. The introduction of the transformations Q and Q^\dagger postulates the existence of a new fermion (boson) supersymmetric partner for each boson (fermion) in the SM. Particles and their superpartners are described by fields organised in *supermultiplets* which can have either vector (for gauge bosons and their superpartners) or chiral (for fermions and their superpartners) representations. In addition, the supersymmetry operators commute with the internal gauge symmetries. Supersymmetric particles and their SM counterparts should have the identical mass and quantum numbers (except for spin) if SUSY is a valid symmetry of the nature. There is, however, no evidence for a supersymmetric particle at the GeV scale. As a result, superpartner masses are predicted to be greater than those of SM particles, implying that SUSY must be a broken symmetry. The SUSY breaking mechanism may be analogous to the electroweak symmetry breaking mechanism, which results in the formation of a hidden symmetry at low energies [43].

2.2 The Minimal Supersymmetric Standard Model

A minimal version of SUSY is the Minimal Supersymmetric Standard Model [52] (MSSM) which only consists of terms that are invariant under the $SU(3)_C \times SU(2)_L \times U(1)_Y$ gauge symmetry, being consistent with the SM interactions. Components of the MSSM Lagrangian are described in the following.

2.2.1 Lagrangian of chiral supermultiplets

The matter in the MSSM is composed of the SM fermions, which include quarks and leptons, and their scalar (spin-0) superpartners, which are scalar quarks (squarks) and scalar leptons (sleptons). Each fermion and its superpartner are represented mathematically by a chiral supermultiplet of the supersymmetry algebra. Due to the fact that the SM fermions' left-handed and right-handed chiral components change differently under the gauge group, their scalar superpartners exhibit the same property. Additionally, there are no right-handed neutrinos in the framework of SM. As a result, no right-handed scalar neutrinos exist. As a spin-0 particle, the Higgs boson must also be represented by the chiral supermultiplet. Table 2.1 summarizes the notations and characteristics of chiral supermultiplets.

Names	Supermultiplets	spin 0	spin $\frac{1}{2}$	$SU(3)_C, SU(2)_L, U(1)_Y$
squarks, quarks ($\times 3$ generations)	Q	$(\tilde{u}_L \ \tilde{d}_L)$	$(u_L \ d_L)$	$(3, 2, \frac{1}{6})$
	\tilde{u}	\tilde{u}_R^*	u_R^\dagger	$(\bar{3}, 1, -\frac{2}{3})$
	\tilde{d}	\tilde{d}_R^*	d_R^\dagger	$(\bar{3}, 1, \frac{1}{3})$
sleptons, leptons ($\times 3$ generations)	L	$(\tilde{\nu}_L \ \tilde{e}_L)$	$(\nu_L \ e_L)$	$(1, 2, -\frac{1}{2})$
	\tilde{e}	\tilde{e}_R^*	e_R^\dagger	$(1, 1, 1)$
Higgs, higgsinos	H_u	$(H_u^+ \ H_u^0)$	$(\tilde{H}_u^+ \ \tilde{H}_u^0)$	$(1, 2, \frac{1}{2})$
	H_d	$(H_d^0 \ H_d^-)$	$(\tilde{H}_d^0 \ \tilde{H}_d^-)$	$(1, 2, -\frac{1}{2})$

Table 2.1: Chiral supermultiplets in the MSSM. The spin-0 fields are complex scalars, the spin-1/2 fields are left-handed Weyl spinors [43].

A free chiral supermultiplet labeled by index i can be described with the Wess-Zumino Lagrangian for non-interacting fields [53], expressed as:

$$\mathcal{L}_{\text{free}}^{\text{chiral}} = -\partial^\mu \phi^{*i} \partial_\mu \phi_i + i\psi^\dagger \bar{\sigma}^\mu \partial_\mu \psi_i + F^{*i} F_i, \quad (2.6)$$

where ϕ_i and ψ_i are the complex scalar field and the left-handed Weyl spinor, respectively, of the supermultiplet, while F_i is a complex scalar and is an auxiliary field added to allow the supersymmetry algebra to close off-shell. The Lagrangian describing

interaction between fields within the chiral supermultiplet is expressed as follows:

$$\mathcal{L}_{\text{int}}^{\text{chiral}} = -\frac{1}{2}W^{ij}\psi_i\psi_j + W^i F_i + h.c, \quad (2.7)$$

where W^{ij} and W^i are given by:

$$W^i = \frac{\partial W}{\partial \phi_i}, \quad W^{ij} = \frac{\partial^2 W}{\partial \phi_i \partial \phi_j}, \quad (2.8)$$

with W is a superpotential defined as:

$$W = \frac{1}{2}M^{ij}\phi_i\phi_j + \frac{1}{6}y^{ijk}\phi_i\phi_j\phi_k + L^i\phi_i. \quad (2.9)$$

In Equation 2.9, M^{ij} represents a symmetric mass matrix for the fermion fields, while y^{ijk} denotes the Yukawa couplings of a scalar with two fermions and L^i are parameters with dimensions of $[\text{mass}]^2$, which affect only the scalar potential part of the Lagrangian. The Lagrangian of chiral supermultiplets is then:

$$\mathcal{L}_{\text{chiral}} = \mathcal{L}_{\text{free}}^{\text{chiral}} + \mathcal{L}_{\text{int}}^{\text{chiral}}. \quad (2.10)$$

By deriving the equations of motions from $\mathcal{L}_{\text{chiral}}$, one can find out the relation between the auxiliary fields F_i and the first-order derivative of the superpotential W as follows:

$$F_i = -W_i^*, \quad F^{*i} = -W^i. \quad (2.11)$$

2.2.2 Lagrangian of gauge supermultiplets

The SM gauge bosons are partnered with fermionic supersymmetric particles referred to as *gauginos* and they are mathematically represented using gauge supermultiplets. According to the transformation from a boson into a fermion of the SUSY operator, all the gauginos have spin of 1/2. They comprise eight *gluinos* (\tilde{g}) being superpartners of the SM $SU(3)_C$ gauge bosons (gluons), three *winos* ($\tilde{W}^\pm, \tilde{W}^0$) and one *bino* (\tilde{B}^0) which are superpartners of the SM $SU(2)_L \times U(1)_Y$ gauge bosons (W^\pm, W^0 and B^0). The MSSM gauge supermultiplets are summarized in Table 2.2.

Names	spin $\frac{1}{2}$	spin 1	$SU(3)_C, SU(2)_L, U(1)_Y$
gluino, gluon	\tilde{g}	g	(8,1,0)
winos, W boson	$\tilde{W}^\pm, \tilde{W}^0$	W^\pm, W^0	(1,3,0)
bino, B boson	\tilde{B}^0	B^0	(1,1,0)

Table 2.2: Gauge supermultiplets in the MSSM [43].

2 Supersymmetry – 2.2 The Minimal Supersymmetric Standard Model

The gauge supermultiplets are described by the following Lagrangian:

$$\mathcal{L}_{\text{gauge}} = -\frac{1}{4}F_{\mu\nu}^a F^{\mu\nu a} + i\lambda^{\dagger a} \bar{\sigma}^{\mu} D_{\mu} \lambda^a + \frac{1}{2}D^a D^a, \quad (2.12)$$

where the notation D^a represents the real bosonic auxiliary field which allows the SUSY algebra to close off-shell; $F_{\mu\nu}^a$ is the usual Yang-Mills field strength:

$$F_{\mu\nu}^a = \partial_{\mu} A_{\nu}^a - \partial_{\nu} A_{\mu}^a + g f^{abc} A_{\mu}^b A_{\nu}^c, \quad (2.13)$$

with g and f^{abc} being the gauge coupling and the anti-symmetric structure constants of the defined gauge group, respectively; and D_{μ} is the covariant derivative of the gaugino field λ^a :

$$D_{\mu} \lambda^a = \partial_{\mu} \lambda^a + g f^{abc} A_{\mu}^b \lambda^c. \quad (2.14)$$

In order to construct a general Lagrangian for a renormalisable supersymmetric theory which contains both the chiral and gauge supermultiplets, the scalar, fermionic and auxiliary fields are firstly required to transform under the gauge group as:

$$X_i \rightarrow X_i + i g \Lambda^a (T^a X)_i, \quad (2.15)$$

where X_i can be ϕ_i , ψ_i or F_i , and T^a are the hermitian matrices of the gauge group. Next, the covariant derivative is then used to replace the partial derivative in the chiral Lagrangian, as followed:

$$\begin{aligned} \partial_{\mu} \phi_i &\rightarrow D_{\mu} \phi_i = \partial_{\mu} \phi_i - i g A_{\mu}^a (T^a \phi)_i, \\ \partial_{\mu} \phi^{*i} &\rightarrow D_{\mu} \phi^{*i} = \partial_{\mu} \phi^{*i} + i g A_{\mu}^a (\phi^{*} T^a)^i, \\ \partial_{\mu} \psi_i &\rightarrow D_{\mu} \psi_i = \partial_{\mu} \psi_i - i g A_{\mu}^a (T^a \psi)_i. \end{aligned} \quad (2.16)$$

In the following step, the possible interaction terms which remain the gauge invariance and involve the gaugino and the auxiliary fields D^a are added. Such interactions are given by:

$$\mathcal{L}_{\text{gauge}}^{\text{int}} = -\sqrt{2}g(\phi^{*} T^a \psi)\lambda^a - \sqrt{2}g\lambda^{\dagger a}(\psi^{\dagger} T^a \phi) + g(\phi^{*} T^a \phi)D^a. \quad (2.17)$$

The supersymmetric Lagrangian can be then formulated as:

$$\mathcal{L}_{\text{SUSY}} = \mathcal{L}_{\text{chiral}} + \mathcal{L}_{\text{gauge}} + \mathcal{L}_{\text{gauge}}^{\text{int}}. \quad (2.18)$$

2.2.3 Lagrangian of soft SUSY breaking in the MSSM

As already mentioned, since no superpartners of the SM particles have been experimentally observed at the GeV scale yet, SUSY has to be a broken symmetry. Although there have been various models of supersymmetry breaking proposed [54, 55], the precise mechanism is still not clear. In order for SUSY to still provide a valid solution

for the hierarchy problem of the Higgs boson mass, the quadratic divergences in the Higgs mass radiative correction must not be re-introduced in the theory after the symmetry breaking, implying that SUSY has to be *softly* broken. The Lagrangian for the soft SUSY breaking in the description of the MSSM can be derived as follows:

$$\begin{aligned}
 \mathcal{L}_{\text{MSSM}}^{\text{soft}} = & -\frac{1}{2} (M_3 \tilde{g} \tilde{g} + M_2 \tilde{W} \tilde{W} + M_1 \tilde{B} \tilde{B} + c.c.) \\
 & - \left(\tilde{u} \mathbf{a}_u \tilde{Q} H_u - \tilde{d} \mathbf{a}_d \tilde{Q} H_d - \tilde{e} \mathbf{a}_e \tilde{L} H_d + c.c. \right) \\
 & - \tilde{Q}^\dagger \mathbf{m}_Q^2 \tilde{Q} - \tilde{L}^\dagger \mathbf{m}_L^2 \tilde{L} - \tilde{u} \mathbf{m}_u^2 \tilde{u}^\dagger - \tilde{d} \mathbf{m}_d^2 \tilde{d}^\dagger - \tilde{e} \mathbf{m}_e^2 \tilde{e}^\dagger \\
 & - m_{H_u}^2 H_u^* H_u - m_{H_d}^2 H_d^* H_d - (b H_u H_d + c.c.). \tag{2.19}
 \end{aligned}$$

In Equation 2.19, the mass terms of gluinos, winos, and bino are given in the first line. Whereas the second line contains the complex 3×3 matrices $\mathbf{a}_{u,d,e}$, in family space, corresponding to the Yukawa couplings in the superpotential. The third line provides the mass terms of squarks and sleptons, where $\mathbf{m}_{Q,L,\tilde{u},\tilde{d},\tilde{e}}^2$ are the 3×3 hermitian matrices. The remaining line consists of the soft SUSY breaking terms to the Higgs potential. Finally, the complete form of the MSSM Lagrangian can be expressed as:

$$\mathcal{L}_{\text{MSSM}} = \mathcal{L}_{\text{SUSY}} + \mathcal{L}_{\text{MSSM}}^{\text{soft}}. \tag{2.20}$$

The addition of the soft SUSY breaking Lagrangian, however, brings a drawback in which 105 free parameters are introduced into the theory, leading to a wide range of options for the mass of superparticles and the couplings.

2.2.4 R-parity

In the context of the MSSM, the superpotential has the following expression:

$$W_{\text{MSSM}} = \tilde{u} \mathbf{y}_u \tilde{Q} H_u - \tilde{d} \mathbf{y}_d \tilde{Q} H_d - \tilde{e} \mathbf{y}_e \tilde{L} H_d + \mu H_u H_d, \tag{2.21}$$

where $\mathbf{y}_{u,d,e}$ are the dimensionless 3×3 matrices of the Yukawa coupling parameters and the μ term represents the supersymmetric higgsino mass. In fact, there are other terms that are also gauge invariant and renormalisable and can be added directly into the MSSM superpotential in Equation 2.21. Such terms are:

$$W_{R_p} = \frac{1}{2} \lambda^{ijk} L_i L_j \bar{e}_k + \lambda'^{ijk} L_i Q_j \bar{d}_k + \mu'^i L_i H_u + \frac{1}{2} \lambda''^{ijk} \bar{u}_i \bar{d}_j \bar{d}_k, \tag{2.22}$$

where $i, j, k = 1, 2, 3$ are generation indices, while λ^{ijk} , λ'^{ijk} , λ''^{ijk} are the coupling constants. However, these terms, the first three ones and the fourth one, introduce interactions that could violate the conservation of the leptonic number (L) and the baryonic number (B), respectively. The existence of such the B - and L -violating terms would allow the rapid proton decay, promptly into $e^+ \pi^0$ for example. Nevertheless

the proton mean life time is known experimentally to be at least 10^{31} years [56]. This implies that the corresponding couplings, λ'^{ijk} and λ''^{ijk} , must be extremely small. In order to avoid the B and L violating interactions and allow only the good terms in equation 2.21, P. Fayet and G.R. Farrar have proposed a new symmetry, called " R -parity" which is defined as [57, 58]:

$$P_R \equiv (-1)^{3(B-L)+2S}, \quad (2.23)$$

where S is the spin number of the particle. The SM particles have the R -parity of $P_R = +1$, while their superpartners have the R -parity of $P_R = -1$. In case the R -parity is a conserved quantum number (R -parity conservation - RPC), it will lead to the following consequences in the phenomenology of the MSSM:

- Sparticles are produced in pair at each vertex.
- The lightest supersymmetric particle (LSP) must be stable. If the LSP is colourless and electrically neutral, it can be a good candidate for Dark Matter.
- Conservation of B and L quantum numbers.
- Other instable sparticles must decay into a final state which consists of an odd number of lighter sparticles.

2.2.5 Neutralinos and charginos sector

Because of the electroweak symmetry breaking, the superpartners of the SM electroweak gauge bosons, the electroweak gauginos, and the superpartners of Higgs, higgsinos, can mix with each other. A 4×4 complex symmetric mass matrix, denoted as M_N , is used to describe the mixing of the neutral gauginos (\tilde{W}^0, \tilde{B}) and the neutral higgsinos ($\tilde{H}_u^0, \tilde{H}_d^0$) at tree-level. The expression of this matrix in the basis of the gauge-eigenstates ($\tilde{W}^0, \tilde{B}, \tilde{H}_u^0, \tilde{H}_d^0$) is given as follows [43]:

$$M_N \equiv \begin{pmatrix} M_1 & 0 & -\frac{1}{2}g_Y v_d & \frac{1}{2}g_Y v_u \\ 0 & M_2 & \frac{1}{2}g_W v_d & -\frac{1}{2}g_W v_u \\ -\frac{1}{2}g_Y v_d & \frac{1}{2}g_W v_d & 0 & -\mu \\ \frac{1}{2}g_Y v_u & -\frac{1}{2}g_W v_u & -\mu & 0 \end{pmatrix}, \quad (2.24)$$

where M_1 and M_2 are the same as those used in Equation 2.19 corresponding to the $U(1)_Y$ and $SU(2)_L$ soft SUSY breaking gaugino mass terms respectively; terms with $-\mu$ are the SUSY higgsino mass terms; the terms containing g_W and g_Y are the result of Higgs-higgsino-gaugino couplings with v_u and v_d being the vacuum expectation values of the two Higgs boson fields H_u^0 and H_d^0 , respectively, and related to the SM Higgs vev (v) by:

$$v^2 = v_u^2 + v_d^2 = \frac{2m_Z^2}{g_W^2 + g_Y^2} = (246 \text{ GeV})^2. \quad (2.25)$$

The M_N matrix can be re-written in terms of the weak mixing angle θ_W as:

$$M_N \equiv \begin{pmatrix} M_1 & 0 & -\cos\beta \sin\theta_W m_W & \sin\beta \sin\theta_W m_Z \\ 0 & M_2 & \cos\beta \cos\theta_W m_Z & -\sin\beta \cos\theta_W m_Z \\ -\cos\beta \sin\theta_W m_W & \cos\beta \cos\theta_W m_Z & 0 & -\mu \\ \sin\beta \sin\theta_W m_Z & -\sin\beta \cos\theta_W m_Z & -\mu & 0 \end{pmatrix}, \quad (2.26)$$

where β is defined as:

$$\tan\beta = \frac{v_u}{v_d}. \quad (2.27)$$

By diagonalising the M_N matrix with $N^* M_N N^{-1}$ where N is a unitary matrix, one can retrieve the four physical *neutralino* states, denoted by $\tilde{\chi}_i^0$ ($i = 1, 2, 3, 4$), and their corresponding masses. By convention, they are labeled in ascending order of mass from 1 to 4. Unless there is a lighter gravitino or unless R -parity is not conserved, the lightest neutralino, $\tilde{\chi}_1^0$, is usually assumed to be the LSP and could therefore be a good candidate constituting Dark Matter. The $\tilde{\chi}_i^0$ are the linear combinations of the neutral gaugino and higgsino states determined by the matrix elements of N and their masses correspond to the singular values of M_N , i.e the positive square roots of the eigenvalues of $M_N^\dagger M_N$. Exact formula for these masses can be found in Ref [59].

The mixing of the charged gauginos (\tilde{W}^\pm) and the charged higgsinos ($\tilde{H}_u^+, \tilde{H}_d^-$), on the other hand, is described, at tree-level, by a 2×2 complex mass matrix M_C which is represented as:

$$M_C \equiv \begin{pmatrix} M_2 & \frac{1}{\sqrt{2}} g_W v_u \\ \frac{1}{\sqrt{2}} g_W v_d & \mu \end{pmatrix} \equiv \begin{pmatrix} M_2 & \sqrt{2} \sin\beta m_W \\ \sqrt{2} \cos\beta m_W & \mu \end{pmatrix}. \quad (2.28)$$

The mass eigenstates can then be retrieved from the gauge eigenstates using two unitary 2×2 matrices U and V , as follows:

$$\begin{aligned} \begin{pmatrix} \tilde{\chi}_1^+ \\ \tilde{\chi}_2^+ \end{pmatrix} &= V \begin{pmatrix} \tilde{W}^+ \\ \tilde{H}_u^+ \end{pmatrix}, \\ \begin{pmatrix} \tilde{\chi}_1^- \\ \tilde{\chi}_2^- \end{pmatrix} &= U \begin{pmatrix} \tilde{W}^- \\ \tilde{H}_d^- \end{pmatrix}, \\ U^* M_C V^{-1} &= \text{diag}(m_{\tilde{\chi}_1^+}, m_{\tilde{\chi}_2^+}), \end{aligned} \quad (2.29)$$

where the term in the right-hand side is the diagonal matrix of (real positive) chargino masses. The physical chargino states are denoted by $\tilde{\chi}_1^\pm$ and $\tilde{\chi}_2^\pm$. They are linear combinations of the charged gaugino and higgsino states determined by the matrix elements of U and V . Their masses correspond to the singular values of M_C , i.e the

positive square roots of the eigenvalues of $M_C^\dagger M_C$:

$$m_{\tilde{\chi}_1^\pm, \tilde{\chi}_2^\pm}^2 = -\frac{1}{2}|\mu|^2 + |M_2|^2 + 2m_W^2 \pm [(|\mu|^2 + |M_2|^2 + 2m_W^2)^2 - 4|\mu|^2|M_2|^2 - 4m_W^4 \sin^2 2\beta + 8m_W^2 \sin 2\beta \text{Re}(\mu M_2)]^{1/2}. \quad (2.30)$$

The chargino or neutralino state can approximately be a particular combination of gaugino or higgsino depending on the values of μ , M_1 and M_2 [43]:

- In case M_1 and m_Z are small compared to M_2 and $|\mu|$, $\tilde{\chi}_1^0$ is nearly pure bino, \tilde{B} .
- In case M_2 and m_Z are small compared to M_1 and $|\mu|$, the lightest chargino and neutralino then constitute a triplet of roughly mass-degenerate pure winos, \tilde{W}^\pm , and \tilde{W}_3^0 .
- In case $|\mu|$ and m_Z are small compared to M_1 and M_2 , $\tilde{\chi}_1^0$ is nearly pure higgsino.

Each of these cases will lead to a different phenomenology. For the SUSY searches presented in this thesis (Chapter 7), the lightest neutralino $\tilde{\chi}_1^0$ is assumed to be a bino-like LSP, while the lightest chargino $\tilde{\chi}_1^\pm$ and next-to-lightest neutralino $\tilde{\chi}_2^0$ are assumed to be wino-like and nearly mass degenerate.

2.3 Supersymmetric models

The MSSM has more than 100 free parameters, 32 of which are masses of undiscovered particles and the others are phases and mixing angles. Constraining such a large phase space experimentally is very challenging. Numerous supersymmetric models exist that introduce a particular mechanism for breaking supersymmetry and predict the particle spectrum of the MSSM with much fewer parameters. Alternatively, some models limit the phase space via the inclusion of extra phenomenological constraints. A few well-known instances of both model types are discussed briefly below.

2.3.1 mSUGRA

The minimal Super GRAvity (mSUGRA) [60] is a supersymmetric model with a specific mechanism for introducing the Lagrangian soft term. Two more particles are included in the minimal expression of the supergravity: the spin-2 boson mediator of gravity, or graviton, and its supersymmetric partner, the spin-3/2 gravitino. Additional models with a complete gravitational hidden sector are also possible. The gravitational interaction breaks supersymmetry, additionally giving mass to the gravitino. One of mSUGRA's advantages is its predictability, as the MSSM phase space can be reduced to just five parameters: a universal scalar mass (M_0), a universal gaugino mass ($M_{1/2}$), a universal trilinear coupling A_0 , the ratio of the vacuum expectation values of the two Higgs doublets $\tan \beta$, and the sign of the higgsino mass parameter μ .

Constraints derived from the Standard Model, such as the mass of the Higgs boson, significantly constrain the realistic values of the aforementioned parameters, simplifying experimental investigations further. Additionally, mSUGRA-type models provide a mechanism for gravity to be included into a quantum theory.

2.3.2 GMSB

Theories with gauge-mediated supersymmetry breaking (GMSB) [61] provide an intriguing alternative to the situation in which the soft terms are generated by gravity. The breaking of SUSY in the GMSB scenario is mediated by conventional gauge interactions. These models typically comprise of a visible sector containing the SM particles and their SUSY partner, as well as a hidden sector that is responsible for the supersymmetry breaking. The messenger sector is the final piece of GMSB. It communicates the SUSY breaking from the hidden to the visible sector through loop diagrams using massive messenger fields. The messengers are novel chiral supermultiplets that are capable of coupling to both the supersymmetry breaking vev and Standard Model particles. As with gravitational models, GMSB models are highly predictive; furthermore, they automatically suppress high rates of high Flavour Changing Neutral Currents (FCNCs) that contradict experimental data.

2.3.3 pMSSM

Assuming a particular mechanism for breaking SUSY may have substantial phenomenological implications. It is possible to define a more generic model that incorporates the MSSM without explicitly specifying the soft SUSY breaking mechanism. To reduce the number of free parameters, one may apply well-motivated phenomenological restrictions. The phenomenological Minimal Supersymmetric Standard Model, or pMSSM, is the most common model of this kind [62]. The phenomenological requirements are designed to guarantee that no new CP violating or FCNC terms are introduced into the Lagrangian, while simultaneously assuming the universality of the first two families of squarks and sleptons. Following these constraints, the number of free parameters is reduced to 19: the ratio of the vacuum expectation values of the two Higgs doublets, the mass of the pseudoscalar Higgs boson, the mass of the higgsino and the three gauginos, three (two) mass parameters for the first and second generation squarks (sleptons), and three (two) mass parameters for the third generation squarks (sleptons). Finally, the three remaining parameters represent the trilinear couplings of third generation quarks and leptons, since their mixing is allowed. The pMSSM is a low scale model since all of the aforementioned parameters are stated at the electroweak scale (in contrast to mSUGRA, which is mostly specified at the GUT scale).

2.3.4 Simplified models

The pMSSM represents SUSY in a broad and realistic way possible. Scanning 19 parameters in an experimental search, on the other hand, may be very difficult and time consuming. Due to the fact that experimental searches are often focused on a subset of parameters, or sparticles, it is frequently advantageous to examine an effective Lagrangian including just the sparticles of interest and their interactions. These are referred to as Simplified Models [63, 64], and are often motivated by experimental requirements. This is because they are often parametrized directly using collider physics observables such as particle masses, production cross-sections, and decay branching ratios. The latter are often considered to be 100% to a particular experimental signature, thus lowering the model's degrees of freedom.

2.4 Search for SUSY electroweak production at the LHC

The ATLAS and CMS experiments performed a large number of searches for SUSY during Run 1/Run 2 of the LHC and, in the absence of a significant excess in any channel, exclusion limits on the masses of SUSY particles were calculated in numerous scenarios, usually in the context of the MSSM. These scenarios include "high-scale" SUSY models such as mSUGRA or GMSB, both of which specify a particular SUSY-breaking mechanism as discussed previously. Most searches use simplified models which permit the development of signature-based search strategies that, taken as an ensemble, have been shown to adequately cover the pMSSM. These models allow us to efficiently address particular features of SUSY such as stop/sbottom production, electroweak production, compressed spectra, massive long-lived particles, R -parity violation, etc. without the need to embed these in a complete SUSY model. Early analyses were dominated by the searches for strongly interacting SUSY particles (gluinos, squarks) because of their large production cross sections (see Figure 2.2).

It also motivated the separate consideration of electroweak SUSY particle production, that is, direct production of particles that have no colour charge such as the charged sleptons, sneutrinos and the electroweakinos (charginos, neutralinos). On the experimental side, depending on the mechanism of SUSY breaking, it could be that strongly interacting squarks and gluinos are too massive to be produced at the LHC. In this case, the primary SUSY production mode is of charginos, neutralinos and sleptons, mediated by electroweak interactions, while on the theory side, weak-scale SUSY has long occupied a central place in the theoretical expectations for the LHC, as the addition of superpartners to the SM particles near the scale of electroweak symmetry breaking solves the hierarchy problem. Given that the superpartners must be heavier than their SM counterparts, the SUSY cancellation of loops protecting the Higgs mass cannot be perfect. The heavier the superpartners, the more finely tuned the original bare mass must be against the loop contributions. For a reduced

2 Supersymmetry – 2.4 Search for SUSY electroweak production at the LHC

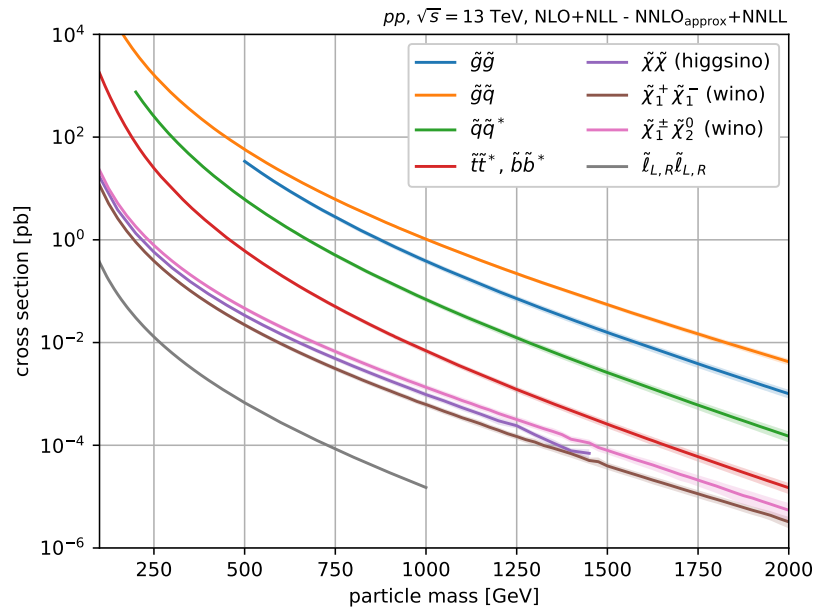


Figure 2.2: Cross section for the production of sparticles at LHC at 13 TeV center-of-mass energy as a function of the average mass of the pair produced [65].

finetuning (theory will be "natural") electroweakinos, especially higgsinos, must be light.

Comparing to the SUSY strong production signatures, the SUSY electroweak productions yield a cleaner signal and can be less prone to systematic uncertainties, due to the fact that the electroweakinos decay to leptons, vector bosons or Higgs bosons and sleptons. The only hadronic activity in the event is due to bosonic decay products, initial- and final-state radiation. The latest exclusion limits at 95% confidence level (CL) of various searches for SUSY electroweak production of charginos and neutralinos at ATLAS are shown in Figure 2.3. These searches are considered in the context of simplified models where electroweakinos decay via Higgs, W and Z bosons. The signatures of these searches are separate by the number of leptons presenting in the final state. The analysis presented in this document (Chapter 7) focuses on searches for the production of charginos and neutralinos via W/Z boson decays with the presence of exactly one charged lepton in the final state.

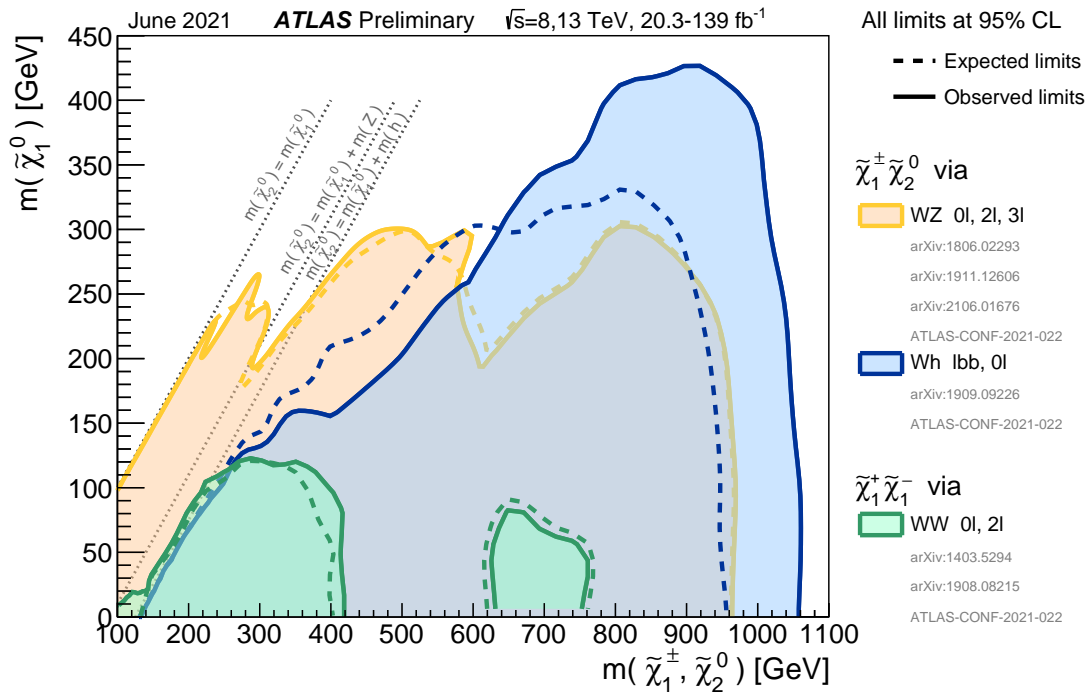


Figure 2.3: The 95% CL exclusion limits on $\tilde{\chi}_1^\pm \tilde{\chi}_1^\mp$ and $\tilde{\chi}_1^\pm \tilde{\chi}_2^0$ production with SM-boson-mediated decays, as a function of the $\tilde{\chi}_1^\pm/\tilde{\chi}_2^0$ and $\tilde{\chi}_1^0$ masses. The production cross-section is for pure wino $\tilde{\chi}_1^\pm$ and $\tilde{\chi}_2^0$. Each individual exclusion contour represents a union of the excluded regions of one or more analyses [66].

3 The Large Hadron Collider and the ATLAS detector

The Large Hadron Collider (LHC) [67], described in Section 3.1, is currently the largest and most sophisticated circular synchrotron accelerator in the world. It is able to collide proton beams or heavy ions, in particular lead nuclei, with high energy and luminosity and therefore makes itself the most powerful experimental machine to study the fundamental particles of nature. The ATLAS detector [68], discussed in Section 3.2, was installed around one of the four interaction points in the LHC ring. It is the largest general-purpose detector ever built, aiming to test the Standard Model (SM) predictions and to search for physics beyond the SM at the TeV scale as well. The analysis presented in this thesis (Chapter 7) is performed with data collected by the ATLAS detector. Procedures which are used to reconstruct physics objects in the ATLAS detector are described in Section 3.3. It is then followed by a description of the collision data simulation chain put in place for the ATLAS physics analyses, given in Section 3.4.

3.1 The Large Hadron Collider

The LHC is a two-ring-superconducting-hadron collider located at the European Organization for Nuclear Research (CERN), near Geneva and across the border between France and Switzerland. The LHC project was approved in 1994 and its construction began in early 2000, at the existing 26.7 km underground tunnel which previously hosted the Large Electron Positron (LEP) collider [69]. The LHC was mainly designed to operate proton-proton (pp) collisions at a center-of-mass energy of up to 14 TeV and thus provides possibilities to extend the energy frontiers of particle physics. Also, instead of using proton beams, the LHC can collide heavy ion beams, such as lead (Pb), with an energy of 2.5 TeV per nucleon to study the particle interactions in environments that imitate ones of the very early universe, like quark-gluon plasma.

The LHC has been officially launched in September 2008, and its first data-taking period, Run 1, was organized between 2010 and 2012, in which proton beams were collided with 7 then 8 TeV center-of-mass energy. After the Run 1 phase, the LHC began the first 2-year shutdown period, from 2013 to 2015, referred to as Long Shutdown (LS) 1. During LS1, upgrades of the machine and detectors were conducted to prepare for the center-of-mass energy of 13 TeV of pp collisions delivered in Run 2 that took place between mid-2015 and 2018. The searches performed in this thesis use data

recorded during the full Run 2 of the LHC. At the moment, the LHC is in the end of LS2 period which has started since 2019 and will then launch Run 3 phase in 2022 with the center-of-mass energy possibly increasing from 13 to 13.5 or 14 TeV. Following Run 3, from 2025, the LHC will enter an upgrade period which will enable it to run with a significant increase in the instantaneous luminosity by a factor of 5-to-7 higher than the nominal design value. This High-Luminosity LHC (HL-LHC) [70] will start in 2027 and is expected to bring researchers ten times more collected data than the LHC.

In general, so far, the LHC has been extremely successful in verifying the consistency of the SM predictions with various precision measurements. One great achievement of this machine was the discovery of Higgs-boson-like particle in 2012 [20, 21]. Measuring Higgs boson properties has consequently become one of the main objectives in the LHC physics program. On the other hand, with the hint for the lepton universality violation that was recently announced in March 2021 [71], the LHC has also pointed out one of many SM limitations and implied the existence of new physics.

3.1.1 The accelerator complex and injection chain

The CERN accelerator complex, as represented in Figure 3.1, consists of the LHC storage ring of 26.7 km in circumference and a pre-acceleration chain which includes several synchrotron and linear accelerators. Before particles are injected to the LHC ring, they are in fact boosted to a certain energy by passing through this chain of pre-accelerators. Specifically, protons, produced by stripping valence electrons of from hydrogen atoms, firstly pass a 30 m long linear accelerator, the LINAC2, to gain an energy of 50 MeV. After being squeezed into high-intensity bunches, they enter the Proton Synchrotron Booster (PSB), a circular machine composed of four super-imposed 150 m synchrotron rings. The PSB increases the protons' energy up to 1.4 GeV and guides them into the first ever CERN synchrotron accelerator of 638 m in circumference, the Proton Synchrotron (PS), where they are accelerated to an energy of 25 GeV. In the final step of the pre-acceleration chain, the protons are transported to the Super Proton Synchrotron (SPS), which is the second largest accelerator at CERN with 7 km in circumference, in order to significantly rise their energy up to 450 GeV before injecting them into the LHC. In the past, the SPS was designed to operate proton-antiproton collisions in the UA1 and UA2 experiments which discovered the W and Z bosons in 1983 [72, 73]. Today, it serves as an injector in the CERN accelerator complex, providing particles for not only the LHC but also other CERN based experiments including the fixed target programs as well as the CERN testbeam areas, where research and design campaigns of future upgrades are being carried out.

The LHC also collides heavy ions that are produced by an electron-cyclotron-resonance plasma source. The procedure to supply these heavy ions for the machine is similar to the proton injection described above. This means that the ions also have to pass the PS and then follow the same steps as for the protons to reach the LHC. However, before being injected into the PS, these ions consecutively go through the LINAC3 and the Low Energy Ion Ring (LEIR) which increase their energy up to 4.2 MeV

and nominally generate a field of 8.3 T. The height and width of the proton beams are tightened by 858 quadrupole magnets which are installed in pairs along the LHC ring. There are also higher order multipole magnets utilized to further focus and counteract divergence-inducing effects which can lead to imperfections in the proton beams.

As being a particle-particle collider, the LHC in fact contains two separate vacuum beam pipes for the counter-rotating beams. The proton beams, after arriving at the LHC, are split and guided into these two pipes. One travels clockwise while the other anti-clockwise and both are accelerated and kept focused in a circular trajectory by the electric and magnetic fields generated from the systems mentioned above. Once the protons reach the target energy, the two beams are collided at four interaction points (IPs) where the four particle detectors including ATLAS [68], CMS [75], ALICE [76] and LHCb [77] are stationed. ATLAS and CMS are both general-purpose detectors but use different technologies in terms of tracking and calorimetry. Both the experiments aim for study of the Higgs sector, measurements of the SM parameters and searches for new physics beyond the SM as well. This allows them not only to cross-check their results but also to enhance precision by combining their collected datasets for measurements of interest for which the statistical uncertainty dominates. The ATLAS detector is discussed in more details in Section 3.2. The LHCb is a forward-based precision experiment which is particularly designed to study heavy-flavour physics and the matter-antimatter asymmetry via the decays of the b - and c -hadrons. The remaining one, ALICE, is a heavy-ion detector dedicated to study physics of the strongly interacting matter at high energies and high densities, where the quark-gluon plasma forms.

3.1.2 Luminosity and pile-up

The luminosity (L) is one of the primary quantities in collider physics from which one can estimate the number of interactions happening in a time interval for a specific physics process. In principle, it is defined as:

$$L = \frac{1}{\sigma} \frac{dN}{dt}, \quad (3.1)$$

where σ denotes the process cross-section, while N is the number of events recorded in a given interval of time dt , and it therefore has the unit of $[\text{length}]^{-2}[\text{time}]^{-1}$. At the LHC, the luminosity directly relates to the structures of the two colliding proton bunches through the following formula:

$$L = \frac{N_1 N_2 f N_b}{4\pi\sigma_x\sigma_y} S, \quad (3.2)$$

where N_1 and N_2 represent the number of protons in the two bunches, N_b is the number of bunches per beam, f is known as the beam revolution frequency (approximately 11 kHz) meaning the number of circulations of each bunch per second, σ_x and σ_y

are the transverse beam sizes at the interaction point and S is a geometric correction factor accounting for the luminosity reduction when the two bunches collide at a crossing angle of about $300 \mu\text{rad}$ in the LHC.

Since the luminosity in Equation 3.2 is computed during short intervals around when the collisions take place, it is called the instantaneous luminosity. Precisely measuring this quantity is essential for all studies at the LHC, indeed in all cross-section measurements in which it plays a crucial role and also contributes as an important systematic uncertainty. In Run 2, multiple dedicated detectors, called luminometers, with different technologies are used to accomplish the accurate measurement of the instantaneous luminosity at ATLAS [78]. Specifically, the LUCID 2 Cherenkov detector [79] located at ± 17 m from the interaction point measures the primary bunch-by-bunch luminosity. This measurement is then complemented with luminosity at the bunch-crossing level provided by the beam conditions monitor (BCM) diamond detectors [80] and followed by a calibration procedure applying the van der Meer (vdM) scans [81]. As seen from Figure 3.2a which illustrates the evolution of the instantaneous luminosity over time during 2018, the LHC has shown up a very good performance with a peak instantaneous luminosity of $2.1 \times 10^{34} \text{cm}^{-2} \text{s}^{-1}$ that exceeds its design value of $10^{34} \text{cm}^{-2} \text{s}^{-1}$.

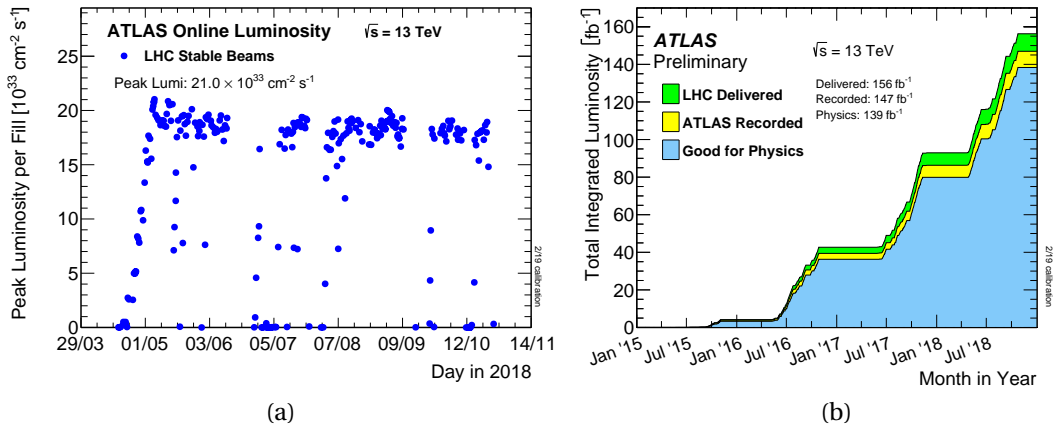


Figure 3.2: 3.2a Peak instantaneous luminosity delivered to ATLAS as a function of time for the 2018 data-taking period. 3.2b Cumulative luminosity versus time delivered to ATLAS (green), recorded by ATLAS (yellow) and certified to be good quality data (blue) during stable beams for pp collisions at 13 GeV center-of-mass energy in 2015-2018 [82].

There is also another quantity named integrated luminosity which characterizes the size of a data collected over a period of time T in the LHC and can be simply computed

based on the instantaneous luminosity as:

$$L_{\text{int}} = \int_0^T L dt. \quad (3.3)$$

During Run 2, from 2015 to 2018, there was a total amount of data corresponding to an integrated luminosity of 156 fb^{-1} ($1\text{b} = 10^{-24} \text{ cm}^2$) delivered to ATLAS by the LHC and this detector registered almost 95% of the data, meaning 147 fb^{-1} . However, only 139 fb^{-1} of the data recorded by ATLAS was attested to be good quality data and used for physics analyses in order to avoid unexpected hardware (and software) issues. The evolution with respect to time of the three integrated luminosities that were delivered to ATLAS, recorded by ATLAS and certified to be good for ATLAS physics analyses in Run 2 is demonstrated in Figure 3.2b.

From Equations 3.1 and 3.3, the total number of events N associated to a specific physics process generated with a cross-section σ can be derived as follows:

$$N = \sigma L_{\text{int}} = \sigma \int_0^T L dt. \quad (3.4)$$

Equation 3.4 shows that the higher the instantaneous luminosity of the LHC, the more signal events it produces. In other words, the increase in the instantaneous luminosity brings a larger possibility to observe the interactions of interest, especially the rare processes, and reaching the highest possible value of this quantity is therefore a key factor for the LHC physics program. As shown in Equation 3.2, this can be achieved by increasing the bunch revolution frequency f and the number of bunches per beam N_b . However, this option is very difficult because the protons inside the LHC are already accelerated close to the speed of light. The other option is to increase the number of protons in each bunch N_1, N_2 and simultaneously reduce the transverse beam size σ_x, σ_y . This second option is in fact the main principle of the High-Luminosity LHC upgrade which is discussed in details in Section 6.1.

Despite the fact that the extremely high instantaneous luminosity provides many benefits in terms of the study of new physics at the LHC by increasing the number of interactions that occur in a given bunch-crossing, it can still be a drawback for the performance of the detectors, mainly due to difficulty to distinguish particles originating from the hard-scatter event, the one with the highest physics interest, from the rest of collisions of the bunch-crossing, referred to as pile-up. The contamination of the hard-scatter event associated to additional interactions in the same bunch-crossing is called in-time pile-up, while the one due to signals from previous bunch-crossings is called out-of-time pile-up. The former can be generally mitigated using the detector tracker, but the latter can result in a non-negligible effect in cases where the detectors process signals with a time significantly larger than the bunch-spacing time of 25 ns. The number of pile-up interactions per bunch-crossing μ is given by

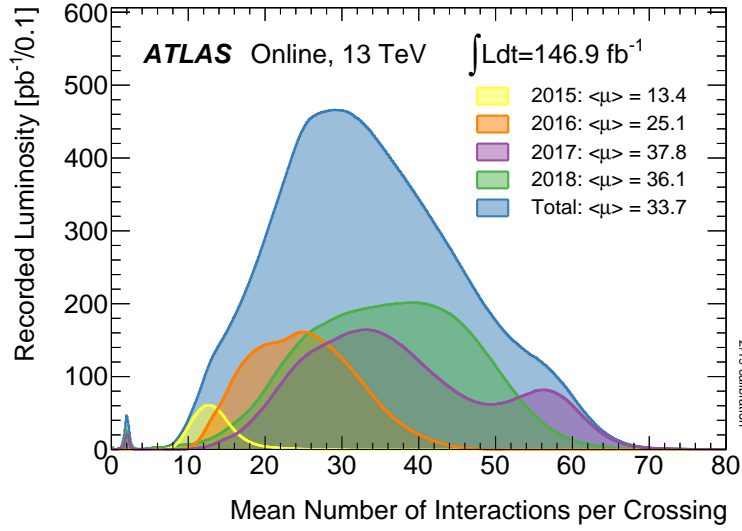


Figure 3.3: Distribution of the mean number of interactions per bunch-crossing for each year of Run 2 data at 13 TeV center-of-mass energy [82].

the following expression:

$$\mu = \frac{\sigma_{\text{inel}}L}{N_b f}, \quad (3.5)$$

where σ_{inel} denotes the pp total inelastic cross-section. The distribution of the mean number of pile-up interactions per bunch-crossing for each year of Run 2 at ATLAS is shown in Figure 3.3. For the entire Run 2, $\langle\mu\rangle$ was approximately 34, challenging the detector performance and calibration.

3.2 The ATLAS detector

As previously mentioned in Section 3.1.1, the ATLAS (A Toroidal LHC ApparatuS) detector [68] is one of the two multi-purpose detectors at the LHC. It exploits the high energy pp collisions of the LHC in order to seek a broad range of particle physics, from the Higgs boson to signs of new physics (such as dark matter, extra dimensions) at the TeV scale. ATLAS is approximately 7000 tons in weight and has the shape of a 44 m long and 25 m high symmetric cylinder consisting of different detecting sub-systems arranged in layers around the interaction point at the center of the detector, as shown in Figure 3.4. In order starting from the innermost to the outermost, these sub-detectors comprise:

- The Inner Detector which is composed of several high granularity tracking layers immersed in an axial magnetic field of 2 T that is generated by the solenoid magnet. It aims to reconstruct the trajectories and measure the momenta of charged

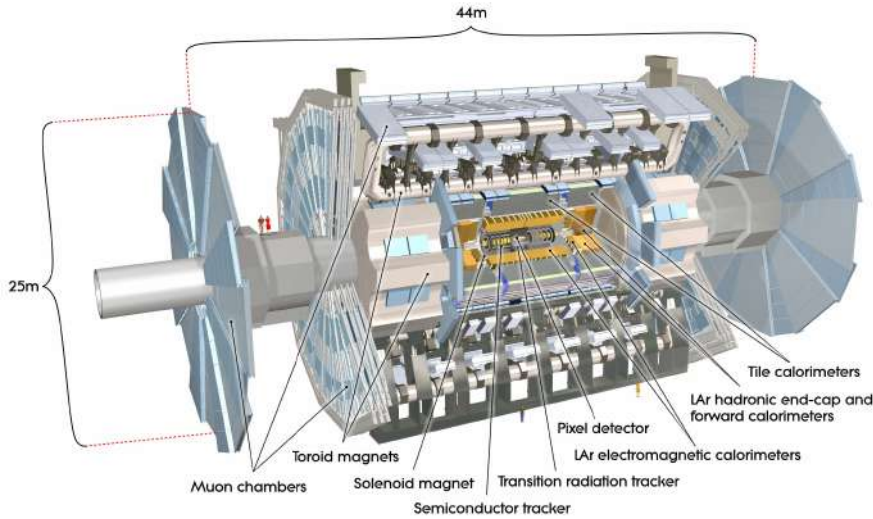


Figure 3.4: A schematic view of the ATLAS detector [68].

particles by making use of their curvatures in the magnetic field. Furthermore, it is also used to determine the interaction vertices of each bunch-crossing.

- The calorimetry system which includes the Liquid Argon (LAr) Calorimeter and the Tile Hadronic Calorimeter. It is designed to absorb most of particles coming from the collisions and then measures the energy they deposit within the system.
- The Muon Spectrometer which is used to detect and measure the momenta of muons escaping the calorimetry system. It consists of gaseous chambers embeded in the toroid magnets. These magnets provide a toroidal magnetic field of 0.5-1.5 T so as to bend the muon trajectories. The particular shape of the toroid magnets is a trademark of ATLAS and has largely driven the detector design.

Additionally, each of the three ATLAS sub-detectors is separated into barrel and end-caps in order to best cover the solid angle around the interaction point. The configuration which has been described allows the ATLAS detector to record the paths, the momenta and the energies of particles coming from the collisions in most directions and identify them individually.

3.2.1 The ATLAS coordinate system

In order to determine directions and positions inside the detector, ATLAS conventionally uses a right-handed cartesian coordinate system which is defined by the origin placed at the nominal interaction point, the z -axis along the beam direction, the x -axis pointing towards the LHC ring center and the y -axis pointing upwards. Besides, as

ATLAS has the shape of a cylinder, spherical coordinates (r, ϕ, θ) are also used for the detecting system. As usual, ϕ denotes the azimuthal angle measured around the beam in the transverse plane (xy -plane) and within a range of $[-\pi, \pi]$, while θ represents the polar angle defined in $[0, \pi]$ with respect to the z -axis.

In practice, it is impossible to retrieve the z -component of the initial partons momentum inside the colliding protons, therefore variables which are invariant under the Lorentz boost along the beam direction are preferable in most analyses of the LHC. Since the distance in θ depends on the longitudinal boost of the reference frame, it is often replaced by the rapidity y , defined as:

$$y = \frac{1}{2} \ln \left(\frac{E + p_z}{E - p_z} \right). \quad (3.6)$$

In the case of ultra-relativistic particle for which the mass is negligible with respect to its energy, y can be approximated to the pseudorapidity η , given by the following formula:

$$\eta = -\ln \left[\tan \left(\frac{\theta}{2} \right) \right]. \quad (3.7)$$

$\eta = 0$ corresponds to the cartesian y -axis of the ATLAS detector, while $\eta \rightarrow \infty$ directs to the beam axis. The distance ΔR between two objects reconstructed in the detector is often defined in the $\eta\phi$ -plane as follows:

$$\Delta R = \sqrt{(\Delta\eta)^2 + (\Delta\phi)^2}, \quad (3.8)$$

where $\Delta\eta$ and $\Delta\phi$ are the differences in η and ϕ of these two objects, respectively.

3.2.2 The Inner Detector

The Inner Detector (INDET) [83], represented in Figure 3.5, is the innermost part of ATLAS. It consists of three sub-detectors contained in a cylindrical envelope with a radius of 1.2 m and a length of 6.2 m along the beam pipe, being able to cover a pseudorapidity range of $|\eta| \leq 2.5$. The INDET is immersed in an axial magnetic field of 2 T which is generated by a surrounding thin superconducting solenoid magnet and is used to bend charged particles' trajectories inside the system. Basically, the INDET can reconstruct the trajectories of these particles by detecting their interactions with the material and consequently measures their momenta as well as their charges. The resolution of the momentum measured by the INDET can be mathematically expressed as a function of the particle transverse momentum p_T with the following formula:

$$\frac{\sigma_{p_T}}{p_T} = a p_T \oplus b, \quad (3.9)$$

where a denotes the intrinsic resolution of the momentum measurement in a magnetic field and b accounts for multiple-scattering effects. The unit of p_T here is in GeV. The studies of the ATLAS detector performance using cosmic-ray muons [84] showed

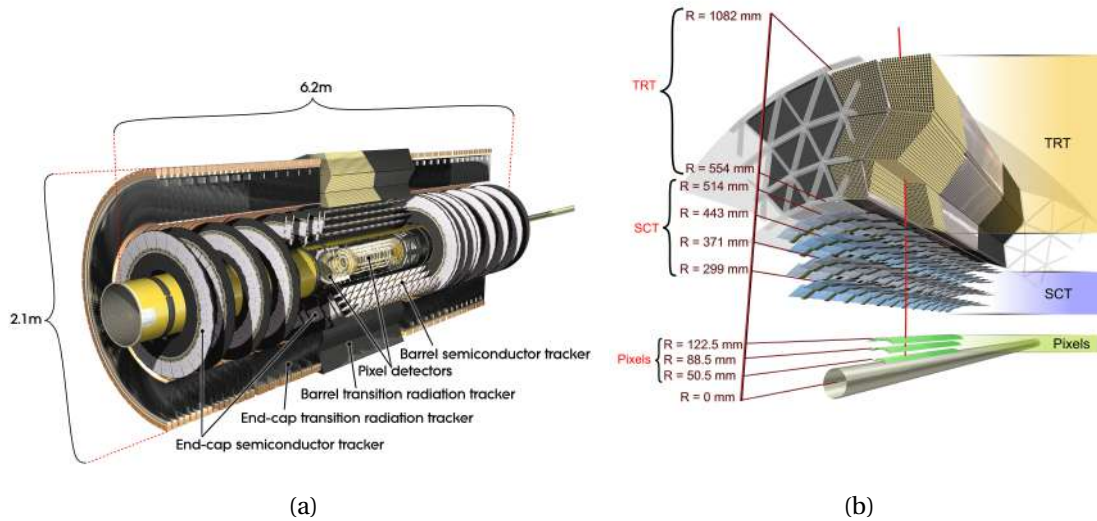


Figure 3.5: [3.5a](#) Cut-away view of the ATLAS Inner Detector. [3.5b](#) Transverse section of the ATLAS Inner Detector with structural elements [68].

that $a = 0.05\%$ and $b = 1.6\%$.

Once the tracks of particles are completely reconstructed, they are then extrapolated to the beam axis so as to define the interaction vertices based on overlaps of the extrapolated points. The ability for a track to match a reference vertex can be evaluated with the longitudinal and the transverse impact parameters. The former, called z_0 , is defined as the distance between the reference vertex and the extrapolated track position in the z -axis, while the latter, labelled as d_0 , is the perpendicular distance between the extrapolated track position and the beam line. In principle, the closer the track position can be extrapolated to the interaction plane, the better the impact parameter resolution is. Nevertheless, this performance can be dramatically deteriorated due to material scattering effects, especially at low particle momentum, calling for extremely light detecting and supporting structures.

The first part of the INDET, which is closest to the interaction point, is the Pixel Detector. It contains three barrel layers placed at radii of 50.5 mm, 88.5 mm and 122.5 mm from the beam axis, respectively. In addition, it has two end-caps, each of which consists of three disks. The Pixel Detector uses in total 1744 silicon pixel modules, each module is made of a planar n^+ -in-n silicon sensor tile which is bump-bonded to 16 front-end electronic chips with 2880 pixels each. The nominal pixel size is $50 \times 400 \mu\text{m}^2$ (about 90% of the pixels) and is dictated by the readout pitch of the front-end electronics [68]. This high granularity allows the Pixel Detector to provide a very good hit resolution of $14 \mu\text{m}$ in $r\phi$ and $115 \mu\text{m}$ in the z direction. During the Long Shutdown 1, a new pixel layer, the Insertable B-Layer (IBL) [85], has been added to the Pixel Detector, at a radius of 33.5 mm from the beam axis. Differently from the

other pixel layers, this additional layer uses silicon sensors based on both the hybrid planar and 3D technologies, with the pixel size of $50 \times 250 \mu\text{m}^2$. This design enables the IBL to provide a high quality of track and vertex measurements in the extreme proximity to the beam pipe where the device suffers a large amount of radiation damage. Furthermore, it is also beneficial in the reconstruction of secondary vertices associated to long-lived particles, such as b -hadrons, and thus improves the flavour tagging performance. The Pixel Detector as well as the IBL are further discussed in Chapter 4.

The middle component of the INDET is the Semi-Conductor Tracker (SCT), which consists of four cylindrical barrel layers and two end-caps with nine planar disks each. The SCT contains in total 4088 modules made of 15919 long, narrow strips each having the dimensions of $80 \mu\text{m}$ long in $r\phi$ and 64 mm long in z . It can therefore cover a large detection area of 63 m^2 and provide an intrinsic resolution of $17 \mu\text{m}$ in $r\phi$ and $580 \mu\text{m}$ in z .

The outer part of the INDET, which surrounds the two INDET sub-detectors mentioned above, is the Transition Radiation Tracker (TRT). This component comprises a barrel and two end-caps, covering a pseudorapidity range of $|\eta| \leq 2$. In the barrel region, there are 52544 straw tubes of 1.44 m length placed parallel to the beam axis, covering a radius range from 0.5 m to 1.1 m . In each end-cap, there are 122880 straw tubes of 0.39 m length placed perpendicularly to the beam axis, covering a geometrical range of $0.8 < |z| < 2.7 \text{ m}$. Each straw tube has a diameter of 4 mm and is filled with a mixture of 70% Xe, 27% CO_2 and 3% O_2 , that ionises when charged particles go through. Electrons produced from the gas ionisation are steered by a high electric field to a gold-plated tungsten anode wire of $31 \mu\text{m}$ in diameter placed in the center of the tube. This creates an avalanche effect which makes the tube acting as a proportional counter and stacking multiple tubes together makes tracking possible. The position resolution of the TRT is 0.17 mm , noticeably worse than the Pixel Detector and the SCT. Beside tracking, the TRT is also able to distinguish between particles using transition radiation materials which fill the spaces between the straws. These materials have widely varying refraction indices and produce radiation depending mostly on the mass of the incident particles. Therefore, the particle identification can be determined based on the intensity of the radiated photons. This design of the TRT helps particularly in the separation of electrons and pions.

3.2.3 Calorimeters

The next components of the ATLAS detector, which surround the ID and the solenoid magnet, are the calorimeters. They are designed with heavy materials (such as lead or steel), in order to completely absorb particles originating from the collisions and consequently measure the energy of these particles. In principle, when particles cross the calorimeters, their energy is gradually degraded through interactions with the materials to produce sequential sets of secondary particles also known as particle showers. Therefore, the energy of the incident particle can be reconstructed by measuring the

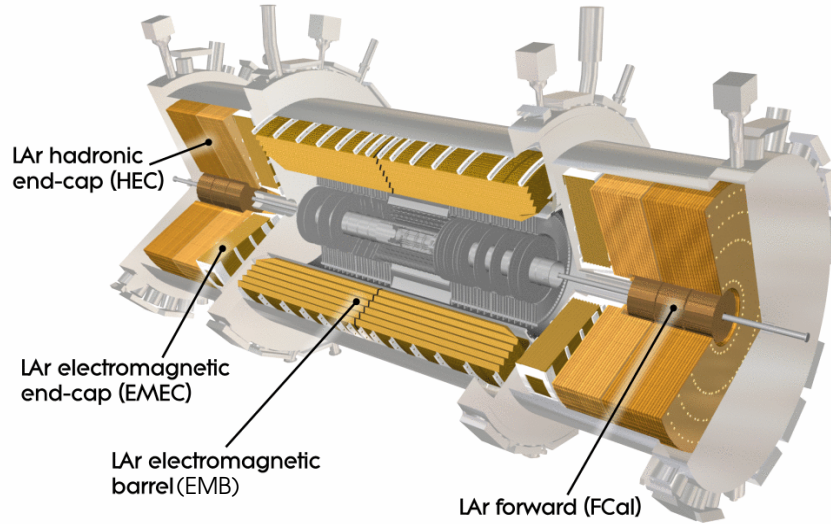


Figure 3.6: A cut-away view of the ATLAS calorimeter system [68].

total energy of particles constituting the shower. In fact, most of the particles including both charged and neutral particles are stopped inside the calorimeters by depositing a large fraction of their energy into the shower, except muons and neutrinos.

In general, particle physics calorimeters can be divided in two categories: sampling calorimeters and homogeneous calorimeters. These two types of calorimeters differ in the technologies used for the measurement of the incident particles. In the case of the sampling calorimeters, the material that produces the particle shower (absorber) can be distinct from the material that measures the deposited energy (active material). In contrast, in the case of the homogeneous calorimeters, a single active material providing both absorption and measurement functionalities is used for the entire area of the calorimeters. The calorimetry system of ATLAS, as shown in Figure 3.6, consists of three different sampling calorimeters, where absorber layers are alternated with layers of active material. These components are:

- The Electromagnetic Calorimeter, which is based on lead/liquid-argon and covers an area within $|\eta| < 3.2$. It provides the measurement of electromagnetic showers initiated by electrons, positrons and photons.
- The Hadronic Calorimeter, positioned at $|\eta| \leq 3.2$ and based on steel/scintillator tiles in the barrel and copper/liquid-argon in the end-caps. It aims at stopping and measuring the energy of hadronic particles such as pions, protons, neutrons, kaons, etc.

- The Forward Calorimeter, measuring the energy of both electromagnetic and hadronic particles in the forward region, between $3.1 < |\eta| < 4.9$. It uses copper or tungsten for the absorber material and liquid-argon for the active material.

All the three calorimeters have full ϕ symmetry and the coverage of the whole system extends up to $|\eta| < 4.9$. The configuration of the ATLAS calorimeter system brings the advantage that a fine segmentation can be achieved also in the longitudinal direction, allowing for a precise reconstruction of the shower evolution in all dimensions. However, this costs the energy resolution, as part of the energy is deposited in the absorber and never measured.

The energy resolution in a calorimeter can be parametrized as follows:

$$\frac{\sigma_E}{E} = \frac{a}{\sqrt{E}} \oplus \frac{b}{E} \oplus c, \quad (3.10)$$

where E denotes the energy and has the unit in GeV; a , b and c denote the sampling, noise and constant terms, respectively, while \oplus represents the quadratic sum. The sampling term accounts for statistical fluctuations of the shower and the signal, along with inefficiencies of the energy deposition in the active material. An example of the latter contribution is the partial loss of shower information in a sampling calorimeter. The noise term corresponds to the effects of electronics noise and pile-up. Lastly, the constant term accounts for systematic effects which includes errors due to the non-uniformity of the energy response/collection, energy leakage caused by non fully contained showers and upstream energy losses. An excellent calibration procedure is required to minimize the constant term. From Equation 3.10, it is also obvious to see that at very low energies the noise term is the dominant term of the calorimeter resolution, while at high energies the dominant one is the constant term that limits the performance.

Electromagnetic Calorimeter

As mentioned, the ATLAS electromagnetic calorimeter (ECAL) [86] is a sampling calorimeter. In the ECAL, liquid Argon (LAr) is used as the active medium. It is kept at around 88 K and filled in gaps of 4.5 mm between the absorber layers made of lead. The ECAL has an accordion geometry which makes it possible to cover the full ϕ range without an instrumentation gap and also allows a fast and azimuthally uniform response.

The ECAL consists of three parts, one barrel and two end-caps, each made of two wheels. The barrel ECAL contains three layers with decreasing granularity and is around $24 X_0$ ¹. It can cover a pseudorapidity range up to $|\eta| < 1.475$. A schematic view of a barrel module is represented in Figure 3.7a. The outer wheels of the end-cap ECAL are also segmented into three longitudinal layers as for the barrel, while the inner

¹The radiation length X_0 describes the mean distance over which the energy of high energetic electrons or photons is reduced by bremsstrahlung by a factor of $1/e$

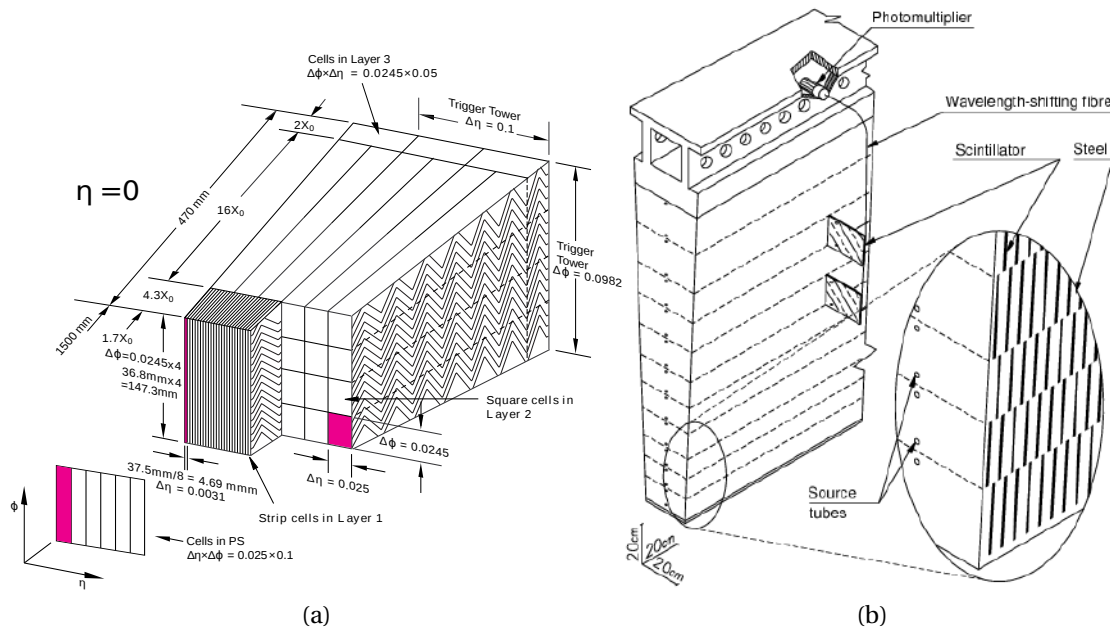


Figure 3.7: **3.7a** View of the accordion geometry of the ECAL. **3.7b** Schematic showing of a tile calorimeter module. The various components of the optical read-out, namely the tiles, the fibres and the photomultipliers, are shown [68].

wheels have two layers with a coarser granularity in both direction. The end-caps can cover a region within $1.375 < |\eta| < 3.2$. The ECAL has been designed to achieve an energy resolution as:

$$\frac{\sigma_E}{E} = \frac{10\%}{\sqrt{E}} \oplus \frac{0.1\%}{E} \oplus c, \quad (3.11)$$

where the constant c is less than 1% in the barrel and 1-2% in the end-caps [87, 88].

Hadronic calorimeter

The hadronic calorimeter (HCAL) [89], surrounding the ECAL, is the outermost part of the ATLAS calorimetry system. Its primary goal is to measure energy deposited from strongly interacting hadrons that escape the ECAL. The HCAL is composed of a barrel and two end-caps with different technologies applied. The barrel HCAL is the Tile calorimeter (TileCal) which contains three sections: a long barrel covering a range up to $|\eta| < 1$ and two extended barrels covering an area within $0.8 < |\eta| < 1.7$. The TileCal uses steel as the absorber and scintillating tiles as the active material. The scintillating tiles are placed in the plane perpendicular to the beam axis and are radially staggered in depth, as shown in Figure 3.7b. The passage of charged particles in the scintillating tiles produces ultraviolet light. The latter is then collected and converted

into visible light via wavelength shifting fibers, before reaching photomultiplier tubes (PMTs) which output an amplified electrical signal. The hadronic end-cap calorimeter (HEC) also uses LAr as the active material for the energy measurement. However, its absorber material is made of copper instead of lead. The HEC is located behind the end-cap ECAL, consists of two independent wheels and covers a pseudorapidity range of $1.5 < |\eta| < 3.2$.

The energy resolution of HCAL is expressed as follows [90, 91]:

$$\frac{\sigma_E}{E} = \frac{50\%}{\sqrt{E}} \oplus \frac{1\%}{E} \oplus 3\%. \quad (3.12)$$

The HCAL resolution is less precise, both in energy magnitude and in localization than the ECAL. The main reason for this decrease is that a significant fraction of the initial energy diverted to low energy nuclear processes is not reconstructed. Additionally, hadronic showers also have electromagnetic components which interact differently with the HCAL than the hadronic parts.

Forward calorimeter

The Forward Calorimeter (FCAL) [92] covers a pseudorapidity range of $3.1 < |\eta| < 4.9$, where the particle flux is extremely high. It is particularly important in the reconstruction of the Missing Transverse Momentum (discussed later) originating from particles that escape the detector, such as neutrinos and BSM particles. The FCAL is segmented into three layers and all of them use LAr as the active material. The first layer uses copper as the absorber material to measure electromagnetic showers, while the two others deploy tungsten absorbers, targeting a reconstruction of hadronic showers.

3.2.4 Muon Spectrometer

Differently from most of other particles, muons are not absorbed but only lose a small fraction of energy when they traverse the calorimeters. Therefore, the detection of muons outside the calorimeters is essential to precisely identify them and complement their momentum measurement that is partially provided by the INDET. The outermost sub-detector of ATLAS, the Muon Spectrometer (MS) [93] represented in Figure 3.8, is dedicated to this purpose. The MS is an extremely large tracking system with its coverage extending up to $|\eta| < 2.7$ and $r = 11$ m. It can measure the momenta of muons based on the curvature of their trajectories in the magnetic field generated by the air-core toroidal magnets system.

The MS consists of gas-based chambers that can be categorised into the precision tracking chambers and the fast trigger chambers. The precision tracking chambers are used for a precise trajectory measurement of the muons. They comprise:

- The Monitored Drift Tube (MDT) chambers which cover a pseudorapidity range of $|\eta| < 2.0$. Each MDT chamber consists of three to eight layers of drift tubes.

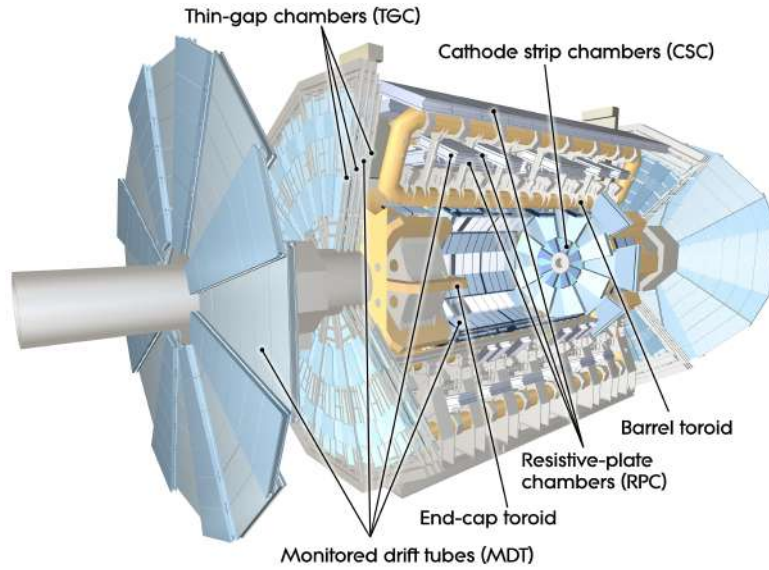


Figure 3.8: A cut-away view of the ATLAS Muon Spectrometer [68].

The tube is made of aluminium, has a diameter of 30 mm and is filled with a gas mixture of 93% Ar and 7% CO₂. In total, there are around 1200 MDT chambers used in ATLAS.

- The Cathode Strip Chambers (CSCs) which are organized into four layers in the forward region ($2 < |\eta| < 2.7$). The CSCs are multi-wire proportional chambers with cathode planes segmented into strips in orthogonal directions. They have finer granularity, higher acceptance rate and time resolution than the MDTs in order to cope with the high background rates in the region close to the beam line.

The fast trigger chambers are designed with a coarser resolution and used for a trigger. This system is composed of:

- The Resistive Plate Chambers (RPCs) which cover a region within $|\eta| < 1.05$. The basic RPC unit is a narrow gas gap formed by two parallel resistive plates.
- The Thin Gap Chambers (TGCs) which are installed in a pseudorapidity range of $1.05 < |\eta| < 2.4$. Due to the high event rates, TGCs are designed in a way similar to the CSCs.

Even though the fast trigger chambers have lower resolution compared to the precision tracking chambers, they can provide much faster signal read-outs required for the Level-1 (L1) muon trigger.

The MS can be used as a standalone detector for the identification and reconstruction of muons. A resolution of the order of 10% is achieved for muons of 1 TeV. The

MS performance can be improved by using in addition the tracking information of the INDET.

3.2.5 Trigger and Data Acquisition

The LHC collides proton bunches in every 25 ns corresponding to a bunch-crossing frequency of around 40 MHz. This results in a huge data rate of approximately 60 TB/s produced by all the ATLAS sub-detectors. It would be impossible to record all the information due to limits of the bandwidth and the storage space available. Additionally, out of all the pp collisions from the LHC, only a few events are of interest for the ATLAS physics analyses. Because of these two reasons, a selection must be performed so as to give priority to some signatures. The ATLAS trigger system [94], whose layout is represented in the Figure 3.9, serves this end. It consists of a hardware-based Level-1 (L1) Trigger and a software-based High Level Trigger (HLT).

Level-1 Trigger

The L1 trigger represents the first stage of the ATLAS online selection process. It is implemented in fast custom-built electronics to trigger on reduced-granularity information from the calorimeters and the Muon Spectrometer within a latency of less than $2.5 \mu\text{s}$. The analogue signal inputs from the calorimeters are analysed by the L1 Calo to identify electron, photon, τ -lepton and jet candidates and missing transverse momentum. The effects of pile-up on these objects are mitigated by a dedicated pedestal correction algorithm in the L1 Calo. The inputs of hits coming from the fast trigger chambers of the MS and the Tile calorimeter are treated by the L1 Muon to search for coincident hits which are consistent with muons originating from the interaction point. The objects identified by L1 Calo and L1 Muon are sent to the L1 Topo, where topological requirements (such as invariant masses or angular distances) are applied to geometric or kinematic combinations between these objects.

The resulting data is finally processed by the Central Trigger Processor (CTP) to form a single-bit decision, called L1 accept. The CTP is also responsible for applying dead time, which limits the minimum time between two consecutive L1 accepts and restricts the number of L1 accepts allowed in a given number of bunch crossings. The former is to avoid overlapping read-out windows, while the latter is to prevent front-end buffers from overflowing.

The L1 accept signal is transmitted across the detector systems either to read-out the full event or to discard it. The data of the accepted event received from all the sub-detectors is then passed to the second stage of the trigger, the HLT. In addition to performing the first selection step, the L1 trigger identifies Regions of Interest (RoIs) in η and ϕ within the detector to be investigated by the second trigger stage. The L1 trigger reduces the event rate from 40 MHz down to 80 kHz.

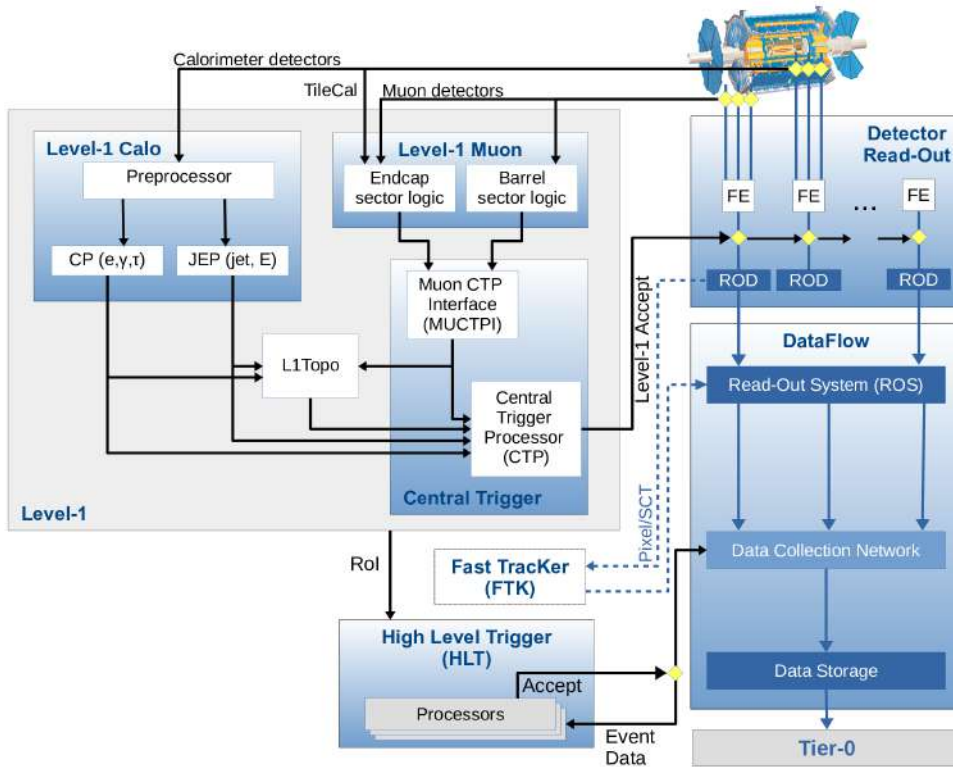


Figure 3.9: Schematic illustration of the ATLAS Run 2 Trigger and Data Acquisition system [94].

High Level Trigger

The HLT is the second stage of the ATLAS trigger system. It firstly performs a reconstruction based on dedicated fast trigger algorithms to early reject the majority of unwanted events. Following this step, a reconstruction using more precise and more CPU-intensive algorithms is performed to make the final selection. A dedicated computing farm made of approximately 40000 selection applications, called Processing Units (PUs), is used to execute these algorithms. The PUs are designed to make decisions within a few hundred milliseconds. The full detector granularity as well as event-data fragments based on the RoIs defined by L1 trigger are also exploited in the HLT. The physics output rate of the HLT during an ATLAS data-taking run is on average 1.2 kHz with an average physics throughput to permanent storage of 1.2 GB/s. Once an event is accepted by the HLT, its data is sent to the Tier-0 machine at CERN's computing centre for the offline reconstruction.

3.3 Physics object reconstruction in the ATLAS detector

Different types of particles interact in different ways with the various detector components, resulting in various detector signals, as shown in Figure 3.10. ATLAS employs several dedicated techniques, which are described below, to identify and reconstruct the different physics objects based on these measurable signals.

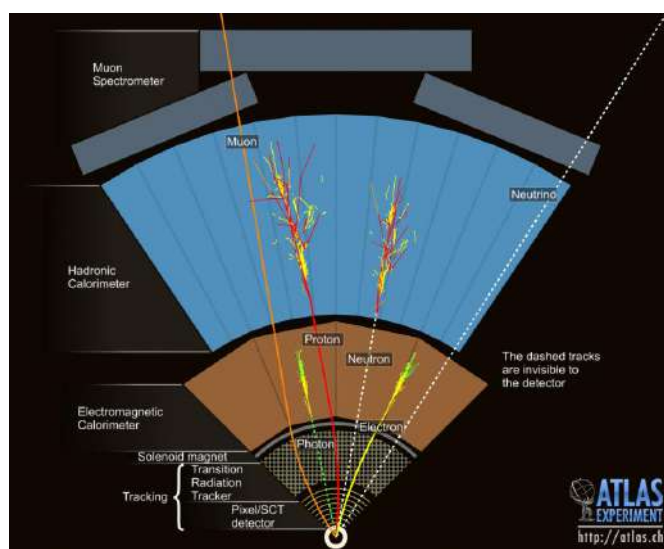


Figure 3.10: Transverse view of an ATLAS detector segment with a representation of the interaction of different types of particles in the different sub-detectors [95]. The solid curves display the tracks of charged particles while the dashed ones correspond to neutral particles. The muon emerging from the interaction region traverses all detector layers and its track is determined by measurements from both the Inner Detector and Muon Spectrometer. The electron and photon are mainly stopped in the Electromagnetic calorimeter and are distinguished from one another by the presence or absence, respectively, of a track matching the corresponding energy deposit in the calorimeter. The proton and neutron are predominantly captured by the hadronic calorimeter with the former additionally leaving a track in the Inner Detector. Lastly, the neutrino goes through the whole detector without leaving any signature.

3.3.1 Tracks

Information from the INDET is used to reconstruct the corresponding tracks. The track reconstruction [96, 97] starts with building clusters based on the deposited energy in the Pixel, SCT and TRT detectors. These clusters are then transformed into

3D space-points which illustrate positions where the track interacts with the INDET active material. Track seeds formed from sets of the space-points are subsequently selected by applying selection criteria. The chosen seeds are then extrapolated through a combinatorial Kalman filter [98] to build a track candidate. In fact, there are two track-finding algorithms used in ATLAS. The first one is an inside-out strategy in which the track seeds in the Pixel and SCT detectors are extended outwards to include the measurements from the TRT. This strategy is used to reconstruct tracks originating from the primary vertices. On the other hand, the second algorithm, which is known as an outside-in or track-backing pattern recognition strategy, makes use of hits that are not selected by the former to build track segments in the TRT and then extrapolates them back to the Pixel detector. The latter strategy is mainly used to reconstruct tracks that are from the secondary vertices of long-lived particles such as Λ or K_S , photon conversions and material interactions occurring in the INDET. After building the track candidates, an ambiguity-solver is applied to resolve ambiguities arising when clusters are assigned to more than one track candidates. Firstly, the ambiguity-solver gives each track candidate an individual track score which can be estimated from measures of the track quality, such as the χ^2 of the track fit and missing hit in the detector after the fit (hole). Tracks with incorrect assigned clusters will result in bad scores and will be therefore suppressed by the solver. The track scores of the remaining candidates are then favourably weighted by requiring that clusters can be shared by no more than two tracks and a track can have a maximum of two shared clusters. This step returns a list of good track candidates ordered according to their scores, from the highest to the lowest. After resolving all the ambiguities, a high-resolution fit is performed for the remaining good track candidates. Finally, the output tracks of the solver are selected through sets of track quality requirements, as follows:

- **Loose:** tracks are required to have $p_T > 400$ MeV and $|\eta| < 2.5$, and at least 7 pixel and SCT hits. There is at most 1 or 2 shared clusters on track in the Pixel module or SCT respectively. At most 2 holes and 1 hole in the silicon detectors and pixel detector, respectively, are allowed. These criteria allow a high track reconstruction efficiency with the price of non-negligible rate of fake tracks.
- **Tight Primary:** On top of the Loose requirements, tracks are further requested to have at least 9 silicon hits in the region of $|\eta| \leq 1.65$ or at least 11 silicon hits in the region of $|\eta| > 1.65$. At least one hit of the innermost two pixel layers and no holes on track in the pixel detector are required. This set of requirements is designed to optimize the primary track selection in which the rate of fake tracks is reduced to a negligible level at high pile-up at the cost of a decrease of track reconstruction efficiency.

Figure 3.11 summarizes the flow of track candidates through the ambiguity-solver. The transverse and longitudinal impact parameter resolutions as functions of p_T in Run 1 (2012) and Run 2 (2015) are represented in Figure 3.12. It can be seen that the implementation of the IBL in Run 2 improved noticeably the resolutions, meaning a better track reconstruction than Run 1.

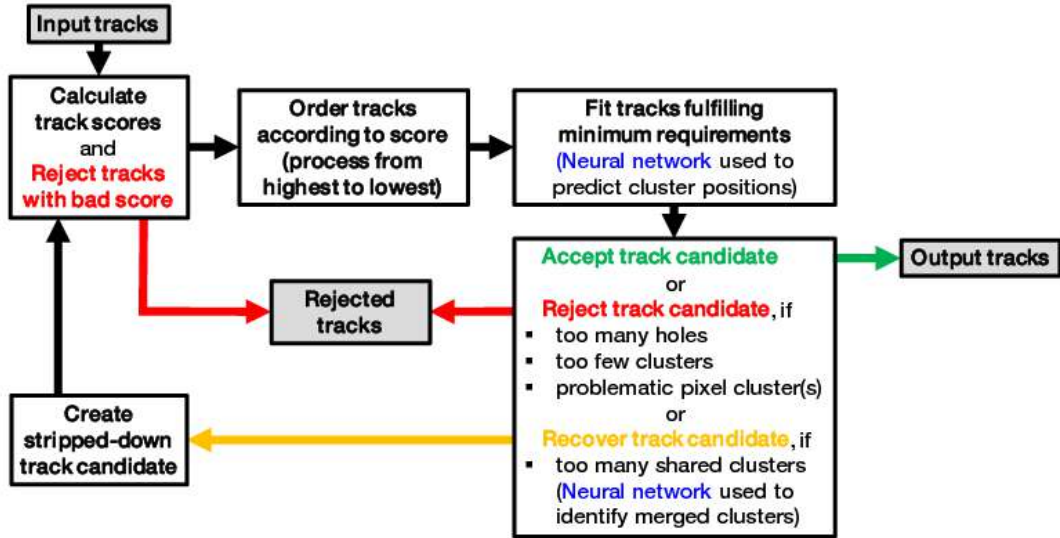


Figure 3.11: Sketch of the flow of tracks through the ambiguity solver [96].

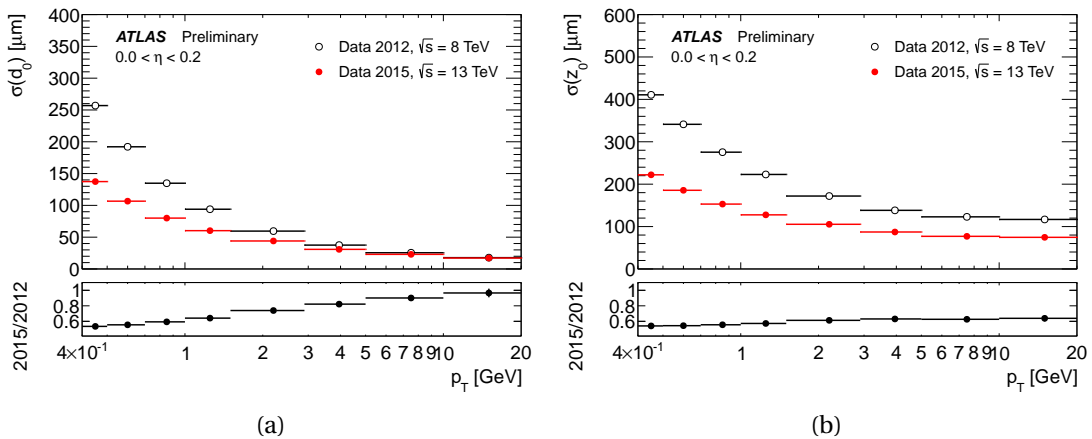


Figure 3.12: The 3.12a transverse and 3.12b longitudinal impact parameter resolutions as functions of p_T in 2015 (with IBL) and 2012 (without IBL) [99]. Tracks were required to pass the Loose selection as discussed.

3.3.2 Primary vertices

An Iterative Vertex Finding procedure [100] is used to reconstruct the spatial position of pp interaction vertices, based on a set of reconstructed tracks which pass the Tight Primary selection with two additional requirements: tracks must have minimum of one hit in the IBL and B-Layer and maximum of one hole in the SCT. The vertex seed is defined as the global maximum z -position of these tracks. The seed position as well as

information of the neighboring tracks are used as inputs for the Adaptive Vertex Fitting algorithm [101] to calculate the vertex position. This algorithm is an iterative fit which makes use of the goodness of χ^2 to test the compatibility of tracks with the vertex. Any tracks which are incompatible with the vertex by more than 7 standard deviations are used to seed another vertex. This procedure is repeated until no additional vertices can be found or no unassociated tracks are left. Vertices are required to associate to at least two tracks.

The number of reconstructed interaction vertices is increased by the presence of pile-up in the event. The main primary vertex which corresponds to the hardest process in the event is chosen as the vertex having the highest sum of the squared transverse momentum of tracks associated to it, while the other primary vertices are considered to be associated with pile-up interactions. Any events containing no primary vertices will be discarded. Vertices which are displaced from the beam collision region are considered as secondary vertices. Figure 3.13 shows the vertex reconstruction efficiency as a function of the number of tracks using a small amount of data collected in 2015, it can be noticed that the vertex reconstruction efficiency is 100% for events which have at least five reconstructed tracks [102].

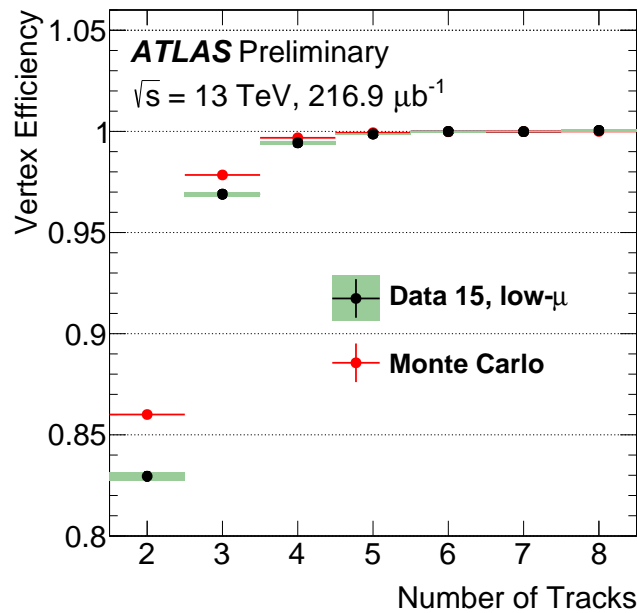


Figure 3.13: Vertex reconstruction efficiency as a function of the number of tracks in low- μ data compared to Monte Carlo simulation (Pythia 8 A2:MSTW2008LO). This measurement uses data corresponding to an integrated luminosity of $216.9 \mu\text{b}^{-1}$ [102].

3.3.3 Electrons and photons

Electrons and photons give analogous signatures in the Electromagnetic calorimeter (ECAL). Both types initiate electromagnetic showers in the ECAL. Therefore, the reconstruction algorithms of electrons [103] and photons [104] are in a similar manner which is based on using information from the ECAL and the INDET.

Within the ATLAS central region where $|\eta| < 2.47$, measurements from both the INDET and the ECAL are combined for the reconstruction of electrons and photons. This procedure starts with splitting the ECAL into a grid of towers. Each tower has a size of 0.025×0.025 in the $\eta \times \phi$ space, which is the same as the granularity of the middle ECAL layer. The total energy deposited in one tower is estimated by summing together the deposited energies in all the three ECAL layers within this element. After that, the full ECAL acceptance is scanned using a sliding-window of 3×5 towers in order to determine cluster seeds whose transverse energy above 2.5 GeV [105]. During the scan, the position of this sliding-window is also adjusted in order that its total transverse energy is a local maximum. A cluster algorithm [106] is then used to reconstruct the clusters around the seeds.

The reconstruction of the clusters is followed by an attempt to link the clusters to track candidates of electrons in the INDET. The procedure to reconstruct these track candidates is similar to the one described in Section 3.3.1, but with a modification to account for potential energy losses due to Bremsstrahlung radiation, which is predicted to be greater for electrons. The space between the track candidate and the ECAL cluster barycenter in the η - ϕ plane is used to evaluate the matching possibility. In case when the matching is possible and the track is compatible with an origin from the primary vertex, the cluster is considered as an electron candidate. If the cluster is matched with a track originating from a displaced vertex, this is the case when a photon conversion, in which a photon splits into a e^+e^- pair, takes place before the ECAL and the cluster is labelled as a converted photon. If the matching fails, the cluster is tagged as an unconverted photon. Backgrounds from conversions and secondary particles created in long-lived particle decays, as well as pile-up interactions, are reduced by imposing additional constraints on the track parameters. The clusters tagged as the electron and converted photon candidates are then rebuilt in the barrel (end-cap) area of the calorimeter using a bigger window size of 3×7 (5×5) units in the last stage of the reconstruction operation. The clusters tagged as unconverted photon candidates in the barrel area, on the other hand, are retained at the same window size of 3×5 due to their reduced lateral size. The cluster energy is then assessed by using a specific calibration technique based on the full detector simulation and real data.

After the electron reconstruction is complete, an identification procedure is employed to exclude background objects that were misidentified as prompt electrons. It uses a collection of calorimeter- and track-based discriminating variables as input. In fact, there are two kinds of identification algorithms: cut-based identification or likelihood-based (LH) identification. The cut-based one applies independent requirements on the discriminating variables, whereas the LH one imposes a single

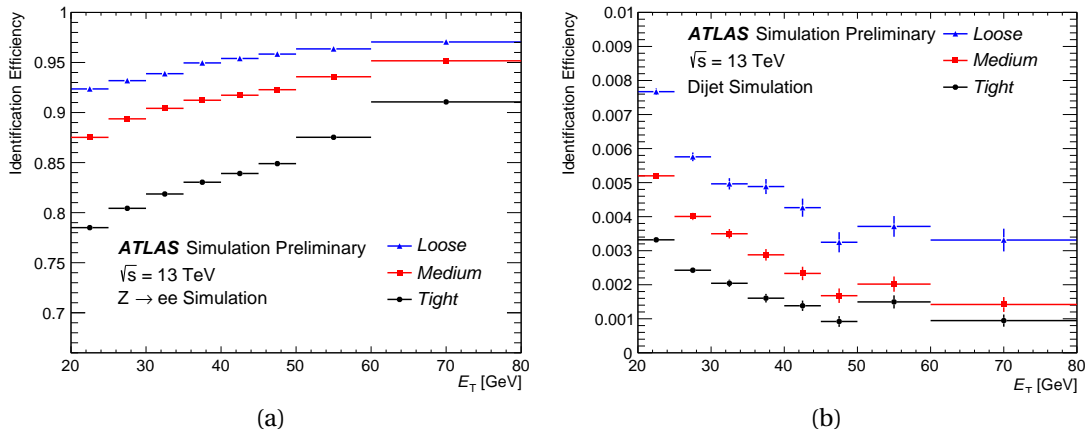


Figure 3.14: 3.14a Prompt electron identification efficiency obtained in simulated $Z \rightarrow ee$ events. 3.14b Fake electron misidentification efficiency obtained from a simulated multijet sample [105].

requirements on a likelihood discriminant which is defined based on the probability density functions of these variables. During Run 2, ATLAS used the latter as the baseline electron identification. The prompt electrons are selected in three working points: Loose, Medium and Tight in order of increasing background rejection. The electron identification efficiency and the the background misidentification efficiency of the three working points are given in Figure 3.14.

In contrast, the identification of photons [107] is accomplished with a cut-based method in which discriminating variables representing the form and features of associated showers in the ECAL as well as the deposited energy in the HCAL are subjected to selection criteria. Two working points are mentioned in particular: Loose and Tight. They are adjusted for unconverted and converted photons individually.

Along with the identification criteria, electron candidates are also required to meet isolation requirements in order to gain the purity of prompt electrons. To quantify the electron isolation, two discriminating variables are used: the calorimetric isolation energy $E_T^{\text{cone}0.2}$ and the track isolation $p_T^{\text{varcone}0.2}$. The former and the latter are defined as the total transverse energy and the total transverse momentum within a cone of $\Delta R < 0.2$ around the electron cluster candidate and around the electron track candidate, respectively. Different sets of requirements categorised into the *efficiency targeted operating points* and the *fixed requirement operating points* are applied on the quantities $E_T^{\text{cone}0.2}/E_T$ and $p_T^{\text{varcone}0.2}/p_T$ to select the isolated electron candidates.

3.3.4 Muons

Muons are reconstructed using a variety of methods that make use of data from the Inner Detector (INDET), the Electromagnetic Calorimeter (ECAL) and the Muon

Spectrometer (MS). There are four different types of the reconstructed muons based on the sub-detectors employed in the reconstruction [108].

- **Combined (CB) muons:** In the INDET and the MS, track candidates of muons are reconstructed separately. After that, a global fit utilizing hits from these two sub-detectors is performed to combine the tracks that are possibly from the same muons. The combined track is then used to reconstruct the muon candidate.
- **Segment-tagged (ST) muons:** The INDET track candidates of muons are extrapolated into the MS. Then the tracks that are linked to at least one local track segment in the initial MS station are used to reconstruct the muon candidates. The ST muons are particularly used when muons traverse only one layer of the MS chambers.
- **Calorimeter-tagged (CT) muons:** Muon candidates belonging to this category are rebuilt by matching an INDET track to an energy deposited in the ECAL consistent with a minimum-ionizing particle. The purity of the CT muons is the lowest among the reconstructed muon types. However, they can recover the acceptance region of $|\eta| < 0.1$ where the MS chambers are absent.
- **Extrapolated (ME) muons:** Only the MS information is used to reconstruct muon tracks. Estimated energy loss in the calorimeters is included into the extrapolation of these tracks from the MS to the interaction point. The ME muons are utilized to expand the acceptance of muon reconstruction into the range of $2.5 < |\eta| < 2.7$, which is not covered by the INDET.

In the identification procedure, muon candidates must also satisfy additional requirements in order to be considered as prompt muons. These additional requirements consist of the compatibility of the INDET and the MS individual momentum and charge measurements, the number of hits in each sub-detector and the χ^2 fit quality. Similarly to the electron identification, by tightening the selection criteria, three distinct efficiency working points are defined: Loose, Medium and Tight in order to cope with the specific needs of various physics analyses. Additionally, there is the High- p_T working point for maximizing the momentum resolution when reconstructing muon tracks with $p_T > 100$ GeV. The muon reconstruction efficiency as a function of η for the four different working points are shown in Figure 3.15.

To suppress muons originating from cosmic rays, any events containing muons with a transverse impact parameter of $d_0 > 0.2$ mm and a longitudinal impact parameter of $z_0 > 1$ mm will be discarded. Additionally, a muon whose angular distance ΔR with the closest jet (see Section 3.3.5) is less than 0.4 is also rejected.

3 The Large Hadron Collider and the ATLAS detector – 3.3 Physics object reconstruction in the ATLAS detector

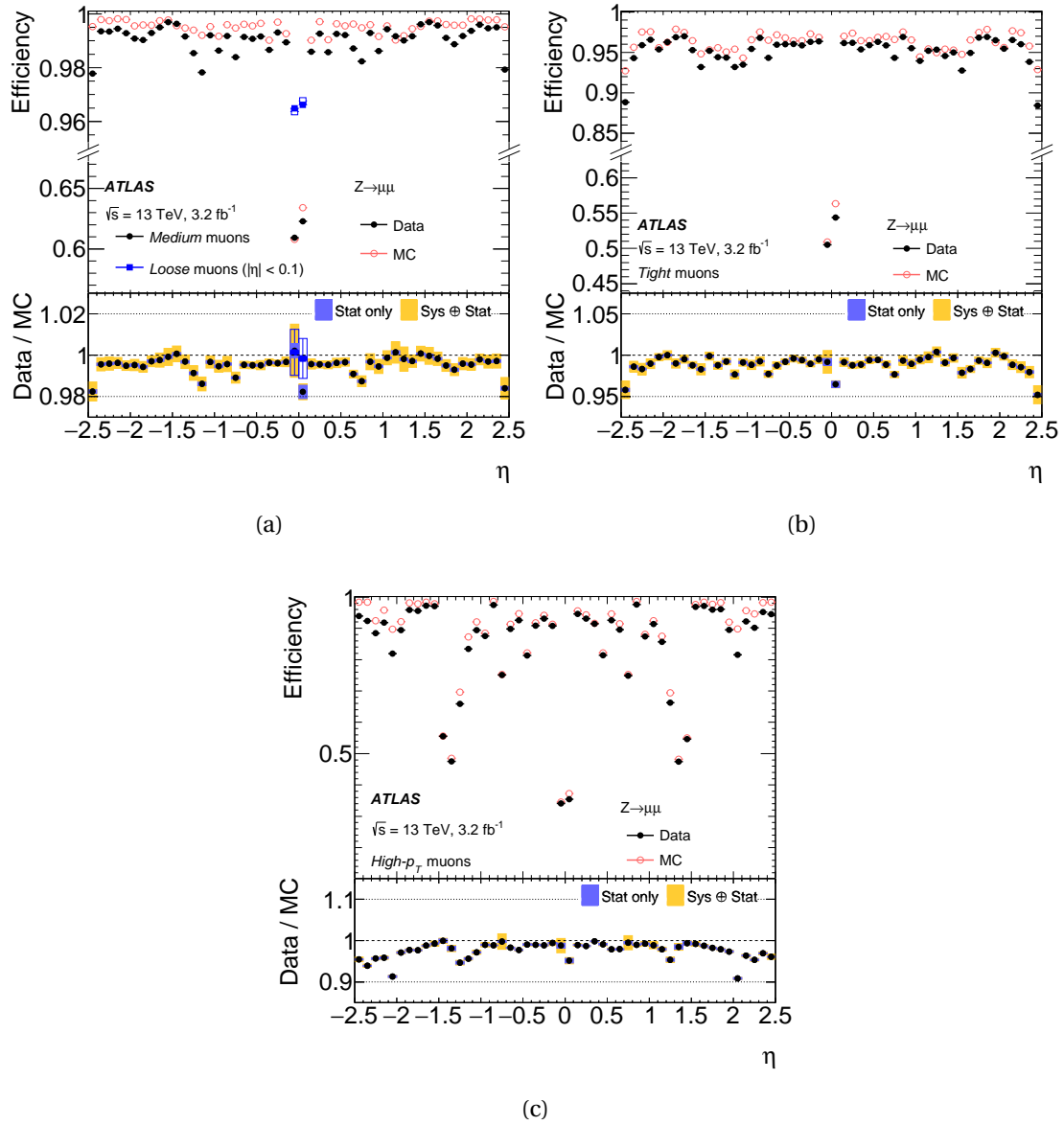


Figure 3.15: Reconstruction efficiency of muon candidates as a function of η for 3.15a Loose, Medium, 3.15b Tight and 3.15c High- p_T identification selection measured in $Z \rightarrow \mu\mu$ events [108].

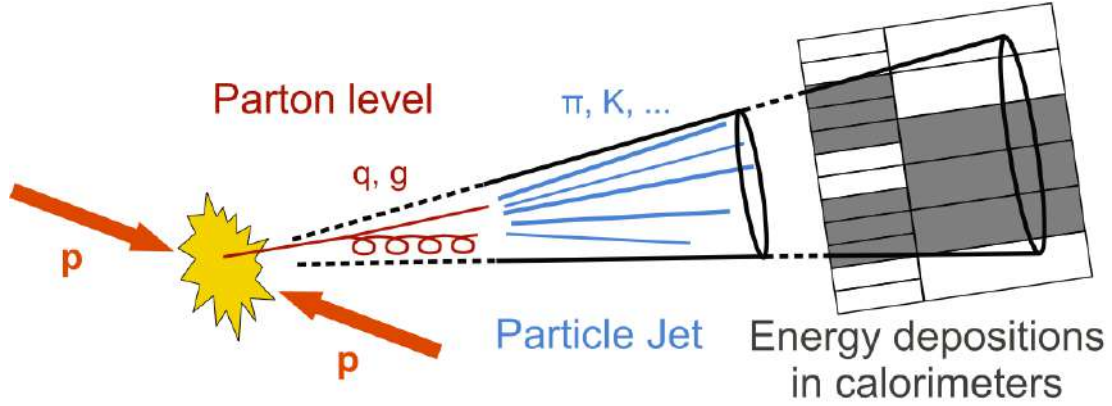


Figure 3.16: Sketch of pp collision and resulting collimated spray of particles, a jet [111].

3.3.5 Jets

As defined by the Standard Model, strongly interacting particles carrying colour, i.e. quarks and gluons, due to colour confinement, hadronise with other particles to create colourless states after they are released in a collision. The relativistic hadrons originating from the hadronisation process of quarks and gluons travel collinearly and eventually form a narrow cone which is referred to as a jet. Figure 3.16 depicts a schematic representation of the creation of a jet. Jet reconstruction procedure begins with clustering topological energy deposits in both ECAL and HCAL [109] in three-dimensions. A clustering algorithm is then used to merge the resulting clusters to form a jet. In fact, there is a variety of clustering algorithms available for the aim of reconstructing jets and ATLAS makes extensive use of the anti-kT algorithm [110].

The anti-kT is a cone algorithm which is iterative. It begins by defining two primary variables which represent the distance d_{ij} between entities (i.e. clusters) i, j and the distance d_{iB} between entity i and the beam B , as follows:

$$d_{ij} = \min\left(\frac{1}{k_{ti}^2}, \frac{1}{k_{tj}^2}\right) \frac{\Delta R_{ij}^2}{R^2}, \quad (3.13)$$

$$d_{iB} = \frac{1}{k_{ti}^2}, \quad (3.14)$$

where $\Delta R_{ij}^2 = (\eta_i - \eta_j)^2 + (\phi_i - \phi_j)^2$ and k_{ti}, η_i, ϕ_i are the transverse momentum, the pseudorapidity, the azimuthal angle of the entity i , respectively. R denotes the radius parameter which defines the radius of the output jet cone and the minimum distance between two unmerged jets as well. In each iteration, the algorithm calculates the distances d_{ij} and d_{iB} and identifies the smallest one. If d_{iB} is the smallest, it treats the entity i as a new jet and eliminates this entity from the input list. Otherwise, the two

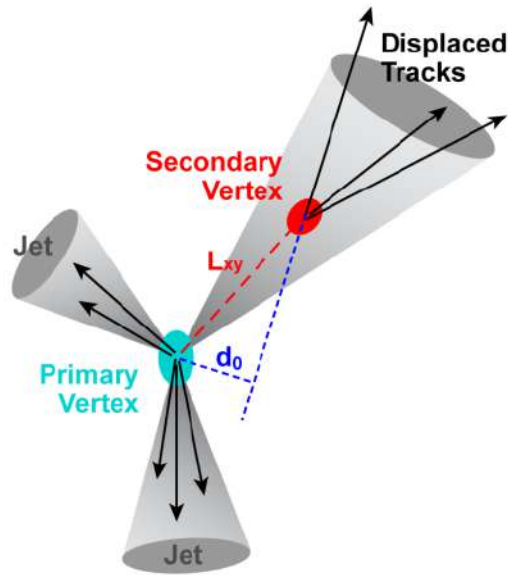


Figure 3.17: A visualization of a secondary vertex characterized by the distance displaced from the primary vertex in the transverse plane L_{xy} and the impact parameter of a track denoted as d_0 which is used for the SV reconstruction [112]

entities i and j are combined to a single larger entity. The anti-kT then recomputes the distances and repeats the same procedure until there are no entities remaining.

On jet candidates, a cleaning process is used to eliminate calorimeter noise, cosmic muons, and beam-induced background. In order to guarantee that jet candidates come from a hard scatter interaction rather than pile-up, they must also go through a pile-up mitigation process. The bipolar signal pulse form of the LAr calorimeter provides resistance to out-of-time pile-up even at the hardware level. An initial cleaning step is conducted at the topological clustering level, taking into account only calorimeter cells that exceed a certain noise threshold. To further minimize pile-up, the cleaning procedure makes use of the cluster energy ratio between the ECAL and the HCAL together with tracking information from the INDET. Following that, a calibration procedure is applied to remove the remaining pile-up contributions in the measured jet energy.

b-jet Tagging

The b -jets, which are produced by the hadronisation of a b -quark, are a particularly intriguing sub-category of jets. It is the relatively long lifetime of B -hadrons that makes the singularity in b -jets. At an energy of approximately 50 GeV, they can travel an average length of 3 mm before decaying into more stable particles. This implies that B -hadrons decay inside the ATLAS tracker most of time. Therefore, the reconstruc-

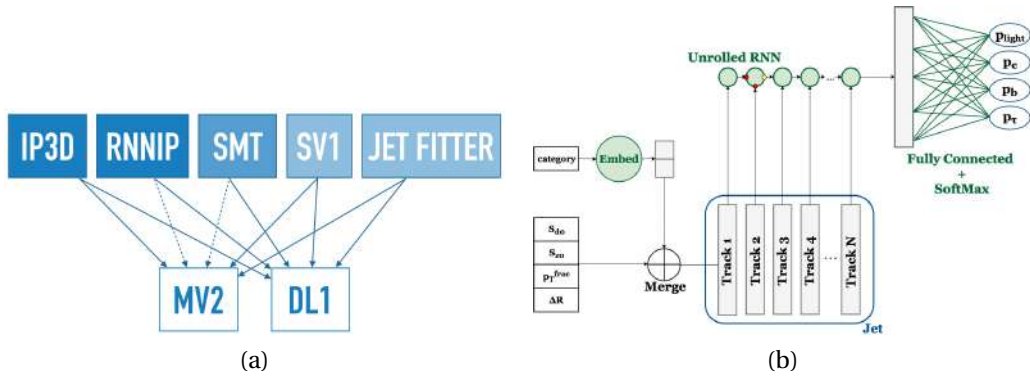


Figure 3.18: 3.18a The set of b -tagging algorithms currently in use in the ATLAS experiment. 3.18b Diagram of the RNNIP tagger from input (left) to output (right) [113].

tion of the secondary displaced vertex of the B -hadron decay, which is visualized in Figure 3.17, can be used to identify b -jets. Another advantage characteristic of b -jets is their tracks' impact parameters. While tracks in light jets have impact parameters close to zero, those from B -hadron decays and consistent with the secondary vertex hypothesis are more likely to deviate from zero. As a result, it is also possible to use the large impact parameters of tracks inside b -jets in order to improve not only the identification but also the separation of b -jets from light jets. Additionally, since heavy-flavour hadrons decay semi-leptonically with a non-negligible branching ratio of about 21%, the presence of soft muons within jets can also be used as yet another discriminating feature for the flavour tagging. The collection of b -tagging algorithms presently in use at the ATLAS experiment comprises five low-level taggers (IP3D, RNNIP, SMT, SV1 and JetFitter) as well as two high-level taggers (MV2 and DL1) which take as inputs combinations of the low-level tagger outputs, as shown in Figure 3.18a.

The low-level taggers are designed to exploit the various discriminative aspects of b -jets mentioned above. Specifically, SV1 [114] and JetFitter [115] are the two secondary vertex-based algorithms. The former is an inclusive secondary vertex algorithm which looks for displaced tracks and groups them in a secondary vertex, while the latter is a multi-vertex finding algorithm which reconstructs the topology and fits the entire decay chain along the hadron line of flight. The other low-level b -tagging approaches which take advantage of the impact parameter properties are IP3D [116] and RNNIP [117]. The IP3D tagger combines the transverse and longitudinal impact parameter significances² of tracks associated to a jet into a log likelihood ratio (LLR) discriminant in which the inputs are compared to pre-determined distributions retrieved from MC simulations for the b - and light flavour hypotheses. RNNIP is a b -tagging classifier based on the Recurrent Neural Networks (RNNs). It is introduced

²The impact parameter significance is defined as the impact parameter divided by its measured uncertainty.

to augment the traditional IP3D tagger. In this algorithm, a jet is treated as a sequence of tracks. Each track is described by a vector including the impact parameter significances and some other quantities representing the track features. RNNIP trains the sequence through the RNNs to predict the probability of the jet associated to each flavour. This output information is then combined into a LLR discriminant as in the IP3D approach. Figure 3.18b illustrates the workflow of the RNNIP tagger. The last low-level tagger, SMT [118], is a muon-based algorithm which relies on information from the reconstructed muons from semi-leptonic decays of heavy-flavour hadrons. This tagger uses a group of 6 hand-engineered variables and combines them in a Boosted Decision Tree (BDT) to obtain a discriminant. SMT helps to provide orthogonal information to the vertex- and the impact parameter-based taggers.

The high-level tagging algorithms integrate the discriminating capabilities of the low-level algorithms into one single discriminant. This helps to simplify the process to include the flavour tagging recommendations into analyses by reducing the number of calibrations needed. The MV2 tagging algorithm [118] is a BDT-based method. It takes as input the outputs of the IP3D, SV1 and JetFitter as well as kinematic properties to train a BDT using the ROOT Toolkit for Multivariate Data Analysis (TMVA) [119]. The output of MV2 is a single score that ranges from -1 to 1, with 1 being more *b*-jet-like. To cope with different analyses, various working points are also defined by choosing different cut values applied on the BDT score. Each restriction value corresponds to a *b*-tagging efficiency. One typical working point is with a 77% *b*-tagging efficiency and with the equivalent mis-tag rate of 16% (0.77%) for *c*-jets (light jets) [120]. Beside the basic MV2 tagger, there are two other MV2 variations developed during Run 2, known as MV2Mu and MV2MuRnn. Each one uses a different set of low-level algorithm variables. In addition to the list of inputs used for MV2, the MV2Mu tagger also includes the SMT output, while the MV2MuRnn tagger includes the outputs of both SMT and RNNIP.

The second high-level *b*-tagging algorithm, DL1 [118], is based on a Deep Neural Network (NN) trained using Keras [121] with the Theano [122] backend and utilizes the Adam optimizer [123] to minimise the cross-entropy loss. This algorithm takes the same inputs as those used for the MV2 algorithm with the addition of the JetFitter *c*-tagging. DL1 has three output nodes which calculate the probabilities for a jet to be a *b*-, *c*- or light-flavour jet, as highly non-linear functions of the input features. A final discriminant for *b*-tagging is then obtained by combining the outputs into one tunable function of the fraction of *c*-jets in the background. This approach allows to choose a posteriori for the *c*-jet fraction in the background in order to optimize the algorithm performance. Similarly to the MV2 tagging algorithm, DL1 also defines several working points based on the cuts imposed to the algorithm discriminant. Other variations of the DL1 family, DL1Mu and DL1r, are also developed with an increasing number of inputs used for training in order to improve the tagging performance as in the MV2 algorithm. DL1Mu takes into account the SMT variables, while the input list used for DL1r is the same as DL1Mu with the addition of the RNNIP variables.

Figure 3.19 represents the rejections of the light-flavour and *c*-jets as functions of

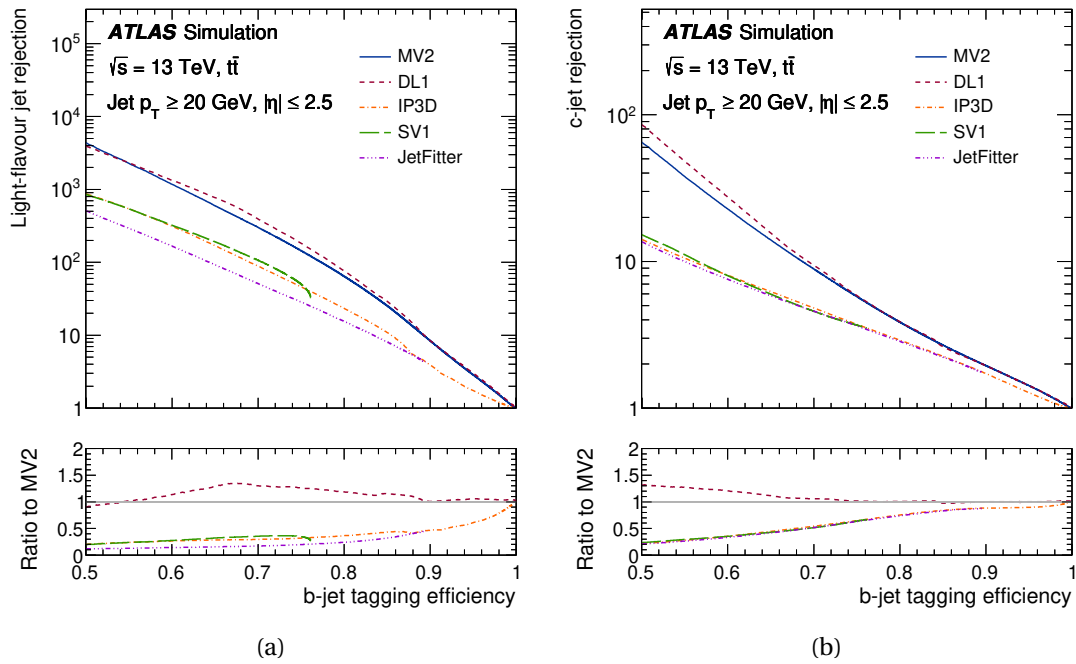


Figure 3.19: 3.19a The light-flavour jet and 3.19b the c-jet rejections versus the b -jet tagging efficiency for the IP3D, SV1, JetFitter, MV2 and DL1 b -tagging algorithms evaluated on the baseline $t\bar{t}$ events [124].

the b -tagging efficiency for the different low- and high-level b -tagging algorithms. It is obvious to see that the combination of the low-level tagging variables in the high-level taggers does improve the tagging performance. At the specific working point of 70% b -tagging efficiency, the light-flavour and c -jet rejections of the MV2 and DL1 algorithms are respectively improved by factors of around 10 and 2.5 with respect to the low-level algorithms. DL1 and MV2 are also found to have similar performance. However, since DL1 is trained with multiple output nodes, it has more flexibility when constructing the final discriminant. Additionally, all the flavours are treated equally during training and thus DL1 can be easily used for both b -jet and c -jet tagging. DL1 also takes less memory footprint than the BDT-based methods due to the use of a multi-class network architecture.

Calibration

The energy measurement given by the calorimeters is accurate for electromagnetic particles (electrons, positrons and photons), but is underestimated for hadronic particles due to their interaction processes which produce undetected energy in the calorimeters. Other detector effects such as pile-up, energy leaks or non-uniform response can also result in energy loss of the final jet measurement. ATLAS employs a

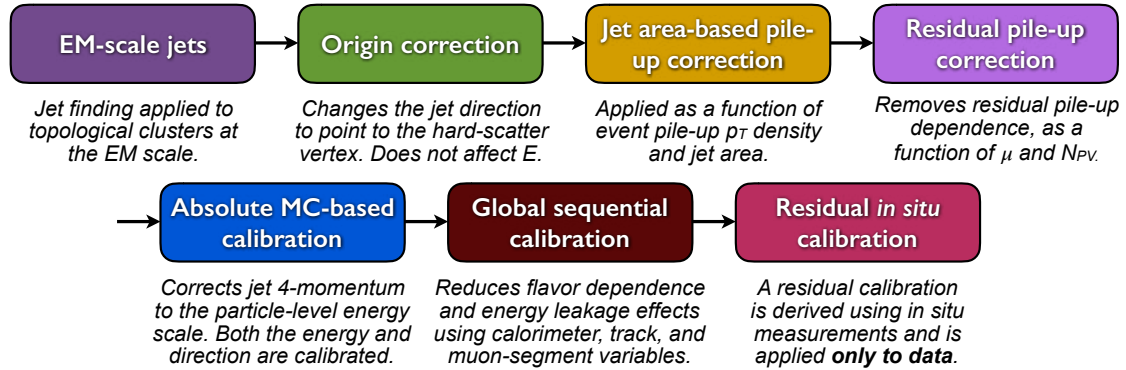


Figure 3.20: Calibration stages for EM-scale jets [125].

multi-step calibration [125] in order to restore the jet energy to the scale of the true particle energy. This method is largely simulation-based, using Monte Carlo (MC) samples.

Figure 3.20 represents the main steps of the Jet Energy Scale (JES) calibration. The first step of the procedure is referred to as *origin correction* in which the jet four-momentum is re-calculated such that it points toward the hard-scatter primary vertex instead of the detector center, while the jet energy is remained unchange. This step helps to improve the pseudorapidity resolution. It is then followed by a *jet area-based* and a *residual pile-up correction* to eliminate the excess energy caused by in-time and out-of-time pile-up. The former subtracts the median pile-up momentum density weighted to the jet area from the p_T of each jet in each event, whereas the latter corrects residual contributions as a function of the number of the primary vertices in the event and the number of interactions per bunch-crossing μ . After removing the effects of pile-up, an *absolute MC-based calibration*, where the truth and the reconstructed energies of simulated jets are compared to each other, is performed in order to bring the reconstructed jet four-momentum to the particle-level energy scale. At this step, the detector geometrical effects such as dead material, lateral and longitudinal leakage of the showers, low energy deposits and non compensation are also taken into account through the parametrization of the calibration function in the jet energy and η . In the following step, calorimeter, track and muon-segment variables are corrected with a *global sequential calibration* so as to reduce the flavour dependence and energy leakage effects on the jet energy. Finally, a *residual in situ calibration* is performed solely to data, using well-measured reference objects like as photons, the Z boson, and calibrated jets, to account for differences in the jet response between data and MC simulation. These discrepancies occur as a result of the detector response and detector material being described imperfectly in MC simulations, as well as in the simulations of hard scatter, underlying event, pile-up, jet formation, and electromagnetic and hadronic interactions with the detector.

Particle flow

The jet reconstruction mentioned earlier is based entirely on calorimetric data. Another method for the jet reconstruction, known as Particle Flow (pFlow), is to combine the energy deposits in the calorimeter with the INDET tracking information. This method shows many advantages: the momentum resolution of the INDET tracker is much better than the HCAL energy resolution, especially for particles having low momentum. Besides, the INDET also has a higher angular resolution than the calorimeters and is capable of pile-up suppression. On the other hand, the calorimeters are superior at reconstructing high- p_T and neutral particles. Their acceptance is also extended in the forward regions. These points result in an appealing complementarity of the two measurements.

The pFlow algorithm in ATLAS [91] works by matching high-quality tracks to clusters in the calorimeter. The energy of clusters that match INDET tracks is eliminated from the computation after they have been identified. Following this subtraction, the remaining clusters in the calorimeter are combined with the selected tracks to reconstruct jets. The anti- k_T algorithm and a calibration process identical to the one described before are also utilized in this procedure. The energy and angular resolution for a true p_T of 30 GeV is enhanced from 17.5% for calorimeter jets to 14% for pFlow jets. There is no improvement in employing pFlow to reconstruct jets associated to highly energetic tracks with $p_T > 40$ GeV while their associated calorimeter energy is difficult to be precisely removed, these tracks are therefore excluded from the pFlow algorithm.

3.3.6 Missing Transverse Momentum

Since the proton beams travel along the beam axis (i.e z -axis), the transverse momentum of the the incident partons can be negligible and thus the total transverse momentum in the initial state is approximately zero. Because of the momentum conservation, the final state must also have a total transverse momentum close to zero. If the total transverse momentum of the final-state reconstructed objects significantly deviates from zero, this could suggest the existence of neutral, weakly-interacting particles which can be either neutrinos or beyond-standard-model (BSM) particles. The missing particles are represented by the missing transverse momentum, $\mathbf{E}_T^{\text{miss}}$ [126], defined as the negative of the vectorial transverse momentum sum of all the reconstructed objects in the detector by the following formula:

$$\mathbf{E}_T^{\text{miss}} = - \sum_{i \in \{\text{hard objects}\}} \mathbf{p}_{T,i} - \sum_{j \in \{\text{soft objects}\}} \mathbf{p}_{T,j}. \quad (3.15)$$

It can be seen from Equation 3.15 that there are two types of the reconstructed objects contributing to the $\mathbf{E}_T^{\text{miss}}$ reconstruction. The first one is the hard objects which are previously mentioned in Sections 3.3.1- 3.3.5. The other one is the soft objects which are reconstructed tracks originating from the primary vertex but not

associated to any hard-scatter objects.

To prevent repeated inclusions of the same energy deposit, the E_T^{miss} computation includes only objects from orthogonal detector signals in a certain order. Electrons are given the highest priority, then followed by photons and other leptons. Jets are suppressed if they overlap with particles with greater priority. The tracks corresponding to the soft term are given the lowest priority. The magnitude of the E_T^{miss} is referred to as the missing transverse energy, E_T^{miss} .

3.4 Monte Carlo event simulation

The simulation of pp collision events is an essential input for many physics analyses in ATLAS. Simulated events can be used with a variety of purposes, including estimating backgrounds and selection efficiencies, examining systematic effects caused by the detector or pile-up mis-modeling, and validating the data-driven background estimation methods. The simulation procedure is carried out through a chain of consecutive steps reflecting the high level of precision targeted by the experiment. It is primarily based on the Monte Carlo (MC) method in which repeated random sampling of variables described by complex probability density functions is used to model various physics processes which are considered in the analyses.

In this section, one reviews the ATLAS Monte Carlo production setup including the different production steps involved in full and fast detector simulation. This multi-step process, as shown in Figure 3.21, includes the event generation, the detector simulation, the digitization and the reconstruction.

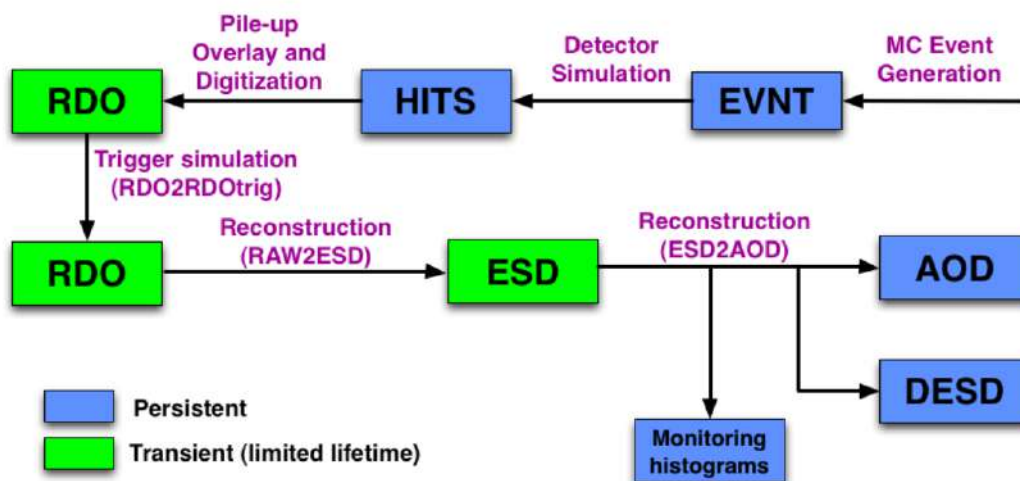


Figure 3.21: ATLAS Monte Carlo simulation flow [127].

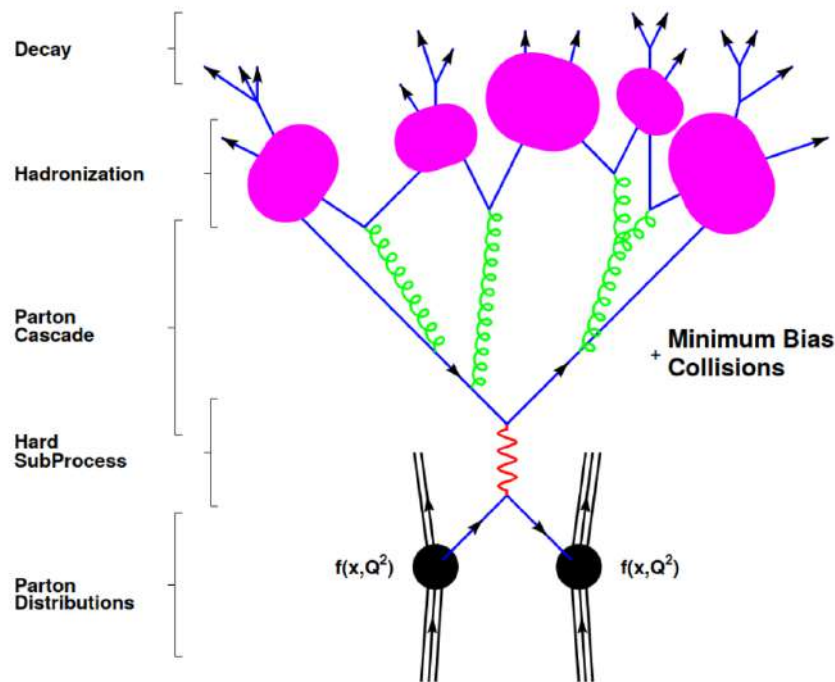


Figure 3.22: Schematic overview of a pp collision event generation emphasizing the different steps involved [129].

3.4.1 Event generation

Event generation is the initial step in the simulation chain. The modeling of pp collision events necessitates a comprehensive description of physics processes occurring at various energy scales that can be handled independently according to the factorisation theorem [128]. Therefore, a physics event can be simulated in a series of sequential stages (Figure 3.22), which include the extraction of partons from incoming protons, hard scattering, the parton shower, and hadronisation followed by hadrons decay.

The momenta of hard-scattering partons inside colliding protons are determined based on the basis of Parton Distribution Functions (PDFs). These affect the likelihood of finding a parton of a certain flavor carrying a specific fraction of the proton momentum. Due to the proton’s non-perturbative nature, its partonic content cannot be properly stated using the SM. Thus, the PDFs are constructed using fits to experimental data mostly from deep-inelastic scattering experiments and hadron colliders.

The hard-scatter phase of the event generation is often referred to as the matrix element (ME) computation. At this stage, the kinematics and flavors of the retrieved partons are utilized to calculate the cross-section of the hard-scatter process in pertur-

bative QCD. This is accomplished by assessing the Feynman diagrams that correspond to the desired process, with varying orders of precision depending on the complexity of the final state. This stage of the event simulation is handled by parton-level generators (or ME generators). Several of these generators permit the addition of one or more additional partons to the primary process. The ME generators MADGRAPH5_AMC@NLO [130], POWHEG-BOX [131, 132, 133] and SHERPA [134] are widely used in the ATLAS physics analyses.

The parton shower (PS) corrects the hard-scatter cross-section by estimating higher order contributions to simulate a full final state. It is modeled using MC generators that mimic the sequential emission of gluons, quarks, and photons from the initial and final state partons. These generators scale the event down from the high energy scale associated with the hard scattering to the PS cut-off scale, where the perturbation theory breaks down and hadronisation models take control. The overlap that occurs when generators with extra partons are linked to parton showers is eliminated using specialized methods called ME-PS matching schemes [135]. When the PS approaches non-perturbative energy scales, the fragmentation and hadronisation occur. Phenomenological models are used to simulate these processes. At this point, partons begin to bind together, resulting in the formation of colorless baryons and mesons. Excited state hadrons are further decayed into more stable particles. The processes of parton showering and hadronisation are carried out by interfacing all of the ME generators mentioned above (excluding SHERPA) with either PYTHIA [136, 137] or HERWIG [138, 139]. SHERPA, on the other hand, has its own showering and hadronisation models and does not need to interface.

Soft processes such as pile-up and underlying event interactions, which mainly involves spectator partons from colliding protons, are also modeled using phenomenological models with parameters adjusted to match experimental data.

The output of the event generation sequence, also called the MC history, is a list of four-vectors of all the particles generated in the event after the hadronisation and decay of the majority of the intermediate unstable particles. The particles contained in the MC history record are often referred to as true or truth particles.

3.4.2 Detector simulation

At the second part of the event simulation procedure, a dedicated simulation of the ATLAS detector built based on the GEANT 4 toolkit [140], is utilized to account for the energy deposited in the detector following the interactions of its material with the particles produced in the event generation step.

The detector simulation phase consumes most of the computational power used for the full event simulation. This is primarily due to the development of electromagnetic particles showers in the ATLAS calorimeter system which requires the longest time to simulate. For instance, for the full detector simulation (Fullsim) using a highly detailed detector description, a single $t\bar{t}$ event requires around 15 mn of CPU time [141]. As such, relying solely on standard Fullsim option would make it impossible to obtain

the required number of simulated events for many physics studies. This is why a faster and less refined alternative simulation, referred to as ATLFAST-II (AFII) [141] was put in place to reduce the amount of CPU time needed to process an event. This is mainly achieved by using pre-simulated electromagnetic showers of low energy particles instead of developing them from scratch. The Fullsim samples generally provide higher precision and are used as the main samples for physics analyses, whereas the AFII samples are used for optimization studies as well as to evaluate theoretical systematic uncertainties.

3.4.3 Digitisation and reconstruction

The digitisation turns the energy deposits simulated in the previous step into a detector response, similarly to the raw data from the real detector, producing RDO files. At this step the response of the readout electronics is simulated. In addition, the effect of multiple pp interactions per bunch crossing (pile-up) is simulated. After this step, the MC processing steps are the same as for real data.

The simulated MC events are reconstructed in the same way as data recorded by the ATLAS detector. In addition, the trigger system is simulated. The main reconstruction process produces the Event Summary Data (ESD), which contains low level quantities as tracks and clusters and high level quantities as jet, electron, photon, muon and tau candidates. After that, the Analysis Object Data (AOD) is produced, which contains mainly high level information.

3.4.4 Production campaign

MC production is divided into campaigns, where the center-of-mass energy, geometry and conditions used in the production correspond to a running period of the LHC. Major campaigns correspond to the calendar year. Minor campaign versions usually reflect improvements in reconstruction software, trigger menu or pile-up simulation. In contrast to data taking and reprocessing campaigns, MC campaigns are run as long as MC events are needed for data analysis. The search presented in this thesis makes use of the three MC production campaigns: MC16a, MC16d and MC16e, which correspond to the full Run 2 data-taking period (2015-2018) of the LHC.

4 The ATLAS pixel detector

The pixel detector, as already introduced in Section 3.2.2, is the innermost sub-system of the ATLAS detector, located immediately outside the beam pipe. Originally designed as a three-layers detector, the pixel detector of ATLAS has been upgraded with the addition of a fourth layer, the Insertable B-Layer (IBL), that is positioned closest to the interaction point. The first part of this chapter, Section 4.1, describes the general geometry and layout of the present pixel detector. The sensor technologies and the readout electronics currently used in the detector are discussed in Sections 4.2 and 4.3, respectively.

4.1 General layout

The pixel detector [142] consists of four barrel layers and two end-caps with three disk layers each, covering the pseudorapidity range of up to $|\eta| < 2.5$ and the full azimuthal angle ϕ . Pixel modules are the fundamental elements of the pixel detector. Each module is composed of the silicon sensor, the front-end electronic readout chips and the flex-hybrids with control circuits. The pixel modules are grouped with the mechanics and the cooling system to form sub-elements called staves in the barrel or sectors in the end-caps. These sub-elements are then mounted together on a supporting structure to form the barrel layers and the disks.

The first barrel layer, IBL [143], which was added during Long Shutdown 1, is positioned at 33.5 mm from the beam axis. In order to accommodate this new layer, a new beam pipe was also installed with the inner radius reduced to 23.5 mm. In the IBL, each stave has 12 modules using double-chip planar sensors of 200 μm thick and 4 modules using single-chip 3D sensors of 230 μm thick (see Section 4.2). As shown in Figure 4.1, the planar modules are positioned in the stave center, while the 3D ones are at two ends of the stave. The IBL module contains two FE-I4B front-end (FE) chips [144] with 336×80 pixel cells each. The pixel cell has a nominal size of $50 \times 250 \mu\text{m}^2$. In order to prevent any gaps in detecting particles, the IBL staves are tilted in the ϕ direction by 14° , as indicated in Figure 4.2, to achieve overlaps between their active areas. This design also helps in compensate for the Lorentz angle drift on the charged particles within the detector.

The three outer barrel layers (B-Layer, Layer 1, Layer 2) and the end-cap disks consist of 1744 modules. Each module is built with a planar sensor of 250 μm thick interconnected to 16 FE-I3 front-end chips [145] each containing 160×18 pixel cells. The pixel size is $50 \times 400 \mu\text{m}^2$. Similarly to the IBL, the staves of these three outer

4 The ATLAS pixel detector – 4.1 General layout

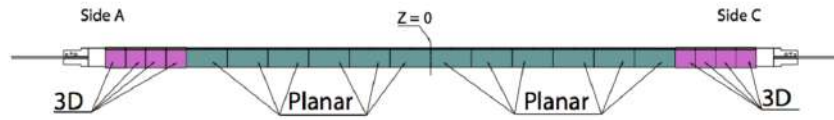


Figure 4.1: A schematic view of the IBL stave [143].

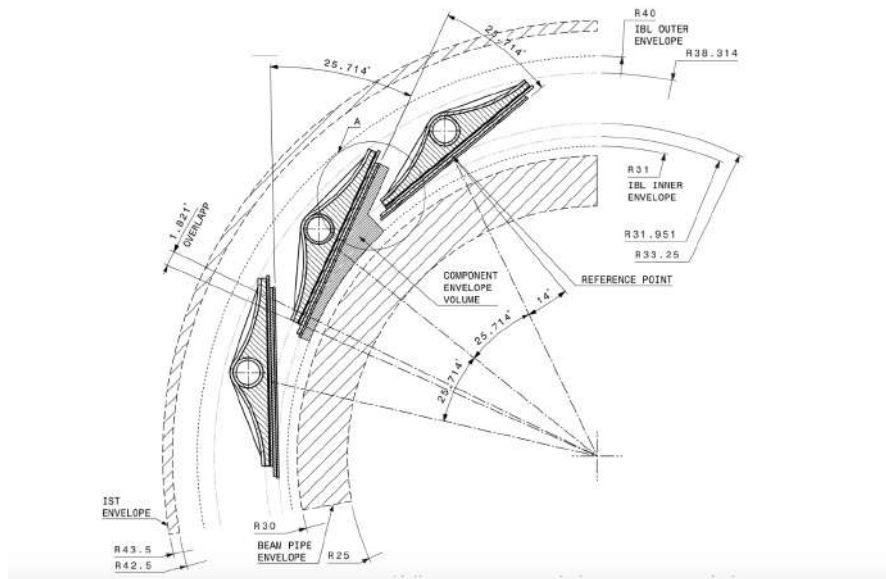


Figure 4.2: Section of the IBL barrel, the beam pipe and the services in r - ϕ [143].

barrel layers are also tilted in ϕ direction but with an angle of 10° . In addition, the modules are mounted on each stave such that they also overlap in z .

A carbon-fiber support is used to mount the barrel and end-cap disk. Services including electronics and cooling are connected inside service panels from patch panels located at the supporting spaceframe ends to the end of the Pixel Support Tube (PST). Connections of these services are then made at Patch Panel 1 (PP1) which is located at the end of the PST, whereas external service connections are established at extra patch panels (PP2, PP4) placed outside the INDET.

It should also be noted that the IBL is developed differently from other pixel layers using a new technology in which the staves have lower density and the modules have lower mass. Overmore, CO_2 evaporative cooling is used instead of C_3F_8 , providing a better cooling efficiency in terms of mass and pipe size. Another essential factor that one need to address throughout the detector development is the material budget, or the quantity of material that makes up the pixel detector. In practice, this has

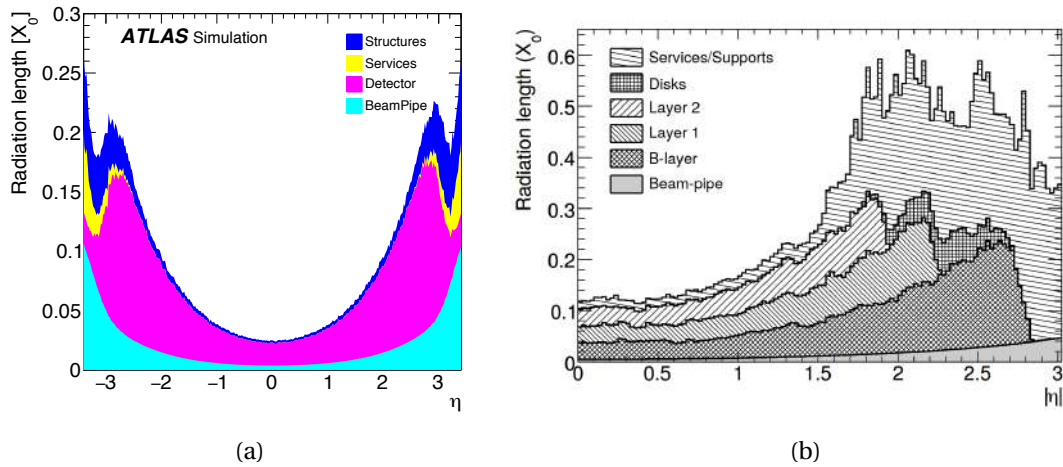


Figure 4.3: Material budget distribution along η in units of radiation length X_0 of (4.3a) the IBL [143] and (4.3b) the pixel detector [142].

to be optimized so as to decrease the multiple particle scattering and improve the performance in tracking as well. The material budget distributions of the IBL, the other pixel layers, the beam pipe and the services, in units of the radiation length X_0 , along the pseudorapidity η are shown in Figure 4.3.

Tables 4.1 and 4.2 summarize the main parameters of the barrel pixel layers. The corresponding information of the end-cap disks is given in Tables 4.3 and 4.4.

Layer name	Mean radius [mm]	Number of staves	Number of modules per stave
IBL	33.5	14	16 (12 planar + 4 3D)
B-Layer	50.5	22	13
Layer 1	88.5	38	13
Layer 2	122.5	52	13

Table 4.1: The mean radius, the number of staves and the number of modules in each stave for the barrel pixel layers.

4.2 Sensors

Sensors are the sensitive part of the pixel detector that is used to detect charged particles and acts as a solid-state ionisation chamber. The sensor must adhere to stringent geometrical restrictions in terms of thickness and granularity, while also

Layer name	Active area [m ²]	Pixel size [μ m]	Sensor thickness [μ m]	Pixel array per FE (rows \times columns)
IBL	0.15	50 \times 250	200/230 (planar/3D)	336 \times 80
B-Layer	0.28	50 \times 400	250	160 \times 18
Layer 1	0.49	50 \times 400	250	160 \times 18
Layer 2	0.67	50 \times 400	250	160 \times 18

Table 4.2: The active area, the pixel size, the sensor thickness and the pixel array per FE for the barrel pixel layers.

Layer name	Mean z [mm]	Number of sectors	Number of modules per sector
Disk 1	495	8	6
Disk 2	580	8	6
Disk 3	650	8	6

Table 4.3: The mean z , the number of sectors and the number of modules in each sector for the end-cap disks.

Layer name	Active area [m ²]	Pixel size [μ m]	Sensor thickness [μ m]	Pixel array per FE (rows \times columns)
Disk 1	0.0475	50 \times 400	250	160 \times 18
Disk 2	0.0475	50 \times 400	250	160 \times 18
Disk 3	0.0475	50 \times 400	250	160 \times 18

Table 4.4: The active area, the pixel size, the sensor thickness and the pixel array per FE for the end-cap disks.

exhibiting a high charge collection efficiency and withstanding significant ionising and non-ionising particle radiation damage. On the one hand, this is reflected in bulk material choices; on the other hand, it has an effect on the design of the pixel structure itself. The present pixel module displaying a sensor is illustrated in Figure 4.4. Two different technologies, planar and 3D, are applied for the design of the sensor structure in the ATLAS pixel detector.

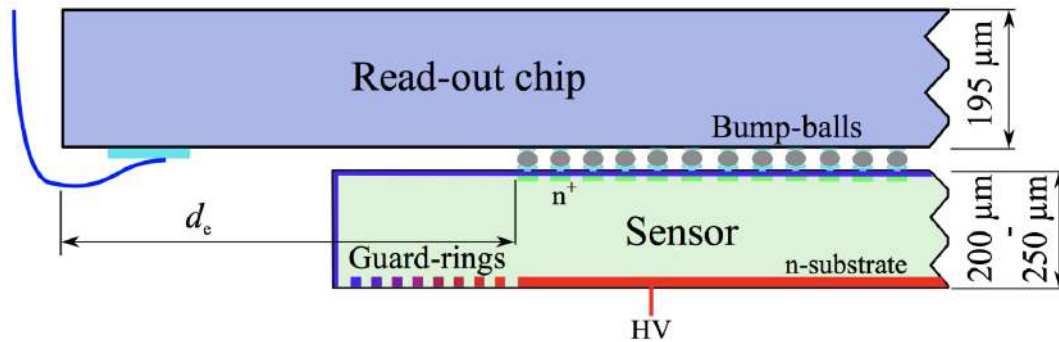


Figure 4.4: The present pixel module displaying a sensor [146].

4.2.1 Planar sensor

The pixel sensor is an array of bipolar diodes placed on a high resistivity n-type bulk. The front side of the sensor is highly doped with n^+ implants, while the back side has a uniform p^+ implant, forming the n^+ -in-n sensor. Electrons and holes from the n- and p^+ -type side are then recombined as a result of the concentration gradient, leading to a small, asymmetric depletion region starting from the p^+ -n junction at the back (p) side. A reverse bias is applied to extend the depletion region over the whole sensor bulk volume and make the sensor fully depleted. This voltage is referred to as the Depletion Voltage and is proportional to the doping concentration in the sensor. It also depends on the thickness and resistivity of the sensor bulk. After reaching the full depletion, charged carriers generated by ionising particles traversing through the active area can freely move to the electrodes where they are collected and detected by the electronics. The n^+ -in-n design of the sensor can ensure isolation of each single pixel. When the sensor is unirradiated, the pixels are able to be isolated from each other by full depletion of the bulk. When radiation damage inverts the bulk type, the junction moves to the front (n) side and therefore maintains the pixel isolation, allowing operation even if the bulk is not fully depleted. This advantage of the depletion region for the n^+ -in-n design can be seen from Figure 4.5. The sensor design also helps to reduce leakage current and make the sensor both testable and radiation resistant.

The thickness of the n-bulk in the planar sensors is $200\ \mu\text{m}$ for the IBL and $250\ \mu\text{m}$ for the other pixel layers. The bulk is made of oxygenated Float Zone (FZ) silicon for better resistance against charged particle radiation [147]. For the IBL, the n-side is designed to be interconnected to two FE-I4B readout electronic chips with an active sensor area of $16.8 \times 40.9\ \text{mm}^2$, while for the other layers it is made to be interconnected to 16 FE-I3 chips, making up an active area of $16.4 \times 60.4\ \text{mm}^2$. Another difference between the IBL and other pixel layers is the number of implemented Guard Rings (GRs) on the p-side of the planar sensors, where the GRs control the potential drop

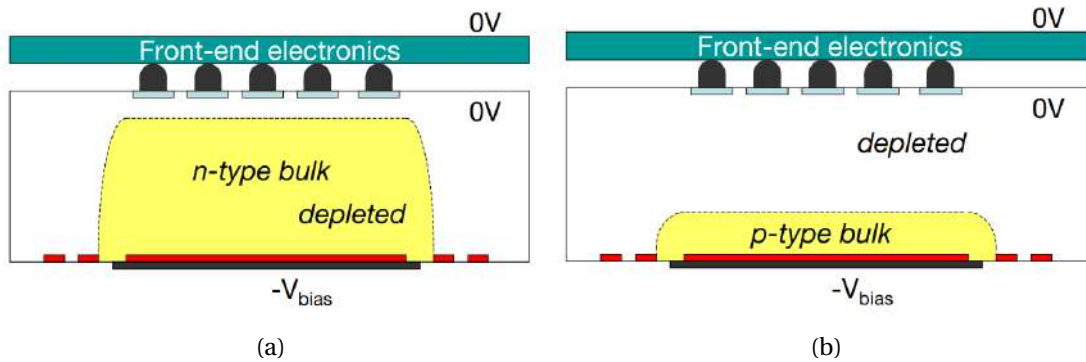


Figure 4.5: Comparison of depletion zones in n^+ -in- n pixel sensors before (4.5a) and after (4.5b) type inversion [142].

from the high voltage applied in the region within the innermost GR on the back side to the ground potential at the module edges and the front side. Specifically, the p-side of the pixel sensor is equipped with 16 GRs, while there are only 13 GRs hosted on the back side of the IBL planar sensor. In addition, these rings are also shifted to the place underneath the outermost n^+ implants situated on the front side and therefore the inactive edge has been reduced from $1100 \mu\text{m}$ for the pixel sensor down to $200 \mu\text{m}$ for the IBL planar sensor, as shown in Figure 4.6. The nominal size of a pixel cell in the IBL planar sensor is $50 \times 250 \mu\text{m}^2$, matched to that of the FE-I4B chip. The two central columns of these double-chip sensors are extended to $450 \mu\text{m}$ rather than $250 \mu\text{m}$ to cover the gap between the two adjacent FE-I4B chips. In the other pixel layers, the nominal cells have a size of $50 \times 400 \mu\text{m}^2$, while long pixel cells have a size of $50 \times 600 \mu\text{m}^2$ instead. Each readout channel in a tile is linked through a punch-through connection to a common structure for the bias voltage, which supplies DC-coupled bias to each channel. This enables the bias voltage to be applied to the sensors without requiring separate connections, while maintaining pixel isolation.

4.2.2 3D sensor

3D pixel sensors [143] have been developed to withstand the high dose of radiation that the pixel has received, while still maintaining low power consumption after irradiation. In contrast to the planar sensor technology where the lowest possible active thickness of the sensor restricts the minimum distance between the two electrodes that can be achieved, the active sensor thickness in the 3D sensor technology can be decoupled from the electrode spacing and thus reducing the drifting distance of the generated electron/hole pairs in the bulk. In the 3D sensors, the electrodes are designed as columns penetrating perpendicularly into the p-type bulk rather than being implanted on the wafer surface. Here, the p-type substrate is selected in order to avoid type inversion of the bulk after high irradiation fluences. The electrodes are produced in

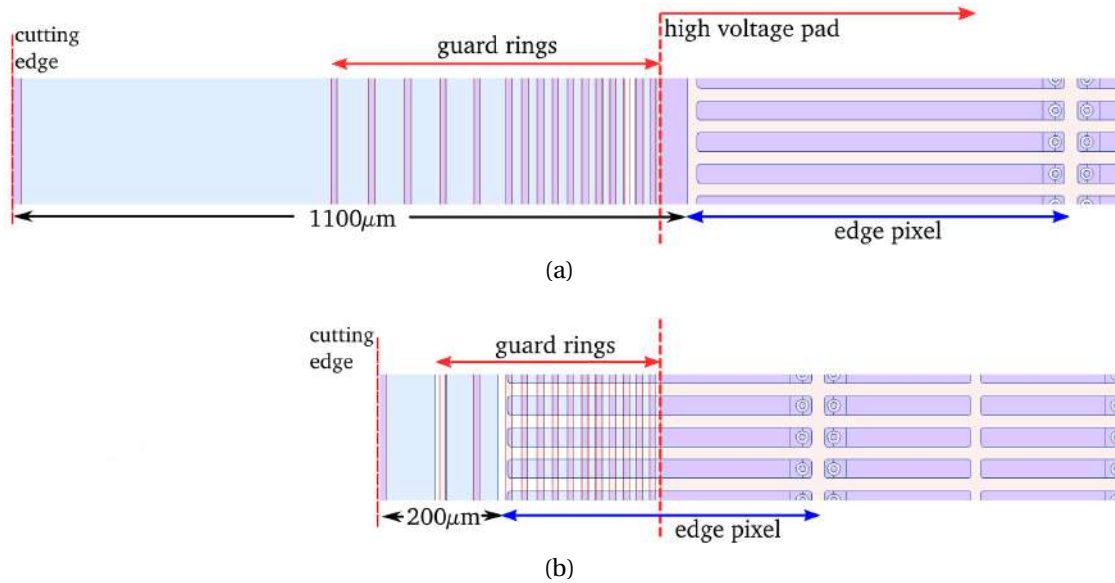


Figure 4.6: Comparison of the edge designs of (4.6a) the ATLAS Pixel detector sensor and (4.6b) the planar IBL pixel sensor [143].

two steps. At first, Deep Reactive Ion Etching (DRIE) [148] is used to etch columns of $\sim 12 \mu\text{m}$ diameter into the bulk substrate. After that, the n^+ and p^+ dose regions are implanted on these columns in such a way that there are two n^+ columns surrounded by in total six p^+ columns in a single pixel cell. With this way, the pixel cell size is defined as the distance between the n^+ columns and the charge collection distance is defined as the spacing between the n^+ and p^+ columns. The depletion electric field is also generated between the oppositely doped neighbouring columns, parallel to the wafer surface. Figure 4.7 represents a schematic view for the design of the 3D sensor technology as well as the planar technology.

In fact, the distance between the electrodes in the 3D sensor can be typically about five times smaller than the sensor thickness, resulting in a significantly decreased depletion voltage compared to the planar sensor. The low depletion voltage implies the lower power dissipation per unit leakage current and the cooling requirements are therefore less demanding. This reduced distance also leads to fast signals, which are robust against charge trapping caused by heavy radiation damage [150]. The signal size is determined by the sensor thickness, independently on the drifting path of charged carriers. This means that the design of the 3D sensor technology does not affect the charge signal. Before irradiation, as long as the 3D sensors have the same thickness as the planar ones, the amount of collected charge remains unchanged for both technologies. The main drawback of the 3D sensors is their more complex fabrication process. For example, it causes the low production yield of 60% calculated on 50 wafers [151] produced for the IBL.

In the IBL, 25% of the modules are produced with the 3D sensor technology, populat-

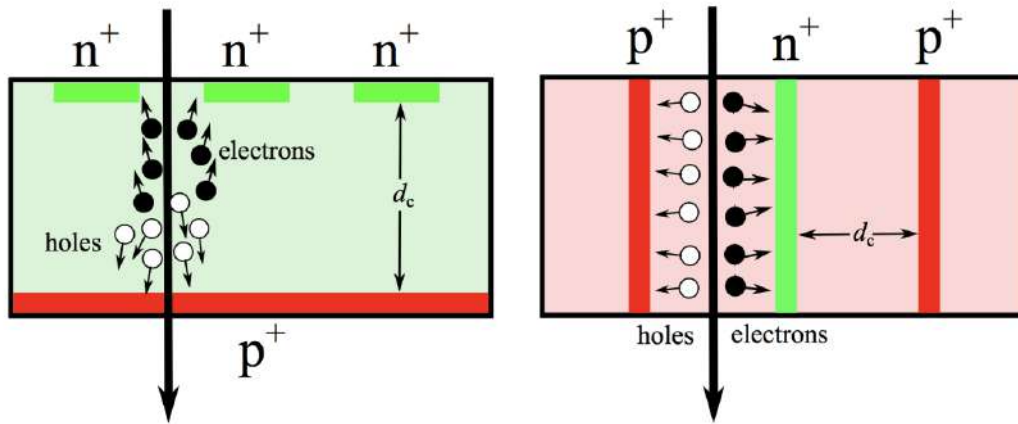


Figure 4.7: A schematic view of (left) the planar n^+ -in- n sensor and (right) the 3D n^+ -in- p sensor. The n^+ electrodes are illustrated in green, while the p^+ electrodes are coloured in red. d_c denotes the charge collection distance. [149].

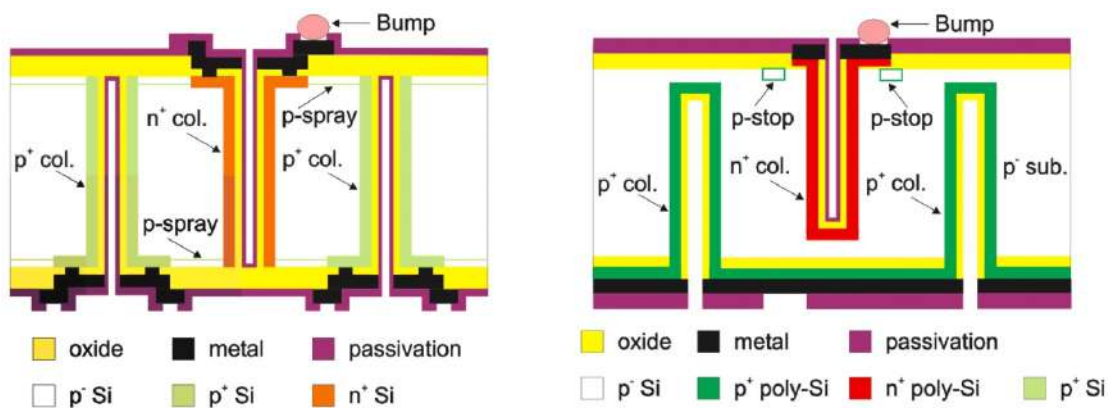


Figure 4.8: Design of the columns of (left) FBK and (right) CNM 3D sensors [143].

ing the outer parts of the staves. The IBL 3D sensors have a thickness of $230 \mu\text{m}$ and the pixel cell size of $50 \times 250 \mu\text{m}^2$, interconnected to the FE-I4B chips. They are fabricated by two silicon processing facilities: CNM¹ [152] and FBK² [153], with a double-sided technology. Both sensor technologies are illustrated in Figure 4.8. The main difference between the two facilities is the etching process of the doped columns. FBK performs etching of full-through columns while CNM performs etching of partially-through $210 \mu\text{m}$ -long columns. The partially-through column sensor configuration enables a collection of the generated electron/hole pairs in the remaining column free and

¹Centre Nacional de Microelectronic

²Fondazione Bruno Kessler

consequently active bulk of $20\ \mu\text{m}$. As a disadvantage, partially-through columns result in a lower electric field after irradiation. The inter-electrode spacing between n^+ and p^+ columns, or the charge collection distance of the IBL 3D sensors is about $67\ \mu\text{m}$.

4.3 Readout electronic chips

As already mentioned, each pixel module of the three outer pixel layers consists of 16 FE-I3 front-end chips, organised in two rows of eight chips each, for the pixel readout. The FE-I3 chip became available in late 2003, it is designed using a commercial $0.25\ \mu\text{m}$ Complementary Metal Oxide Semiconductor (CMOS) process. The chip contains 2880 readout cells of $50 \times 400\ \mu\text{m}^2$ arranged in a 160×18 pixel matrix, achieving an active area of $7.2 \times 10.8\ \text{mm}^2$. In every readout cell, there is an analogue block with a preamplifier implemented and connected to each sensor pixel via a bump ball. The sensor charge signal is amplified by this component and then processed using a programmable discriminator threshold with an achievable minimum threshold value of $2.5\ \text{ke}$ [154]. In addition, a digital circuitry is also integrated in order to transfer the hit pixel address, a hit leading edge (LE) timestamp, and a trailing edge (TE) timestamp to the buffers at the chip periphery. In these buffers a Time-over-Threshold (ToT) is calculated by subtracting the TE from the LE timestamp. These hit-buffers monitor the time of each stored hit by inspecting the LE timestamp. When a hit time becomes longer than the latency of the L1 trigger (approximately $3.2\ \mu\text{s}$) and no trigger signal is recorded, the hit information is deleted. Hits marked by trigger signals are selected for readout. Triggered hit data are then transmitted serially out of the chip in the same order as the trigger arrival. Data from the FE-I3 chips are transmitted through the Low Voltage Differential Signaling (LVDS) serial links to the Module Control Chip (MCC) and are then read out to the Read-out Drivers (RODs) of the off-detector. The modules and the RODs are connected using optical fiber links (opto-links). A single DC supply is used to provide power supply through lengthy cables and thus necessitating the use of low-voltage regulator boards. Figure 4.9 depicts the electronic architecture of B-Layer for an example.

The IBL modules, in contrast, contain two FE-I4B front-end chips. The FE-I4B chip was firstly fabricated in 2011 [155, 156] using the $0.13\ \mu\text{m}$ CMOS process and tailored to fully satisfy the IBL requirements. It is designed to withstand an irradiation fluence of $5 \times 10^{15}\ \text{n}_{\text{eq}}\ \text{cm}^{-2}$ by avoiding minimal size transistors and systematically using GRs for analog and sensitive digital circuitry [157]. The chip consists of 26880 hybrid pixel cells arranged in 80 columns of $250\ \mu\text{m}$ pitch by 336 rows of $50\ \mu\text{m}$ pitch, making up a larger active chip surface of $16.8 \times 20.2\ \text{mm}^2$ compared to the one of the FE-I3. The smaller size of the pixel cell in the beam direction provides a lower occupancy per channel at the same particle fluence. Similarly to the FE-I3, each FE-I4B pixel cell also contains an analog stage which is a free running clock-based amplification stage with adjustable shaping, followed by a discriminator with an independently adjustable

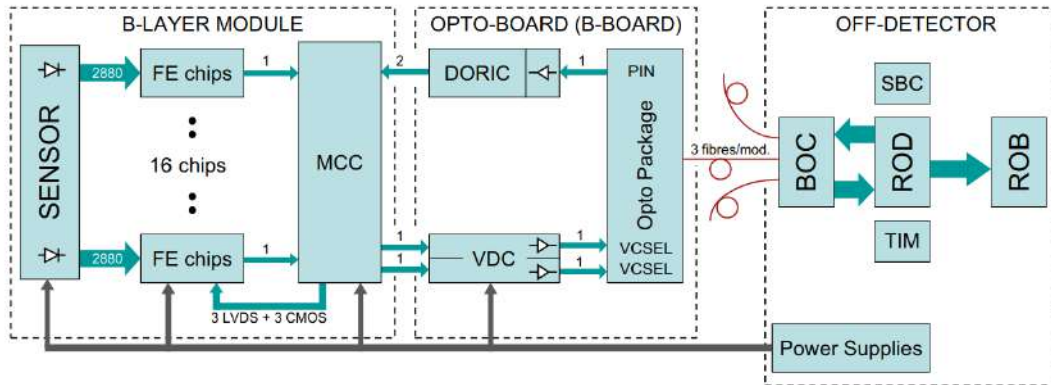


Figure 4.9: Block diagram for the system architecture of B-Layer [142].

threshold. The amplifier of the analog component is optimized for low noise and low power operation with fast rise time and thus allow to decrease the threshold down to 1 ke. On the other hand, the digital readout part of the FE-I4B is shared among four readout channels instead of a single one as in the FE-I3 case. It keeps track of the hit timestamp for each discriminator as well as the 4-bit ToT. The chip keeps hit information from all the firing discriminators for a latency interval programmable up to 255 LHC clock cycles of 25 ns and the hit will be retrieved if a trigger is supplied within this latency. The FE-I4B transmits output data with a rate of 160 Mb/s [158], which is four times higher than the transmission rate of the FE-I3. Differently from modules of the outer pixel layers, the IBL modules are not equipped with the MCC. Data from the FE-I4B chips are sent directly to the RODs.

5 Instrumental measurements on the Pixel Detector during Run 2

The study of pixel-level leakage current measurements and the estimation of pixel-hit loss rate in the pixel detector are described in Sections 5.1 and 5.2, respectively, in this chapter.

5.1 Pixel-level leakage current measurements

In an ideal p-n junction without an external bias, the diffusion of majority carriers and drift of minority carriers across the junction will cancel and thus there will be no current across the junction. Nevertheless, when a reverse bias voltage is applied on the junction, one can observe a current which is called *leakage current* or *reverse current*. This current is composed of three basic components. The first one, the minority carrier current, arises from the drift of minority carriers in the reverse electric field. It is usually small and does not greatly contribute to the overall leakage current of the junction. The second component is the surface current which can occur due to high electric fields at the junction edge or the surface contamination. It depends on various factors such as humidity, the fabrication process, irregularities and damage of the surface, making it difficult to be quantified. Similarly to the minority carrier current, contribution of the surface current in the total leakage current is normally small and can be neglected. The last component, the generation current, is the majority of the junction leakage current. It arises when electron-hole pairs are thermally generated in the depletion region and then drift in the electric field to produce a current. The generation current is enhanced by the generation centres which are deep impurity levels energetically located close to the middle of the band-gap and increasing the probability of the thermal excitation of an electron from the valence band to the conduction band.

The leakage current I_{leak} can be expressed as follows:

$$I_{\text{leak}} = \frac{en_iAW}{2\tau}, \quad (5.1)$$

where τ is the effective charge carrier lifetime which is inversely proportional to the density of generation centres, n_i is the intrinsic carrier density, A and W denote the area of the junction and the width of the depletion region, respectively. At constant temperature, according to Equation 5.1, the leakage current is proportional to the

depleted width and therefore depends on the voltage V in the same way,

$$I_{\text{leak}} \propto W \propto \sqrt{V}. \quad (5.2)$$

When the applied voltage reaches the depletion voltage, $V = V_{\text{dep}}$, the sensor is fully depleted and the depletion width cannot increase anymore, the leakage current then saturates and remains constant with increasing reverse bias voltage.

A further important feature of the leakage current is the strong temperature dependence. The expected leakage current for a given T can be obtained from a measurement at a reference temperature T_{ref} , as:

$$I_{\text{leak}}(T) = I_{\text{leak}}(T_{\text{ref}}) \left(\frac{T}{T_{\text{ref}}} \right)^2 \exp \left(-\frac{E_g}{2k_B} \left[\frac{1}{T} - \frac{1}{T_{\text{ref}}} \right] \right), \quad (5.3)$$

where $I_{\text{leak}}(T_{\text{ref}})$ is the current measurement at T_{ref} . According to this formula, the leakage current approximately doubles every 7 K and thus cooling is imperative to reduce the leakage current to an acceptable level.

The leakage current of a silicon sensor is also altered by radiation damage from high energy particles penetrating through the sensor. Specifically, when interacting inside the silicon bulk, incident particles transfer energy to the nuclei, disrupting the lattice structure and causing the radiation damage in silicon. This is termed the Non-Ionising Energy Loss (NIEL). The amount of damage to the lattice depends on both the type and the energy of incident particles. While heavy charged particles can exhibit both inelastic interaction with atomic electrons and NIEL, neutrons can only lose energy through the latter. In contrast, most of light particles such as electrons, muons and photons can not generally have sufficient energy to cause disruption of the lattice. The NIEL from an incident particle displaces a silicon atom out of its lattice site. This dislodged atom is referred to as the Primary Knock-on Atom (PKA). The displacement of the PKA results in presence of a Frenkel pair consisting of an atom not in a lattice site, called an interstitial, and an empty lattice site, called a vacancy. Both the interstitial and the vacancy are mobile in the lattice at the room temperature and can be annihilated with each other when the radiation damage no longer remains. Alternatively, both can migrate through the lattice and may finally form point defects with impurity atoms being stable in the silicon. The PKA can itself displace other atoms in case it has sufficient energy, leading to a cascade of displacements in a localised area, referred to as a cluster-like defect.

The radiation-induced defects introduce new energy levels into the middle of the band-gap, acting similarly to the generation centres. This means that probability of electrons being thermally excited from the valence band to the conduction band is increased and therefore the sensor leakage current is also enhanced. The leakage current is found to be linearly increasing with particle fluence [159], as:

$$\Delta I_{\text{leak}} = \alpha \Phi V, \quad (5.4)$$

5 Instrumental measurements on the Pixel Detector during Run 2 – 5.1 Pixel-level leakage current measurements

where α is the proportionality factor for the current related damage rate, while V is the sensor volume and ΔI_{leak} is the increase in the leakage current after irradiation to a fluence Φ . In general, the increase of the leakage current after irradiation is not beneficial for the detector operation in terms of the noise contribution and the power consumption. Furthermore, it leads to constant heating and possibly destroy the sensor due to the so-called thermal runaway. As a result, the detector needs to be cooled to decrease the leakage current after irradiation.

From the relation between the leakage current and the radiation fluence as shown in Equation 5.4, the sensor leakage current measurement becomes one of the best characterized methods in order to monitor the silicon radiation damage. In the Pixel layers (B-Layer, Layer 1, Layer 2) and disks of the ATLAS pixel detector, the leakage currents are measured using two independent sub-systems: the per-module high-voltage patch panel sub-system [160] (HVPP4) and the multi-module power supply sub-system. The HVPP4 serves as a fan-out point for the bias voltages delivered to the pixel modules from the Iseg high-voltage power supplies [161] and monitors the leakage currents at the module granularity level by means of a Current Monitoring Board system. The HVPP4 sub-system is used to measure the leakage current of each module individually in LHC Run 1 and Run 2. On the other hand, the power supply sub-system is used during Run 2 to measure the total leakage current of the modules that are supplied by a common power supply unit. The power supply measurement is then used to confirm and augment the HVPP4 measurement. The leakage current data of the Pixel layers and disks are recorded by the Detector Control System [162] (DCS) and can be retrieved with the DCS data viewer [163] (DDV). In the IBL, there is a 10-bit analog-to-digital converter (ADC) on each of the FE-I4 readout chips bonded to the IBL sensors. This ADC is associated with an 8-to-1 analogue multiplexer that can be used to select and read out the temperature, power supply voltages, voltage references, leakage current and other detector control system analogue voltages. The leakage currents are measured at the nominal operation temperature and bias voltage settings. The total leakage currents for pairs of the IBL modules are also recorded and retrieved using DCS and DDV respectively.

This section, however, concentrates on the leakage current measurements at the pixel granularity level. Based on measuring the pixel-level leakage currents, one can monitor the radiation damage in details and thus know which pixels are degrading and how fast their performances are degraded due to the radiation damage. In addition, the pixel-level leakage current can be parametrized as a function of the particle fluence in order to calibrate the received fluence with a finer granularity. The leakage currents in different types of pixels can be compared to each other. Beside monitoring the radiation damage, the leakage current measurement at the pixel level can also be used to detect hardware issues. It can be used to detect hot pixels which always have high leakage currents, resulting in high noise even before irradiation. Alternatively, it can be used to determine pixels with broken bump bonds which do not draw any currents, leading to a complete absence of the leakage currents in these pixel even after irradiation. In fact, it is very difficult to measure directly the leakage current at the pixel

5 Instrumental measurements on the Pixel Detector during Run 2 – 5.1 Pixel-level leakage current measurements

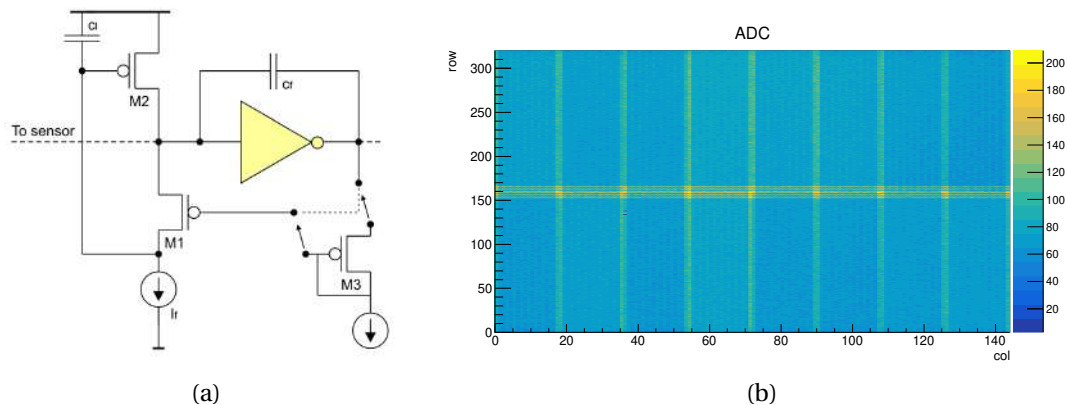


Figure 5.1: 5.1a Feedback circuit [164]. 5.1b ADC map for the module L0_B04_S2_A7_M1A.

granularity level. The MonLeak (monitoring of the leakage current) mechanism [144, 145] is used to read the leakage current pixel by pixel for modules in the IBL and in the Pixel layers and disks. The following describes in details how to obtain the pixel-level leakage currents from measurements of the MonLeak scans.

5.1.1 Pixel-level leakage current measurements in the Pixel layers and disks

For each pixel of the FE-I3 readout chips, the leakage current can only be measured in a combination with the feedback current from the feedback circuit (Figure 5.1a) connected to that pixel. The feedback current can be controlled by the IFDAC, FDAC and TrimIF registers of the pixel preamplifier. Specifically, the IFDAC is an 8-bit global digital-to-analog converter (DAC) globally controlling the feedback current of the preamplifier of every pixel, whereas the FDAC is a 3-bit pixel register that locally configures the feedback current of the preamplifier of each pixel. The remaining one, TrimIF, is a global 8-bit DAC that changes the step size of the FDAC, measured in mA/DAC. By default, the MonLeak scans are performed with the feedback current set to the smallest well-defined value which corresponds to IFDAC = TrimIF = 1 and FDAC = 0. Furthermore, in order to avoid large noise in the detector during the scans, the TDAC, a 7-bit pixel register that determines the threshold of each pixel, is increased to its maximum value of 127 DACs.

The measurable value per pixel obtained from the MonLeak scans is then digitised to a precision of 0.125 nA in a range up to 128 nA using a 10-bit reference current comparator, resulting in an ADC value per pixel within a range of [0, 1023]. All pixels whose measured ADC values are of 65535 or higher than 1023 seem to be errors and will therefore be rejected in all further calculations. One ADC map obtained from a MonLeak scan that was performed for the module L0_B04_S2_A7_M1A of B-Layer is

5 Instrumental measurements on the Pixel Detector during Run 2 – 5.1 Pixel-level leakage current measurements

shown in Figure 5.1b for an example. The leakage current in one pixel, I_{leak} , can be computed from the ADC value of that pixel with the following formula:

$$I_{\text{leak}} = 125 \text{ [pA]} \times \text{ADC}. \quad (5.5)$$

There were three MonLeak scans performed to measure the pixel-level leakage currents of all modules in the Pixel layers and disks:

- **SCAN_S000051508**: was performed on 14th December 2015, from 09:22 to 10:19 GMT+2. This scan ran with the nominal high voltage (HV) of 250 V for B-Layer and 150 V for the other barrel Pixel layers and disks.
- **SCAN_S000074820**: was performed on 16th July 2019, from 16:49 to 19:00 GMT+2. This scan ran with nominal HV of 400 V for B-Layer and 250 V for the other barrel Pixel layers and disks.
- **SCAN_S000075304**: was performed on 12th September 2019, from 12:46 to 14:01 GMT+2. This scan ran with nominal HV of 400 V for B-Layer and 250 V for the other barrel Pixel layers and disks.

In order to evaluate the accuracy of the measurements obtained from one specific MonLeak scan, the sum of the pixel-level leakage current values measured by the scan is calculated for the modules supplied by a common power supply unit and then compared to the power supply data recorded by DCS during the time period when the scan took place. The comparisons of the three scans with the power supply measurements can be seen from the ratio plots shown in Figures 5.2, 5.3 and 5.4. For SCAN_S000051508 performed in 2015, one can observe discrepancies between the MonLeak measurements and the power supply measurements. The MonLeak values of the module groups in B-Layer, Layer 1, Layer 2 and disks are higher than the DCS ones by factors of ~ 2.3 , ~ 3 , ~ 4 and ~ 5 respectively. For the two other scans performed in 2019, SCAN_S000074820 and SCAN_S000075304, the MonLeak measurements exceed the DCS ones by a factor of ~ 2 in all the Pixel layers and disks. The differences observed here are understandable since the MonLeak scans did not monitor the pixel-level leakage current alone but in the combination with the feedback current, as mentioned above. Although the discrepancies still exist, the 2019 scans have shown an improvement of the MonLeak mechanism (with the smaller factor in the comparisons between MonLeak and DCS) in monitoring the leakage current at the pixel granularity level after the LHC Run 2.

In the MonLeak scans, the leakage current of a given module can be obtained by calculating the sum of leakage current values of all the pixels within that module. The module-level leakage currents of B-Layer, Layer 1 and Layer 2, obtained from the scan SCAN_S000051508, are shown in Figure 5.5. For this 2015 scan, except some modules with significantly high leakage currents, the measured values of most of the modules in the three Pixel layers are around 0.08 mA, 0.05 mA and 0.04 mA, respectively. The module-level leakage currents of the Pixel layers obtained from the two 2019 scans are

5 Instrumental measurements on the Pixel Detector during Run 2 – 5.1 Pixel-level leakage current measurements

represented in Figures 5.6 and 5.7. For these two 2019 scans, while most of the modules in B-Layer have the leakage currents of around 0.45 mA, those in Layer 1 and Layer 2 have the smaller values that are around 0.28 mA and 0.2 mA respectively. It should be noted again that these MonLeak measurements are not precise due to the presence of the feedback currents; however, one can observe from these measurements that the leakage currents of B-Layer are always higher than the ones of the two other Pixel layers. This is reasonable since B-Layer is closer to the beam pipe and thus has suffered more radiation damage than the other Pixel layers. Besides, one can also observe a significant increase in the leakage currents of all the Pixel layers from 2015 to 2019, being consistent with the increase of the irradiation fluence after Run 2.

The z -dependence of the leakage current in one Pixel layer can also be seen from the MonLeak measurements by taking the average of the leakage current values over all the modules that are located at the same η position in the layer, except those deactivated. Figures 5.8 represents the z -dependence of the leakage current in the barrel Pixel layers for the three MonLeak scans mentioned above.

5 Instrumental measurements on the Pixel Detector during Run 2 – 5.1 Pixel-level leakage current measurements

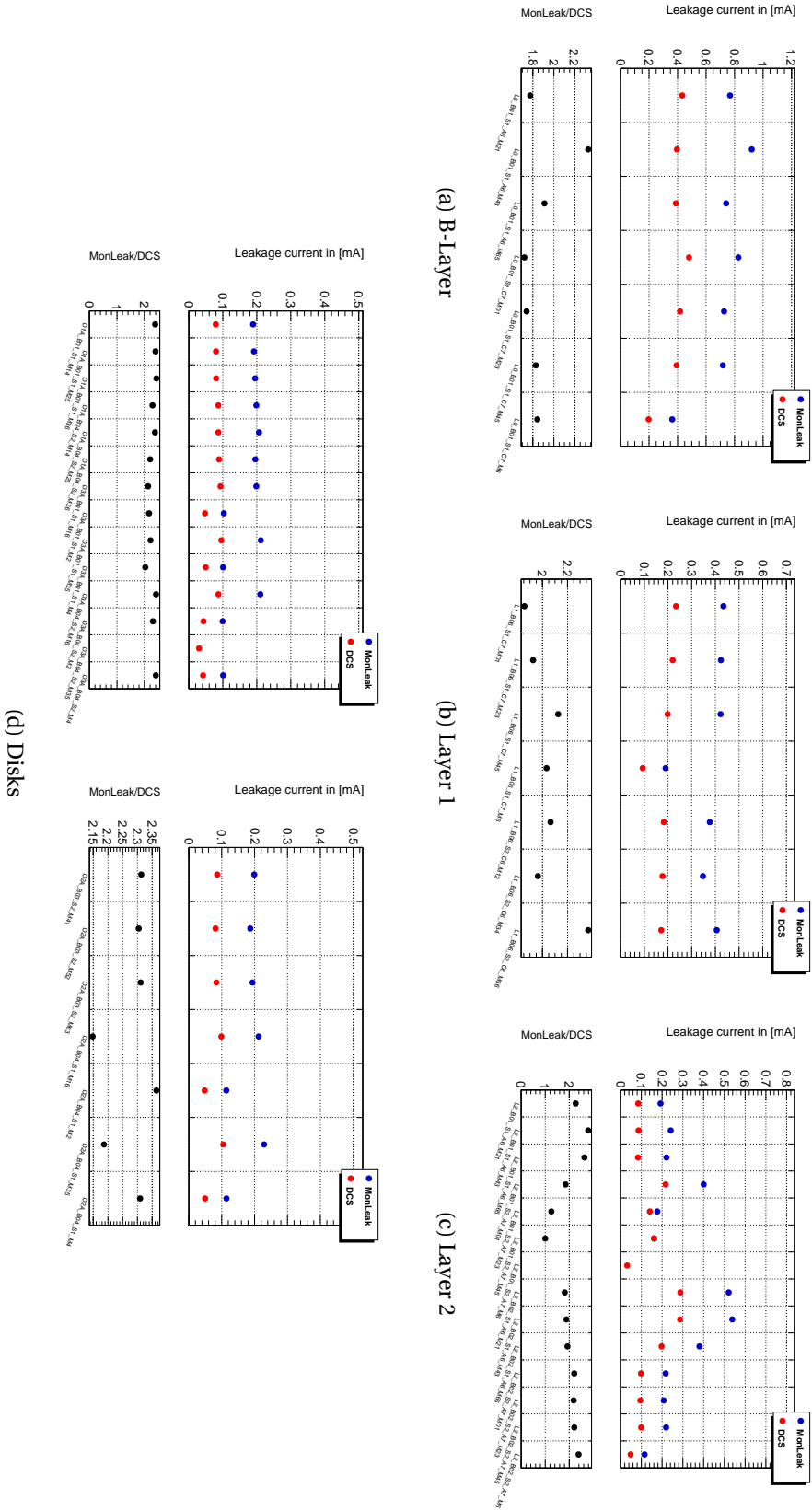


Figure 5.3: The total leakage currents measured by SCAN_S000074820 (in blue) or the power supply (in red) of some module groups, each supplied by a common power supply unit, in (5.3a) B-Layer, (5.3b) Layer 1, (5.3c) Layer 2 and (5.3d) disks. The lower pads show the ratios of the MonLeak measurements to the power supply measurements. The power supply data were recorded by DCS during the time period when the scan took place. The unit is [mA].

5 Instrumental measurements on the Pixel Detector during Run 2 – 5.1 Pixel-level leakage current measurements

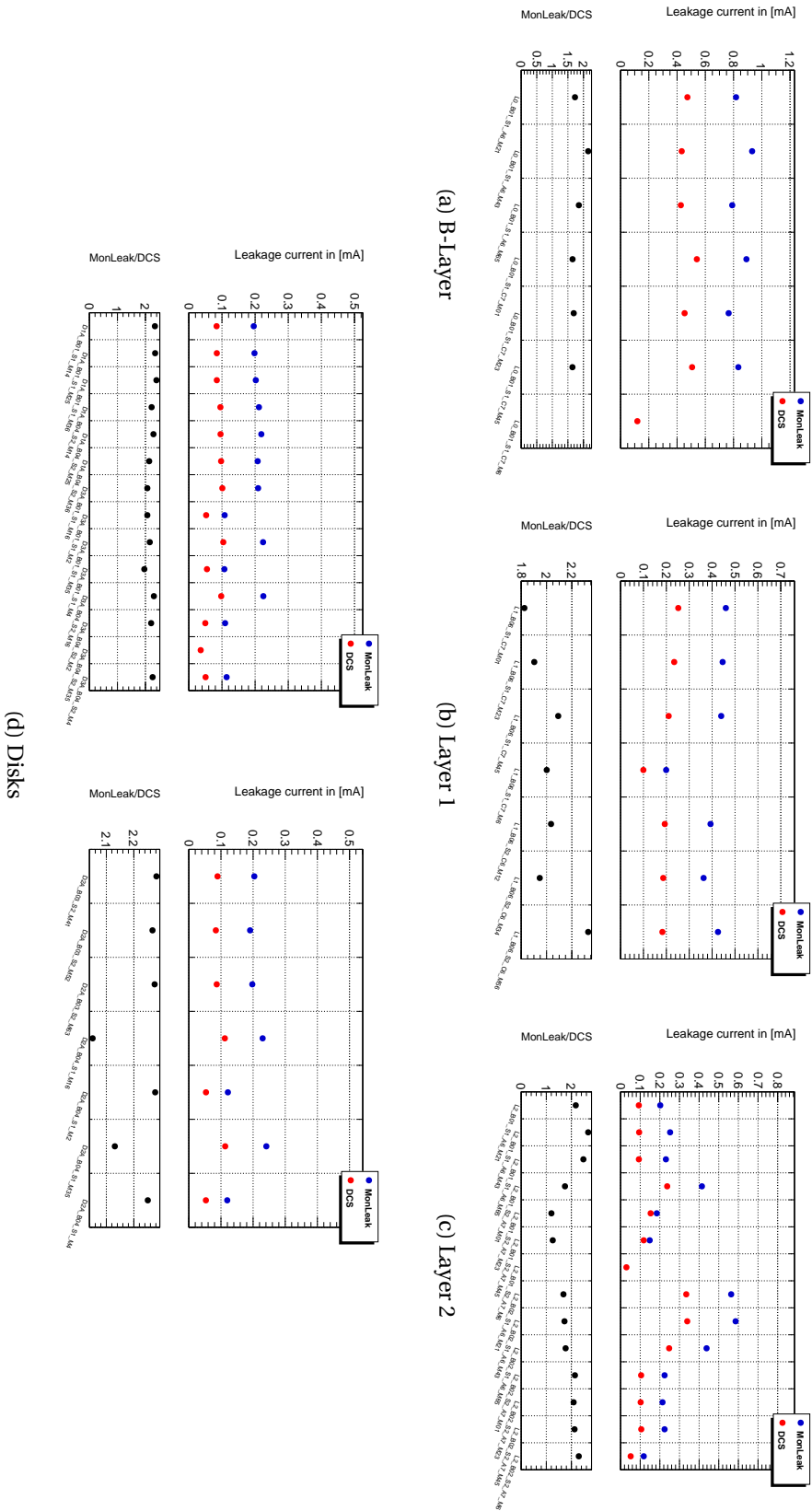
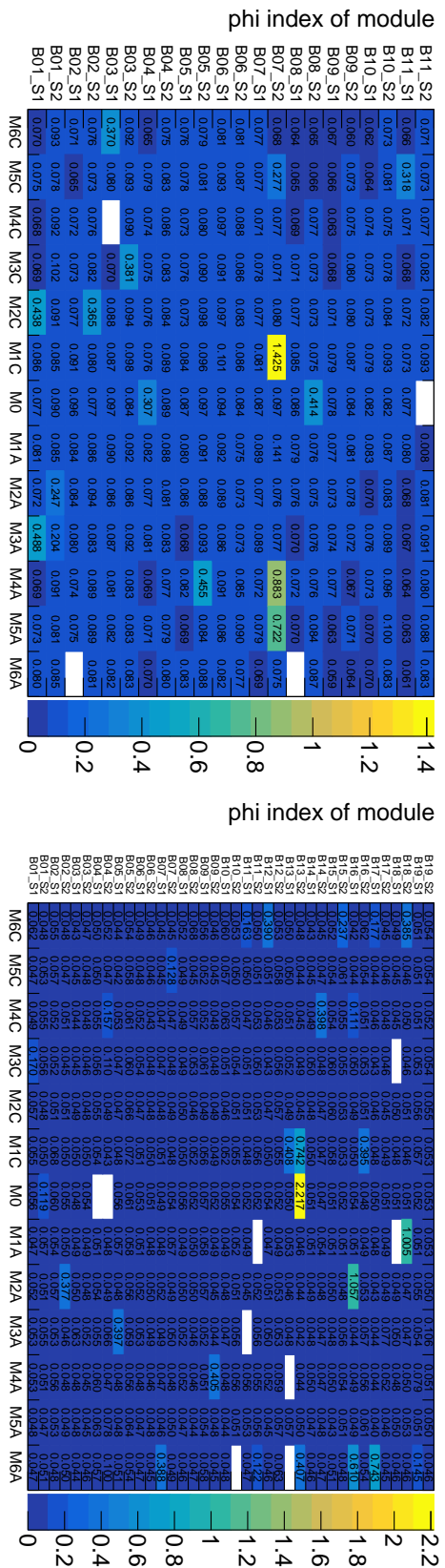
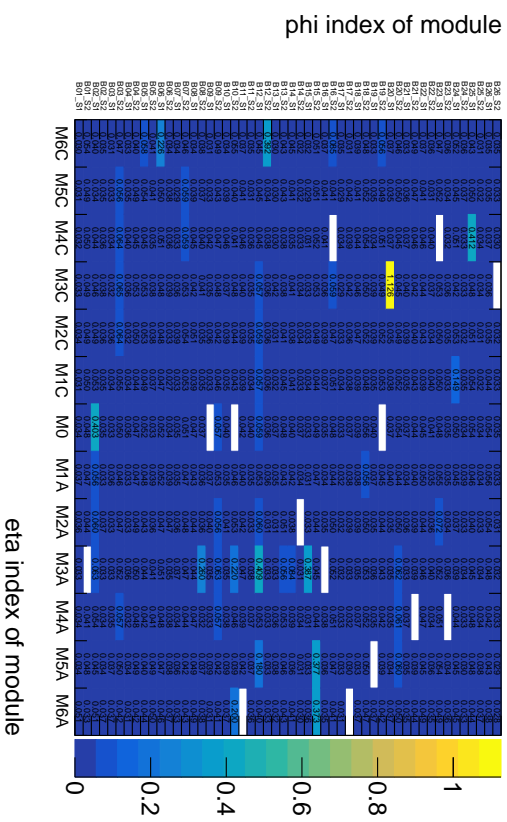


Figure 5.4: The total leakage currents measured by SCAN_S000075304 (in blue) or the power supply (in red) of some module groups, each supplied by a common power supply unit, in (5.4a) B-Layer, (5.4b) Layer 1, (5.4c) Layer 2 and (5.4d) disks. The lower pads show the ratios of the MonLeak measurements to the power supply measurements. The power supply data were recorded by DCS during the time period when the scan took place. The unit is [mA].

5 Instrumental measurements on the Pixel Detector during Run 2 – 5.1 Pixel-level leakage current measurements



(a) B-Layer



(b) Layer 1

(c) Layer 2

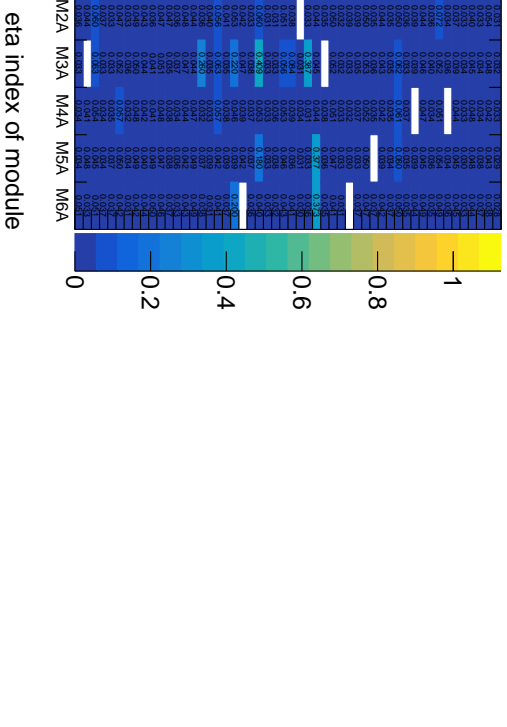
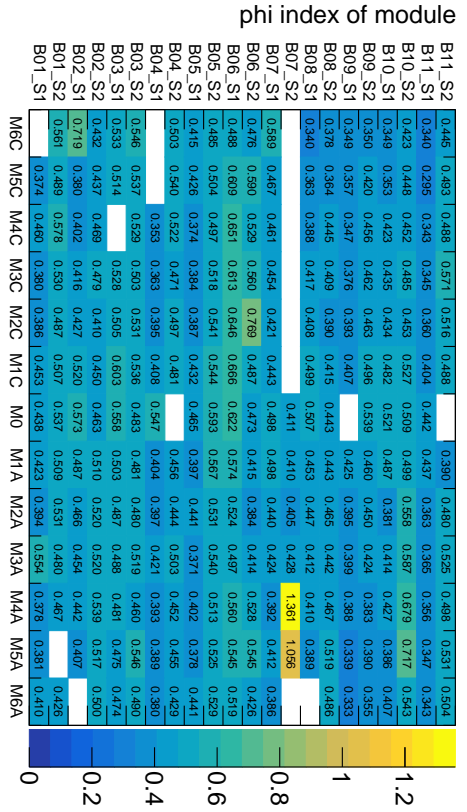
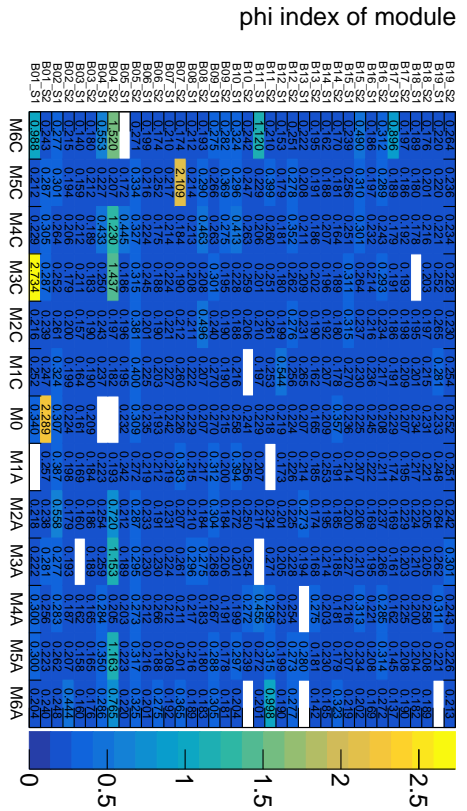


Figure 5.5: The leakage currents in [mA] of the modules in (5.5a) B-Layer, (5.5b) Layer 1 and (5.5c) Layer 2 obtained from the MonLeak scan SCAN_S000051508. The blank cells represent the modules deactivated during the scan.

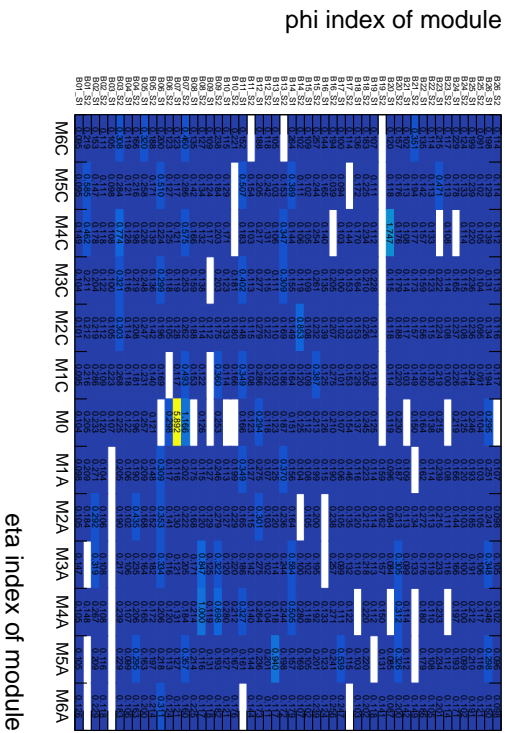
5 Instrumental measurements on the Pixel Detector during Run 2 – 5.1 Pixel-level leakage current measurements



(a) B-Layer



(b) Layer 1



(c) Layer 2

Figure 5.7: The leakage currents in [mA] of the modules in (5.7a) B-Layer, (5.7b) Layer 1 and (5.7c) Layer 2 obtained from the MonLeak scan SCAN_S000075304. The blank cells represent the modules deactivated during the scan.

5 Instrumental measurements on the Pixel Detector during Run 2 – 5.1 Pixel-level leakage current measurements

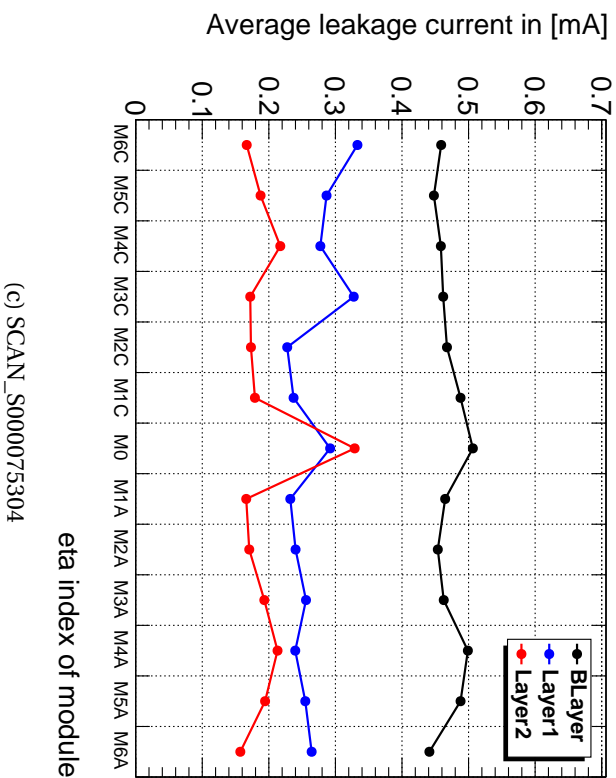
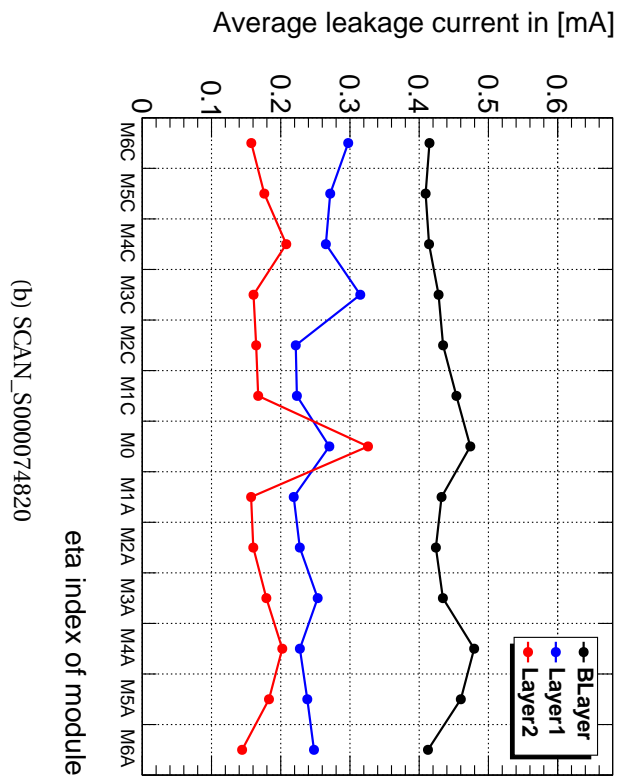
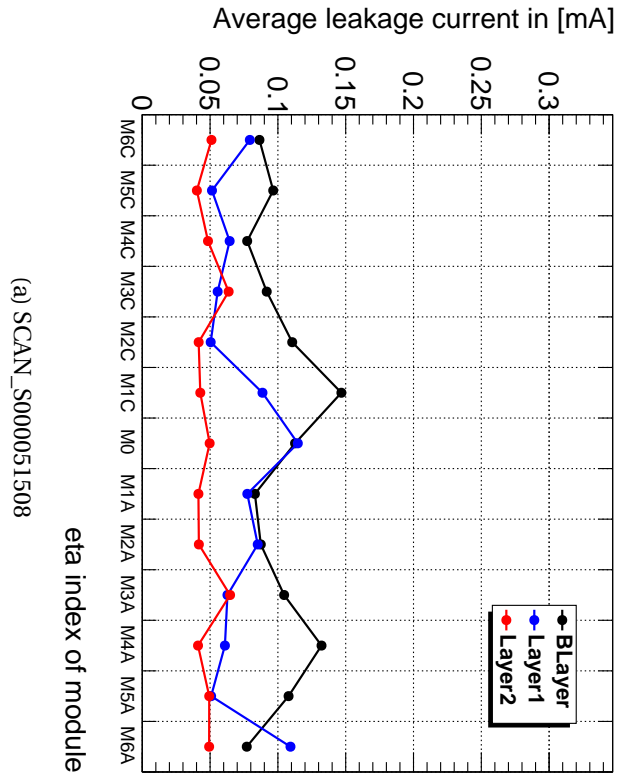


Figure 5.8: The z -dependence of the leakage current for B-Layer (black), Layer 1 (blue) and Layer 2 (red) in (5.8a) SCAN_S000051508, (5.8b) SCAN_S000074820 and (5.8c) SCAN_S000075304.

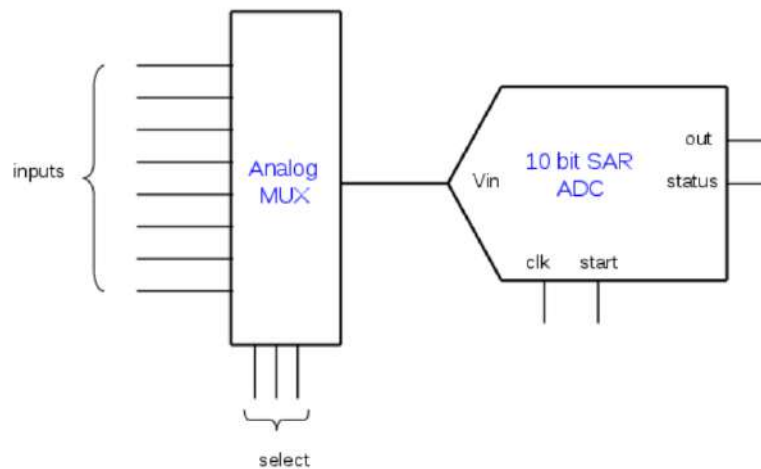


Figure 5.9: Block diagram of the GADC [144].

5.1.2 Pixel-level leakage current measurements in the IBL

For the FE-I4B readout chip, the MonLeak scan can measure the leakage current pixel by pixel using the on chip generic ADC (GADC). The GADC is a general purpose 10-bit Analog-to-Digital Converter designed for test and monitoring. Its block diagram is shown in Figure 5.9. It contains an 8-to-1 analog multiplexer that has eight sets of switches connecting eight analog input channels to a common output. The signals connected to these GADC input channels are defined in Table 5.1. The input channel is selected using a 3-bit address decoded with combinatorial logic. The input stage is then followed by a 10-bit ADC based on the Successive Approximation Register (SAR) architecture. The successive-approximation ADC is the most popular architecture for data-acquisition applications, especially when multiple channels require input multiplexing.

In order to measure the pixel-level leakage current in the MonLeak scan, only the channel 7 is chosen to be in the ON state. In addition, the pixel registers are also enabled and the leakage current bus is set into the resistance of 10 k Ω or 90 k Ω . The GADC output per pixel is then digitised into decimal numbers, resulting in a GADC value per pixel. When the high voltage (HV) is on, the GADC obtained from the MonLeak scan for a given pixel contains an off-set which can be determined with the MonLeak scan performed when the HV is off. By subtracting this off-set from the measured GADC, one can determine the true GADC corresponding to the leakage current of the pixel. In pixels where their off-set is higher than their measured GADC, their true GADC is set to be 0. Similarly to the MonLeak scans in the Pixel layers and disks, all pixels that have the error GADC value of 65535 will be rejected in all further calculations.

Each FE-I4B chip connects to a readout Rx channel that scans the corresponding

5 Instrumental measurements on the Pixel Detector during Run 2 – 5.1 Pixel-level leakage current measurements

GADC input channel	Selected signal to digitise
0	Temperature sensor
1	GADC reference voltage
2	Analog ground
3	Analog MUX output
4	Analog regulator current sense
5	10-bit DAC output
6	Half of regulated analog voltage
7	Leakage current

Table 5.1: Selection of GADC inputs [144].

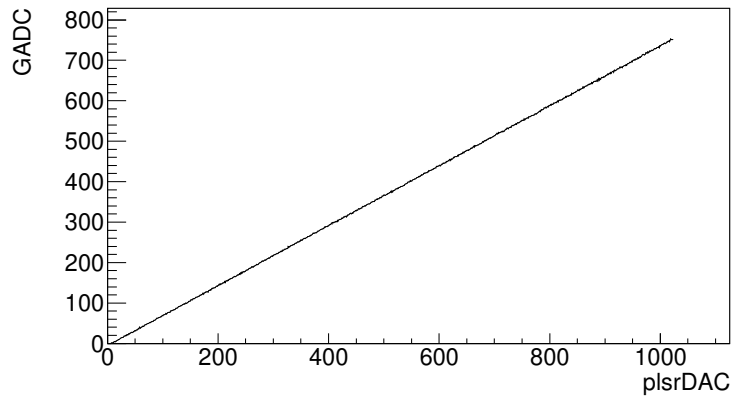


Figure 5.10: GADC as a function of pulser DAC, scanned by a Rx channel.

GADC value for each pulser DAC value (Figure 5.10). Normally, the GADC increases linearly with respect to the pulser DAC as the following function:

$$\text{GADC} = p_0 + p_1 \times \text{pulserDAC}, \quad (5.6)$$

where p_0 and p_1 are the two parameters of the linear function and can be obtained by fitting this function to the Rx scan of the FE-I4B chip.

Once the function slope p_1 is known, the leakage current per pixel, I_{leak} , in the chip can be estimated as follows:

$$I_{\text{leak}} = \frac{V_{c_1}}{R p_1} \times \text{GADC}, \quad (5.7)$$

where V_{c_1} denotes the parameter obtained in calibration voltage of the FE chip with the pulser DAC, different for each FE. R is the resistance which can be either 90 k Ω or 10 k Ω . For an example, the two GADC-versus-pulserDAC scans of the two Rx channels

5 Instrumental measurements on the Pixel Detector during Run 2 – 5.1 Pixel-level leakage current measurements

that are connected to the two FE-I4B chips of the module LI_S05_A_M1_A1 are shown in Figure 5.11a. These Rx scans are fitted using the linear function mentioned in Equation 5.6 in order to determine the slope p_1 of each FE chip. The resulting p_1 values are then used together with the V_{C1} values so as to compute the pixel-level leakage current from the pixel's true GADC using Equation 5.7. The leakage current map obtained for LI_S05_A_M1_A1 is shown in Figure 5.11b.

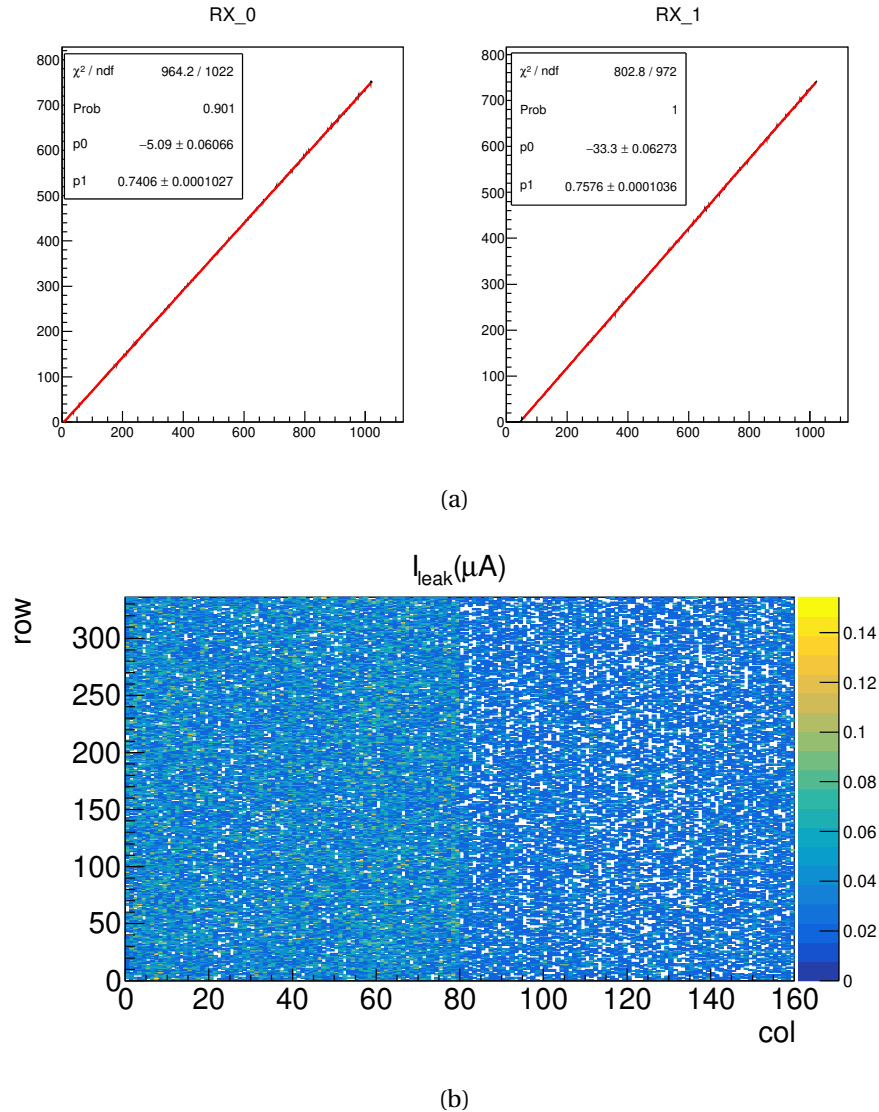


Figure 5.11: 5.11a The GADC-versus-pulserDAC scans of the two Rx channels connected to the two FE-I4B chips of the module LI_S05_A_M1_A1, fitted with the linear function in Equation 5.6. 5.11b The leakage current map (in μA) obtained from a MonLeak scan for the module LI_S05_A_M1_A1.

5 Instrumental measurements on the Pixel Detector during Run 2 – 5.1 Pixel-level leakage current measurements

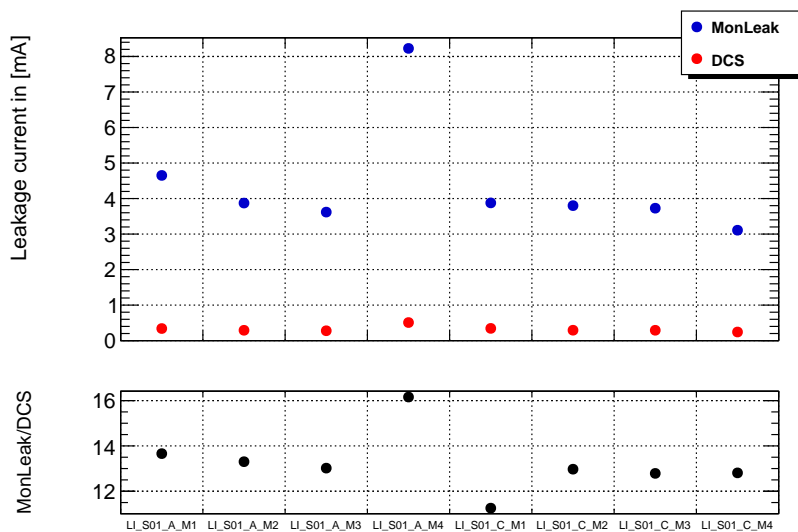
There were two MonLeak scans performed with the HV ON in the entire IBL to measure the pixel-level leakage currents of the IBL modules. Both ran with the GADC leakage current bus set into the resistance of 90 k Ω . These scans are:

- **SCAN_S000074783**: performed on 15th July 2019, at around 10:00 GMT+2.
- **SCAN_S000075396**: performed on 18th September 2019, from 12:27 to 16:12 GMT+2.

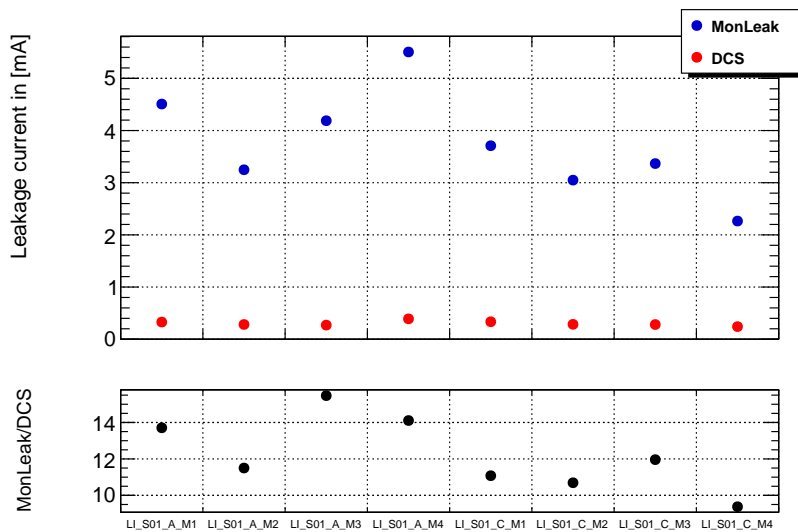
Each of these two scans was accompanied by a scan performed in the same conditions and time period but with the HV OFF in order to measure the off-set of the measured GADC per pixel. As done in the Pixel layers and disks, the accuracy of the MonLeak measurements for the IBL are also evaluated by comparing the sum of the pixel-level leakage currents of the module groups with the data recorded in DCS during the same time periods when the two scans took place. The comparisons can be seen from the MonLeak-DCS ratio plots given in Figure 5.12. For both the scans, one can observe a huge discrepancy with the MonLeak values much greater than the DCS ones by a factor of ~ 14 . This indeed means that the MonLeak mechanism does not work well in monitoring the leakage currents at the pixel granularity level for the IBL and thus the GADC needs to be further calibrated.

The leakage current per module as well as the average value of the current at each η position (the z -dependence) in the IBL are also computed and shown in Figures 5.13 and 5.14, respectively, for both the scans. It can be seen that, in the centre regions of the IBL staves where the planar modules populate, the MonLeak scans give the module-level leakage current of around 2 mA, while the MonLeak measurements of the 3D modules located at the ends of the IBL staves are significantly higher and may not be reliable.

5 Instrumental measurements on the Pixel Detector during Run 2 – 5.1 Pixel-level leakage current measurements



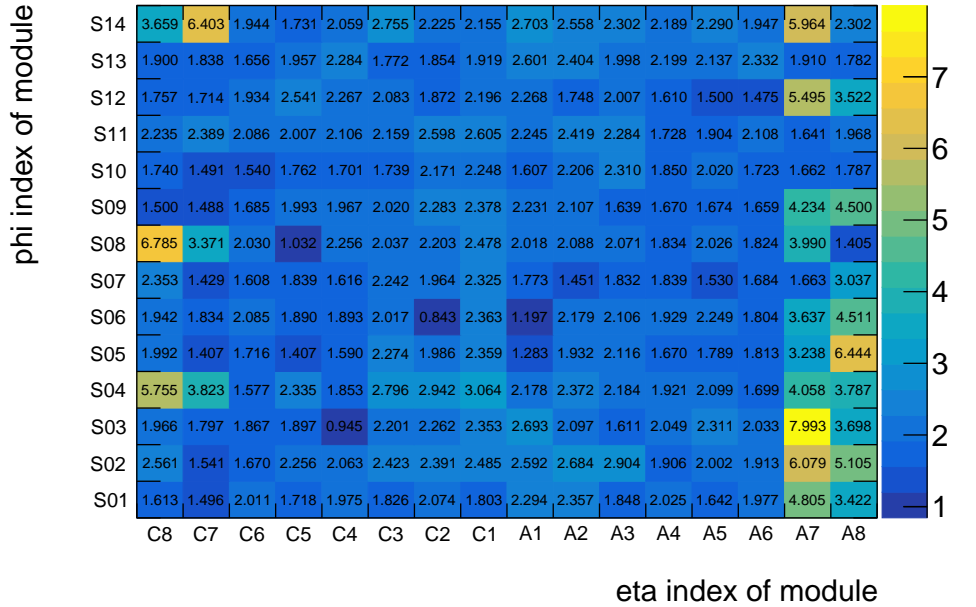
(a) SCAN_S000074783



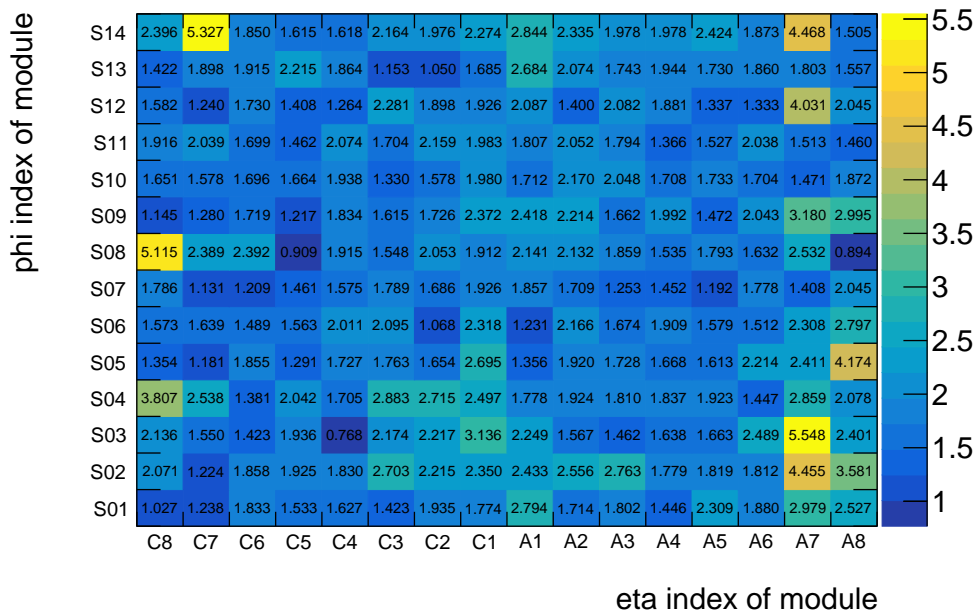
(b) SCAN_S000075396

Figure 5.12: The total leakage currents of some module groups in the IBL, measured from (5.12a) SCAN_S000074783 or (5.12b) SCAN_S000075396 (in blue) with the data recorded by DCS (in red) during the same time periods when the two scans took place. The lower pads show the ratios of the MonLeak measurements to the DCS data. The unit is [mA].

5 Instrumental measurements on the Pixel Detector during Run 2 – 5.1 Pixel-level leakage current measurements



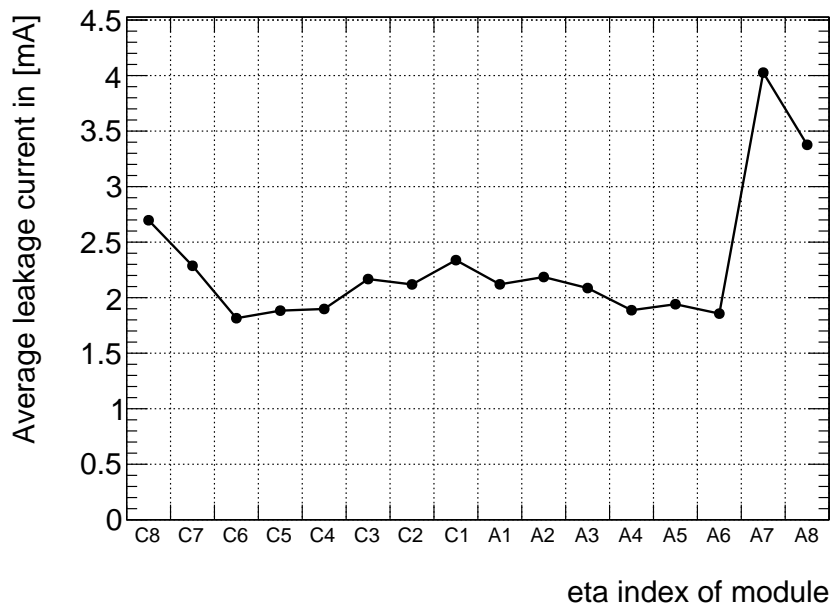
(a) SCAN_S000074783



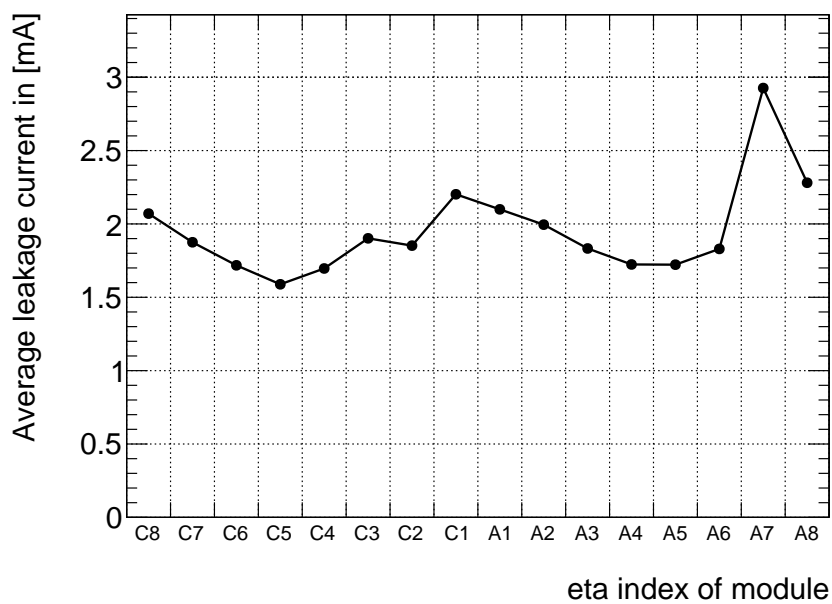
(b) SCAN_S000075396

Figure 5.13: The leakage currents in [mA] of the modules in the IBL obtained from the MonLeak scans (5.13a) SCAN_S000074783 and (5.13b) SCAN_S000075396.

5 Instrumental measurements on the Pixel Detector during Run 2 – 5.1 Pixel-level leakage current measurements



(a) SCAN_S000074783



(b) SCAN_S000075396

Figure 5.14: The z -dependence of the leakage current for the IBL in (5.14a) SCAN_S000074783 and (5.14b) SCAN_S000075396.

5.1.3 Summary

The leakage current arises when the reverse bias voltage is applied to a sensor mainly due to the crystal impurity of the sensor bulk that creates the generation centres close to the middle of the band-gap and thus increases the probability of the thermal excitation of electrons from the valence band to the conduction band. It is proportional to the depleted width (Equation 5.2) and strongly depends on the temperature (Equation 5.3). The sensor leakage current is also found to be linearly increasing with the irradiation fluence (Equation 5.4) and therefore measuring it becomes one of the best characterized methods to monitor the silicon radiation damage. In the ATLAS pixel detector, while the leakage current can be measured precisely at the module granularity level, it is much more difficult to achieve precise measurements at the pixel granularity level for the leakage current. This section has described the approach making use of the MonLeak mechanism to monitor the leakage current pixel by pixel for the IBL, the Pixel layers (B-Layer, Layer 1, Layer 2) and disks.

In the Pixel layers and disks, the MonLeak scans can only measure the pixel-level leakage current in the combination with the feedback current of the pixel preamplifier. Three MonLeak scans, one scan in 2015 and two scans in 2019, were performed to measure the pixel-level leakage current of the modules in the Pixel layers and disks. Although the measurements of these MonLeak scans show discrepancies when comparing with the power supply measurements recorded by DCS, one can still observe a reasonable trend for the leakage currents in these scans, being consistent with the amount of radiation damage that each of the Pixel layers has suffered. Furthermore, an improvement of the MonLeak approach in monitoring the pixel-level leakage current has also been shown from the 2019 scans.

In the IBL, the MonLeak scans measure the leakage current per pixel using the general purpose 10-bit ADC (GADC) implemented on each FE-I4B chip. There were two scans performed in 2019 to measure the pixel-level leakage current of the IBL modules. From these scans, one can observe a huge discrepancy with the MonLeak measurements for the IBL modules, especially the 3D modules, extremely higher than the DCS data by a factor of around one order of magnitude. Therefore, the pixel-level leakage current obtained from these MonLeak scans for the IBL are unreliable and the GADC must be further calibrated. One possibility for this is tuning the internal reference voltage of the GADC, which will affect both the GADC outputs and the GADC-versus-pulserDAC scan of the Rx channel connected to the chip. It is also desirable to consider not only the z -dependence but also the ϕ -dependence of the leakage current in the IBL for further studies.

5.2 Estimation of pixel-hit loss rate using real data

At the high luminosities of the LHC, the readout system can not always cope with the high rate of hits from the pixel detector and therefore the pixel hits can be lost during the readout mechanism. There are several sources contributing to this inefficiency, as

5 Instrumental measurements on the Pixel Detector during Run 2 – 5.2 Estimation of pixel-hit loss rate using real data

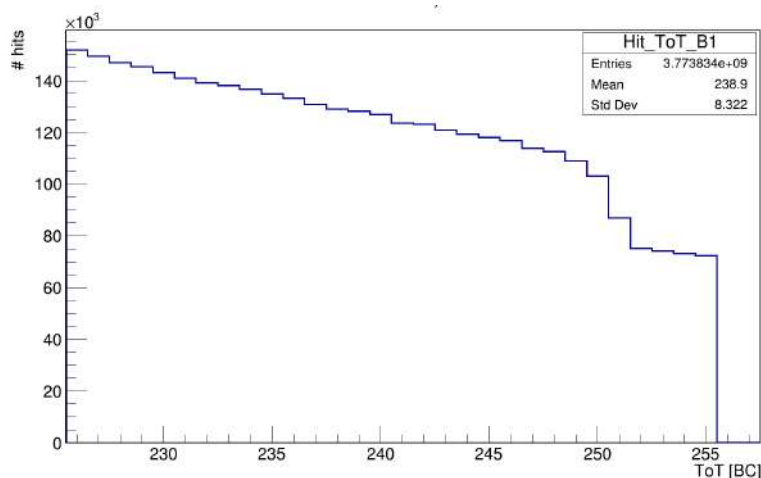


Figure 5.15: The ToT distribution of Layer 1. An unnatural decrease of the number of hits can be observed in the high-ToT region (ToT > 250 BC).

follows:

Double-hit (DH) inefficiency After a pixel receives a hit, it is busy during a certain amount of time for charge released by the hit to be drained. If the pixel receives a new hit while the charge is still above the threshold, the second hit will be lost.

Busy/Waiting (BW) inefficiency After being drained, hits wait in readout cells of double-columns (DC) until they are transferred to End-of-Column (EoC) buffers at the edge of the readout chip. The maximum rate for transferring pixel hits is of 0.5 hits per 25 ns for one DC. If the DC hit rates are too high, there will be many hits waiting to be transferred and thus the DC bus will be very busy. When the DC bus becomes saturated, new hits can not be accepted and are then lost.

Late copying (LC) inefficiency Hits transferred into the EoC buffers wait for the trigger L1 accept (L1A) signal which arrives at a latency to determine whether a hit is read out or deleted. The process of copying pixel hit data from the DCs down to the buffers is time-consuming and hits can be lost due to the late copying if they have the sum of the time over threshold (ToT) and the time to copy greater than the L1A latency. The effect of the LC inefficiency can be seen directly from an unnatural decrease of the number of high-ToT hits in the ToT distribution as shown in Figure 5.15.

Buffer overflow (BO) inefficiency There are two types of hits occupying the EoC buffer: hits waiting for the L1A signal and hits already accepted by the L1 trigger, waiting to be read out. In fact, the EoC buffer can only store 64 hits and thus any additional hits are discarded.

MCC inefficiency The readout of the FE-I3 chips is done by the Module Control Chip (MCC). The data of pixel hits, accepted by the L1 trigger, is transferred from the chip buffers to the MCC buffers throughout the Low Voltage Differential Signaling (LVDS) before it is transferred to the Read-out Drivers (RODs). If the data arrives the MCC buffers faster than the speed of transferring data to the RODs, at one point the MCC buffers will be able to become saturated. Any additional hits will make the buffers overflow and will therefore be discarded.

At the latency of 256 bunch-crossings (BC, 1 BC = 25 ns), the BO inefficiency was the dominant source; however, since the latency has been set to 120 BC, the DH inefficiency becomes dominant and the other sources stay negligible, even in Run 3. So far the pixel-hit losses from these inefficiency sources have not been simulated yet. In order to account for the inefficiency, only an ad-hoc fraction of 0.9% of Monte-Carlo (MC) hits was discarded randomly, regardless of the hit ToT and of the luminosity. This was fine for Run 1, but during Run 2, an underestimation of the pixel hole rate was found in MC with this assumption, implying that the hit loss rate must be higher than the canonical 0.9% applied to MC. For the incoming Run 3 as well as the future High-Luminosity LHC where the luminosities will be significantly increased, it is important and necessary to replace this ad-hoc value by a more precise loss rate computed for the inefficiency in each layer.

As mentioned, the main contribution of the lost hits is from the DH inefficiency source. For each layer, the DH loss rate can be estimated from the pixel-ToT distribution of the layer with the following steps:

1. One should firstly compute the average occupancy Occ of the layer from its occupancy map by taking the average of the occupancy values of all the modules in the layer, except those deactivated.
2. From the ToT distribution of the layer, one can estimate the fraction f_i of hits having $ToT = i$ BC in the layer as:

$$f_i = \frac{N_i}{\sum_{j=ToTmin}^{ToTmax} N_j}, \quad (5.8)$$

where N_i denotes the number of hits in the bin i of the ToT distribution. This fraction corresponds to the fraction of pixels staying busy during i BC in the layer.

3. If one assumes that the ToT distribution is the same at each BC, the total fraction L_i of pixels which were still above the threshold since i BC should be:

$$L_i = i \times f_i. \quad (5.9)$$

4. To get the same fraction, L_i^{layer} , for all the pixels of the layer, not only for those

5 Instrumental measurements on the Pixel Detector during Run 2 – 5.2 Estimation of pixel-hit loss rate using real data

having a hit, one should multiply with the average occupancy Occ computed in the first step:

$$L_i^{\text{layer}} = L_i \times Occ. \quad (5.10)$$

5. Finally, by taking contributions of all the ToT bins into account, the measurement of the DH hit loss rate, DH^{layer} , can be obtained with the final formula as:

$$DH^{\text{layer}} = \sum_{i=\text{ToTmin}}^{\text{ToTmax}} L_i^{\text{layer}} = \frac{Occ}{\sum_{j=\text{ToTmin}}^{\text{ToTmax}} N_j} \sum_{i=\text{ToTmin}}^{\text{ToTmax}} i \times N_i. \quad (5.11)$$

A simple ROOT macro was built implementing all of these steps to compute the DH loss rate from the ToT distribution and the occupancy map stored in the data quality root file for each of the barrel layers and end-caps. It was used to estimate the DH loss rate using data from the LHC run 362776, which took place from 21:10:33 on 04/10 to 10:22:43 on 05/10 in 2018, contained 2544 colliding proton bunches separated by 25 ns. The occupancy maps and the ToT distributions of the barrel layers and end-caps in this run are shown in Figures 5.16 and 5.17, respectively. The measurements of the DH loss rate and the average occupancy computed for each barrel layer and each end-cap using data of this run are represented in Table 5.2. The resulting loss rate obtained for B-Layer is 0.96%, while in the others, the loss rates are within a range of [0.45%, 0.7%]. The first preliminary results for the estimation of the DH loss rate are in an expected range.

Layer	Average Occupancy	DH loss rate [%]
B-Layer	0.000597	0.96
Layer 1	0.000284	0.70
Layer 2	0.000187	0.45
End-cap A	0.000256	0.60
End-cap C	0.000257	0.61
IBL	0.000832	0.63
IBL planar modules	0.000815	0.61
IBL 3D modules	0.000882	0.69

Table 5.2: The average occupancy and the DH loss rate computed for each of barrel layers and end-caps using data of the run 362776.

5 Instrumental measurements on the Pixel Detector during Run 2 – 5.2 Estimation of pixel-hit loss rate using real data

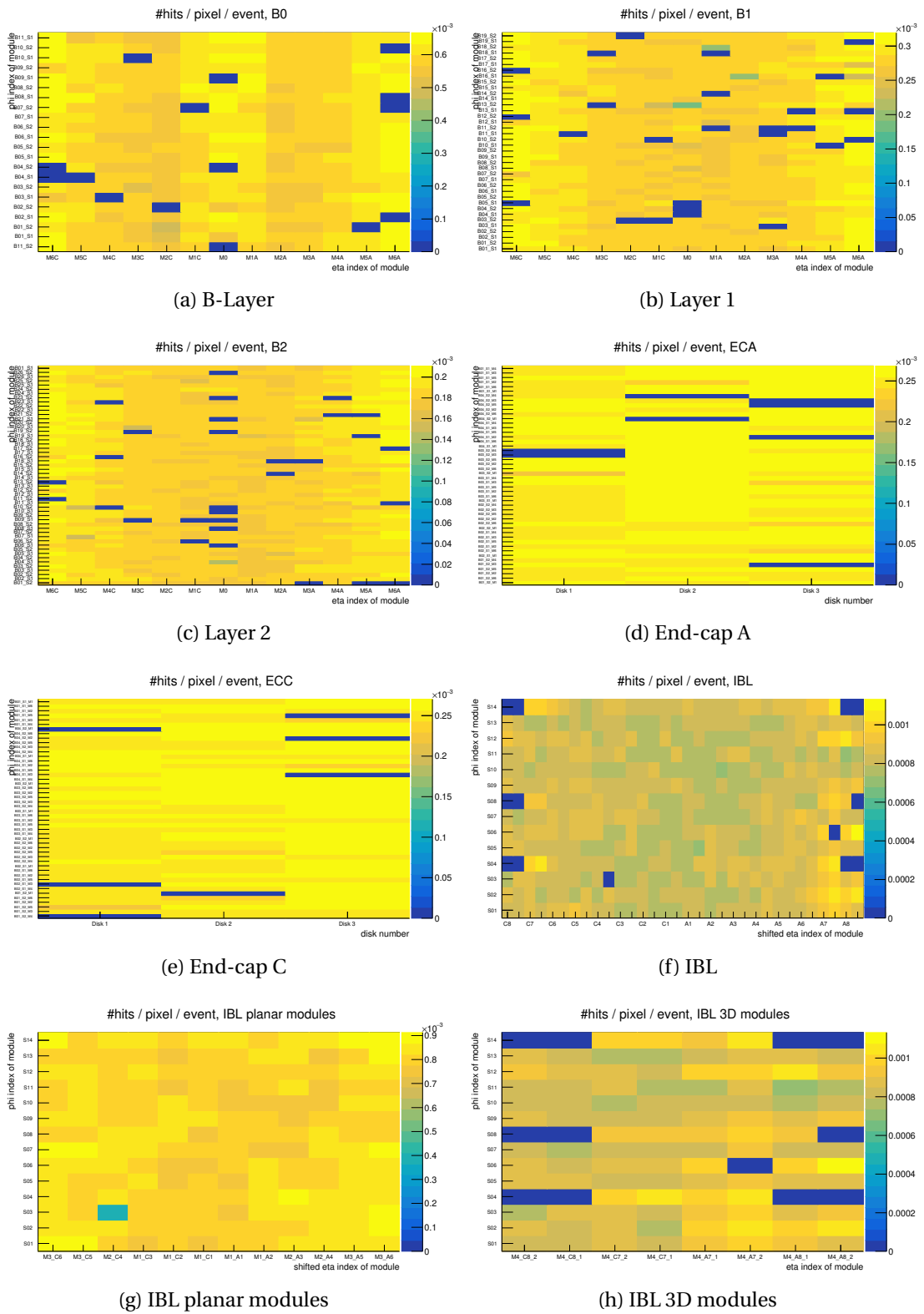


Figure 5.16: Occupancy maps of the barrel layers and end-caps in the run 362776.

5 Instrumental measurements on the Pixel Detector during Run 2 – 5.2 Estimation of pixel-hit loss rate using real data

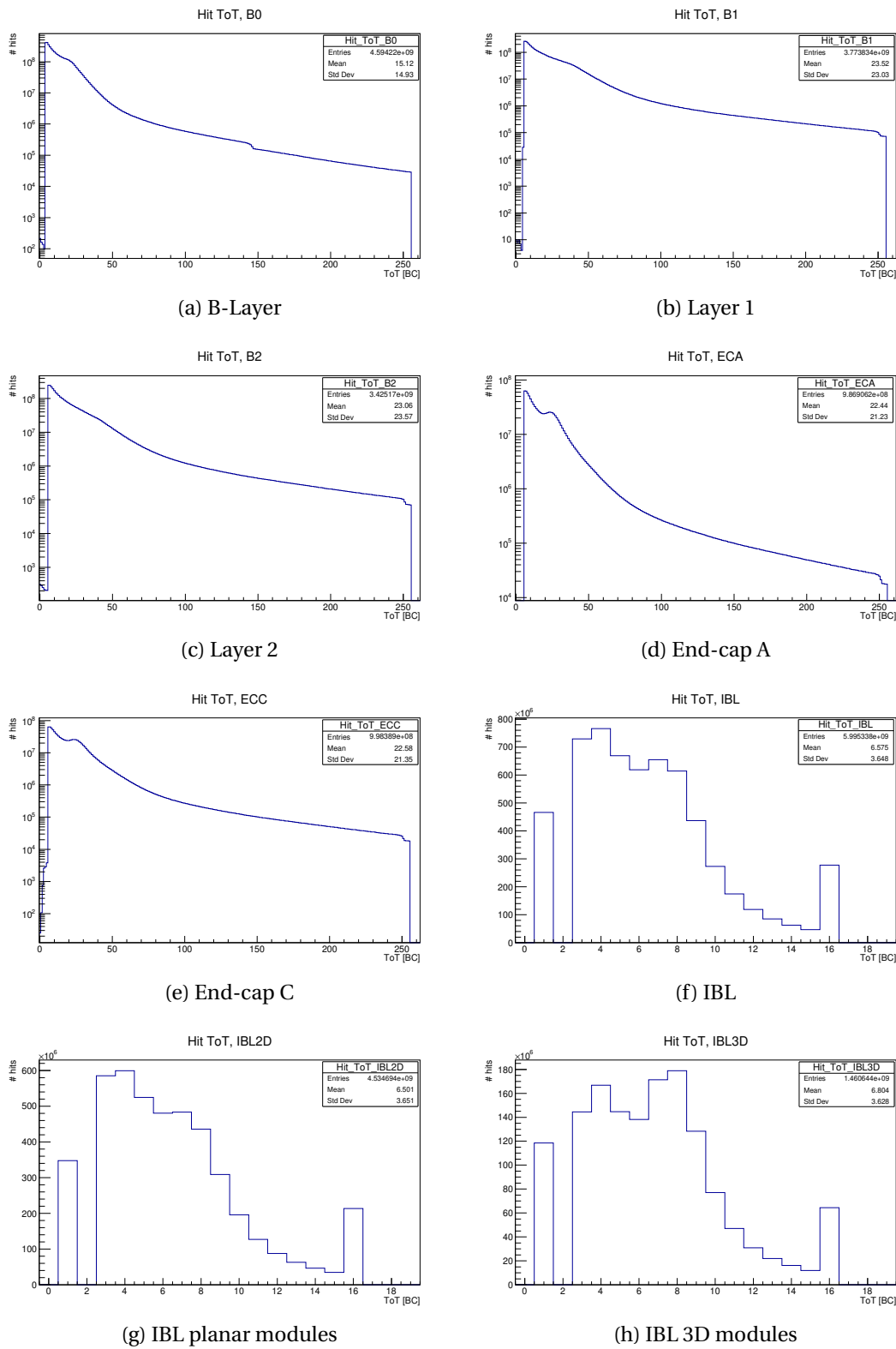


Figure 5.17: ToT distributions of the barrel layers and end-caps in the run 362776.

5 Instrumental measurements on the Pixel Detector during Run 2 – 5.2 Estimation of pixel-hit loss rate using real data

The effect of the LC inefficiency is visible with the unnatural decrease in number of hits at the end of the ToT distribution. One can also estimate the pixel-hit loss rate of this inefficiency from the ToT distribution of each layer. The estimation begins with a very simple assumption in which the number of hits decreases exponentially in the high-ToT region of the distribution with an exponential function given as:

$$N_{\text{hits}} = p_0 10^{-p_1 \times \text{ToT}}, \quad (5.12)$$

where p_0 and p_1 are the two parameters of the function. One then fits this function with several ToT bins just before the ToT bin where the unnatural decrease starts occurring (LC point). The values obtained for the parameters are used to extrapolate the function into the region after the LC point and then estimate the number of lost hits in this region. Finally, the LC loss rate is defined as follows:

$$LC^{\text{layer}} = \frac{N_{\text{lost-hits}}^{\text{est}}}{N_{\text{hits}}^{\text{total}} + N_{\text{lost-hits}}^{\text{est}}}, \quad (5.13)$$

where $N_{\text{lost-hits}}^{\text{est}}$ is the number of lost hits in the region after the LC point, estimated from the extrapolation of the exponential function, while $N_{\text{hits}}^{\text{total}}$ is the total number of hits in the ToT distribution of the layer. Implementation of the LC loss rate estimation was also done in a ROOT macro. This was used to compute the loss rates of the LC inefficiency in the Pixel layers and end-caps using data of the run 362776. The ToT distributions of this run together with the corresponding fit results at the high-ToT region around the LC point are shown in Figure 5.18. The number of lost hits and the LC loss rate estimated for each Pixel layer and each end-caps in this run can be seen from Table 5.3. While B-Layer has the LC loss rate of 0.052%, the other layers and end-caps have the rates of about 0.004%, much lower than the B-Layer one.

Layer	$N_{\text{lost-hits}}^{\text{est}}$	LC loss rate [%]
B-Layer	2389868.148	0.052
Layer 1	149165.486	0.004
Layer 2	141002.050	0.004
End-cap A	33846.125	0.003
End-cap C	34529.833	0.003

Table 5.3: The number of lost hits and the LC loss rate computed for each of Pixel layers and end-caps using data of the run 362776.

5 Instrumental measurements on the Pixel Detector during Run 2 – 5.2 Estimation of pixel-hit loss rate using real data

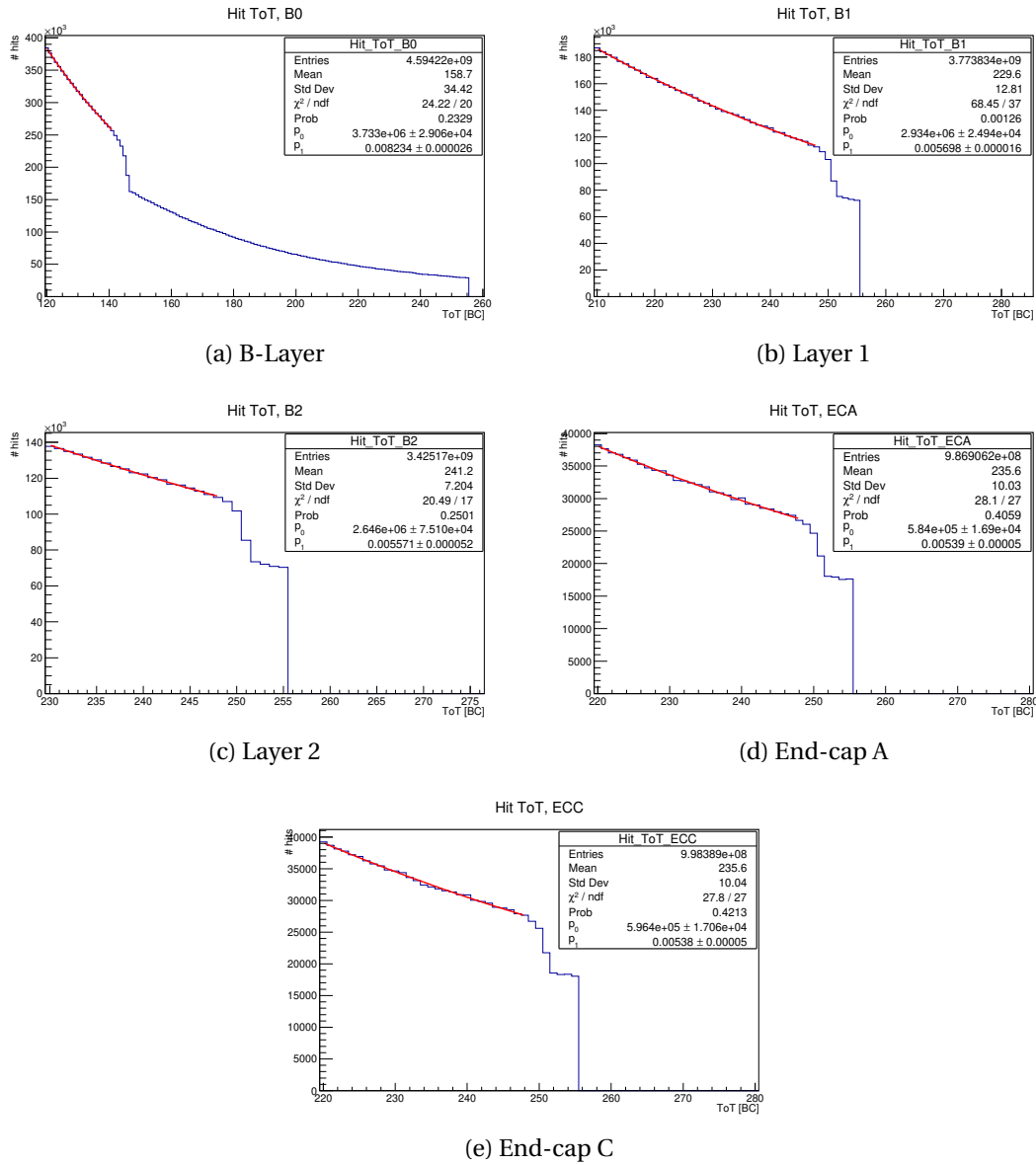


Figure 5.18: ToT distributions at high-ToT region of the Pixel barrel layers and end-caps in the run 362776. The exponential function in Equation 5.12 is fitted with several ToT bins just before the LC point.

5 Instrumental measurements on the Pixel Detector during Run 2 – 5.2 Estimation of pixel-hit loss rate using real data

Regarding the remaining inefficiency sources at the moment, while there are no obvious ideas about how to measure the BW inefficiency with data, the BO and the MCC inefficiency sources are flagged in data and thus their hit loss rates are possible to be evaluated.

The preliminary results obtained from the methods which have been described in this section are indeed promising. For B-Layer, the estimated DH loss rate is of 0.96%, already higher than the ad-hoc fraction of 0.9% applied for the MC simulation. However, these methods still need further validations. They will be applied to estimate the hit loss rate per layer using data from the other runs. After that, these resulting rates will be used rather than the old fraction of 0.9% to digitise and reconstruct a new MC sample. The hole rate in this MC sample will then be compared to the one in data for validating the methods. If the agreement is improved, one can go to the next step where these methods will be included into the Athena code for Run 3.

It should also be noted that there are other sources which also contributes to the loss and thus the obtained result of 0.96% here for B-Layer should be considered as a lower limit for the loss rate in this layer. The same exercises with other runs with different instantaneous luminosities will be performed in order to know how the loss rates scales with luminosity.

6 ATLAS during the High Luminosity LHC

The LHC physics program, as shown in Figure 6.1, will be extended with an upgrade of the accelerator in 2024 to reach the highest levels of luminosity and to deliver even more pp collisions to the experiments from 2027 onwards. This running phase is the so-called High-Luminosity LHC (HL-LHC) and its technical challenges as well as the physics motivation for the HL-LHC program will be briefly discussed in Section 6.1.

With an upgraded accelerator, the beam conditions for the experiments will also change dramatically posing new challenges to the detectors. As an example, an average pile-up of $\langle \mu \rangle = 200$ as well as unprecedented levels of radiation are expected for the HL-LHC operation, requiring upgraded detector systems to withstand these harsh conditions as well as to maintain the high measurement precision. For the ATLAS experiment, the so-called ATLAS Phase-2 Upgrade program was developed. In this program the different sub-detectors will be upgraded, including the inner tracking detector, the calorimeter system, the muon spectrometer and the Trigger and Data Acquisition (TDAQ) system. The technical details of the developed upgrade plans for each sub-system are published in Technical Design Reports (TDRs).



Figure 6.1: The LHC baseline program including the HL-LHC [165].

The range of the involved upgrade activities spans from replacements of readout electronic boards in the calorimeters, over the installation of faster signal transmissions and upgraded logic processors for the TDAQ system to a full replacement of the current tracking detector by a new system, the ATLAS Inner Tracker (ITk). An overview about the planned ITk detector with its design choices to fulfill the physics requirements and to cope with the challenging environment of the HL-LHC is given in Section 6.2.

Due to the severe radiation damage in the HL-LHC phase, the innermost pixel layers of the ITk should be replaced after the first-half of the HL-LHC. For this thesis, one possible solution, in which the Complementary-Metal-Oxide-Semiconductor (CMOS) sensor technology will be employed instead of the current sensor technology, is discussed. Section 6.3 describes an overview of the CMOS sensor and simulation of the CMOS sensor for the replacement of the innermost ITk layers in the HL-LHC second-half.

6.1 The High-Luminosity LHC

Increasing the luminosity of the LHC would greatly enhance the physics reach of ATLAS and of all the LHC experiments. In fact, a major purpose of the LHC experiments is the search for extremely rare phenomena, in particular new physics signatures. Moreover, all the Standard Model precision measurements would be greatly improved with additional statistics. For this reason, after the end of 2024 when the Run 3 of the LHC will be completed and ATLAS will collect an amount of data more than 300 fb^{-1} [166], the LHC will be upgraded to the High-Luminosity LHC (HL-LHC) [70], which is expected to start operations in 2027 (Figure 6.1).

As shown in Equation 3.2, the luminosity can be increased by increasing the number of colliding particles and also by reducing the size of the colliding beams. The increase in luminosity for the HL-LHC is accomplished with an increase in the number of protons per bunch to 2.2×10^{11} (from 1.15×10^{11} in the LHC) [70] and with a reduced beam size. To reduce the size of the beams, new 11 T quadrupole magnets will be implemented in the final focus systems [167]. To achieve this effect a larger crossing angle is needed, reducing the geometrical factor S to about 0.31, down from 0.84 in the LHC [70]. This effect will be mitigated with the use of novel crab cavities, devices that can rotate longitudinally the bunches and therefore improve the overlap between them. The use of crab cavities will increase the geometric loss factor in the HL-LHC to a value of 0.83 [70].

The HL-LHC will run for about 10 years with an instantaneous luminosity of up to $7.5 \times 10^{34} \text{ cm}^{-2}\text{s}^{-1}$ [70]. The total integrated luminosity recorded at the end of the HL-LHC operations will be up to 4000 fb^{-1} , about ten times larger than that at the end of the LHC lifetime. The HL-LHC will greatly enhance the physics reach of the ATLAS experiment. For example, at the end of the HL-LHC lifetime, the Higgs boson mass is expected to be measured with a precision of a few tens of MeV [168], one order of

magnitude better than the currently achieved precision. Figure 6.2 shows two further examples of the enhanced physics reach offered by the HL-LHC. The HL-LHC will create huge opportunities in terms of physics prospects but it will also generate a much harsher environment for the detectors. The biggest challenges are related to the much higher number of interactions per bunch crossing, which will increase from an average of 24 (in 2016) to an average of 200 inelastic pp collisions, and much higher radiation levels. By the end of 2039, the innermost tracker layer will be exposed to a fluence of $2 \times 10^{16} \text{ n}_{\text{eq}}/\text{cm}^2$, which is 4-6 times the IBL fluence at the end of the LHC Run 3.

ATLAS Simulation

$\sqrt{s} = 14 \text{ TeV}$: $\int Ldt=300 \text{ fb}^{-1}$; $\int Ldt=3000 \text{ fb}^{-1}$

$\int Ldt=300 \text{ fb}^{-1}$ extrapolated from 7+8 TeV

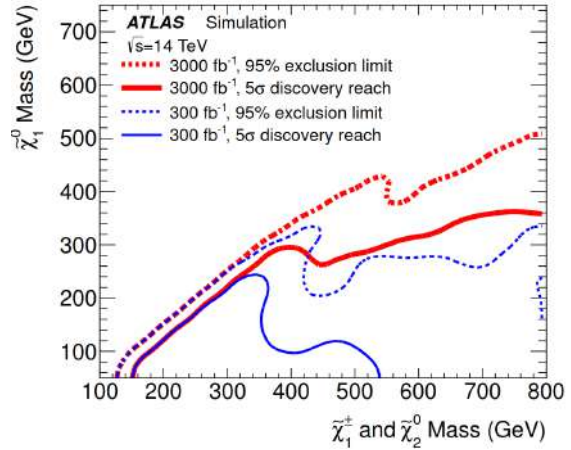
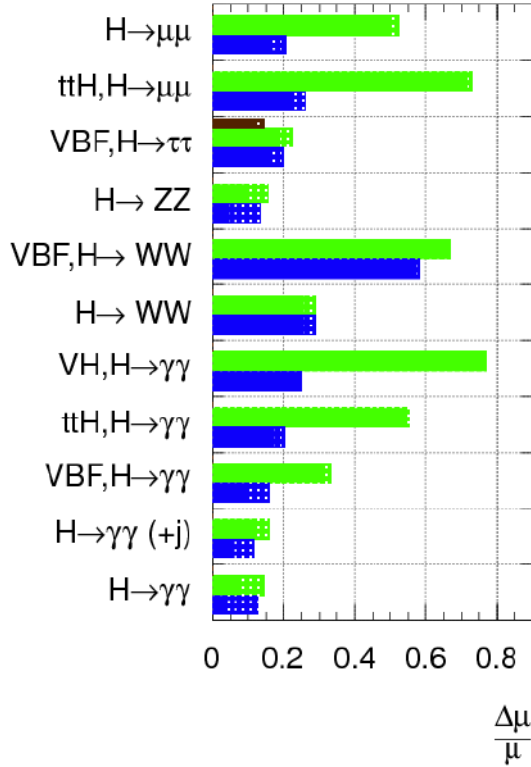


Figure 6.2: Comparison of physics reach expected at the end of lifetime of the LHC and at the end of lifetime of the HL-LHC. The left plot shows uncertainty in the Higgs boson signal strengths. The right plot shows discovery reach (solid lines) and exclusion limits (dashed lined) for charginos and neutralinos in $\tilde{\chi}_1^\pm \tilde{\chi}_2^0 \rightarrow W^{(*)} \tilde{\chi}_1^0 Z^{(*)} \tilde{\chi}_1^0$ decays. Both taken from [169].

In order to cope with such harsh conditions, ATLAS needs to be upgraded to continue its investigation of the high energy physics spectrum. In terms of performance,

this upgrade should allow ATLAS to compete with or even exceed the actual physics performance of the current detector. The ATLAS inner detector (INDET) will be fully replaced by a new all-silicon tracker, the Inner Tracker (ITk) made of pixels in its inner part and of strips in its outer part. The all-silicon option was decided because of the need of highly radiation-hard materials and for data rates and occupancy considerations (the TRT occupancy would reach 100% at the HL-LHC).

The other detectors (the calorimeters and the muon spectrometer) will also undergo some upgrades [170]. The Liquid Argon calorimeter and the hadronic calorimeter's electronics will be upgraded to cope with the high radiation level: the entire LAr calorimeter readout chain will be upgraded and the hadronic calorimeter will undergo an upgrade of its readout electronics and associated mechanics.

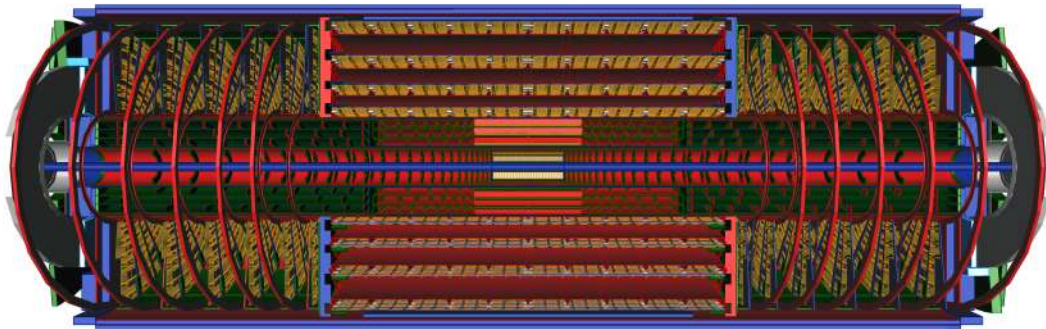
A new detector, the High Granularity Timing Detector (HGTD) [171] will be added into the high pseudorapidity region of $2.4 < |\eta| < 4$. Its goal will be to add timing information on forward tracks. The high timing resolution (30 ps) will help to disentangle pile-up tracks which origin collision points (primary vertices) are spatially close but separated in time.

6.2 The ATLAS Inner Tracker

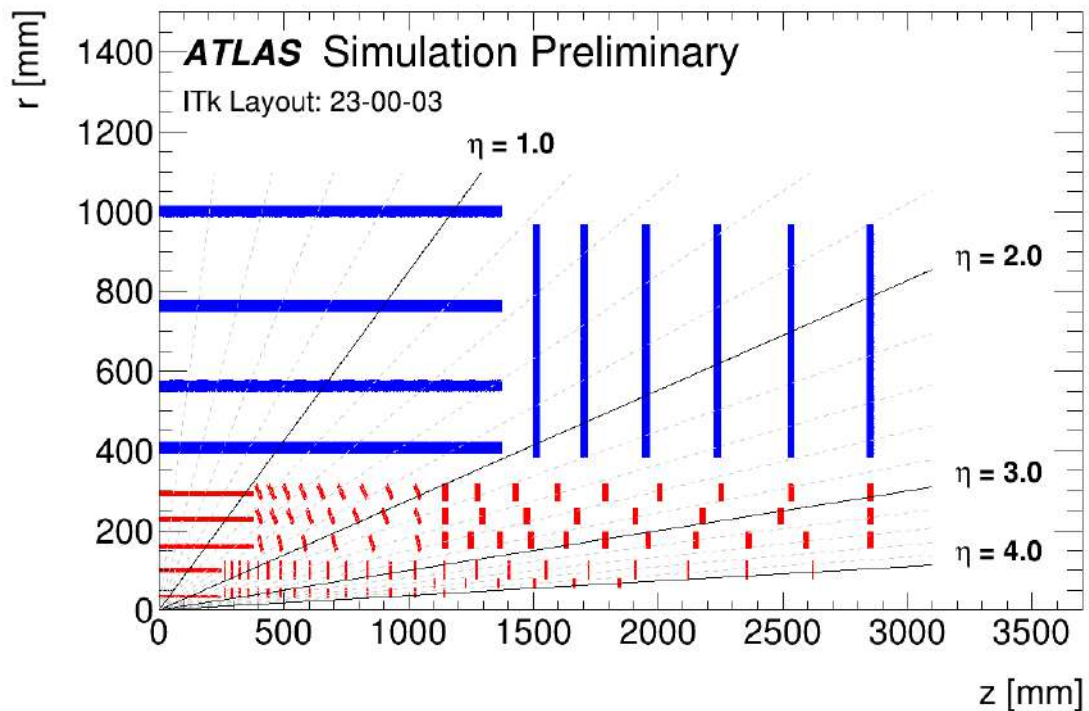
The ATLAS ITk detector consists of a silicon pixel detector sub-system (the ITk Pixel detector) in the region closest to the beam pipe and a silicon microstrip detector sub-system (the ITk Strip detector) at higher radii from the beam pipe. With this separation, the granularity of the detector is optimised to resolve nearby tracks while minimising against the number of readout channels and cost of the system. Similarly to the INDET, each sub-detector is divided into a barrel region with multiple concentric layers around the beam direction and two end-caps composed of disks (for the Strip detector) or rings (for the Pixel detector) placed perpendicularly to the beam line, covering the forward regions. The layout of the ITk is shown in Figure 6.3. The ITk is surrounded by the same 2T solenoid magnet as for the current INDET for the momentum measurements. The study presented in this thesis is based on the ITk layout version 23-00-03. The following describes the layouts of the ITk Pixel and Strip detectors in this version.

6.2.1 The ITk Pixel detector

The ITk Pixel detector consists of five layers in the barrel region. Each barrel layer contains a flat part in the centre, where modules are placed parallel to the beam line. Furthermore, each flat part of the three outermost barrel layers is followed by inclined rings, where modules are tilted at an oblique angle of about 56° with respect to the beam line. Two types of modules are used for the barrel layers. The first one, used in the innermost barrel layer, is the triplet modules which consist of three connected readout chips, each associated with a $2 \times 2 \text{ cm}^2$ sensor. The second one, used in the other



(a)



(b)

Figure 6.3: (6.3a) Display of the Inner Tracker layout for the HL-LHC phase of ATLAS. (6.3b) Schematic layout of the ITk with Strip (blue) and Pixel (red) detectors showing only one quadrant and only active detector elements; the horizontal axis is along the beam line with zero being the interaction point and the vertical axis is the radius measured from the interaction region [172].

Barrel layer	Radius [mm]	Rows of sensors	Flat barrel $ z $ [mm]	Flat sensors per row	Inclined rings $ z $ [mm]	Inclined rings	Module type
L0	34	12	0-245	24	-	-	triplets
L1	99	20	0-245	12	-	-	quads
L2	160	32	0-372	18	380-1035	2×6	quads
L3	228	44	0-372	18	380-1035	2×8	quads
L4	291	56	0-372	18	380-1035	2×9	quads

Table 6.1: Parameters for the ITk pixel flat barrel and inclined rings, taken from [172].

The number of sensors per row refers to a complete stave in the central, flat part of the barrel where sensors are placed parallel to the beam line. The number of inclined rings refers to both sides of the detector.

Ring layer	Radius [mm]	$ z $ [mm]	Rings	Sensors per ring	Module type
R0	33.20	263-1142	2×15	18	triplets
R0.5	58.70	1103-1846	2×6	30	triplets
R1	80.00	263-2621	2×23	20	quads
R2	154.50	1145.5-2850	2×11	32	quads
R3	214.55	1145.5-2850	2×8	44	quads
R4	274.60	1145.5-2850	2×9	52	quads

Table 6.2: Parameters for the ITk pixel end-caps, taken from [172]. The radii refer to the innermost point of the modules on a ring. The number of rings refers to both sides of the detector.

barrel layers, is the quad modules which are made of four connected readout chips associated with a single $4 \times 4 \text{ cm}^2$ sensor. Table 6.1 summarizes parameters for the ITk pixel barrel layers. The end-cap system of the ITk Pixel detector, covering the forward region, is composed of six ring layers containing modules placed perpendicularly to the beam line. The innermost two ring layers are populated with the triplet modules, while the others are populated with the quad modules. Parameters of the ITk pixel end-caps are summarized in Table 6.2.

The layout of the ITk Pixel detector, which has been described, is based on the *Inclined layout* [173]. This design allows to minimise the material induced performance deterioration in the barrel/end-cap transition region. Additionally, it enables to reduce the amount of silicon needed as the inclined modules have a larger angular coverage in this region. The detector can provide hermetic tracking coverage up to $|\eta| = 4$.

Both the planar and 3D sensor technologies, discussed in Section 4.2, are considered for the ITk Pixel detector. Choices of the sensor design and technology used for each region of the detector have to meet the required level of radiation tolerance and also

need to guarantee stable thermal operation and high intrinsic efficiency over the active lifetime of the sensors, under the HL-LHC conditions. For the innermost barrel layer (L0) and the innermost two end-cap ring layers (R0 and R0.5), the baseline option is making use of the 3D sensors that are designed with the thickness reduced to $150\ \mu\text{m}$ and the pixel pitch reduced to $25 \times 100\ \mu\text{m}^2$ (in L0) or $50 \times 50\ \mu\text{m}^2$ (in R0 and R0.5). The planar n-in-p sensors are the preferred option for the rest of the detector. The n-in-p design is selected due to its simpler (and hence cheaper) fabrication procedures compared to the n-in-in design. The outer barrel and end-cap ring layers use the sensors which have the pixel pitch of $50 \times 50\ \mu\text{m}^2$ and the thickness of $100\ \mu\text{m}$ (in L1 and R1) or $150\ \mu\text{m}$ (in the others). The smaller thickness together with the smaller pixel pitch of the sensor design can help to increase the detector radiation hardness, improve the intrinsic position resolution, reduce the detector occupancy and keep leakage currents under control after irradiation as well.

The ITk Pixel detector uses a new front-end (FE) chip, RD53, which is being developed jointly by ATLAS and CMS in the RD53 collaboration framework [174]. The new readout chip is based on a 65 nm CMOS technology. The RD53 chip is a 20 mm wide by 21 mm tall die with 153600 pixels (400×384). The chip contains approximately 500 M transistors (to be compared to the IBL FE-I4 with 90 M). The pixel input bump pitch is $50 \times 50\ \mu\text{m}^2$, which was chosen to keep the same bump minimum spacing as in the original Pixel Detector and the IBL, to minimise bump bonding development and risk. This is compatible with sensors having square pixels of $50 \times 50\ \mu\text{m}^2$ size, but also with other pixel shapes, such as $25 \times 100\ \mu\text{m}^2$, as long as the bump locations remain on a $50\ \mu\text{m}$ by $50\ \mu\text{m}$ grid.

Due to the severe radiation damage (up to $2 \times 10^{16}\ \text{n}_{\text{eq}}/\text{cm}^2$) accumulating especially in the innermost pixel layers, the design of the detector allows a potential replacement of the innermost two barrel layers (L0 and L1) as well as the innermost three end-cap ring layers (R0, R0.5 and R1). These layers are expected to be exchanged after having integrated half of the expected luminosity of the HL-LHC.

6.2.2 The ITk Strip detector

The ITk Strip detector [173] uses silicon microstrip modules with different strip lengths and pitch sizes depending on the location in barrel or end-cap. The implementation of a stereo angle allows to measure the second track coordinate and the basic strip concept can be compared to the ATLAS SCT detector.

The barrel section consists of four layers with the two inner layers equipped with strips of 24.1 mm length (short strip/SS) and the two outer with 48.2 mm length (long strip/LS). The strip pitch is $75.5\ \mu\text{m}$ and a stereo angle of $\pm 26\ \text{mrad}$ is implemented for each side of the layer by rotating the relative sensor position. The end-cap section is built up of six disks along the beam axis with strip modules radially distributed and the strips pointing to the center of the beam axis. The strip length is changing as function of radius to allow for a constant occupancy level. The same is the case for the strip pitch for the different wedge shaped sensor segments. A stereo angle of ± 20

mrad for each side of the disk is implemented by rotating the sensing strips relative to the radial orientation of each disk. Overall, the ITk Strip detector extends to hermetic coverage of up to $|\eta| = 2.7$ and provides 60 M readout channels for a total silicon area of roughly 165 m^2 .

6.3 CMOS sensor for ITk replacement in second-half of HL-LHC

As already mentioned, the design of the ITk Pixel detector allows its innermost two barrel layers (L0 and L1) and its innermost three end-cap ring layers (R0, R0.5 and R1) to be replaceable. During the entire HL-LHC lifetime, an expected integrated luminosity of up to 4000 fb^{-1} will be delivered to the ATLAS detector and thus these layers will be exposed to a corresponding accumulated radiation fluence of up to $2 \times 10^{16} \text{ n}_{\text{eq}}/\text{cm}^2$. However, with the sensor designs and technologies mentioned in Section 6.2.1, the ITk pixel sensors can only withstand the maximum fluence of roughly $10^{16} \text{ n}_{\text{eq}}/\text{cm}^2$ [175]. This means that these innermost layers should be replaced by the half-life of the HL-LHC.

For this replacement, the pixel sensors produced exploiting the CMOS technology, CMOS sensors, are particularly attractive to replace the traditional pixel sensors (3D and planar sensors). While the technologies used for the production of these traditional sensors are very specific for High-Energy-Physics (HEP) and do not have a large commercial market outside of this area, the CMOS sensor technology is highly mature and used in chip industry for a long time. The CMOS sensors are widely used for personal cameras and medical clinics. Beside having a commercially mature technology, the CMOS sensors can also bring many advantages to the ITk Pixel detector. The CMOS sensors can efficiently be operated with depletion layer thicknesses between $20 \mu\text{m}$ and $100 \mu\text{m}$. Sensor thinning to thicknesses between $50 \mu\text{m}$ and $100 \mu\text{m}$ will reduce the material budget of the CMOS pixel module by a factor of 3 compared to the traditional pixel modules. The thinner depletion layer results in a smaller cluster size, reducing data size and bandwidth requirements correspondingly. There is also the potential of reduced pixel size in the CMOS sensors, improving the granularity of the ITk Pixel detector. Designs with $25 \times 25 \mu\text{m}^2$ can be achievable. In recent years, the CMOS sensors became available for the possibility to have radiation-hard pixels equipped with sufficiently complex circuitry to meet the rate and timing requirements of the ITk Pixel volume [176]. If the CMOS technology is ready to produce pixel sensors with radiation hardness of up to $1.6 \times 10^{16} \text{ n}_{\text{eq}}/\text{cm}^2$ by the HL-LHC half-life, the CMOS sensors could become the most promising candidates for the replacement of the innermost ITk layers where the b - and τ -taggings would directly benefit from these sensors.

Another important advantage of the CMOS sensor is that the sensor and the readout electronics can be accommodated together in the same silicon bulk. This helps to achieve a monolithic design for the CMOS pixel module with its sensor and electronics

being one entity, in contrast to the hybrid design of the traditional module in which the sensor and the electronics are in different dies and connected via small metallic bonds. The CMOS monolithic devices have been successfully developed for several HEP experiments (e.g the ALICE ITS [177]). The CMOS monolithic pixel module has a simpler production process than the hybrid ones since only one sensor is needed instead of sensor plus readout chip. This simplification allows for a quick supply with a quick reaction time in case of problems with the production. Furthermore, as there is no need of hybridization processes including bump-bonding and flip-chipping, less material is needed and thus leading to much lower detector cost (by a factor of 2.5-3 compared to the hybrid detector [175]) as well as reduction of the multiple scattering effect which causes the spatial resolution deterioration.

In order for the existing hybrid pixel modules to be easily replaced, the CMOS pixel modules would be used as a drop-in replacement. This means that the CMOS modules must be compatible with the electrical, mechanical, and cooling environment of the ITk Pixel detector.

In the following, the simulation of the ITk Pixel detector with the CMOS sensors used in the innermost barrel layers (L0 and L1) and the innermost end-cap ring layers (R0, R0.5 and R1) is described. The detector layout used for the simulation is the same as the layout 23-00-03 described in Section 6.2.1. However, the innermost layers are modified to implement the CMOS sensors with a new geometry. This is referred to as CMOS layout. Based on what has been discussed above, the CMOS sensor thickness is chosen to be 50 μm . With this thickness, the most probable value of charge released by the Minimum Ionising Particle¹ (MIP) will be about 4000 electrons. In addition, the CMOS sensor pixel size is chosen as $25 \times 25 \mu\text{m}^2$. This pixel size is already feasible with the CMOS sensor design. It will be difficult to achieve a smaller pixel size with the present services scheme of the ITk. However, one still stays open for possible future developments. The detector simulation with this CMOS layout is performed using GEANT 4 [140] and a sample of 250000 single muons with $p_T = 100 \text{ GeV}$. The detector simulation is then followed by a digitization of simulated energy deposits into the actual detector read-out data format. At this step, the front-end electronics in-time threshold is set to 600 electrons and noise is set to 50 electrons. The same charge-to-ToT conversion as for the ITk layout (layout 23-00-03) is used. Following the digitization step, the digitized data is then used for event reconstruction. This step begins with the formation of clusters from individual channels with a hit for the Strip and Pixel Detectors respectively. The cluster position is determined using an algorithm which only uses the information that a pixel has a hit, this is known as the *Digital Clustering* algorithm. Tracks are then reconstructed based on the same approach used for the current ATLAS Inner Detector during Run 2 (see Section 3.3.1) but tuned for the ITk geometry with the first optimization for 200 pile-up. Besides, the same simulation chain is also performed for the ITk layout and then comparisons between the simulation results of the new CMOS layout and the ITk layout are done in order to

¹The Minimum Ionising Particle is a particle which has an energy loss corresponding to the minimum of the Bethe-Bloch equation when traversing through the sensor bulk.

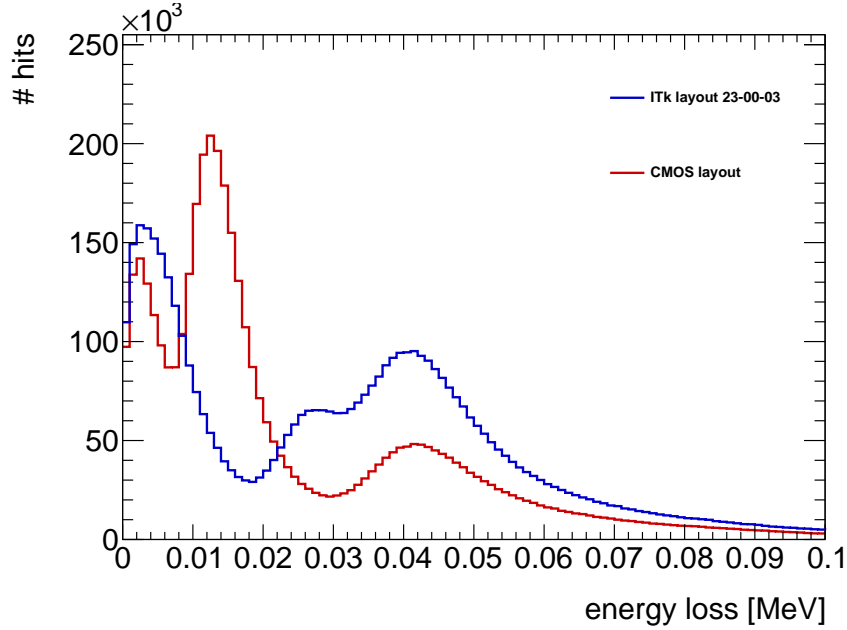


Figure 6.4: Muon energy loss distribution for the CMOS layout (in red) and for the ITk layout 23-00-03 (in blue).

validate the use of the CMOS sensors. For the event reconstruction in the ITk layout, not only the Digital Clustering but also the *Analogue Clustering* algorithm is used to determine the cluster position. This algorithm makes use of the analogue information capabilities of the readout chip to further refine the precision of the cluster position interpolating the charge measurement of the first and last pixel hit in both directions.

Figure 6.4 shows the distributions of the energy loss of each muon crossing any sensor in the pixel detector for the CMOS layout and the ITk layout. The three peaks observed in the distribution of the ITk layout represent the cases when the muons cross the sensors with different angles and the last two peaks correspond to when the muons traverse through the full sensor thicknesses of $100\ \mu\text{m}$ in L1 and R1 (the middle peak) and $150\ \mu\text{m}$ in the other barrel and end-cap ring layers (the last peak). There are also three peaks observed in the distribution of the CMOS layout. It can be seen from this CMOS distribution the absence of the peak corresponding to the thickness of $100\ \mu\text{m}$. Instead, there is a peak at a lower energy loss value, implying the sensor thickness reduced to $50\ \mu\text{m}$ in L1 and R1. In addition, the number of hits of the peak corresponding to the thickness of $150\ \mu\text{m}$ in the CMOS distribution is smaller than the one in the ITk distribution, reflecting the replacement of the $150\ \mu\text{m}$ thick sensors by the $50\ \mu\text{m}$ thick CMOS sensors in L0, R0 and R0.5. The comparisons which have been described reflect the use of CMOS sensors in the innermost ITk layers and thus validate the detector simulation step.

Figures 6.5, 6.6 and 6.7 demonstrate the distributions of the cluster ToT, the trans-

6 ATLAS during the High Luminosity LHC – 6.3 CMOS sensor for ITk replacement in second-half of HL-LHC

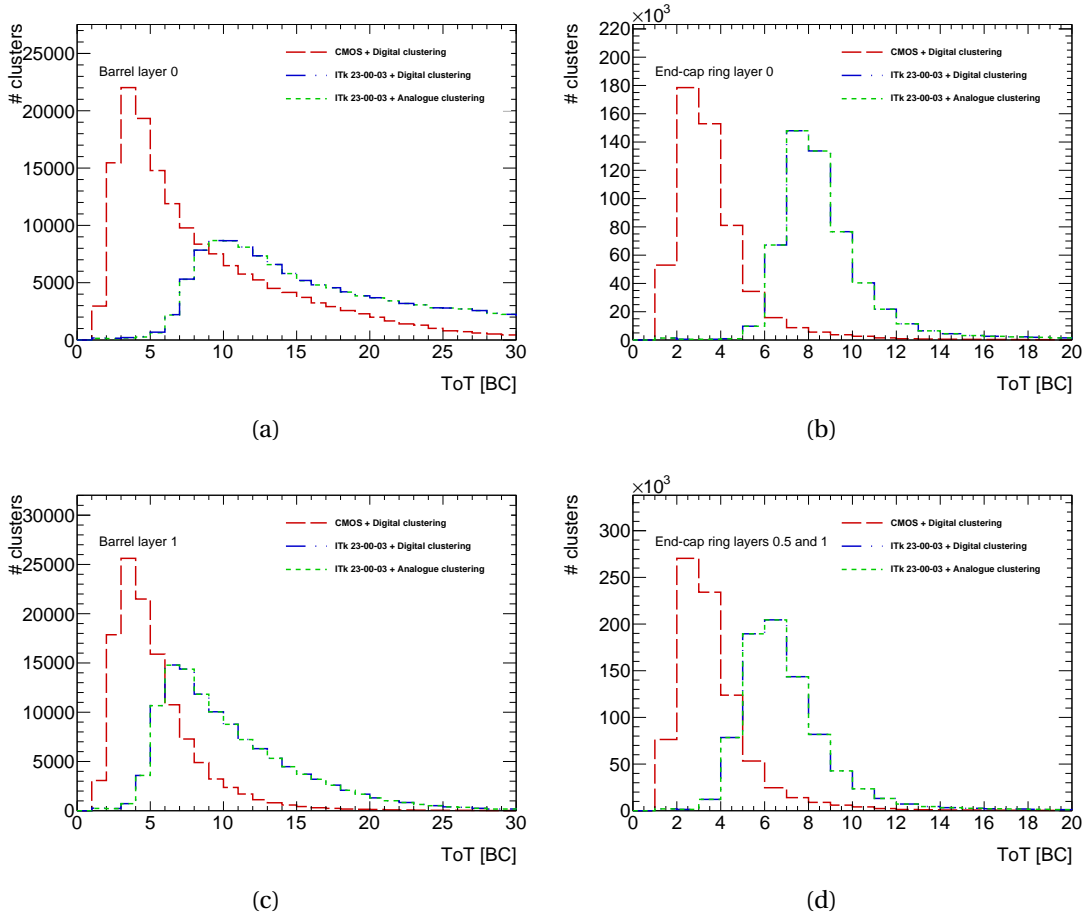


Figure 6.5: ToT distributions after digitization and clusterization using CMOS layout with Digital Clustering (in red) or ITk layout with Digital Clustering (in blue) or ITk layout with Analogue Clustering (in green) in (6.5a) L0, (6.5b) R0, (6.5c) L1, (6.5d) R0.5 and R1.

verse cluster width and the cluster z -width, respectively, in the innermost ITk layers, obtained after the digitization and clusterization steps using the CMOS layout with Digital Clustering, or the ITk layout with Digital Clustering and Analogue Clustering. In Figure 6.5, it can be seen that the cluster ToT has decreased in all the layers when using the CMOS sensors with the smaller thickness. The same situation can also be observed for the transverse width of clusters in L0 (Figure 6.6a), while in the end-cap ring layers (Figures 6.6b and 6.6c), the transverse cluster width is quite similar between the CMOS and the ITk layout because the incidence is normal and there is no charge sharing due to the angle. Regarding the cluster width in z , there is also a similarity between the CMOS and the ITk layout in R0, R0.5 and R1 (Figures 6.7b and 6.7d). In the barrel layers (Figures 6.7a and 6.7c), the z -width is an interplay between the thinner

6 ATLAS during the High Luminosity LHC – 6.3 CMOS sensor for ITk replacement in second-half of HL-LHC

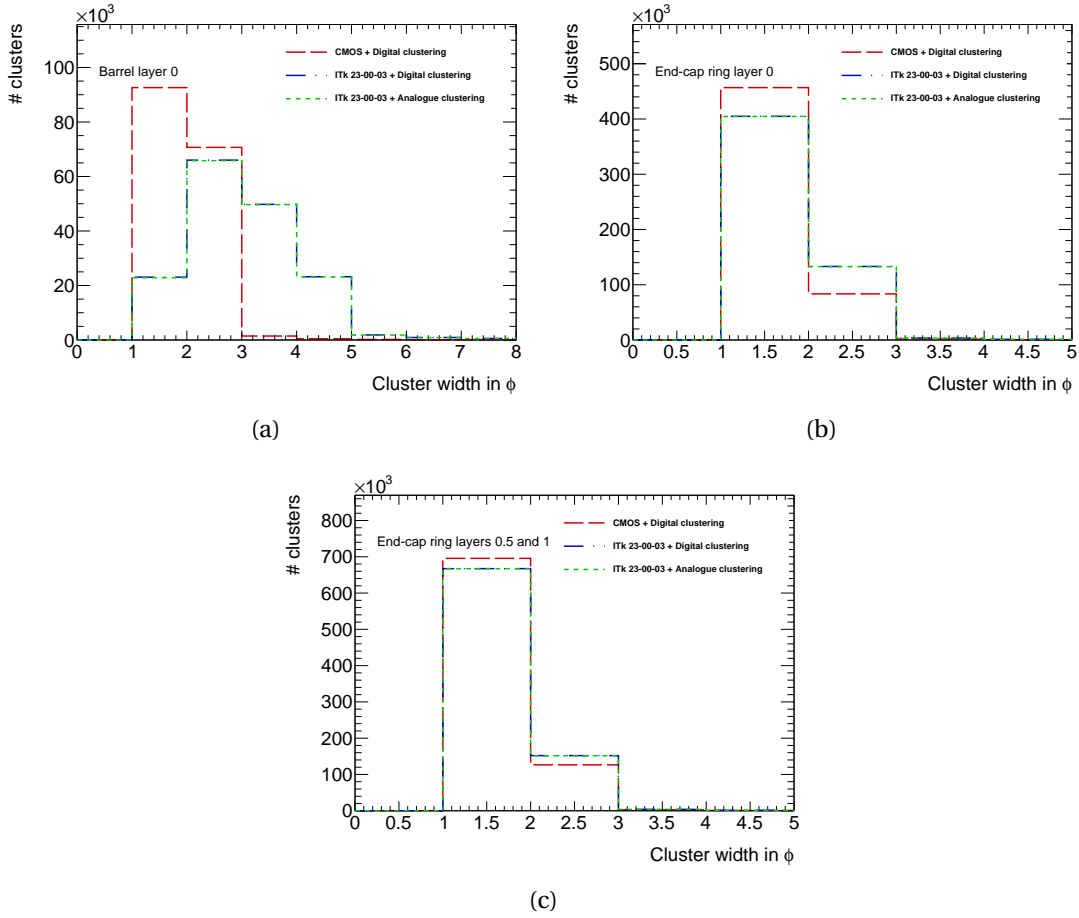


Figure 6.6: Cluster transverse width distributions after digitization and clusterization using CMOS layout with Digital Clustering (in red) or ITk layout with Digital Clustering (in blue) or ITk layout with Analogue Clustering (in green) in (6.6a) L0, (6.6b) R0, (6.6c) R0.5 and R1.

sensor thickness which causes shorter cluster and the smaller pixel size which favours larger cluster. One can also observe the smaller z -width of clusters in L1 compared to those in L0. This is because incidence angles are in average smaller in L1, leading to shorter clusters.

Figure 6.8 represents the distributions of the reconstructed track p_T , η , ϕ and transverse parameter d_0 obtained using the CMOS layout with Digital Clustering, or the ITk layout with Digital Clustering and Analogue Clustering. While there are no differences in the reconstructed track p_T , η and ϕ between these configurations, the advantage of CMOS sensors can be seen from the reconstructed track d_0 distribution (Figure 6.8d). The CMOS + Digital Clustering configuration reconstructs the transverse impact parameter with a similar precision as the reconstruction of the ITk + Analogue Clustering

6 ATLAS during the High Luminosity LHC – 6.3 CMOS sensor for ITk replacement in second-half of HL-LHC

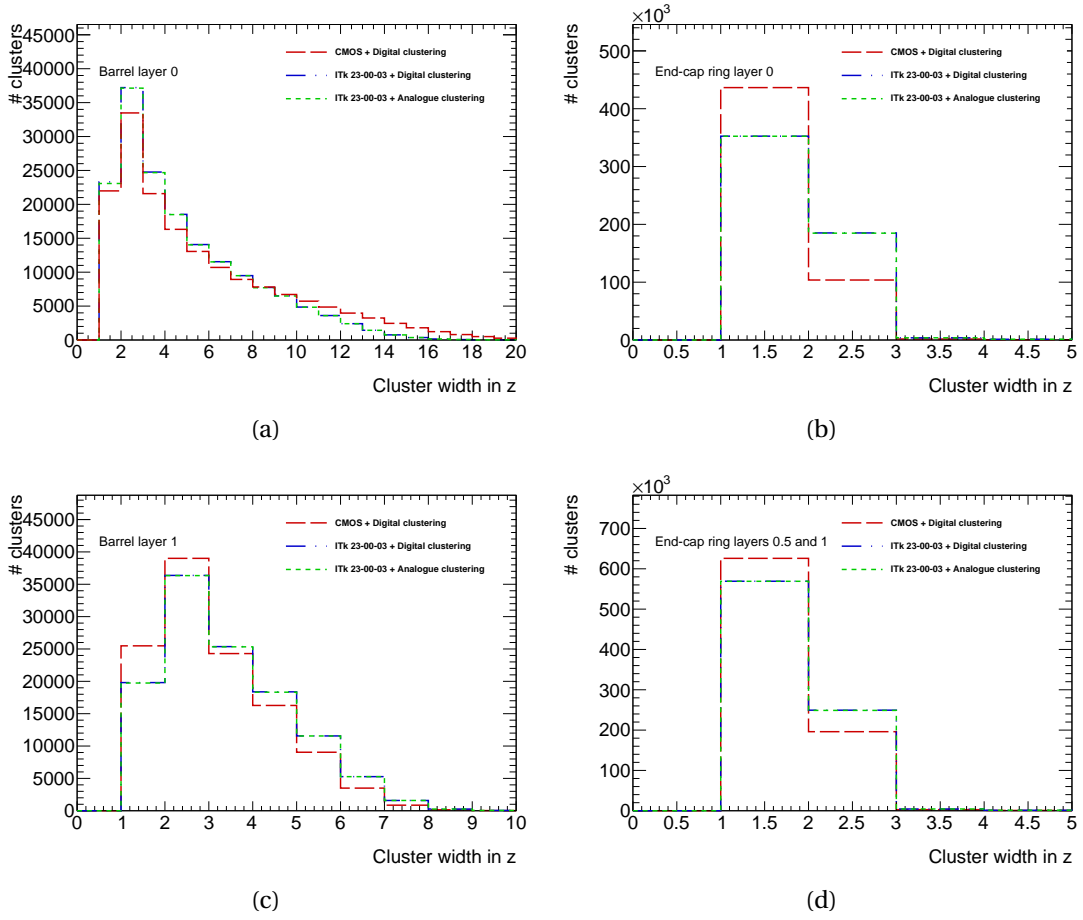


Figure 6.7: Cluster z -width distributions after digitization and clusterization using CMOS layout with Digital Clustering (in red) or ITk layout with Digital Clustering (in blue) or ITk layout with Analogue Clustering (in green) in (6.7a) L0, (6.7b) R0, (6.7c) L1, (6.7d) R0.5 and R1.

configuration. By comparing the reconstructions between the digital and analogue clusterization in the ITk layout, one can have an idea of what would be gained by applying the Analogue Clustering algorithm to the CMOS data.

The resolutions of the track transverse and longitudinal impact parameters as functions of η , obtained from the simulations of the three aforementioned configurations: CMOS + Digital Clustering, ITk + Digital Clustering and ITk + Analogue Clustering with the $p_T = 100$ GeV single muon sample, are shown in Figures 6.9a and 6.9b, respectively. As seen from these figures, the track impact parameter resolution achieved with the CMOS layout and Digital Clustering is quite comparable to the resolution achieved with the ITk layout and Analogue Clustering, and is better than the resolution of the ITk layout with Digital Clustering used. Particularly in the forward regions, where the

6 ATLAS during the High Luminosity LHC – 6.3 CMOS sensor for ITk replacement in second-half of HL-LHC

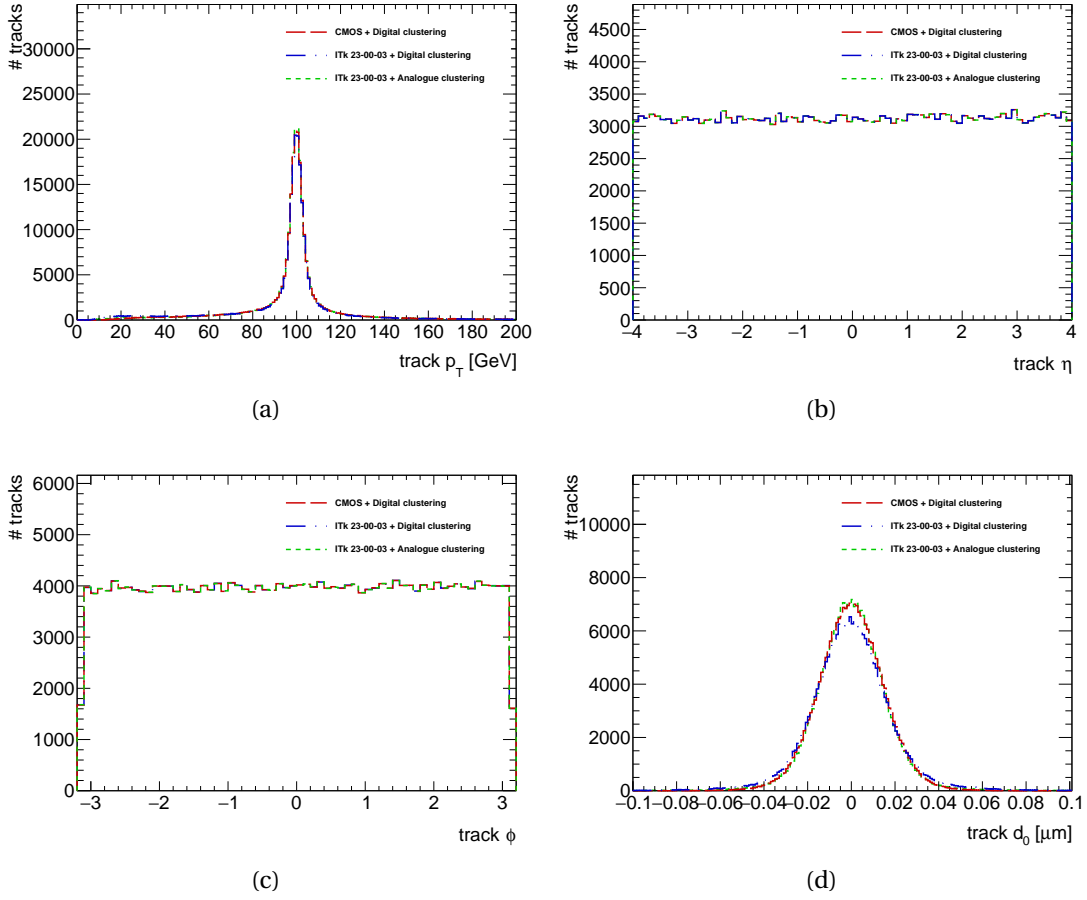


Figure 6.8: Distributions of the reconstructed track (6.8a) p_T , (6.8b) η , (6.8c) ϕ and (6.8d) transverse parameter d_0 , obtained using CMOS + Digital Clustering (in red), or ITk + Digital Clustering (in blue), or ITk + Analogue Clustering (in green).

true momentum of tracks is much higher than 100 GeV and thus less affected by the multiple scattering effect, the CMOS layout with the reduced sensor thickness and pixel size provides a noticeable improvement in the resolution. Two other samples of single muons with $p_T = 10$ GeV and $p_T = 1$ GeV are also used for the simulations of the CMOS and the ITk layout. The track impact parameter resolutions as functions of η obtained using the $p_T = 10$ GeV sample are shown in Figures 6.9c and 6.9d, while those obtained using the $p_T = 1$ GeV sample are shown in Figures 6.9e and 6.9f. At these lower p_T values, the resolution becomes worse due to the multiple scattering effect and the improvement in the resolution of the CMOS layout becomes less significant. This implies that the use of the CMOS sensors with smaller thickness and pixel size would be benefit for the case of high p_T physics.

6 ATLAS during the High Luminosity LHC – 6.3 CMOS sensor for ITk replacement in second-half of HL-LHC

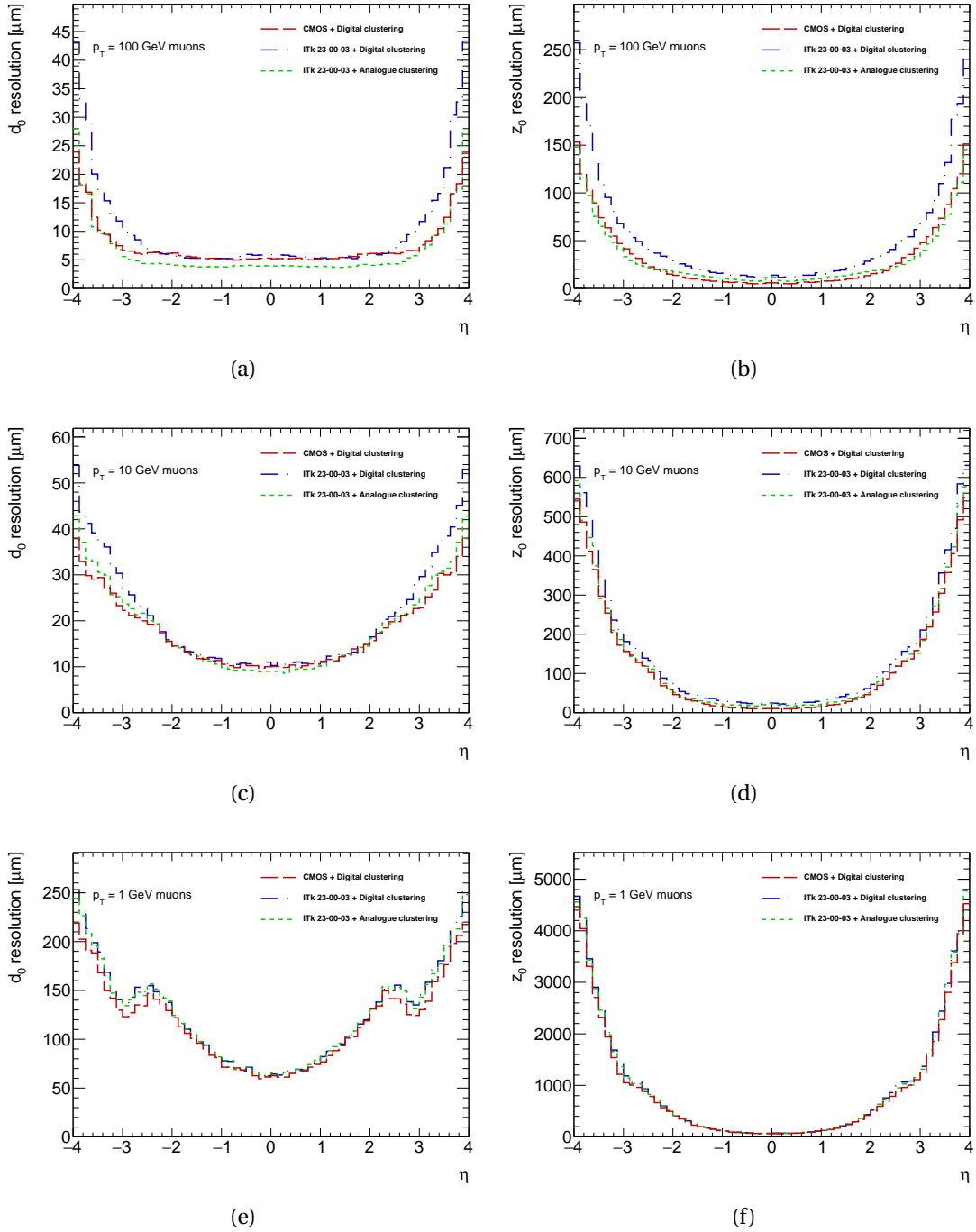


Figure 6.9: The transverse impact parameter resolution σ_{d_0} (left plots) and the longitudinal impact parameter resolution σ_{z_0} (right plots) as functions of η for the three configurations: CMOS + Digital Clustering (in red), ITk + Digital Clustering (in blue) and ITk + Analogue Clustering (in green). From top to bottom, the plots are shown for the simulations using the $p_T = 100$ GeV, $p_T = 10$ GeV and $p_T = 1$ GeV muon samples.

This preliminary study has demonstrated the advantage of the thinner and coarser innermost layers using the CMOS sensors for $p_T = 100$ GeV muons. The next step would be to quantify this advantage as a function of p_T . This could be achieved by looking to not only the impact parameters, but also the single hit resolution and efficiency for muons of different p_T . In the future, detailed simulation of heavy flavour jets will estimate the gain in the b -tagging performance, especially at high p_T .

7 Search for electroweak production of charginos and neutralinos in final states with one lepton, jets and missing transverse momentum

As mentioned in Chapter 1, The Standard Model (SM) has proved to be a very successful theory, managing to describe most of the properties of elementary particles and their interactions. It, however, leaves many open questions: such as the hierarchy problem, unification of strong and electroweak interactions, and the presence of cold dark matter in the universe. The discovery in 2012 of the SM Higgs boson [20, 21], by the ATLAS and CMS collaborations, confirmed the mechanism of the electroweak symmetry breaking and highlighted the hierarchy problem [178]. Supersymmetry, a theoretical extension of the SM, directly addresses the hierarchy problem by postulating the existence of a new fermion (boson) supersymmetric partner for each boson (fermion) in the SM. As no SUSY particle has been observed yet, SUSY has to be a broken symmetry, with the supersymmetric particles masses different from their SM partner ones. In SUSY models where the R-parity is conserved [179], the SUSY particles are produced in pairs. Furthermore, the lightest supersymmetric particle (LSP) is stable and weakly interacting, thus constituting a viable dark-matter candidate.

In SUSY scenarios, the partners of the SM Higgs boson (h) and the gauge bosons, known as the higgsinos, winos (partners of the $SU(2)_L$ gauge fields), and bino (partner of the $U(1)$ gauge field) are collectively referred to as electroweakinos. Charginos $\tilde{\chi}_i^\pm$ ($i = 1, 2$) and neutralinos $\tilde{\chi}_j^0$ ($j = 1, 2, 3, 4$) are the electroweakino mass eigenstates which are linear superpositions of higgsinos, winos, and bino. For the models considered in this thesis, the lightest neutralino ($\tilde{\chi}_1^0$) is a bino-like LSP. The lightest chargino ($\tilde{\chi}_1^\pm$) and next-to-lightest neutralino ($\tilde{\chi}_2^0$) are wino-like and nearly mass degenerate.

Naturalness considerations [50, 51] suggest that the lightest of the electroweakinos have masses near the electroweak scale. In scenarios where the strongly produced SUSY particles are heavier than a few TeV, the direct production of electroweakinos may be the dominant SUSY production mechanism at the LHC. Scenarios with light electroweakinos also provide a possible explanation for the discrepancy between the muon anomalous magnetic moment $g - 2$ measurement and the SM predictions [180, 181].

7 Search for electroweak production of charginos and neutralinos in final states with one lepton, jets and missing transverse momentum

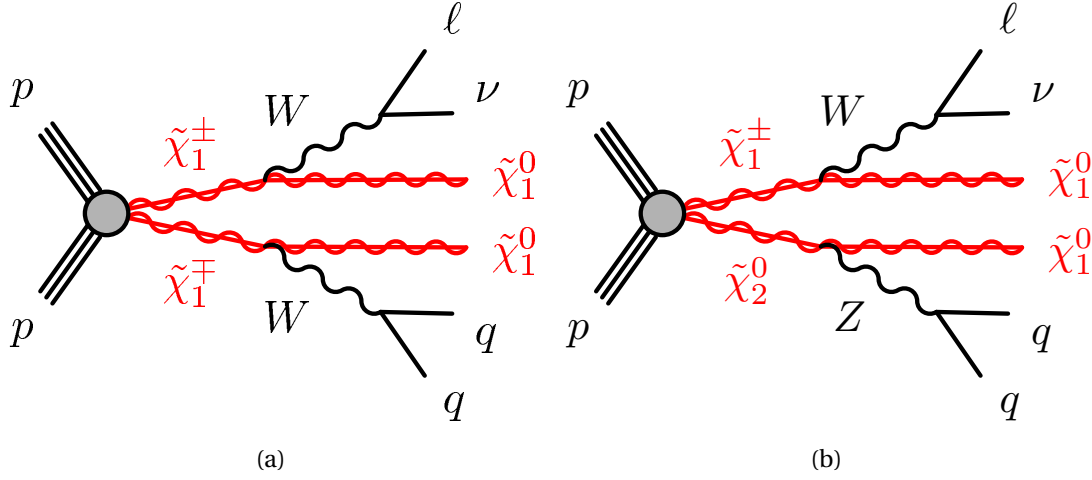


Figure 7.1: Feynman diagram for electroweakino (7.1a) $\tilde{\chi}_1^\pm \tilde{\chi}_1^\mp$ and (7.1b) $\tilde{\chi}_1^\pm \tilde{\chi}_2^0$ pair production. One $\tilde{\chi}_1^\pm$ subsequently decays to a $\tilde{\chi}_1^0$ and a W boson which further decays leptonically. The other $\tilde{\chi}_1^\pm$ or $\tilde{\chi}_2^0$ subsequently decays to a $\tilde{\chi}_1^0$ and a W or Z boson which further decays hadronically.

This chapter presents an analysis targeting two dedicated SUSY searches for electroweak production of charginos and neutralinos:

- **C1C1-WW:** A search for direct production of a chargino pair ($\tilde{\chi}_1^\pm \tilde{\chi}_1^\mp$) where each $\tilde{\chi}_1^\pm$ subsequently decays into an W boson and a $\tilde{\chi}_1^0$ ($\tilde{\chi}_1^\pm \rightarrow W \tilde{\chi}_1^0$). This search focuses on a scenario where one of the W bosons decays hadronically and the other decays leptonically through a light lepton (electron or muon) and a neutrino (Figure 7.1a). The final state is then characterized by the presence of one lepton, two or three jets, and missing transverse momentum originating from the neutrino and the LSPs.
- **C1N2-WZ:** A search for direct production of a chargino-neutralino pair ($\tilde{\chi}_1^\pm \tilde{\chi}_2^0$), where the $\tilde{\chi}_2^0$ decays into a Z boson and a $\tilde{\chi}_1^0$, and the $\tilde{\chi}_1^\pm$ into a W boson and a $\tilde{\chi}_1^0$. This search targets a scenario where the Z boson decays hadronically and the W boson decays leptonically through a light lepton (electron or muon) and a neutrino (Figure 7.1b). The final state is expected to present one lepton, two or three jets, and missing transverse momentum originating from the neutrino and the LSPs.

The signal models considered in the two searches above are in the context of the simplified SUSY model in which the branching ratios of $\tilde{\chi}_1^\pm \rightarrow W \tilde{\chi}_1^0$ and $\tilde{\chi}_2^0 \rightarrow Z \tilde{\chi}_1^0$ are assumed to be 100%, while the branching ratios of the W or Z boson decays are taken to be as the SM ones. The results will be interpreted in a two-dimensional space of two parameters, the first being the mass $m_{\tilde{\chi}_1^\pm/\tilde{\chi}_2^0}$ of the $\tilde{\chi}_1^\pm$ and $\tilde{\chi}_2^0$ (which are assumed to

be equal), and the second being the mass $m_{\tilde{\chi}_1^0}$ of the $\tilde{\chi}_1^0$. The C1C1-WW and C1N2-WZ searches via one lepton final state channel are performed for the first time at ATLAS and target an integrated luminosity of 139 fb^{-1} , corresponding to the full Run 2 data collected at the ATLAS detector. It should be noted that the analysis is not approved at the time of writing and therefore the analysis results presented in this chapter are obtained with the observed data still being blind in signal regions of the analysis.

7.1 Data and simulated samples

7.1.1 Dataset

The data used in this analysis were produced in proton-proton collisions with a center-of-mass energy of 13 TeV and collected by the ATLAS detector in the full Run 2 period between 2015 and 2018. Three different periods can be distinguished, with different pileup conditions: in 2015-2016, the average number of pileup interactions was $\langle\mu\rangle = 20$, increasing to $\langle\mu\rangle = 38$ in 2017 and to $\langle\mu\rangle = 37$ in 2018. After applying beam, detector and data-quality criteria [182], the integrated luminosity over the full period is 139 fb^{-1} , with an uncertainty of 1.7% [78].

7.1.2 Simulated samples

Monte Carlo (MC) simulated samples are used to model the SM backgrounds and evaluate signal selection efficiency and yields. All simulated samples were produced using the full ATLAS simulation infrastructure and GEANT 4, or a faster simulation based on a parameterisation of the calorimeter response and GEANT 4 for the other detector systems. All simulated events were generated with a varying number of inelastic pp interactions overlaid on the hard-scattering event to model the multiple proton-proton interactions in the same and nearby bunch crossings. The pile-up events are generated with PYTHIA 8.186 [137] using the NNPDF2.3LO set of PDFs [183] and the A3 tune [184]. The simulated events were reconstructed with the same algorithms as those used for data. Three separate campaigns, denoted as MC16a for 2015-2016, MC16d for 2017 and MC16e for 2018 have been produced, in order to account for the different pileup, trigger, and detector conditions.

Signal samples

Signal samples for different mass points, $(m_{\tilde{\chi}_1^\pm/\tilde{\chi}_2^0}, m_{\tilde{\chi}_1^0})$, were generated in simplified models according to the scenarios represented in Figure 7.1. They were generated using MADGRAPH5_AMC@NLO v2.6.2 [185] and PYTHIA 8.230 with the A14 [186] set of tuned parameters for the modelling of the parton showering (PS), hadronisation and underlying event. The matrix element (ME) calculation is performed at tree level and includes the emission of up to two additional partons. The ME-PS matching is done using the CKKW-L prescription, with a matching scale set to one quarter of the

chargino and next-to-lightest neutralino mass. The NNPDF2.3LO [183] PDF set was used.

Signal cross-sections are calculated at next-to-leading-order (NLO) accuracy in the strong coupling constant, adding the resummation of soft gluon emission at next-to-leading-logarithm accuracy (NLO+NLL) [187, 188, 189, 190]. The nominal cross-section and its uncertainty are taken as the midpoint and half-width of an envelope of cross-section predictions using different PDF sets and factorisation and renormalisation scales [191].

The signal samples presenting a mass splitting $\Delta m(\tilde{\chi}_1^\pm/\tilde{\chi}_2^0, \tilde{\chi}_1^0) = m_{\tilde{\chi}_1^\pm/\tilde{\chi}_2^0} - m_{\tilde{\chi}_1^0} \geq 300$ GeV were produced with the full ATLAS detector simulation based on GEANT 4 in order to include the full jet substructure modelling information. This allows a further dedicated study on the boosted jets (i.e. reconstruct large-R jet) for large mass splitting signals. The signal samples with $\Delta m(\tilde{\chi}_1^\pm/\tilde{\chi}_2^0, \tilde{\chi}_1^0) < 300$ GeV were produced using the fast ATLAS simulation, allowing a 10-100 times faster processing than the full ATLAS simulation.

As MadSpin was not applied, the spin information is missing in the current signal samples used in the analysis. Therefore, an extra weight has been computed and applied to the signal samples in order to account for the polarization effect.

SM background samples

All SM backgrounds relevant to this analysis are simulated. Depending on the process, different matrix element generators, cross-section calculation orders, parton distribution functions (PDFs), parton shower and underlying event generators are used. A summary of all the SM background processes together with their dedicated generation details is given in Table 7.1.

Process	Generator	Parton shower and hadronisation	Tune	PDF	Cross-section
$t\bar{t}$	POWHEG-BOX v2 [133]	PYTHIA 8.230	A14	NNPDF2.3LO	NNLO+NNLL [192]
Single top	POWHEG-BOX v2	PYTHIA 8.230	A14	NNPDF2.3LO	NLO+NNLL [193]
W/Z+jets	SHERPA 2.2.1 [194]	SHERPA 2.2.1	SHERPA standard	NNPDF3.0NNLO	NNLO [195]
Diboson	SHERPA 2.2.1 & 2.2.2	SHERPA 2.2.1 & 2.2.2	SHERPA standard	NNPDF3.0NNLO	NLO
Multiboson	SHERPA 2.2.1	SHERPA 2.2.1	SHERPA standard	NNPDF3.0NNLO	NLO
$t\bar{t}V$	MADGRAPH5_AMC@NLO	PYTHIA 8.210	A14	NNPDF2.3LO	NLO
$t\bar{t}H$	POWHEG-BOX v2	PYTHIA 8.230	AZNLO [196]	CTEQ6L1 [197]	NLO
VH	POWHEG-BOX v2	PYTHIA 8.212	A14	NNPDF2.3LO	NLO

Table 7.1: The SM background MC simulation samples used in this analysis. The generators, the parton showers, tunes used for the underlying event, PDF sets and order in α_s of cross-section calculations used for yield normalisation are shown.

For all samples showered with PYTHIA, the EvtGen v1.2.0 [198] program was used to simulate the properties of the bottom- and charm-hadron decays. All the samples were produced using the full ATLAS detector simulation.

7.2 Reconstructed objects and triggers

7.2.1 Object definition

The physics objects used for the analysis are based on the definitions from the SUSY working group common package SUSYTools corresponding to AnalysisBase 21.2.148 release. The detailed description of the object reconstruction strategy in ATLAS is given in Section 3.3. The primary vertex (PV) of the event is reconstructed as the vertex with the largest quadratic sum of p_T of associated tracks and is required to have at least two such tracks with $p_T > 500$ MeV.

Electrons and muons are classified into *baseline* and *signal* objects. Baseline objects have a smaller purity but a higher acceptance and are used in the computation of the missing transverse momentum as well as in resolving possible reconstruction ambiguities. Signal objects are a subset of the baseline objects with stricter requirements on the isolation and identification criteria. Signal objects are used as the physical objects within this analysis.

Electron candidates are reconstructed from energy deposits in the electromagnetic calorimeter that are matched to charged-particle tracks in the Inner Detector (IN-DET) [199]. Baseline electrons are required to have a minimum p_T of 7 GeV as well as $|\eta| < 2.47$ and pass the LooseAndBLayerLLH [199] identification criterion. Baseline electron tracks are further required to fulfil $|z_0 \sin \theta| < 0.5$ mm, where z_0 is the longitudinal impact parameter relative to the primary vertex (PV). In order to guarantee a low misidentification rate, signal electrons are required to pass the tighter TightLLH identification working point. The significance of the transverse impact parameter d_0 of signal electrons' tracks needs to pass $|d_0/\sigma(d_0)| < 5$. Signal electrons with $p_T < 75$ GeV need to satisfy the FCLoose isolation working point, while those with larger p_T are required to pass the FCHighPtCaloOnly isolation working point, as described in Ref. [199].

Muon candidates are reconstructed from matching tracks in the INDET and muon spectrometer, refined through a global fit which uses the hits from both sub-detectors [200]. Baseline muons are required to have a minimum p_T of 6 GeV, $|\eta| < 2.5$ and pass the medium [200] identification requirement. Baseline muon tracks are further required to fulfil $|z_0 \sin \theta| < 0.5$ mm. The tracks of signal muons additionally need to satisfy $|d_0/\sigma(d_0)| < 3$. Signal muons furthermore need to be within $|\eta| < 2.5$. Signal muons with $p_T < 75$ GeV need to satisfy the Loose_VarRad isolation working point, while those with larger p_T need to pass the TightTrackOnly_VarRad isolation working point [200]. Finally, a bad muon veto is applied, rejecting events where $\frac{\sigma(q/p)}{|q/p|} > 0.4$.

Beside baseline and signal, lepton candidates in this analysis are also classified into *combi-baseline* objects. Combi-baseline leptons are selected using the same selection criteria as baseline leptons, but with looser requirements on p_T and η . Combi-baseline electrons are required to have $p_T > 4.5$ GeV, while the combi-baseline muons are required to pass $p_T > 3$ GeV and $|\eta| < 2.7$. The combi-baseline leptons are used to

keep the one lepton analysis orthogonal to other analyses in the combination study.

Jet candidates are reconstructed using the anti- k_t Particle Flow (pFlow) algorithm, described in Section 3.3.5, with a radius parameter of 0.4. Jets with $p_T < 120$ GeV and $|\eta| < 2.8$ have to be matched to the primary vertex through the jet vertex tagger (JVT) [201] using the medium working point, suppressing jets from pile-up. Additionally, jets are calibrated following the procedure mentioned in Section 3.3.5. Furthermore, jets are required to have a minimum p_T of 30 GeV and $|\eta| < 2.8$. In order to identify and reconstruct jets containing a b -hadron (b -jets), an algorithm based on Deep Neural Network, named DL1r, is deployed at a pseudo-continuous 77% efficiency working point.

The analysis also uses large-R jets in order to better exploit the high p_T phase spaces, looking at the substructure of the collimated objects. These large-R jets are reconstructed using the anti- k_t clustering algorithm with a large radius parameter of $R = 1.0$. Moreover, in order to reduce the pile-up inside the large-R jet, a trimming algorithm [202] has been applied to the object with a $R_{\text{sub}} = 0.2$ and a $f_{\text{cut}} = 0.05$ parameters. The large-R jets with $p_T > 200$ GeV and with $|\eta| < 2.0$ are used for the analysis. In order to identify the large-R jet originating from a boosted W boson (W -tagged) or a boosted Z boson (Z -tagged), two boson taggers, W -tagger and Z -tagger [203], are used for the analysis. These taggers are based on simple cut-based tagging techniques. They are optimized with respect to signal jets that were matched to a truth W or Z boson and that have a truth groomed jet mass of [50, 100] GeV for W -tagging or [60, 110] GeV for Z -tagging. The taggers are optimized using the signal sample that is generated with $W' \rightarrow WZ \rightarrow qq\bar{q}\bar{q}$ process described in the Heavy Vector Triplets (HVT) framework [204]. This sample is generated with a resonant mass of 2 TeV and the cross-section is reweighted to produce a relatively flat distribution of jets with $200 < p_T < 3000$ GeV. The background sample used for the tagger optimization contains QCD multijet events. Both the W and Z taggers use a window cut on the jet mass as well as one-sided cuts on the energy correlation function ratio¹ $D_2^{\beta=1}$ [205] and the number of tracks ghost-associated to the original ungroomed jet n_{track} . All three cuts are optimized simultaneously in bins of p_T such that the signal efficiency is of 50%. The same smooth functions as defined in [206] are fit to the optimal cut values in p_T bins to produce a smooth tagger with a fixed signal efficiency of 50%. The window cuts on jet mass for the W and Z taggers at the 50% signal efficiency working point are shown in Figures 7.2a and 7.2b, respectively, while Figure 7.2c illustrates the jet mass window cut for the Higgs boson tagger at the 68% signal efficiency working point [207]. One can observe that, for the same p_T value, the W/Z taggers require the lower mass window cut than the Higgs tagger and thus these taggers are less sensitive

¹ D_2^β is used to identify boosted jets coming from the decay into two charged particles (2-prong decays),

define as: $D_2^\beta = \frac{e_3^\beta}{(e_2^\beta)^3}$, where e_2^β and e_3^β are two- and three-point energy correlation functions,

respectively, which have been shown to be among the most powerful observables for identifying the hadronic decays of boosted W/Z boson.

7 Search for electroweak production of charginos and neutralinos in final states with one lepton, jets and missing transverse momentum – 7.2 Reconstructed objects and triggers

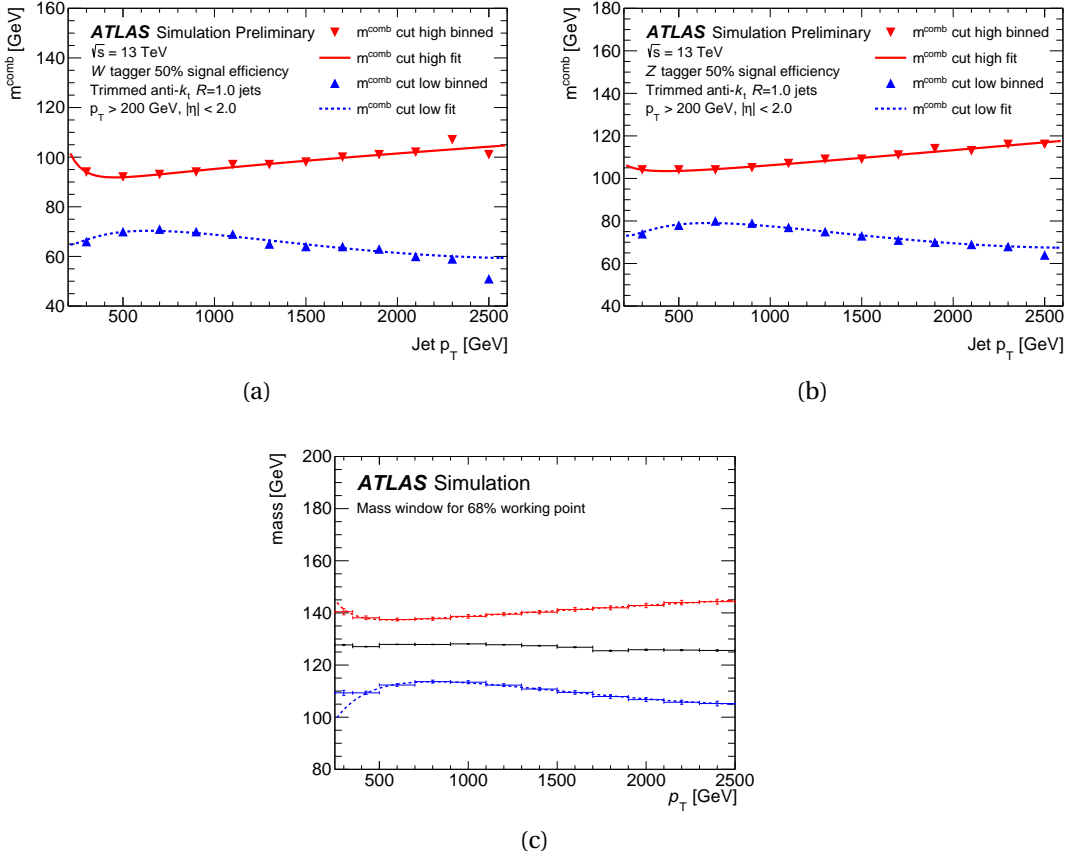


Figure 7.2: The jet mass window cuts for (7.2a) the W -tagger and (7.2b) the Z -tagger at the 50% signal efficiency working point and (7.2c) the Higgs-tagger at the 68% signal efficiency working point.

to the Higgs boson.

The missing transverse momentum is reconstructed by using the set of reconstructed and fully calibrated baseline objects, i.e. electrons, muons, photons and jets. Tracks not associated to reconstructed object (track soft terms, TST) are also included. In this analysis, the tight working point, where the jets with $|\eta| > 2.4$ are required to have $p_T > 30$ GeV, is used for the missing transverse momentum.

7.2.2 Overlap removal

During the reconstruction procedure, it can happen that the same tracks or energy deposits are reconstructed and identified as two separate physics objects. In order to prevent double-counting of objects and reduce ambiguities, a so-called overlap removal (OR) procedure is carried out on the baseline objects. The OR uses $\Delta R = \sqrt{(\Delta\eta)^2 + (\Delta\phi)^2}$ as distance measure and applies the following steps [208]:

1. In case two electrons share the same INDET track, the one with the lower p_T is discarded.
2. Electrons sharing the same INDET track with a muon are rejected.
3. Electrons within a cone of size $\min(0.4, 0.04 + 10\text{GeV}/p_T)$ around a jet are removed.
4. Reject jets within $\Delta R < 0.2$ of a muon or where muons have been matched to the jet through ghost association [209].
5. Muons within a cone, defined in the same way as for electrons, around any remaining jet are removed.

7.2.3 Triggers

The trigger used in the analysis is a logical OR combination of multiple single-electron and single muon-triggers. The event will pass the trigger selection if it passes one of the single lepton triggers combined with an offline requirement for the lepton p_T . The offline requirement ensures that the selected events are in the plateau region of the corresponding trigger. The details of the used single-electron and single-muon triggers with the corresponding offline thresholds are listed in Tables 7.2 and 7.3, respectively.

trigger name	year	HLT cut [GeV]	Offline cut [GeV]
HLT_e24_lhmedium_L1EM20VH	2015	24	25
HLT_e60_lhmedium	2015	60	61
HLT_e120_lhloose	2015	120	121
HLT_e26_lhtight_nod0_ivarloose	2016-2018	26	27
HLT_e60_lhmedium_nod0	2016-2018	60	61
HLT_e140_lhloose_nod0	2016-2018	140	141

Table 7.2: The single-electron triggers which are used in the analysis.

trigger name	year	HLT cut [GeV]	Offline cut [GeV]
HLT_mu20_loose_L1MU15	2015	20	21
HLT_mu26_ivarmedium	2016-2018	26	27.3
HLT_mu50	2015-2018	50	52.5

Table 7.3: The single-muon triggers which are used in the analysis.

7.3 Event selection

After identifying and reconstructing the objects of interest as mentioned above, events are categorized to signal regions based on criteria on discriminating variables. Starting from the definition of this analysis' key variables, the selection procedure is described in detail.

7.3.1 Discriminating variables

In order to be able to distinguish signal events from the SM background processes, it is necessary to use different discriminating kinematic variables. The list of these variables is as follows:

- Number of baseline leptons $N_{\text{lep}}^{\text{base}}$ and number of signal leptons $N_{\text{lep}}^{\text{sig}}$.
- Leading lepton transverse momentum p_{T}^{ℓ} .
- Number of jets N_{jet} with $p_{\text{T}} > 30$ GeV.
- Number of b -jets $N_{b\text{-jet}}$ with $p_{\text{T}} > 30$ GeV.
- Leading jet transverse momentum $p_{\text{T}}^{j_1}$.
- Sub-leading jet transverse momentum $p_{\text{T}}^{j_2}$.
- Missing transverse momentum $E_{\text{T}}^{\text{miss}}$.
- Azimuthal angle $\Delta\phi(\ell, E_{\text{T}}^{\text{miss}})$ between transverse momentum of the leading lepton p_{T}^{ℓ} and the missing transverse momentum $E_{\text{T}}^{\text{miss}}$.
- Invariant mass of the 2 leading jets m_{jj} ,

$$m_{\text{jj}} = \sqrt{2p_{\text{T}}^{j_1} p_{\text{T}}^{j_2} [\cosh(\eta_{j_1} - \eta_{j_2}) - \cos(\phi_{j_1} - \phi_{j_2})]}. \quad (7.1)$$

- Missing transverse energy significance $\sigma_{E_{\text{T}}^{\text{miss}}}$, defined as the log-likelihood ratio. A high $E_{\text{T}}^{\text{miss}}$ significance indicates that the $E_{\text{T}}^{\text{miss}}$ is not well explained by resolution smearing alone and suggests that the event is more likely to contain unseen objects.

$$\sigma_{E_{\text{T}}^{\text{miss}}}^2 = 2 \ln \left[\frac{\max_{\mathbf{p}_{\text{T}}^{\text{inv}} \neq 0} \mathcal{L}(E_{\text{T}}^{\text{miss}} | \mathbf{p}_{\text{T}}^{\text{inv}})}{\max_{\mathbf{p}_{\text{T}}^{\text{inv}} = 0} \mathcal{L}(E_{\text{T}}^{\text{miss}} | \mathbf{p}_{\text{T}}^{\text{inv}})} \right]. \quad (7.2)$$

- Transverse mass m_{T} ,

$$m_{\text{T}} = \sqrt{2p_{\text{T}}^{\ell} E_{\text{T}}^{\text{miss}} [1 - \cos \Delta\phi(\ell, E_{\text{T}}^{\text{miss}})]}. \quad (7.3)$$

7 Search for electroweak production of charginos and neutralinos in final states with one lepton, jets and missing transverse momentum – 7.3 Event selection

- Effective mass m_{eff} ,

$$m_{\text{eff}} = \sum_{\text{leptons}} p_T^\ell + \sum_{\text{jets}} p_T^{\text{jet}} + E_T^{\text{miss}}. \quad (7.4)$$

- Number of large-R jets $N_{\text{large-R jets}}$.
- W -tagger and Z -tagger decisions of the leading large-R jet at 50% signal efficiency working point.
- Leading large-R jet transverse momentum $p_T^{\text{large-R jet}}$.
- Leading large-R jet mass $m_{\text{large-R jet}}$.

7.3.2 Event preselection

The preselection used in this analysis is a logical OR combination of two sets of cuts. The first set is defined as follows:

- Exactly one lepton, i.e $N_{\text{lep}}^{\text{base}} = N_{\text{lep}}^{\text{sig}} = 1$,
- single-lepton triggers fired,
- 1-3 jets with $p_T > 30$ GeV,
- $E_T^{\text{miss}} > 200$ GeV,
- $m_T > 50$ GeV,
- less than three combi-baseline leptons,
- less than two combi-baseline leptons with $p_T > 8$ GeV.

While the second set includes:

- Exactly two leptons, i.e $N_{\text{lep}}^{\text{base}} = N_{\text{lep}}^{\text{sig}} = 2$,
- single-lepton triggers fired,
- 1-3 jets with $p_T > 30$ GeV,
- $E_T^{\text{miss}} > 200$ GeV,
- $m_T > 50$ GeV.

The two-lepton preselection defined here is for a control region used to estimate contribution from sub-processes with at least two leptons in the final state of the diboson background. This will be discussed later in Section 7.4. Distributions of some of the discriminating variables at the preselection level are shown in Figures 7.3 and 7.4. All show a good agreement between MC and data.

7 Search for electroweak production of charginos and neutralinos in final states with one lepton, jets and missing transverse momentum – 7.3 Event selection

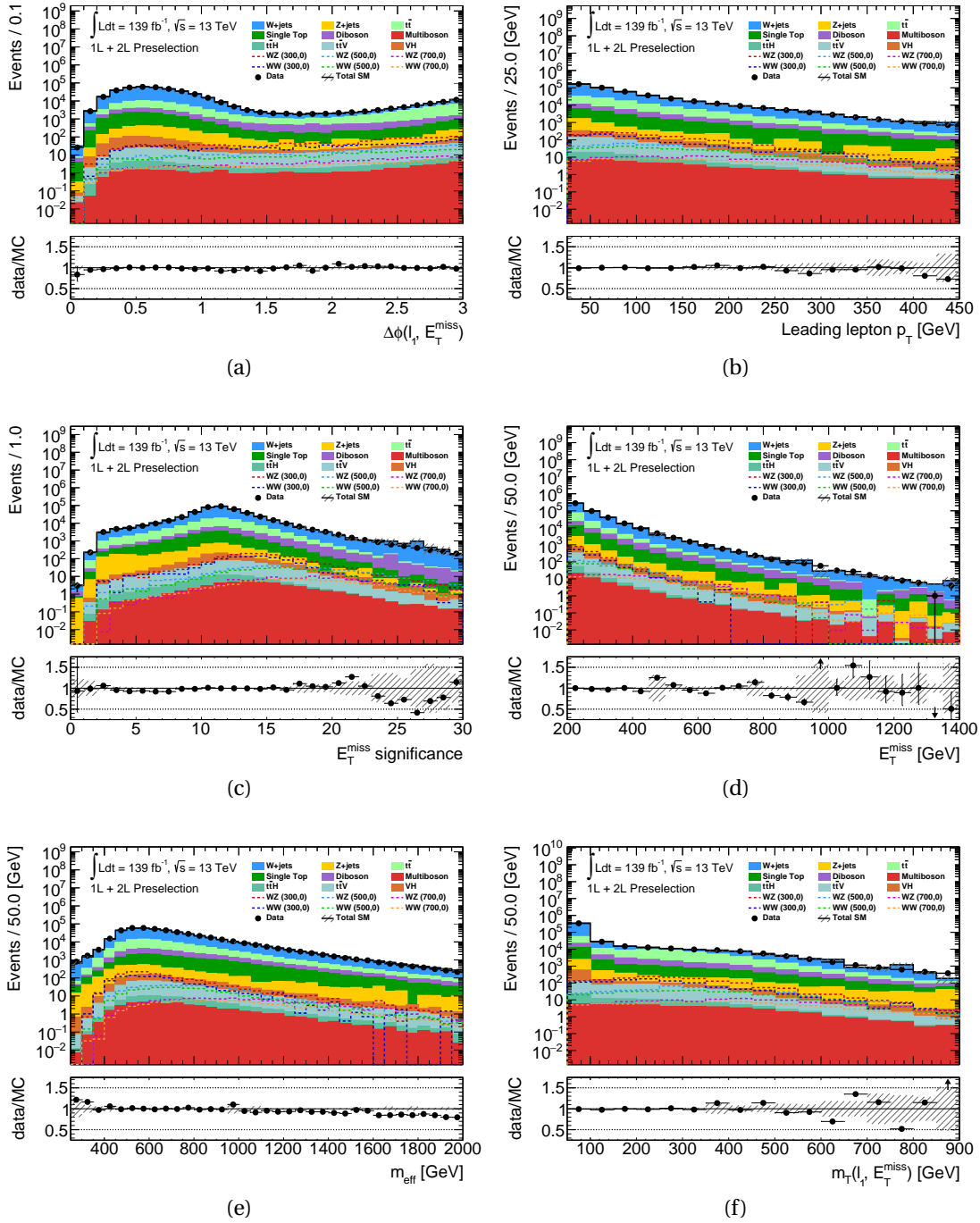


Figure 7.3: Data/MC comparisons for discriminating variables used in the analysis. Only statistical uncertainties are considered in the error band.

7 Search for electroweak production of charginos and neutralinos in final states with one lepton, jets and missing transverse momentum – 7.3 Event selection

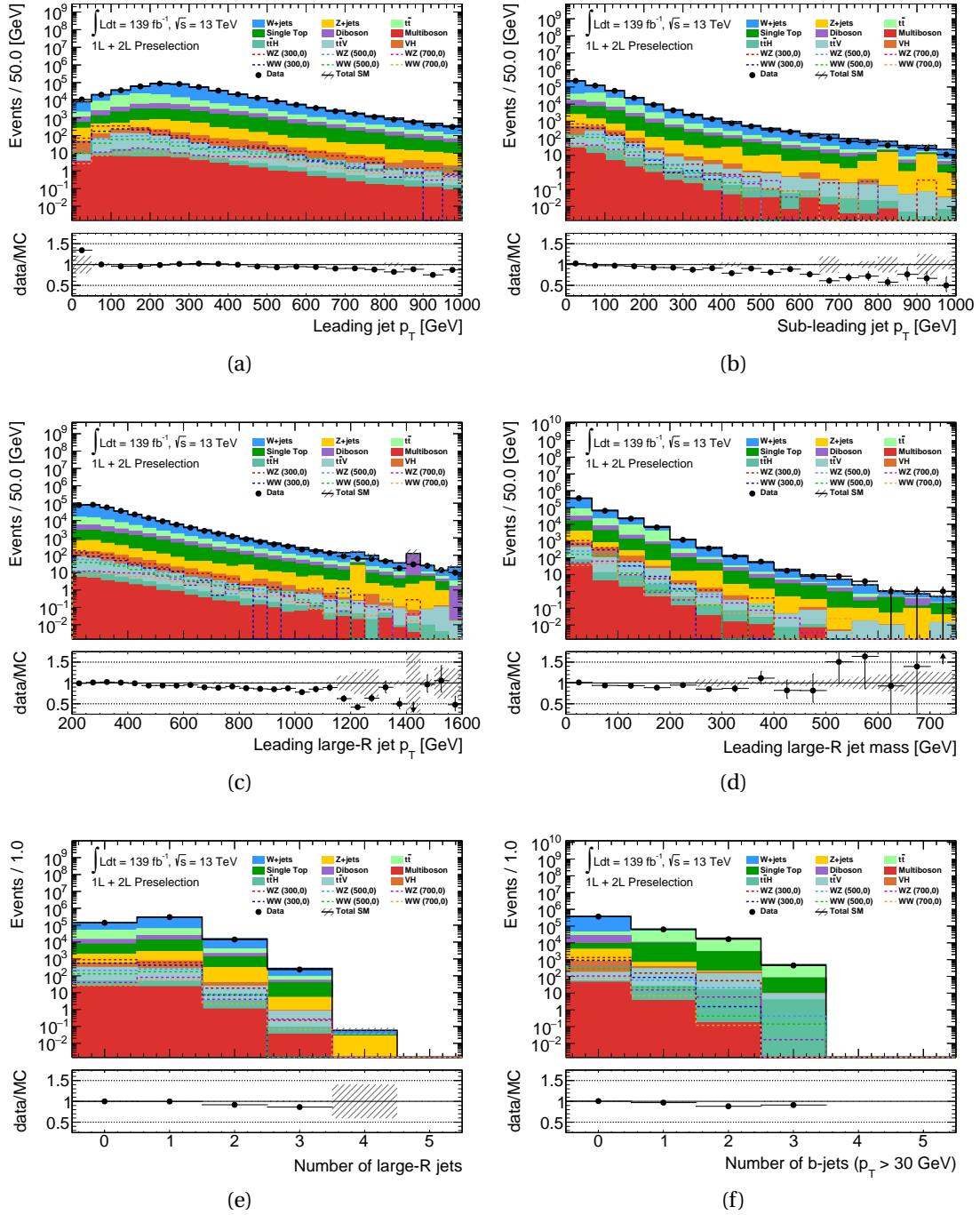


Figure 7.4: Data/MC comparisons for discriminating variables used in the analysis. Only statistical uncertainties are considered in the error band.

7.3.3 Signal region optimization for C1C1-WW search

The discriminating variables mentioned in Section 7.3.1 are then used to define the signal regions (SRs) for the C1C1-WW search. The cuts on these variables are determined

with an optimization procedure described in the following.

Because the final state of signal events is characterized by the presence of only one isolated lepton, one requires exactly one lepton, $N_{\text{lep}}^{\text{base}} = N_{\text{lep}}^{\text{sig}} = 1$, in the signal regions (SRs). The number of large-R jets, $N_{\text{large-R jets}}$, is used to define two kinds of SR: **resolved** and **boosted**. The resolved SR aiming for signal points with low $\Delta m(\tilde{\chi}_1^\pm, \tilde{\chi}_2^0, \tilde{\chi}_1^0)$ concentrates on a scenario where jets from the hadronic W boson are separate from each other, resulting in no large-R jets being observed in events, $N_{\text{large-R jets}} = 0$. In contrast, the boosted SR targeting signals with high $\Delta m(\tilde{\chi}_1^\pm, \tilde{\chi}_2^0, \tilde{\chi}_1^0)$ focuses on another scenario where jets from the hadronic W boson are more collinear and possibly merge with each other into large-R jets. Therefore, in the boosted SR, one requires at least one large-R jet, $N_{\text{large-R jets}} \geq 1$, and the leading one must be tagged as W boson.

Cuts on the other variables are determined and optimized using the same strategy as in the first wave analysis [1]. A multidimensional cut scan [210] is performed for each of benchmark points. These benchmark points are chosen in order that they can cover both low and high mass regions of the signal grid. For each variable, basing on its kinematic distribution at the preselection level, ranges of discrete cut values are selected and used as input of the scan. The train-test approach is also applied during the scan in order to avoid selecting kinematic regions that are too tight with the available MC statistics. This step results in one promising cut candidate per benchmark point, which provides a high significance value while still keeping enough statistics. And by comparing these promising cut combinations, one can obtain the first glance for the definition of resolved and boosted SRs.

The rough cuts obtained for resolved and boosted SRs are then optimized through a round of $N - 1$ plots. This also allows to reduce number of variables used by removing useless cuts that do not noticeably increase sensitivity of the SRs. At this stage, the optimal cut on m_T is found that it highly depends on $m_{\tilde{\chi}_1^\pm / \tilde{\chi}_2^0}$ and $\Delta m(\tilde{\chi}_1^\pm, \tilde{\chi}_2^0, \tilde{\chi}_1^0)$. Consequently, to optimize the sensitivity for all regions of the signal grid, the resolved SR is splitted into two m_T bins while the boosted one is splitted into three m_T bins. The best choice for the ranges of these bins is determined by a shape fit performed with HistFitter [211]. In addition, this shape fit is used in parallel so as to validate the tuned cuts seen from the round of $N - 1$ plots.

The proposed definition of the resolved and boosted SRs obtained from the optimization procedure, which has been described, for 139 fb^{-1} is summarized in Table 7.4. The set of $N - 1$ plots with significance scans for the inclusive boosted and resolved SRs (including all m_T bins) is listed in Figures 7.5 and 7.6. The significance is calculated using the RooStats::NumberCountingUtils::BinomialExpZ with 30% added for the total background relative uncertainty.

7.3.4 Signal region optimization for C1N2-WZ search

The optimization procedure of this search uses a similar list of discriminating kinematic variables and the same optimization strategy as discussed in 7.3.3. In general, two kinds of SR, resolved and boosted, are also designed and each concentrates on a

7 Search for electroweak production of charginos and neutralinos in final states with one lepton, jets and missing transverse momentum – 7.3 Event selection

Variable	Cuts				
	SRLM resolved	SRHM resolved	SRLM boosted	SRMM boosted	SRHM boosted
N_{lep}	1		1		
p_{T}^{ℓ} [GeV]	> 25		> 25		
$N_{\text{jet}} (p_{\text{T}}^{\text{jets}} > 30 \text{ GeV})$	2 - 3		≤ 3		
$N_{\text{b-jet}} (p_{\text{T}}^{\text{jets}} > 30 \text{ GeV})$	0		-		
$E_{\text{T}}^{\text{miss}}$ [GeV]	> 200		> 200		
$\Delta\phi(\ell, E_{\text{T}}^{\text{miss}})$	< 2.8		< 2.6		
m_{jj} [GeV]	70 - 105		-		
$N_{\text{large-Rjets}}$	0		≥ 1		
W-tagged large-R jet	-		yes		
$p_{\text{T}}^{\text{large-Rjet}}$ [GeV]	-		> 300		
$E_{\text{T}}^{\text{miss}}$ significance	-		> 12		
m_{T} [GeV]	200 - 380	> 380	120 - 220	220 - 320	> 320

Table 7.4: Definition of the resolved and boosted SRs for C1C1-WW search, obtained from the optimization procedure.

specific scenario where jets from hadronic Z boson decay can be either separate or merged. The resolved and boosted SRs are also splitted into two and three m_{T} bins respectively so as to be able to cover all regions of the signal grid.

The proposed definition of the resolved and boosted SRs obtained from the optimization procedure for 139 fb^{-1} is summarized in Table 7.5. The set of $N - 1$ plots with significance scans for the inclusive boosted and resolved SRs (including all m_{T} bins) is listed in Figures 7.7 and 7.8.

Variable	Cuts				
	SRLM resolved	SRHM resolved	SRLM boosted	SRMM boosted	SRHM boosted
N_{lep}	1		1		
p_{T}^{ℓ} [GeV]	> 25		> 25		
$N_{\text{jet}} (p_{\text{T}}^{\text{jets}} > 30 \text{ GeV})$	2 - 3		≤ 3		
$N_{\text{b-jet}} (p_{\text{T}}^{\text{jets}} > 30 \text{ GeV})$	0		-		
$E_{\text{T}}^{\text{miss}}$ [GeV]	> 200		> 200		
$\Delta\phi(\ell, E_{\text{T}}^{\text{miss}})$	< 2.8		< 2.6		
m_{jj} [GeV]	70 - 105		-		
$N_{\text{large-Rjets}}$	0		≥ 1		
Z-tagged large-R jet	-		yes		
$p_{\text{T}}^{\text{large-Rjet}}$ [GeV]	-		> 300		
$E_{\text{T}}^{\text{miss}}$ significance	-		> 12		
m_{T} [GeV]	200 - 380	> 380	120 - 220	220 - 320	> 320

Table 7.5: Definition of the resolved and boosted SRs for C1N2-WZ search, obtained from the optimization procedure.

7 Search for electroweak production of charginos and neutralinos in final states with one lepton, jets and missing transverse momentum – 7.3 Event selection

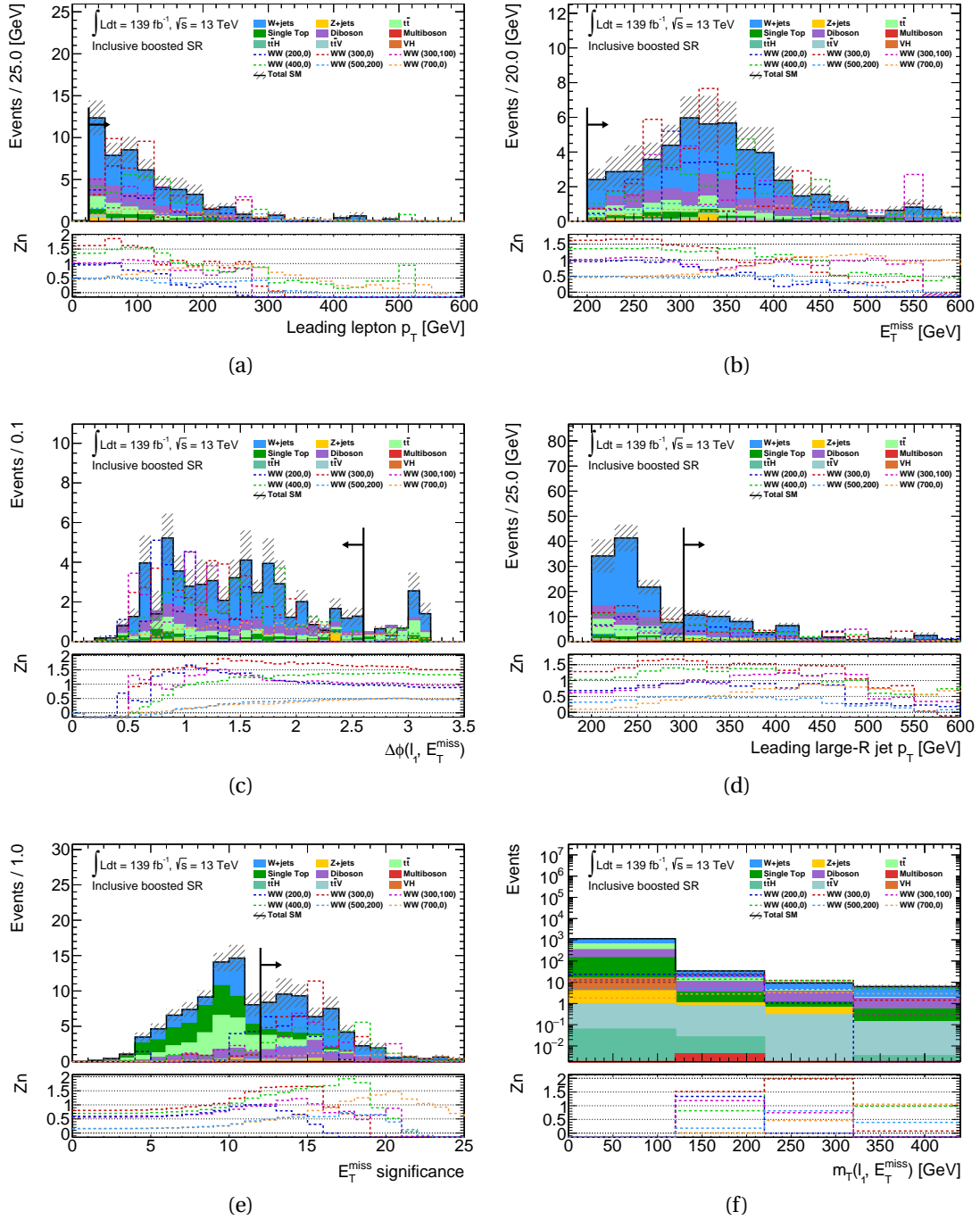


Figure 7.5: $N - 1$ plots for the boosted SR of the C1C1-WW search, with exemplary signal points and all m_T bins included. In all figures except 7.5f, the significance in the lower pad is obtained by summing up all the events in the direction of the cut arrow and includes 30% uncertainty as well as MC statistical uncertainty. In 7.5f the significance is only computed on a bin-by-bin basis, i.e. not summing up all events in the direction of the cut arrow. Only statistical uncertainties are considered in the error band.

7 Search for electroweak production of charginos and neutralinos in final states with one lepton, jets and missing transverse momentum – 7.3 Event selection

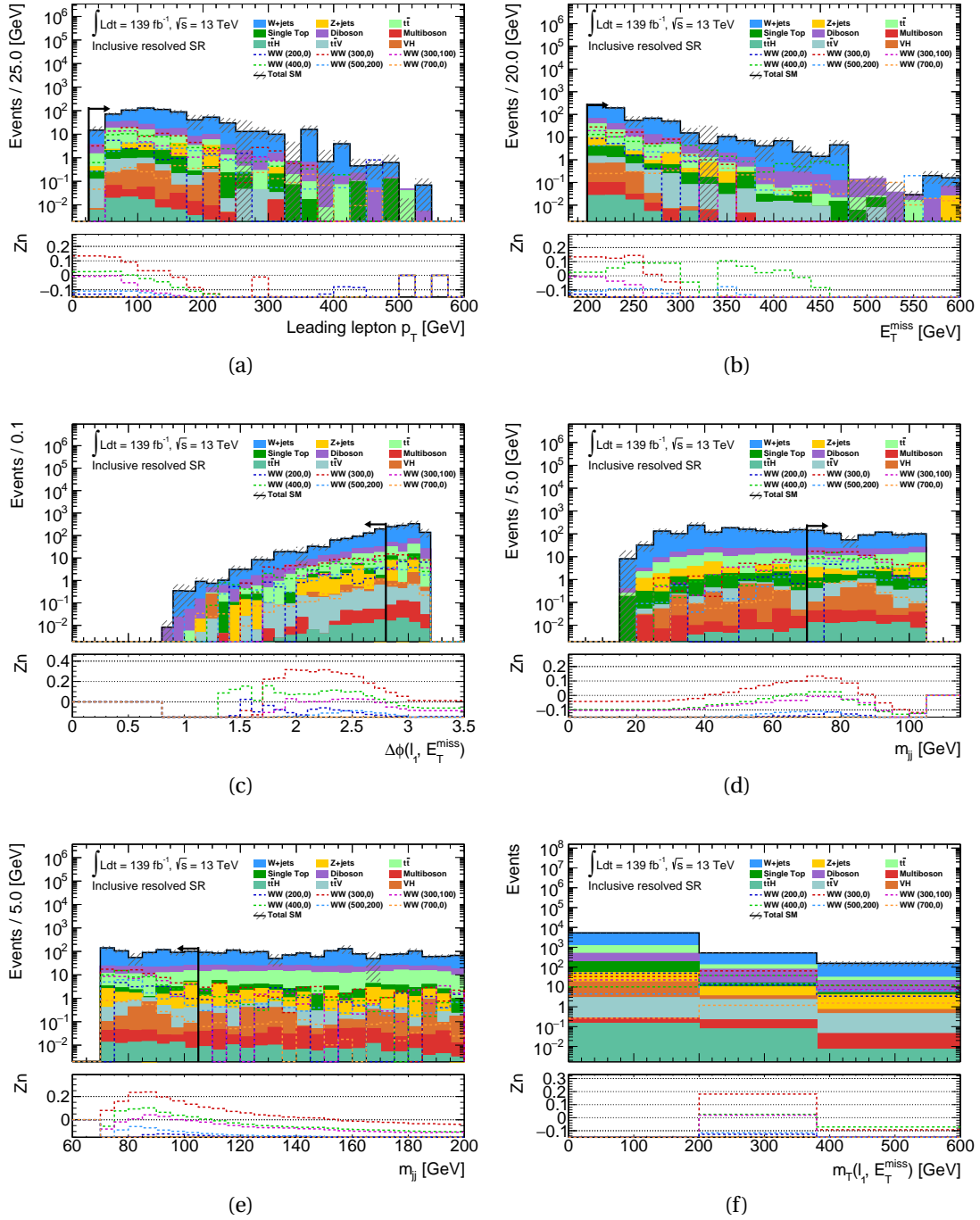


Figure 7.6: $N - 1$ plots for the resolved SR of the C1C1-WW search, with exemplary signal points and all m_T bins included. In all figures except 7.6f, the significance in the lower pad is obtained by summing up all the events in the direction of the cut arrow and includes 30% uncertainty as well as MC statistical uncertainty. In 7.6f the significance is only computed on a bin-by-bin basis, i.e. not summing up all events in the direction of the cut arrow. Only statistical uncertainties are considered in the error band.

7 Search for electroweak production of charginos and neutralinos in final states with one lepton, jets and missing transverse momentum – 7.3 Event selection

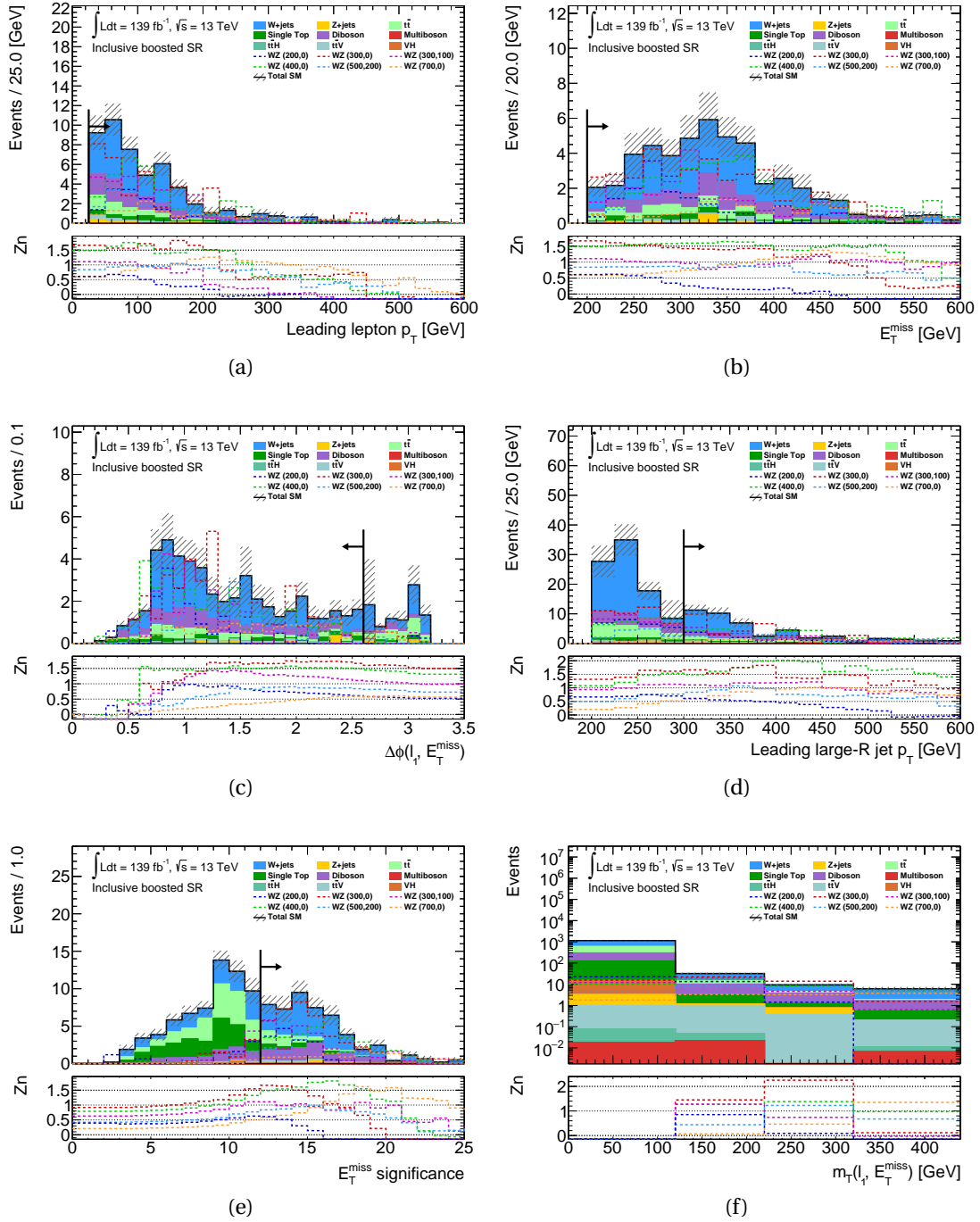


Figure 7.7: $N - 1$ plots for the boosted SR of the C1N2-WZ search, with exemplary signal points and all m_T bins included. In all figures except 7.7f, the significance in the lower pad is obtained by summing up all the events in the direction of the cut arrow and includes 30% uncertainty as well as MC statistical uncertainty. In 7.7f the significance is only computed on a bin-by-bin basis, i.e. not summing up all events in the direction of the cut arrow. Only statistical uncertainties are considered in the error band.

7 Search for electroweak production of charginos and neutralinos in final states with one lepton, jets and missing transverse momentum – 7.3 Event selection

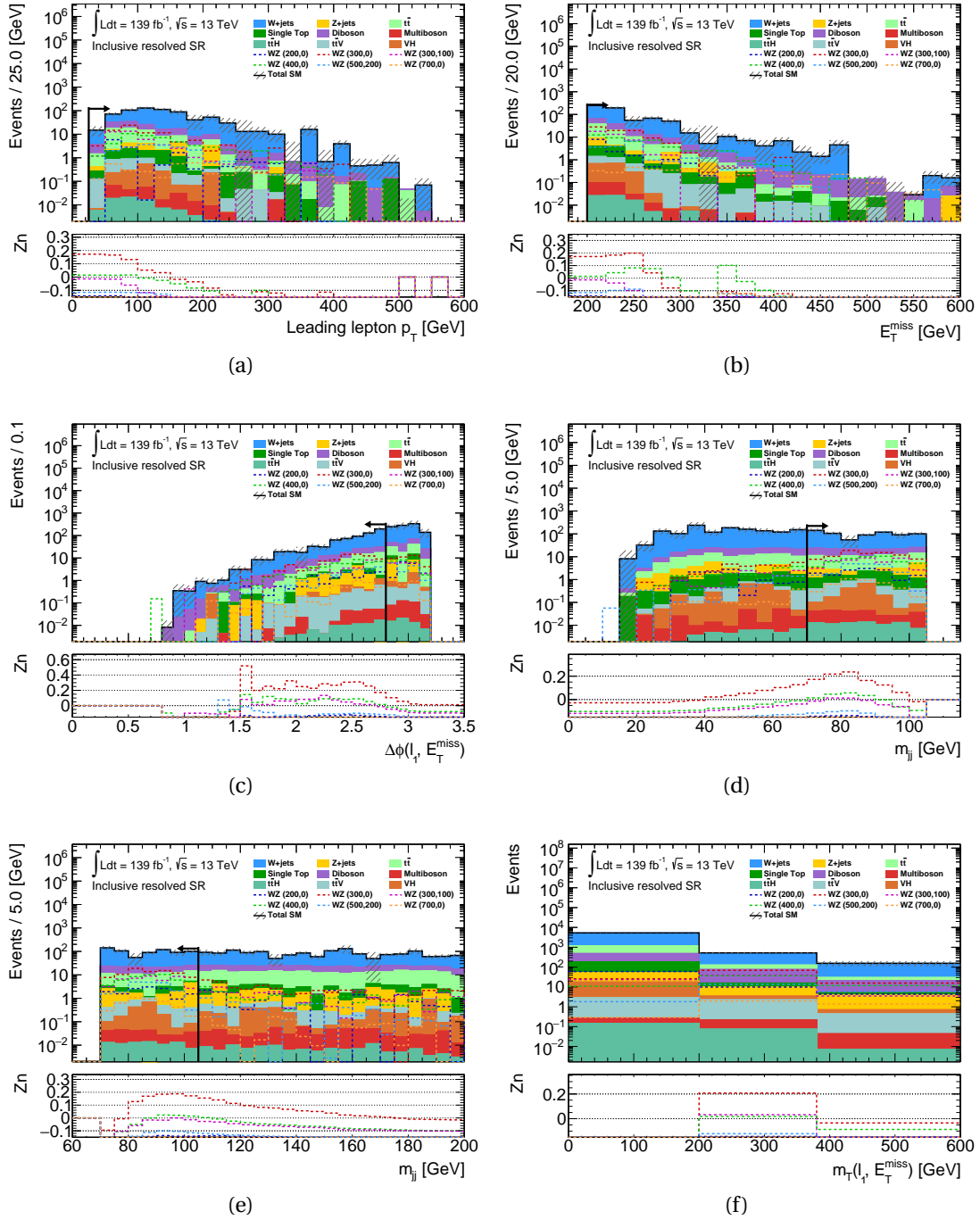


Figure 7.8: $N - 1$ plots for the resolved SR of the C1N2-WZ search, with exemplary signal points and all m_T bins included. In all figures except 7.8f, the significance in the lower pad is obtained by summing up all the events in the direction of the cut arrow and includes 30% uncertainty as well as MC statistical uncertainty. In 7.8f the significance is only computed on a bin-by-bin basis, i.e. not summing up all events in the direction of the cut arrow. Only statistical uncertainties are considered in the error band.

7.4 Background estimation

The major background processes in the analysis are W +jets, diboson and $t\bar{t}$. Therefore, the expected yields of these backgrounds in the SRs will be estimated with an extrapolation from their dedicated Control Regions (CRs) to the SRs. These CRs are designed to be non-overlapping with the SRs and also mutually exclusive. The extrapolation is checked in Validation Regions (VRs), which are typically placed between the CRs and VRs. The VRs do not overlap with the SRs and CRs. The other background processes including Z +jets, single top, multiboson, $t\bar{t} + V$, $t\bar{t} + h$ and Vh are minor and thus will be estimated directly from the MC predictions.

In the diboson background, the contribution from sub-processes with at least two leptons in the final state (diboson 2L) is found to be evenly dominant compared to the one from sub-processes with only one lepton in the final state (diboson 1L). Therefore, it is desirable to design a separate estimation for each type of the diboson background. The contribution from sub-processes which do not have any lepton in the final state (diboson 0L) is negligible in this analysis.

7.4.1 Diboson 2L estimation

A dedicated control region has been designed for diboson contribution coming from processes with at least two leptons in the final state, and a dedicated and completely orthogonal validation region has been built. Both are shown in Table 7.6. The main difficulties in this effort have been to design regions with enough statistics, keeping a good diboson purity while reducing the $t\bar{t}$ and signal contamination. An additional difficulty comes from the potential overlap with the 2L2J analysis signal regions, which has to be reduced as much as possible in sight of a future combination. In order to minimize the overlap, a veto on the m_{jj} variable has been required, where the 2L2J regions show a peak in the signal distributions.

The purity of diboson 2L is found to be about 50% in DB2L CR and 58% in DB2L VR. The highest C1C1-WW signal contamination is about 0.45% in both DB2L CR and VR while the highest C1N2-WZ signal contamination in DB2L CR and VR are 8% and 12%, respectively. This means the signal contamination in these regions is at an acceptable level.

7.4.2 W +jets and diboson 1L estimation

Diboson 1L and W +jets backgrounds will be estimated together in combined W +jets and diboson 1L regions. The CRs and VRs dedicated to these two backgrounds are defined separately for boosted and resolved scenarios.

Boosted regime

A dedicated control region has been designed for W jets and diboson 1L contributions coming from processes in the boosted regime (orthogonal with respect to the resolved

7 Search for electroweak production of charginos and neutralinos in final states with one lepton, jets and missing transverse momentum – 7.4 Background estimation

Variable	Cuts	
	DB2LCR	DB2LVR
N_{lep}	2	2
$p_{\text{T}}^{\ell} [\text{GeV}]$	> 25	> 25
$N_{\text{jet}} (p_{\text{T}}^{\text{jets}} > 30 \text{ GeV})$	≤ 3	≤ 3
$N_{\text{b-jet}} (p_{\text{T}}^{\text{jets}} > 30 \text{ GeV})$	0	0
$E_{\text{T}}^{\text{miss}} [\text{GeV}]$	> 200	> 200
$\Delta\phi(\ell, E_{\text{T}}^{\text{miss}})$	< 2.9	< 2.9
$E_{\text{T}}^{\text{miss}}$ significance	> 12	> 10
$m_{\ell\ell} [\text{GeV}]$	70 – 100	70 – 100
$m_{\text{jjveto}} [\text{GeV}]$	75 – 95	75 – 95
$m_{\text{T}} [\text{GeV}]$	50 – 200	200 – 350

Table 7.6: Summary of the selection requirements for both DB2L CR and VR.

regions), and two dedicated and completely orthogonal validation regions have been built, extrapolating on m_{T} and $E_{\text{T}}^{\text{miss}}$ significance. All these regions are shown in Table 7.7. The main goal have been to design regions with enough statistics, keeping a good W+jets and diboson 1L (at least 10%) purity while reducing the $t\bar{t}$ and signal contamination.

Variable	Cuts		
	WDB1LCRboosted	WDB1LVR1boosted	WDB1LVR2boosted
N_{lep}	1	1	1
$p_{\text{T}}^{\ell} [\text{GeV}]$	> 25	> 25	> 25
$N_{\text{jet}} (p_{\text{T}}^{\text{jets}} > 30 \text{ GeV})$	≤ 3	≤ 3	≤ 3
$N_{\text{b-jet}} (p_{\text{T}}^{\text{jets}} > 30 \text{ GeV})$	0	0	0
$E_{\text{T}}^{\text{miss}} [\text{GeV}]$	> 200	> 200	> 200
$\Delta\phi(\ell, E_{\text{T}}^{\text{miss}})$	< 2.9	< 2.9	< 2.9
$E_{\text{T}}^{\text{miss}}$ significance	< 14	< 12	> 14
$N_{\text{large-Rjets}}$	≥ 1	≥ 1	≥ 1
W-tagged large-R jet	yes	yes	yes
$p_{\text{T}}^{\text{large-Rjet}} [\text{GeV}]$	> 250	> 250	> 250
$m_{\text{T}} [\text{GeV}]$	50 – 80	> 80	50 – 120

Table 7.7: Summary of the selection requirements for WDB1L boost CR, VR1 and VR2.

The purities of W+jets in these boosted regions are about 50% while the purities of diboson 1L in these boosted regions are 15% (in WDB1LCRboosted), 12%

7 Search for electroweak production of charginos and neutralinos in final states with one lepton, jets and missing transverse momentum – 7.4 Background estimation

(in WDB1LVR1boosted) and 25% (in WDB1LVR2boosted). The highest C1C1-WW signal contamination is 1%, 3.5% and 3% in the boosted WDB1L CR, VR1 and VR2 respectively. The highest C1N2-WZ signal contamination is 0.6%, 2.5% and 3% in the boosted WDB1L CR, VR1 and VR2 respectively. These numbers are at an acceptable level.

Resolved regime

A dedicated control region is also designed to control the W+jets and diboson 1L contributions in resolved regions, and a dedicated validation region is built to validate the extrapolation using the m_T variable. The definition of the resolved WDB1L CR and VR are shown in Table 7.8. The main goal have been to design regions with enough statistics, keeping a good W+jets and diboson 1L purity while reducing the $t\bar{t}$ and signal contamination. This goal is achieved by requiring the E_T^{miss} significance > 12 .

Variable	Cuts	
	WDB1LCRresolved	WDB1LVRresolved
N_{lep}		1
$p_T^\ell [\text{GeV}]$		> 25
$N_{\text{jet}} (p_T^{\text{jets}} > 30 \text{ GeV})$		$2 \leq N_{\text{jet}} \leq 3$
$N_{b\text{-jet}} (p_T^{\text{jets}} > 30 \text{ GeV})$		0
$m_{jj} [\text{GeV}]$		70 - 105
$E_T^{\text{miss}} [\text{GeV}]$		> 200
$\Delta\phi(\ell, E_T^{\text{miss}})$		< 2.8
E_T^{miss} significance		> 12
$N_{\text{large-Rjets}}$		0
$m_T [\text{GeV}]$	50 – 80	80 – 200

Table 7.8: Summary of the selection requirements for WDB1L resolved control and validation regions.

The purities of W+jets in these resolved CR and VR are about 70%, while the ones of diboson 1L are about 7%. The highest signal contamination of about 0.7% is observed in these regions for both C1C1-WW and C1N2-WZ models.

7.4.3 $t\bar{t}$ estimation

For the $t\bar{t}$ background, the CRs and VRs are also designed separately for the boosted and resolved scenarios. In fact, all the cuts used to define the $t\bar{t}$ regions are the same as in the WDB1L regions, except the cut on number of b -jets and the cut on E_T^{miss} significance. In order to gain the $t\bar{t}$ purity and statistics, $N_{b\text{-jet}} > 0$ is required for all the CRs and VRs of $t\bar{t}$, while the cut on E_T^{miss} significance is removed in the $t\bar{t}$ resolved

7 Search for electroweak production of charginos and neutralinos in final states with one lepton, jets and missing transverse momentum – 7.4 Background estimation

CR and VR. The boosted and resolved regions of $t\bar{t}$ are summarized in Tables 7.9 and 7.10, respectively.

Variable	Cuts		
	TCRboosted	TVR1boosted	TVR2boosted
N_{lep}	1	1	1
$p_{\text{T}}^{\ell} [\text{GeV}]$	> 25	> 25	> 25
$N_{\text{jet}} (p_{\text{T}}^{\text{jets}} > 30 \text{ GeV})$	≤ 3	≤ 3	≤ 3
$N_{\text{b-jet}} (p_{\text{T}}^{\text{jets}} > 30 \text{ GeV})$	> 0	> 0	> 0
$E_{\text{T}}^{\text{miss}} [\text{GeV}]$	> 200	> 200	> 200
$\Delta\phi(\ell, E_{\text{T}}^{\text{miss}})$	< 2.9	< 2.9	< 2.9
$E_{\text{T}}^{\text{miss}}$ significance	< 14	< 12	> 14
$N_{\text{large-Rjets}}$	≥ 1	≥ 1	≥ 1
W-tagged large-R jet	yes	yes	yes
$p_{\text{T}}^{\text{large-Rjet}} [\text{GeV}]$	> 250	> 250	> 250
$m_{\text{T}} [\text{GeV}]$	50 – 80	> 80	50 – 120

Table 7.9: Summary of the selection requirements for Top boost CR, VR1 and VR2.

Variable	Cuts	
	TCRresolved	TVRresolved
N_{lep}	1	
$p_{\text{T}}^{\ell} [\text{GeV}]$	> 25	
$N_{\text{jet}} (p_{\text{T}}^{\text{jets}} > 30 \text{ GeV})$	$2 \leq N_{\text{jet}} \leq 3$	
$N_{\text{b-jet}} (p_{\text{T}}^{\text{jets}} > 30 \text{ GeV})$	> 0	
$m_{\text{jj}} [\text{GeV}]$	70 - 105	
$E_{\text{T}}^{\text{miss}} [\text{GeV}]$	> 200	
$\Delta\phi(\ell, E_{\text{T}}^{\text{miss}})$	< 2.8	
$N_{\text{large-Rjets}}$	0	
$m_{\text{T}} [\text{GeV}]$	50 – 80	80 – 200

Table 7.10: Summary of the selection requirements for Top resolved control and validation regions.

The purities of $t\bar{t}$ in these regions are above 50% and the signal contamination in these regions are always below 2%.

7.5 Systematic uncertainties

Besides the statistical uncertainty coming from the finite number of events in the MC samples, the signal and background estimation is also affected by systematic uncertainties that can be categorized into two sources, experimental and theoretical: the experimental uncertainties are due to the finite precision of the calibration of the reconstructed objects and the non-perfect description of the experimental conditions, for example luminosity or pile-up; while theoretical uncertainties arise from the imperfect modelling of the processes in MC generators. The dominant experimental and theoretical uncertainties on the various signal regions are detailed in the following.

7.5.1 Experimental uncertainties

The experimental uncertainties considered for this analysis are:

- Jet Energy Scale (JES): These take into account the effects of the nuisance parameters associated to the Jet Energy Scale correction.
- Jet Energy Resolution (JER): Uncertainties on the jet resolution are evaluated by smearing the jet energies using a Gaussian, whose mean and width values are determined from the difference between the jet resolutions measured in MC and data.
- Lepton scale, resolution and efficiency: Uncertainties on the calibration of electron/muon energy/momentum and resolution are included in the analysis. Uncertainties on lepton scale factors are considered as well.
- Flavour-tagging: Scale factors are applied to correct the simulated b-tagging (in)efficiencies to better match the data. Uncertainties on these scale factors are determined from variations in the various jet flavour components and for the extrapolation of systematics into regions where the measurements are statistically limited.
- E_T^{miss} soft term: Uncertainties on the hard object components in the E_T^{miss} are propagated from the systematics on the selected objects. Additional uncertainties on the soft E_T^{miss} component are applied as variations on the scale of the TST, and smearing of the TST by the difference between data and MC resolutions in two orthogonal projections of the soft term with respect to the balancing hard terms.
- Pileup-reweighting: Two variations are applied to the data scale factor used for pileup-reweighting, accounting for uncertainties on the degree of mismodelling of the minimum bias overlay used in MC pileup simulation.
- Jet Vertex Tagger: The efficiencies for tagging pileup (hard scatter) jets with the JVT discriminant are corrected in MC simulation by applying scale factors

derived by measurement of jet rates in pileup-enriched (depleted) phase space regions.

7.5.2 Theoretical uncertainties

The theoretical systematic uncertainties are due to the imperfect modelling of the processes in MC generators, they are determined by varying the MC generator parameters, such as the renormalisation and factorisation scales, the model used for the parton showering or the extent of the emission of additional partons in the initial or final states. Depending on the MC generator, the theoretical uncertainties are propagated by either event weights accounting for a variation of a parameter by its uncertainty or by generating new MC samples where the theoretical parameter of interest is varied by its uncertainty. As the W +jets, diboson 2L, diboson 1L and $t\bar{t}$ yields are determined in dedicated CRs, uncertainties in those processes only affect the extrapolation from the control into the signal region (and amongst the various control regions). Therefore, no cross-section uncertainty is considered and transfer factors representing the ratio of the predicted yields between the SR and the corresponding CR(x) defined in Equation 7.5 are used to evaluate the various systematic uncertainties.

$$TF^{\text{Process}} = \frac{N_{\text{SR}}}{N_{\text{CR}(\text{process})}}. \quad (7.5)$$

The systematic uncertainty on a transfer factor is given by comparing transfer factors derived using variation samples to ones derived using a ‘nominal’ sample as:

$$\Delta TF_{\text{Syst}}^{\text{Process}} = \frac{TF^{\text{Variation}} - TF^{\text{Nominal}}}{TF^{\text{Nominal}}}. \quad (7.6)$$

For the other minor or sub-dominant background samples with no dedicated CRs, their yields are entirely estimated from simulation. Therefore, instead of using the transfer factor approach as for major backgrounds, the theoretical uncertainties of these backgrounds can be computed directly from their expected yields in the analysis regions. For a specific systematic variation in a particular region, the corresponding uncertainty can be derived by comparing the yield of this variation to the nominal yield in the same region. This uncertainty, namely ΔN_{sys} , on the yield is defined as follows:

$$\Delta N_{\text{sys}} = \frac{N_{\text{region}}^{\text{sys}} - N_{\text{region}}^{\text{nominal}}}{N_{\text{region}}^{\text{nominal}}}, \quad (7.7)$$

where $N_{\text{region}}^{\text{sys}}$ denotes the variation yields in the region of interest, while $N_{\text{region}}^{\text{nominal}}$ denotes the nominal yield in that region.

Uncertainties in the modelling of $t\bar{t}$ and single-top production are estimated by comparing the nominal sample listed in Table 7.1 with alternative generators. The systematic uncertainty due to the hard-scattering process is evaluated using a comparison of the nominal sample with the sample generated with MADGRAPH5@NLO

interfaced to PYTHIA 8. Fragmentation or hadronization uncertainties are assessed using a comparison of the nominal sample with a sample generated with POWHEG-BOX interfaced to the HERWIG 7 package for parton showering. Initial- and final-state radiation (ISR/FSR) uncertainties of single-top can be estimated using dedicated weights in the nominal sample. The ISR uncertainty of $t\bar{t}$ is estimated by comparing nominal sample with POWHEG+PYTHIA8+EVTGEN sample, while the $t\bar{t}$ FSR uncertainty is computed using the internal weight in the nominal sample. For single-top, uncertainty of the Wt interference with $t\bar{t}$ is also estimated.

Uncertainties in the modelling of W/Z +jets are estimated by considering different merging (CKKW-L) and resummation (qsf) scales, PDF and strong coupling constant (α_s) variations from the NNPDF3.0NNLO replicas [212], and variations of factorisation and renormalisation scales in the matrix element calculations. The last two are evaluated using 7 point variations, changing the renormalisation and factorisation scales by factors of 0.5 and 2, such that when one scale is increased the other is decreased, and vice-versa. The scale uncertainty is then calculated by the maximum shift of the envelope with respect to the nominal.

Uncertainties in diboson production due to PDF, strong coupling constant, and renormalisation and factorization scale uncertainties are estimated in a similar way as for the W/Z +jets modelling uncertainties.

For other minor backgrounds ($t\bar{t}V$, $t\bar{t}h$ and Vh), renormalisation and factorisation scale uncertainties, PDF uncertainties are also estimated using similar way. In addition, for $t\bar{t}h$, the ISR and FSR uncertainties are also computed using internal weights in the nominal sample.

Theory uncertainties in the expected yields for SUSY signals are estimated by varying by a factor of two the parameters corresponding to the factorisation, renormalisation, and CKKW-L matching scales, as well as the PYTHIA 8 shower tune parameters.

7.6 Results

7.6.1 Background-only fit

The expected backgrounds in each signal region are determined in a profile likelihood fit, referred to as a "background-only fit". In this fit, the normalisation of the backgrounds is adjusted to match the data in control regions with negligible signal contamination. The resulting normalisation factors are then used to correct the expected yields of the corresponding backgrounds in the various signal regions. A probability density function is defined for each of the control regions. The inputs are the observed event yield and the predicted background yield from simulation with Poisson statistical uncertainties as well as with systematic uncertainties as nuisance parameters. The nuisance parameters are constrained by Gaussian distributions with widths corresponding to the sizes of the uncertainties. The product of all the probability density functions forms the likelihood. Normalisation and nuisance parameters

7 Search for electroweak production of charginos and neutralinos in final states with one lepton, jets and missing transverse momentum – 7.6 Results

are correlated in all regions participating in the fit. The likelihood is maximised by adjusting the normalisation and nuisance parameters. The extrapolation of the adjusted normalisation and nuisance parameters to the signal regions is checked in validation regions. The normalization factors of $t\bar{t}$, diboson 2L, W +jets and diboson 1L obtained from the background-only fit in this analysis are $\mu_{\text{Top}} = 0.72^{+0.09}_{-0.10}$, $\mu_{\text{DB2L}} = 1.08^{+0.17}_{-0.20}$ and $\mu_{\text{WBD1L}} = 0.98^{+0.05}_{-0.05}$, respectively.

Figure 7.9 shows the pulls obtained after the background-only fit in all the control and validation regions, while the signal regions are kept blinded. The compatibility of the observed and expected event yields in the control and validation regions can be seen from this figure. Figure 7.10 shows the correlation matrix of the background-only fit. Figure 7.11 shows the values of the normalization parameters and of the nuisance parameters after the background-only fit. The two largest pulling parameters come from JES Flavor uncertainties. The kinematics for the uncertainty up and down have been checked in the preselection level, while no strange behaviour is observed. But it was found that those two parameters have large correlation with each other.

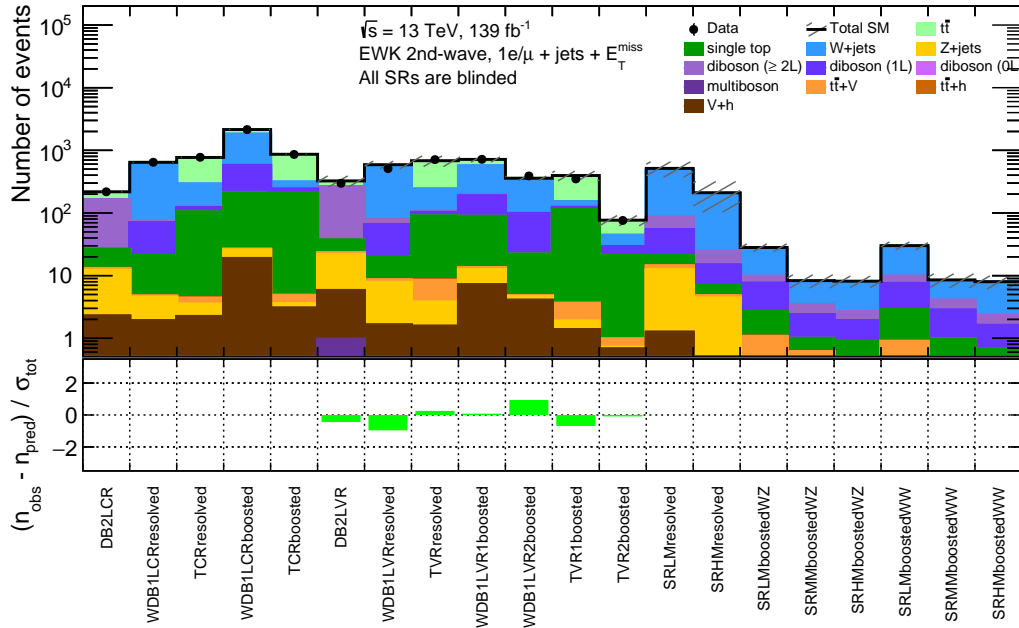


Figure 7.9: The pulls between the number of events observed and the total background expected after-fit in control, validation and signal regions.

7.6.2 Model-dependent fit

Model-dependent exclusion limits at 95% confidence level (CL) are placed on the signal models. These limits are shown as a function of the masses of the supersym-

7 Search for electroweak production of charginos and neutralinos in final states with one lepton, jets and missing transverse momentum – 7.6 Results

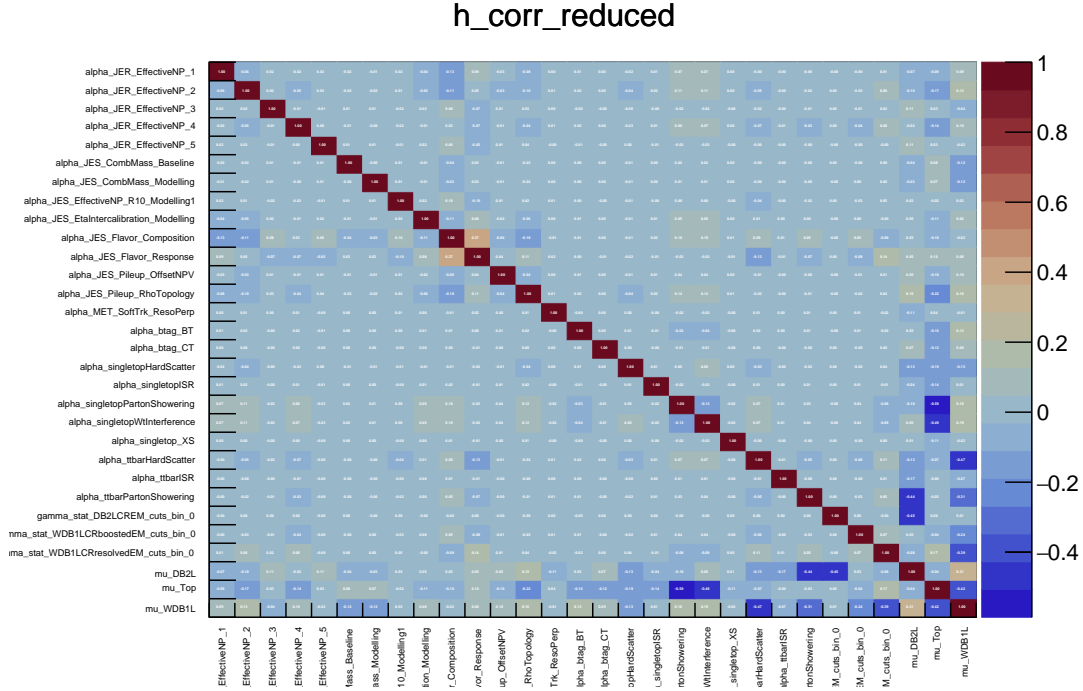
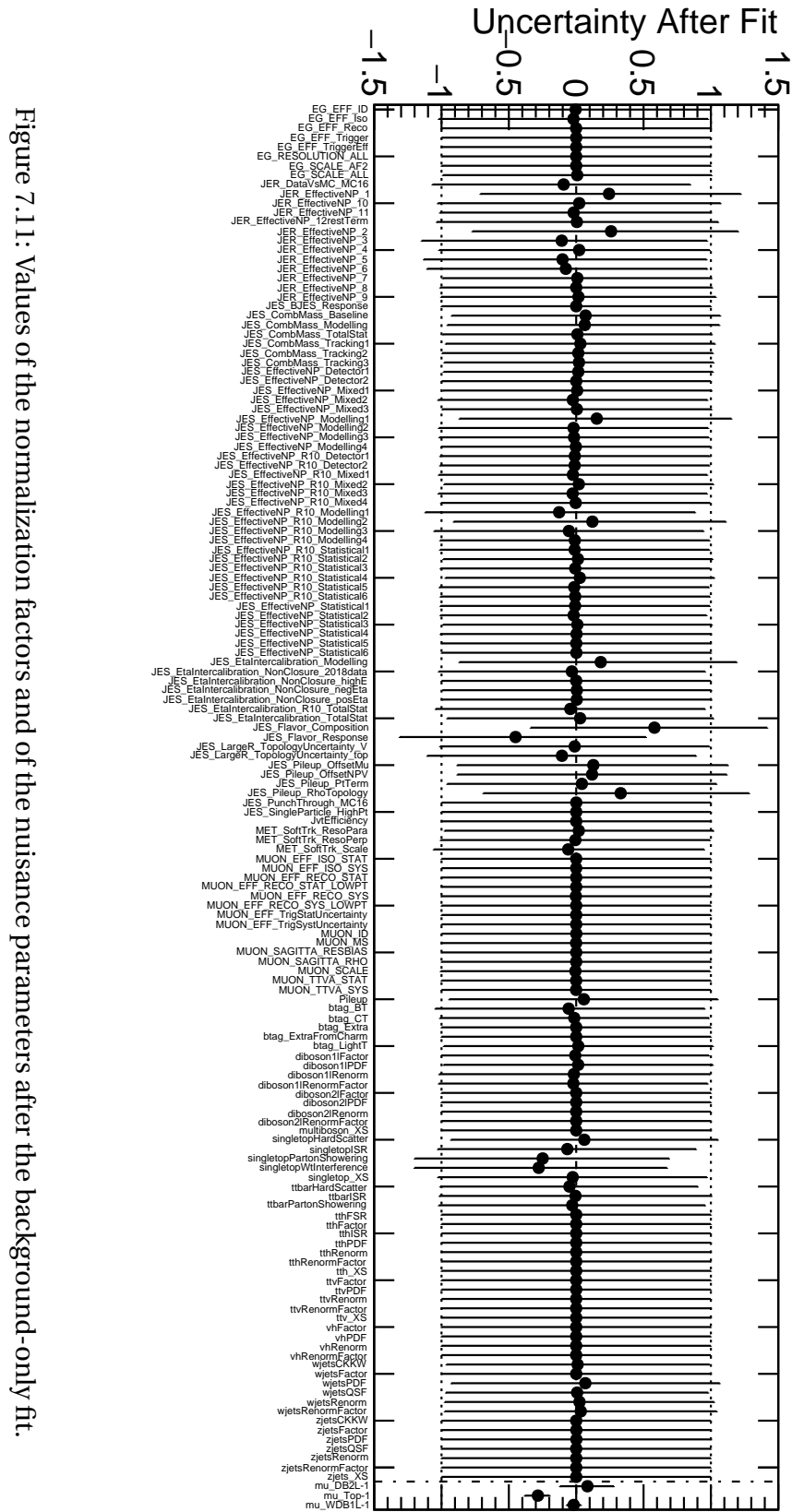


Figure 7.10: Correlation matrix of the background-only fit.

metric particles. They are determined interpolating between the simulated mass points, but no smoothing procedure is applied so that local fluctuations in the limit can be present. A likelihood similar to the one used in the background-only fit, but with additional terms for the SRs, is used for the calculation. The exclusion SRs thus participate in the fit and are used to constrain normalisation and nuisance parameters. A signal is allowed in this likelihood in both the CRs and SRs. The VRs are not used in the fit. The CL_s method [213] is used to derive the confidence level of the exclusion for a particular signal model; signal models with a CL_s value below 0.05 are excluded at 95% CL. The exclusion limits at 95% of both searches are shown in Figures 7.13 and Figures 7.12. The expected limit of the C1C1-WW model extends up to 680 GeV in $m(\tilde{\chi}_1^\pm)$ for massless $\tilde{\chi}_1^0$ and up to $m(\tilde{\chi}_1^\pm)$ of 600 GeV for $m(\tilde{\chi}_1^0)$ of 200 GeV. In the C1N2-WZ search, the expected limit extends up to 720 GeV in $m(\tilde{\chi}_1^\pm/\tilde{\chi}_2^0)$ for massless $\tilde{\chi}_1^0$ and up to $m(\tilde{\chi}_1^\pm/\tilde{\chi}_2^0)$ of 600 GeV for $m(\tilde{\chi}_1^0)$ of 200 GeV.

7 Search for electroweak production of charginos and neutralinos in final states with one lepton, jets and missing transverse momentum – 7.6 Results



7 Search for electroweak production of charginos and neutralinos in final states with one lepton, jets and missing transverse momentum – 7.6 Results

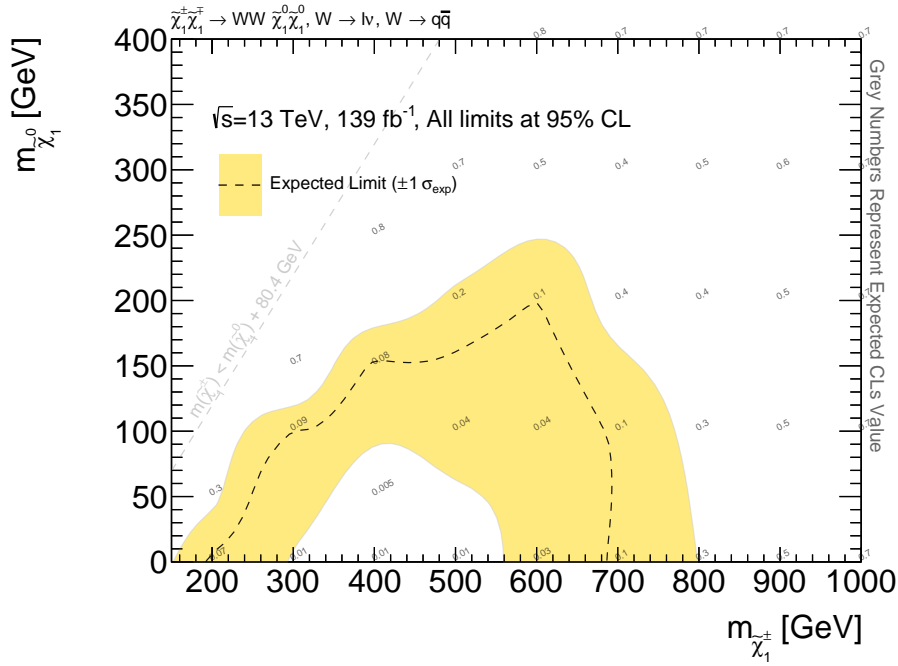


Figure 7.12: Expected exclusion limits at 95% for the C1C1-WW search.

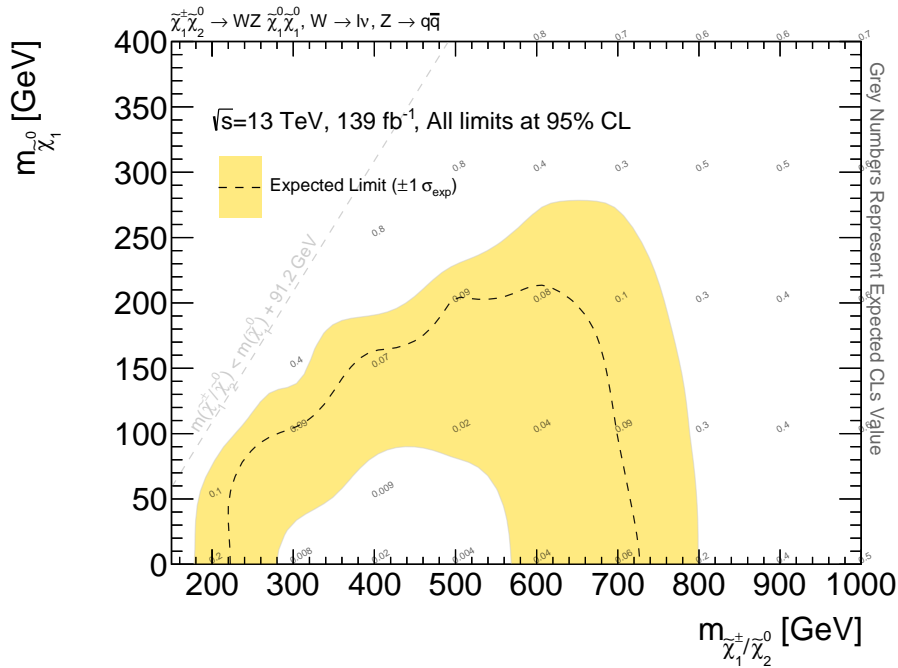


Figure 7.13: Expected exclusion limits at 95% for the C1N2-WZ search.

Conclusion

There are three main parts addressed in this thesis.

The first part targets the instrumental measurements on the ATLAS Pixel Detector during the LHC Run 2. It consists of two studies. One is a study of the pixel-level leakage current measurements. While the leakage current can be measured precisely at the module granularity level, it is much more difficult to achieve precise measurements at the pixel granularity level for the leakage current. This study makes use of the MonLeak mechanism to monitor the leakage current pixel by pixel for the IBL, the Pixel layers (B-Layer, Layer 1, Layer 2) and disks. In the Pixel layers and disks, the MonLeak scans can only measure the pixel-level leakage current in the combination with the feedback current of the preamplifier implemented in each pixel of the FE-I3 chips. Three MonLeak scans (one in 2015 and two in 2019) were performed to measure the pixel-level leakage current of the modules in the Pixel layers and disks. The MonLeak measurements show discrepancies with the power supply measurements recorded by DCS (a factor of 2 in 2019). However, one still observe a reasonable trend for the leakage currents in these MonLeak scans, being consistent with the amount of radiation damage that each of the Pixel layers has suffered. In the IBL, the MonLeak scans measure the leakage current per pixel using the general purpose 10-bit ADC (GADC) implemented on each FE-I4B chip. Two scans in 2019 were performed. Their measurements show a huge discrepancy with the DCS data (higher by a factor of one order of magnitude). Therefore, the MonLeak measurements for the IBL are not reliable and the GADC must be further calibrated. The study for the pixel-level leakage current measurements is my qualification task for the ATLAS authorship. The other study related to the ATLAS Pixel Detector is a study of pixel-hit loss rate estimation using real data. At the high luminosities of the LHC, the readout system can not always cope with the high rate of hits from the pixel detector and thus the pixel hits can be lost during the readout mechanism. There are several sources contributing to this inefficiency. So far the pixel-hit losses from these sources has not been simulated yet. In stead, only an ad-hoc fraction of 0.9% has been applied to Monte Carlo (MC) samples. This assumption was fine for Run 1, but no longer suitable for Run 2. This study develops methods in order to estimate more precisely the pixel-hit loss rates of the Double-hit (DH) inefficiency source, which is due to the loss of a hit arriving a pixel while this pixel is still busy with the previous hit, and the Late Copying (LC) inefficiency source, which is due to the loss of hits arriving Double-Columns buffers later than the trigger latency. The loss rates of these two sources can be computed for each of the pixel layers and end-caps using the pixel-ToT distribution of the layer. The preliminary DH loss rate for B-Layer, obtained with the new method using data from

the run 362776, is of 0.96%, already higher than the ad-hoc fraction of 0.9% applied for the MC simulation. This new DH loss rate should be considered as a lower limit for the loss rate in B-Layer. The new estimation methods developed in this study will also be used to compute the hit loss rates with data of the other runs for further validation as well as for studying how the loss rates scale with the luminosity.

The second part targeted in this thesis is a preliminary study of the CMOS sensor for the ITk replacement in the second-half of the HL-LHC. The current ATLAS Inner Detector will be fully replaced by an all-silicon detector referred to as the Inner Tracker (ITk) in the HL-LHC phase. The innermost barrel and end-cap ring layers of the ITk Pixel Detector are designed to be replaceable and are expected to be exchanged after having integrated half of the HL-LHC integrated luminosity (2000 fb⁻¹), i.e by the half-life of the HL-LHC. For this replacement, the CMOS pixel sensors, which are produced exploiting the CMOS technology, are particularly attractive to replace the traditional pixel sensors. The CMOS sensors have been widely used in chip industry for 20 years. They can efficiently be operated with a reduced thickness and a reduced pixel pitch size, improving the granularity and decreasing the material budget of the ITk Pixel Detector. The b - and τ -taggings would also benefit directly from the use of the CMOS sensors for the innermost ITk layers. Furthermore, the CMOS pixel module can have a monolithic design with the sensor and the electronics accommodated in the same silicon bulk. Therefore, it has a simpler production process, allowing for a quick supply with a quick reaction time. Besides, less material is needed and thus leading to much lower detector cost and reduction of the multiple scattering effect. In this thesis, the ITk Pixel Detector layout with the CMOS sensors of 50 μm thick and $25 \times 25 \mu\text{m}^2$ pixel pitch used in the innermost layers is simulated using Geant 4 and a sample of 250000 single muons with $p_T = 100$ GeV. The simulation has demonstrated the advantages of thinner and coarser innermost layers achieved by using the CMOS sensors with a reduction in the cluster ToT, width and an improved precision in the reconstruction of track transverse parameter d_0 . In the next steps, these advantages will be quantified for samples of muons with different p_T . In the future, this new detector layout with the CMOS sensors used will be simulated with samples of heavy flavor jets in order to estimate the gain in b -tagging performance, especially at high p_T .

The third part of this thesis is an analysis targeting two dedicated SUSY searches for electroweak production of charginos and neutralinos. One search, labeled C1C1-WW, is for direct production of a lightest charginos pair ($\tilde{\chi}_1^\pm \tilde{\chi}_1^\mp$) where each $\tilde{\chi}_1^\pm$ subsequently decays into a W boson and a lightest neutralino ($\tilde{\chi}_1^0$). This search focuses on a scenario where one of the W bosons decays hadronically and the other decays leptonically through a light lepton (electron or muon) and a neutrino. The other search, labeled C1N2-WZ, is for direct production of a pair of a lightest chargino and a next-to-lightest neutralino ($\tilde{\chi}_1^\pm \tilde{\chi}_2^0$), where the $\tilde{\chi}_2^0$ subsequently decays into a Z boson and a $\tilde{\chi}_1^0$, while the $\tilde{\chi}_1^\pm$ into a W boson and a $\tilde{\chi}_1^0$. This search targets a scenario where the Z boson decays hadronically and the W boson decays leptonically through a light lepton (electron or muon) and a neutrino. The signal models considered in these two searches are in the

context of the R -parity conserving simplified model, in which the $\tilde{\chi}_1^0$ is the lightest supersymmetric particle (LSP), being stable, weakly interacting and thus invisible to the detector; the $\tilde{\chi}_1^\pm$ and $\tilde{\chi}_2^0$ are nearly mass degenerate; the branching ratios of $\tilde{\chi}_1^\pm \rightarrow W\tilde{\chi}_1^0$ and $\tilde{\chi}_2^0 \rightarrow Z\tilde{\chi}_1^0$ are assumed to be 100%, while the branching ratios of the W and Z boson decays are taken to be as the SM ones. The final state is then characterized by the presence of exactly one lepton (either electron or muon) accompanied by jets and missing transverse momentum originating from the LSPs and neutrino. The C1C1-WW and C1N2-WZ searches via this one lepton final state channel are performed for the first time at ATLAS and this analysis targets an integrated luminosity of 139 fb^{-1} , corresponding to the full Run 2 data collected at the ATLAS detector. The analysis exploits reconstructed large- R jets to enhance the analysis sensitivity. Two kinds of signal region (SR), boosted SR and resolved SR, are defined. The boosted SR targets a scenario where jets from the hadronic W/Z boson decay are collinear and possibly merge with each other into large- R jets. Therefore, in the boosted SR, at least one large- R jet observed in event is required. This SR aims for signals with high mass splitting between the $\tilde{\chi}_1^\pm/\tilde{\chi}_2^0$ and the $\tilde{\chi}_1^0$. In contrast, the resolved SR focuses on another scenario where jets from the W/Z boson decay are separate from each other and thus no large- R jets observed in event is required in this SR. The resolved SR aims for signals with low mass splitting between the $\tilde{\chi}_1^\pm/\tilde{\chi}_2^0$ and the $\tilde{\chi}_1^0$. Beside the number of large- R jets, other discriminating kinematic variables are also used to define the boosted and resolved SRs. A multi-dimensional cut scan together with $N - 1$ plots are used to optimize cuts on these variables. At this stage, both the resolved and boosted SRs are split into orthogonal bins in the transverse mass m_T in order to optimize the sensitivity for all phase-space regions of the signal grid. Dedicated control regions (CRs) are defined for estimation of the expected yields of dominant backgrounds (W +jets, diboson, $t\bar{t}$) in the SRs. These CRs are designed to be orthogonal to each other and non-overlapping with the SRs. Contribution from sub-processes with at least two leptons in the final state of the diboson background (DB2L) is estimated using a separate CR which requires exactly two leptons observed in the event. This CR is also designed to minimize the overlap with 2L2J analysis SRs. In the other hand, the expected yields of diboson from sub-processes having only one lepton in the final state (DB1L) is determined using the same CRs that are designed for W +jets estimation. These CRs are defined separately for boosted and resolved scenarios. Similarly, the $t\bar{t}$ estimation relies on CRs which are also separate for resolved and boosted regimes. The other backgrounds that are minor in this analysis are determined directly from the simulation. Corresponding validation regions (VRs), being orthogonal to each other and non-overlapping with the SRs and CRs, are designed in between the SRs and CRs in order to check the extrapolation of the background estimation from the CRs to the SRs. Both the experimental and theoretical systematic uncertainties are included in the analysis. For the major backgrounds with dedicated CRs, these uncertainties are computed using the transfer factor approach, while for the minor backgrounds estimated directly from simulation, they are computed using directly the expected yields. The results obtained in this analysis has shown a compatibility of the observed

7 Search for electroweak production of charginos and neutralinos in final states with one lepton, jets and missing transverse momentum – 7.6 Results

and expected event yields in the CRs and the VRs. The model-dependent exclusion limit at 95% CL is expected to extend up to 680 (720) GeV in $m_{\tilde{\chi}_1^\pm/\tilde{\chi}_2^0}$ for massless $\tilde{\chi}_1^0$ in the C1C1-WW (C1N2-WZ) search.

Bibliography

- [1] ATLAS Collaboration. *Search for squarks, gluinos and electroweakinos in events with an isolated lepton, jets and missing transverse momentum at $\sqrt{s} = 13$ TeV with the ATLAS detector*. Tech. rep. Geneva: CERN, Nov. 2018. URL: <https://cds.cern.ch/record/2648719> (cit. on pp. 28, 162).
- [2] G. Zweig. “An SU(3) model for strong interaction symmetry and its breaking. Version 2”. In: *DEVELOPMENTS IN THE QUARK THEORY OF HADRONS. VOL. 1. 1964 - 1978*. Ed. by D. B. Lichtenberg and Simon Peter Rosen. Feb. 1964, pp. 22–101 (cit. on p. 30).
- [3] Murray Gell-Mann. “A Schematic Model of Baryons and Mesons”. In: *Phys. Lett.* 8 (1964), pp. 214–215. DOI: [10.1016/S0031-9163\(64\)92001-3](https://doi.org/10.1016/S0031-9163(64)92001-3) (cit. on p. 30).
- [4] H. Fritzsch, Murray Gell-Mann, and H. Leutwyler. “Advantages of the Color Octet Gluon Picture”. In: *Phys. Lett. B* 47 (1973), pp. 365–368. DOI: [10.1016/0370-2693\(73\)90625-4](https://doi.org/10.1016/0370-2693(73)90625-4) (cit. on p. 30).
- [5] G. D. Rochester and C. C. Butler. “Evidence for the Existence of New Unstable Elementary Particles”. In: *Nature* 160 (1947), pp. 855–857. DOI: [10.1038/160855a0](https://doi.org/10.1038/160855a0) (cit. on p. 30).
- [6] F. J. Dyson. “The Radiation Theories of Tomonaga, Schwinger, and Feynman”. In: *Phys. Rev.* 75 (3 Feb. 1949), pp. 486–502. DOI: [10.1103/PhysRev.75.486](https://doi.org/10.1103/PhysRev.75.486). URL: <https://link.aps.org/doi/10.1103/PhysRev.75.486> (cit. on p. 30).
- [7] Steven Weinberg. “Conceptual Foundations of the Unified Theory of Weak and Electromagnetic Interactions”. In: *Rev. Mod. Phys.* 52 (1980). Ed. by S. Lundqvist, pp. 515–523. DOI: [10.1103/RevModPhys.52.515](https://doi.org/10.1103/RevModPhys.52.515) (cit. on pp. 31, 34).
- [8] Abdus Salam. “Gauge unification of fundamental forces”. In: *Rev. Mod. Phys.* 52 (3 July 1980), pp. 525–538. DOI: [10.1103/RevModPhys.52.525](https://doi.org/10.1103/RevModPhys.52.525). URL: <https://link.aps.org/doi/10.1103/RevModPhys.52.525> (cit. on pp. 31, 34).
- [9] F. Englert and R. Brout. “Broken Symmetry and the Mass of Gauge Vector Mesons”. In: *Phys. Rev. Lett.* 13 (9 Aug. 1964), pp. 321–323. DOI: [10.1103/PhysRevLett.13.321](https://doi.org/10.1103/PhysRevLett.13.321). URL: <https://link.aps.org/doi/10.1103/PhysRevLett.13.321> (cit. on p. 31).
- [10] Peter W. Higgs. “Broken Symmetries and the Masses of Gauge Bosons”. In: *Phys. Rev. Lett.* 13 (1964). Ed. by J. C. Taylor, pp. 508–509. DOI: [10.1103/PhysRevLett.13.508](https://doi.org/10.1103/PhysRevLett.13.508) (cit. on p. 31).

- [11] Peter W. Higgs. “Broken symmetries, massless particles and gauge fields”. In: *Phys. Lett.* 12 (1964), pp. 132–133. DOI: [10.1016/0031-9163\(64\)91136-9](https://doi.org/10.1016/0031-9163(64)91136-9) (cit. on p. 31).
- [12] D. V. Forero, M. Tórtola, and J. W. F. Valle. “Global status of neutrino oscillation parameters after Neutrino-2012”. In: *Physical Review D* 86.7 (Oct. 2012). ISSN: 1550-2368. DOI: [10.1103/physrevd.86.073012](https://doi.org/10.1103/physrevd.86.073012). URL: <http://dx.doi.org/10.1103/PhysRevD.86.073012> (cit. on p. 32).
- [13] F. Halzen and Alan D. Martin. *QUARKS AND LEPTONS: AN INTRODUCTORY COURSE IN MODERN PARTICLE PHYSICS*. 1984. ISBN: 978-0-471-88741-6 (cit. on p. 34).
- [14] David J. Gross and Frank Wilczek. “Ultraviolet Behavior of Non-Abelian Gauge Theories”. In: *Phys. Rev. Lett.* 30 (26 June 1973), pp. 1343–1346. DOI: [10.1103/PhysRevLett.30.1343](https://doi.org/10.1103/PhysRevLett.30.1343). URL: <https://link.aps.org/doi/10.1103/PhysRevLett.30.1343> (cit. on p. 34).
- [15] H. David Politzer. “Reliable Perturbative Results for Strong Interactions?” In: *Phys. Rev. Lett.* 30 (26 June 1973), pp. 1346–1349. DOI: [10.1103/PhysRevLett.30.1346](https://doi.org/10.1103/PhysRevLett.30.1346). URL: <https://link.aps.org/doi/10.1103/PhysRevLett.30.1346> (cit. on p. 34).
- [16] C. S. Wu, E. Ambler, R. W. Hayward, et al. “Experimental Test of Parity Conservation in β Decay”. In: *Phys. Rev.* 105 (1957), pp. 1413–1414. DOI: [10.1103/PhysRev.105.1413](https://doi.org/10.1103/PhysRev.105.1413) (cit. on p. 34).
- [17] John Ellis. “Higgs Physics”. In: (Dec. 2013), 117–168. 52 p. DOI: [10.5170/CERN-2015-004.117](https://doi.org/10.5170/CERN-2015-004.117). arXiv: [1312.5672](https://arxiv.org/abs/1312.5672). URL: <https://cds.cern.ch/record/1638469> (cit. on p. 37).
- [18] Nicola Cabibbo. “Unitary Symmetry and Leptonic Decays”. In: *Phys. Rev. Lett.* 10 (1963), pp. 531–533. DOI: [10.1103/PhysRevLett.10.531](https://doi.org/10.1103/PhysRevLett.10.531) (cit. on p. 38).
- [19] Makoto Kobayashi and Toshihide Maskawa. “CP Violation in the Renormalizable Theory of Weak Interaction”. In: *Prog. Theor. Phys.* 49 (1973), pp. 652–657. DOI: [10.1143/PTP.49.652](https://doi.org/10.1143/PTP.49.652) (cit. on p. 38).
- [20] ATLAS Collaboration. “Observation of a new particle in the search for the Standard Model Higgs boson with the ATLAS detector at the LHC”. In: *Physics Letters B* 716.1 (2012), pp. 1–29. ISSN: 0370-2693. DOI: <https://doi.org/10.1016/j.physletb.2012.08.020>. URL: <https://www.sciencedirect.com/science/article/pii/S037026931200857X> (cit. on pp. 38, 39, 41, 59, 150).
- [21] CMS Collaboration. “Observation of a new boson at a mass of 125 GeV with the CMS experiment at the LHC”. In: *Physics Letters B* 716.1 (2012), pp. 30–61. ISSN: 0370-2693. DOI: <https://doi.org/10.1016/j.physletb.2012.08.021>. URL: <https://www.sciencedirect.com/science/article/pii/S0370269312008581> (cit. on pp. 38, 41, 59, 150).

- [22] ATLAS Collaboration. “Measurement of the Higgs boson mass in the $H \rightarrow ZZ^* \rightarrow 4\ell$ and $H \rightarrow \gamma\gamma$ channels with $\sqrt{s} = 13$ TeV pp collisions using the ATLAS detector”. In: *Phys. Lett. B* 784 (June 2018), 345–366. 22 p. DOI: [10.1016/j.physletb.2018.07.050](https://doi.org/10.1016/j.physletb.2018.07.050). arXiv: [1806.00242](https://arxiv.org/abs/1806.00242). URL: <https://cds.cern.ch/record/2621113> (cit. on pp. 39, 40).
- [23] ATLAS Collaboration. “Observation of Higgs boson production in association with a top quark pair at the LHC with the ATLAS detector”. In: *Phys. Lett. B* 784 (June 2018), 173–191. 19 p. DOI: [10.1016/j.physletb.2018.07.035](https://doi.org/10.1016/j.physletb.2018.07.035). arXiv: [1806.00425](https://arxiv.org/abs/1806.00425). URL: <https://cds.cern.ch/record/2621167> (cit. on p. 40).
- [24] Albert M Sirunyan et al. “Observation of $t\bar{t}H$ production”. In: *Phys. Rev. Lett.* 120.23 (2018), p. 231801. DOI: [10.1103/PhysRevLett.120.231801](https://doi.org/10.1103/PhysRevLett.120.231801). arXiv: [1804.02610](https://arxiv.org/abs/1804.02610) [hep-ex] (cit. on p. 40).
- [25] A. M. Sirunyan et al. “Observation of Higgs boson decay to bottom quarks”. In: *Phys. Rev. Lett.* 121.12 (2018), p. 121801. DOI: [10.1103/PhysRevLett.121.121801](https://doi.org/10.1103/PhysRevLett.121.121801). arXiv: [1808.08242](https://arxiv.org/abs/1808.08242) [hep-ex] (cit. on p. 40).
- [26] ATLAS Collaboration. “Observation of $H \rightarrow b\bar{b}$ decays and VH production with the ATLAS detector”. In: *Phys. Lett. B* 786 (2018), pp. 59–86. DOI: [10.1016/j.physletb.2018.09.013](https://doi.org/10.1016/j.physletb.2018.09.013). arXiv: [1808.08238](https://arxiv.org/abs/1808.08238) [hep-ex] (cit. on p. 40).
- [27] Albert M Sirunyan et al. “Observation of the Higgs boson decay to a pair of τ leptons with the CMS detector”. In: *Phys. Lett. B* 779 (2018), pp. 283–316. DOI: [10.1016/j.physletb.2018.02.004](https://doi.org/10.1016/j.physletb.2018.02.004). arXiv: [1708.00373](https://arxiv.org/abs/1708.00373) [hep-ex] (cit. on p. 40).
- [28] ATLAS Collaboration. “Cross-section measurements of the Higgs boson decaying into a pair of τ -leptons in proton-proton collisions at $\sqrt{s} = 13$ TeV with the ATLAS detector”. In: *Phys. Rev. D* 99 (2019), p. 072001. DOI: [10.1103/PhysRevD.99.072001](https://doi.org/10.1103/PhysRevD.99.072001). arXiv: [1811.08856](https://arxiv.org/abs/1811.08856) [hep-ex] (cit. on p. 40).
- [29] ATLAS Collaboration. “Observation and measurement of Higgs boson decays to WW^* with the ATLAS detector”. In: *Phys. Rev. D* 92.1 (2015), p. 012006. DOI: [10.1103/PhysRevD.92.012006](https://doi.org/10.1103/PhysRevD.92.012006). arXiv: [1412.2641](https://arxiv.org/abs/1412.2641) [hep-ex] (cit. on p. 40).
- [30] ATLAS Collaboration. “Combined measurements of Higgs boson production and decay using up to 80 fb^{-1} of proton-proton collision data at $\sqrt{s} = 13$ TeV collected with the ATLAS experiment”. In: *Phys. Rev. D* 101 (Sept. 2019), 012002. 48 p. DOI: [10.1103/PhysRevD.101.012002](https://doi.org/10.1103/PhysRevD.101.012002). arXiv: [1909.02845](https://arxiv.org/abs/1909.02845). URL: <https://cds.cern.ch/record/2688596> (cit. on pp. 41, 42).
- [31] Emanuele Di Marco. “Studies of the Higgs boson spin and parity using the $\gamma\gamma$, ZZ , and WW decay channels with the CMS detector”. In: *Nucl. Part. Phys. Proc.* 273-275 (2016), pp. 746–752. DOI: [10.1016/j.nuclphysbps.2015.09.114](https://doi.org/10.1016/j.nuclphysbps.2015.09.114) (cit. on p. 43).

- [32] G. Arnison et al. “Experimental Observation of Isolated Large Transverse Energy Electrons with Associated Missing Energy at $\sqrt{s} = 540$ GeV”. In: *Phys. Lett. B* 122 (1983), pp. 103–116. DOI: [10.1016/0370-2693\(83\)91177-2](https://doi.org/10.1016/0370-2693(83)91177-2) (cit. on p. 41).
- [33] G. Arnison et al. “Experimental Observation of Lepton Pairs of Invariant Mass Around 95-GeV/c² at the CERN SPS Collider”. In: *Phys. Lett. B* 126 (1983), pp. 398–410. DOI: [10.1016/0370-2693\(83\)90188-0](https://doi.org/10.1016/0370-2693(83)90188-0) (cit. on p. 41).
- [34] F. Abe, H. Akimoto, A. Akopian, et al. “Observation of Top Quark Production in $p\bar{p}$ Collisions with the Collider Detector at Fermilab”. In: *Physical Review Letters* 74.14 (Apr. 1995), pp. 2626–2631. ISSN: 1079-7114. DOI: [10.1103/PhysRevLett.74.2626](https://doi.org/10.1103/PhysRevLett.74.2626). URL: <http://dx.doi.org/10.1103/PhysRevLett.74.2626> (cit. on p. 41).
- [35] S. Abachi, B. Abbott, M. Abolins, et al. “Observation of the Top Quark”. In: *Physical Review Letters* 74.14 (Apr. 1995), pp. 2632–2637. ISSN: 1079-7114. DOI: [10.1103/PhysRevLett.74.2632](https://doi.org/10.1103/PhysRevLett.74.2632). URL: <http://dx.doi.org/10.1103/PhysRevLett.74.2632> (cit. on p. 41).
- [36] K. Kodama et al. “Observation of tau neutrino interactions”. In: *Phys. Lett. B* 504 (2001), pp. 218–224. DOI: [10.1016/S0370-2693\(01\)00307-0](https://doi.org/10.1016/S0370-2693(01)00307-0). arXiv: [hep-ex/0012035](https://arxiv.org/abs/hep-ex/0012035) (cit. on p. 41).
- [37] E. Aliu et al. “Evidence for muon neutrino oscillation in an accelerator-based experiment”. In: *Phys. Rev. Lett.* 94 (2005), p. 081802. DOI: [10.1103/PhysRevLett.94.081802](https://doi.org/10.1103/PhysRevLett.94.081802). arXiv: [hep-ex/0411038](https://arxiv.org/abs/hep-ex/0411038) (cit. on p. 42).
- [38] E. Corbelli and P. Salucci. “The extended rotation curve and the dark matter halo of M33”. In: *Monthly Notices of the Royal Astronomical Society* 311.2 (Jan. 2000), pp. 441–447. ISSN: 1365-2966. DOI: [10.1046/j.1365-8711.2000.03075.x](https://doi.org/10.1046/j.1365-8711.2000.03075.x). URL: <http://dx.doi.org/10.1046/j.1365-8711.2000.03075.x> (cit. on p. 42).
- [39] F. Zwicky. “Die Rotverschiebung von extragalaktischen Nebeln”. In: *Helv. Phys. Acta* 6 (1933), pp. 110–127. DOI: [10.1007/s10714-008-0707-4](https://doi.org/10.1007/s10714-008-0707-4) (cit. on p. 42).
- [40] Gianfranco Bertone, Dan Hooper, and Joseph Silk. “Particle dark matter: evidence, candidates and constraints”. In: *Physics Reports* 405.5-6 (Jan. 2005), pp. 279–390. ISSN: 0370-1573. DOI: [10.1016/j.physrep.2004.08.031](https://doi.org/10.1016/j.physrep.2004.08.031). URL: <http://dx.doi.org/10.1016/j.physrep.2004.08.031> (cit. on p. 42).
- [41] A. D. Sakharov. “Violation of CP Invariance, C asymmetry, and baryon asymmetry of the universe”. In: *Pisma Zh. Eksp. Teor. Fiz.* 5 (1967), pp. 32–35. DOI: [10.1070/PU1991v034n05ABEH002497](https://doi.org/10.1070/PU1991v034n05ABEH002497) (cit. on p. 43).
- [42] JM Cline. “Status of electroweak phase transition and baryogenesis”. In: *Pramana* 55.1-2 (July 2000), pp. 33–42. ISSN: 0973-7111. DOI: [10.1007/s12043-000-0081-6](https://doi.org/10.1007/s12043-000-0081-6). URL: <http://dx.doi.org/10.1007/s12043-000-0081-6> (cit. on p. 43).

- [43] STEPHEN P. MARTIN. “A SUPERSYMMETRY PRIMER”. In: *Advanced Series on Directions in High Energy Physics* (July 1998), pp. 1–98. ISSN: 1793-1339. DOI: [10.1142/9789812839657_0001](https://doi.org/10.1142/9789812839657_0001). URL: http://dx.doi.org/10.1142/9789812839657_0001 (cit. on pp. 45–48, 51, 53).
- [44] Yu. A. Golfand and E. P. Likhtman. “Extension of the Algebra of Poincare Group Generators and Violation of p Invariance”. In: *JETP Lett.* 13 (1971), pp. 323–326 (cit. on p. 45).
- [45] J.-L. Gervais and B. Sakita. “Field theory interpretation of supergauges in dual models”. In: *Nuclear Physics B* 34.2 (1971), pp. 632–639. ISSN: 0550-3213. DOI: [https://doi.org/10.1016/0550-3213\(71\)90351-8](https://doi.org/10.1016/0550-3213(71)90351-8). URL: <https://www.sciencedirect.com/science/article/pii/0550321371903518> (cit. on p. 45).
- [46] D.V. Volkov and V.P. Akulov. “Is the neutrino a goldstone particle?” In: *Physics Letters B* 46.1 (1973), pp. 109–110. ISSN: 0370-2693. DOI: [https://doi.org/10.1016/0370-2693\(73\)90490-5](https://doi.org/10.1016/0370-2693(73)90490-5). URL: <https://www.sciencedirect.com/science/article/pii/0370269373904905> (cit. on p. 45).
- [47] Stuart Raby. *Supersymmetric Grand Unified Theories: From Quarks to Strings via SUSY GUTs*. Vol. 939. Springer, 2017. ISBN: 978-3-319-55253-8, 978-3-319-55255-2. DOI: [10.1007/978-3-319-55255-2](https://doi.org/10.1007/978-3-319-55255-2) (cit. on p. 45).
- [48] John R. Ellis, J. S. Hagelin, Dimitri V. Nanopoulos, et al. “Supersymmetric Relics from the Big Bang”. In: *Nucl. Phys. B* 238 (1984). Ed. by M. A. Srednicki, pp. 453–476. DOI: [10.1016/0550-3213\(84\)90461-9](https://doi.org/10.1016/0550-3213(84)90461-9) (cit. on p. 45).
- [49] Fabrizio Rompineve. “Weak Scale Baryogenesis in a Supersymmetric Scenario with R-parity violation”. In: *JHEP* 08 (2014), p. 014. DOI: [10.1007/JHEP08\(2014\)014](https://doi.org/10.1007/JHEP08(2014)014). arXiv: [1310.0840 \[hep-ph\]](https://arxiv.org/abs/1310.0840) (cit. on p. 46).
- [50] R. Barbieri and G.F. Giudice. “Upper bounds on supersymmetric particle masses”. In: *Nuclear Physics B* 306.1 (1988), pp. 63–76. ISSN: 0550-3213. DOI: [https://doi.org/10.1016/0550-3213\(88\)90171-X](https://doi.org/10.1016/0550-3213(88)90171-X). URL: <https://www.sciencedirect.com/science/article/pii/055032138890171X> (cit. on pp. 46, 150).
- [51] B. de Carlos and J.A. Casas. “One-loop analysis of the electroweak breaking in supersymmetric models and the fine-tuning problem”. In: *Physics Letters B* 309.3-4 (July 1993), pp. 320–328. ISSN: 0370-2693. DOI: [10.1016/0370-2693\(93\)90940-j](https://doi.org/10.1016/0370-2693(93)90940-j). URL: [http://dx.doi.org/10.1016/0370-2693\(93\)90940-J](http://dx.doi.org/10.1016/0370-2693(93)90940-J) (cit. on pp. 46, 150).
- [52] CSABA CSÁKI. “THE MINIMAL SUPERSYMMETRIC STANDARD MODEL”. In: *Modern Physics Letters A* 11.08 (Mar. 1996), pp. 599–613. ISSN: 1793-6632. DOI: [10.1142/S021773239600062x](https://doi.org/10.1142/S021773239600062x). URL: <http://dx.doi.org/10.1142/S021773239600062X> (cit. on p. 47).

- [53] J. Wess and B. Zumino. “A lagrangian model invariant under supergauge transformations”. In: *Physics Letters B* 49.1 (1974), pp. 52–54. ISSN: 0370-2693. DOI: [https://doi.org/10.1016/0370-2693\(74\)90578-4](https://doi.org/10.1016/0370-2693(74)90578-4). URL: <https://www.sciencedirect.com/science/article/pii/0370269374905784> (cit. on p. 47).
- [54] Edward Witten. “Constraints on Supersymmetry Breaking”. In: *Nucl. Phys. B* 202 (1982), p. 253. DOI: [10.1016/0550-3213\(82\)90071-2](https://doi.org/10.1016/0550-3213(82)90071-2) (cit. on p. 49).
- [55] Edward Witten. “Dynamical breaking of supersymmetry”. In: *Nuclear Physics B* 188.3 (1981), pp. 513–554. ISSN: 0550-3213. DOI: [https://doi.org/10.1016/0550-3213\(81\)90006-7](https://doi.org/10.1016/0550-3213(81)90006-7). URL: <https://www.sciencedirect.com/science/article/pii/0550321381900067> (cit. on p. 49).
- [56] C. Patrignani et al. “Review of Particle Physics”. In: *Chin. Phys. C* 40.10 (2016), p. 100001. DOI: [10.1088/1674-1137/40/10/100001](https://doi.org/10.1088/1674-1137/40/10/100001) (cit. on p. 51).
- [57] Pierre Fayet. “Spontaneously Broken Supersymmetric Theories of Weak, Electromagnetic and Strong Interactions”. In: *Phys. Lett. B* 69 (1977), p. 489. DOI: [10.1016/0370-2693\(77\)90852-8](https://doi.org/10.1016/0370-2693(77)90852-8) (cit. on p. 51).
- [58] Glennys R. Farrar and Pierre Fayet. “Phenomenology of the Production, Decay, and Detection of New Hadronic States Associated with Supersymmetry”. In: *Phys. Lett. B* 76 (1978), pp. 575–579. DOI: [10.1016/0370-2693\(78\)90858-4](https://doi.org/10.1016/0370-2693(78)90858-4) (cit. on p. 51).
- [59] Monoranjan Guchait. “Exact solution of the neutralino mass matrix”. In: *Z. Phys. C* 57 (1993). [Erratum: *Z.Phys.C* 61, 178 (1994)], pp. 157–164. DOI: [10.1007/BF01555748](https://doi.org/10.1007/BF01555748) (cit. on p. 52).
- [60] Ali H. Chamseddine, Richard L. Arnowitt, and Pran Nath. “Locally Supersymmetric Grand Unification”. In: *Phys. Rev. Lett.* 49 (1982), p. 970. DOI: [10.1103/PhysRevLett.49.970](https://doi.org/10.1103/PhysRevLett.49.970) (cit. on p. 53).
- [61] G.F. Giudice and R. Rattazzi. “Theories with gauge-mediated supersymmetry breaking”. In: *Physics Reports* 322.6 (Dec. 1999), pp. 419–499. ISSN: 0370-1573. DOI: [10.1016/S0370-1573\(99\)00042-3](https://doi.org/10.1016/S0370-1573(99)00042-3). URL: [http://dx.doi.org/10.1016/S0370-1573\(99\)00042-3](http://dx.doi.org/10.1016/S0370-1573(99)00042-3) (cit. on p. 54).
- [62] G. Aad, B. Abbott, J. Abdallah, et al. “Summary of the ATLAS experiment’s sensitivity to supersymmetry after LHC Run 1 - interpreted in the phenomenological MSSM”. In: *Journal of High Energy Physics* 2015.10 (Oct. 2015). ISSN: 1029-8479. DOI: [10.1007/jhep10\(2015\)134](https://doi.org/10.1007/jhep10(2015)134). URL: [http://dx.doi.org/10.1007/JHEP10\(2015\)134](http://dx.doi.org/10.1007/JHEP10(2015)134) (cit. on p. 54).
- [63] Johan Alwall, Philip C. Schuster, and Natalia Toro. “Simplified models for a first characterization of new physics at the LHC”. In: *Physical Review D* 79.7 (Apr. 2009). ISSN: 1550-2368. DOI: [10.1103/physrevd.79.075020](https://doi.org/10.1103/physrevd.79.075020). URL: <http://dx.doi.org/10.1103/PhysRevD.79.075020> (cit. on p. 55).

- [64] Daniele Alves, Nima Arkani-Hamed, Sanjay Arora, et al. “Simplified models for LHC new physics searches”. In: *Journal of Physics G: Nuclear and Particle Physics* 39.10 (Sept. 2012), p. 105005. ISSN: 1361-6471. DOI: [10.1088/0954-3899/39/10/105005](https://doi.org/10.1088/0954-3899/39/10/105005). URL: <http://dx.doi.org/10.1088/0954-3899/39/10/105005> (cit. on p. 55).
- [65] LHC SUSY Cross Section Working. *Public Results*. URL: <https://twiki.cern.ch/twiki/bin/view/LHCPhysics/SUSYCrossSections> (cit. on p. 56).
- [66] *SUSY Summary Plots June 2021*. Tech. rep. All figures including auxiliary figures are available at <https://atlas.web.cern.ch/Atlas/GROUPS/PHYSICS/PUBNOTES/ATL-PHYS-PUB-2021-019>. Geneva: CERN, June 2021. URL: <http://cds.cern.ch/record/2771785> (cit. on p. 57).
- [67] Lyndon R Evans and Philip Bryant. “LHC Machine”. In: *JINST* 3 (2008). This report is an abridged version of the LHC Design Report (CERN-2004-003), S08001. 164 p. DOI: [10.1088/1748-0221/3/08/S08001](https://doi.org/10.1088/1748-0221/3/08/S08001). URL: <https://cds.cern.ch/record/1129806> (cit. on p. 58).
- [68] ATLAS Collaboration. “The ATLAS Experiment at the CERN Large Hadron Collider”. In: *JINST* 3 (2008). Also published by CERN Geneva in 2010, S08003. 437 p. DOI: [10.1088/1748-0221/3/08/S08003](https://doi.org/10.1088/1748-0221/3/08/S08003). URL: <https://cds.cern.ch/record/1129811> (cit. on pp. 58, 61, 64, 65, 67, 69, 71, 73).
- [69] *LEP design report*. By the LEP Injector Study Group. Geneva: CERN, 1983. URL: <https://cds.cern.ch/record/98881> (cit. on p. 58).
- [70] G Apollinari, I Béjar Alonso, O Brüning, et al. *High-Luminosity Large Hadron Collider (HL-LHC): Preliminary Design Report*. CERN Yellow Reports: Monographs. Geneva: CERN, 2015. DOI: [10.5170/CERN-2015-005](https://doi.org/10.5170/CERN-2015-005). URL: <https://cds.cern.ch/record/2116337> (cit. on pp. 59, 135).
- [71] LHCb Collaboration. *Test of lepton universality in beauty-quark decays*. Tech. rep. Geneva: CERN, Mar. 2021. arXiv: [2103.11769](https://arxiv.org/abs/2103.11769). URL: <https://cds.cern.ch/record/2758740> (cit. on p. 59).
- [72] M. Banner et al. “Observation of single isolated electrons of high transverse momentum in events with missing transverse energy at the CERN pp collider”. In: *Physics Letters B* 122.5 (1983), pp. 476–485. ISSN: 0370-2693. DOI: [https://doi.org/10.1016/0370-2693\(83\)91605-2](https://doi.org/10.1016/0370-2693(83)91605-2). URL: <https://www.sciencedirect.com/science/article/pii/0370269383916052> (cit. on p. 59).
- [73] G. Arnison et al. “Experimental observation of lepton pairs of invariant mass around 95 GeV/c² at the CERN SPS collider”. In: *Physics Letters B* 126.5 (1983), pp. 398–410. ISSN: 0370-2693. DOI: [https://doi.org/10.1016/0370-2693\(83\)90188-0](https://doi.org/10.1016/0370-2693(83)90188-0). URL: <https://www.sciencedirect.com/science/article/pii/0370269383901880> (cit. on p. 59).

- [74] Esma Mobs. “The CERN accelerator complex - August 2018. Complexe des accélérateurs du CERN - Août 2018”. In: (Aug. 2018). General Photo. URL: <https://cds.cern.ch/record/2636343> (cit. on p. 60).
- [75] CMS Collaboration. “The CMS experiment at the CERN LHC. The Compact Muon Solenoid experiment”. In: *JINST* 3 (2008). Also published by CERN Geneva in 2010, S08004. 361 p. DOI: [10.1088/1748-0221/3/08/S08004](https://doi.org/10.1088/1748-0221/3/08/S08004). URL: <https://cds.cern.ch/record/1129810> (cit. on p. 61).
- [76] ALICE Collaboration. “The ALICE experiment at the CERN LHC. A Large Ion Collider Experiment”. In: *JINST* 3 (2008). Also published by CERN Geneva in 2010, S08002. 259 p. DOI: [10.1088/1748-0221/3/08/S08002](https://doi.org/10.1088/1748-0221/3/08/S08002). URL: <https://cds.cern.ch/record/1129812> (cit. on p. 61).
- [77] LHCb Collaboration. “The LHCb Detector at the LHC”. In: *JINST* 3 (2008). Also published by CERN Geneva in 2010, S08005. DOI: [10.1088/1748-0221/3/08/S08005](https://doi.org/10.1088/1748-0221/3/08/S08005). URL: <https://cds.cern.ch/record/1129809> (cit. on p. 61).
- [78] ATLAS Collaboration. *Luminosity determination in pp collisions at $\sqrt{s} = 13$ TeV using the ATLAS detector at the LHC*. Tech. rep. Geneva: CERN, June 2019. URL: <https://cds.cern.ch/record/2677054> (cit. on pp. 62, 152).
- [79] Avoni et al. “The new LUCID-2 detector for luminosity measurement and monitoring in ATLAS”. In: *JINST* 13 (2018), P07017. 33 p. DOI: [10.1088/1748-0221/13/07/P07017](https://doi.org/10.1088/1748-0221/13/07/P07017). URL: <http://cds.cern.ch/record/2633501> (cit. on p. 62).
- [80] Cindro et al. “The ATLAS beam conditions monitor”. In: *JINST* 3 (2008), P02004. DOI: [10.1088/1748-0221/3/02/P02004](https://doi.org/10.1088/1748-0221/3/02/P02004) (cit. on p. 62).
- [81] P Grafstrom and W Kozanecki. “Luminosity determination at proton colliders”. In: *Prog. Part. Nucl. Phys.* 81 (2015), 97–148. 52 p. DOI: [10.1016/j.pnnp.2014.11.002](https://doi.org/10.1016/j.pnnp.2014.11.002). URL: <https://cds.cern.ch/record/2153734> (cit. on p. 62).
- [82] “ATLAS Luminosity Public Results in Run 2”. In: (). URL: <https://twiki.cern.ch/twiki/bin/view/AtlasPublic/LuminosityPublicResultsRun2> (cit. on pp. 62, 64).
- [83] ATLAS Collaboration. “The ATLAS Inner Detector commissioning and calibration. The ATLAS Inner Detector commissioning and calibration”. In: *Eur. Phys. J. C* 70 (June 2010). Comments: 34 pages, 25 figures, 787–821. 34 p. DOI: [10.1140/epjc/s10052-010-1366-7](https://doi.org/10.1140/epjc/s10052-010-1366-7). arXiv: [1004.5293](https://arxiv.org/abs/1004.5293). URL: <https://cds.cern.ch/record/1262789> (cit. on p. 66).
- [84] ATLAS Collaboration. “Studies of the performance of the ATLAS detector using cosmic-ray muons”. In: *The European Physical Journal C* 71.3 (Mar. 2011). ISSN: 1434-6052. DOI: [10.1140/epjc/s10052-011-1593-6](https://doi.org/10.1140/epjc/s10052-011-1593-6). URL: <http://dx.doi.org/10.1140/epjc/s10052-011-1593-6> (cit. on p. 66).

- [85] M Capeans, G Darbo, K Einsweiler, et al. *ATLAS Insertable B-Layer Technical Design Report*. Tech. rep. Sept. 2010. URL: <https://cds.cern.ch/record/1291633> (cit. on p. 67).
- [86] *ATLAS liquid-argon calorimeter: Technical Design Report*. Technical design report. ATLAS. Geneva: CERN, 1996. URL: <https://cds.cern.ch/record/331061> (cit. on p. 70).
- [87] ATLAS Collaboration. “Electron and photon energy calibration with the ATLAS detector using 2015-2016 LHC proton-proton collision data”. In: *JINST* 14 (Dec. 2018). Submitted to JINST, P03017. 61 p. DOI: [10.1088/1748-0221/14/03/P03017](https://doi.org/10.1088/1748-0221/14/03/P03017). arXiv: [1812.03848](https://arxiv.org/abs/1812.03848). URL: <https://cds.cern.ch/record/2650720> (cit. on p. 71).
- [88] Nikiforos Nikiforou. *Performance of the ATLAS Liquid Argon Calorimeter after three years of LHC operation and plans for a future upgrade*. Tech. rep. June 2013. DOI: [10.1109/ANIMMA.2013.6728060](https://doi.org/10.1109/ANIMMA.2013.6728060). arXiv: [1306.6756](https://arxiv.org/abs/1306.6756). URL: <https://cds.cern.ch/record/1558820> (cit. on p. 71).
- [89] *ATLAS tile calorimeter: Technical Design Report*. Technical design report. ATLAS. Geneva: CERN, 1996. URL: <https://cds.cern.ch/record/331062> (cit. on p. 71).
- [90] Adragna et al. “Testbeam Studies of Production Modules of the ATLAS Tile Calorimeter”. In: *Nucl. Instrum. Methods Phys. Res., A* 606 (Feb. 2009), 362–394. 73 p. DOI: [10.1016/j.nima.2009.04.009](https://doi.org/10.1016/j.nima.2009.04.009). URL: <http://cds.cern.ch/record/1161354> (cit. on p. 72).
- [91] ATLAS Collaboration. “Jet reconstruction and performance using particle flow with the ATLAS Detector”. In: *Eur. Phys. J. C* 77 (Mar. 2017), 466. 67 p. DOI: [10.1140/epjc/s10052-017-5031-2](https://doi.org/10.1140/epjc/s10052-017-5031-2). arXiv: [1703.10485](https://arxiv.org/abs/1703.10485). URL: <https://cds.cern.ch/record/2257597> (cit. on pp. 72, 90).
- [92] ATLAS Collaboration. “The ATLAS Forward Calorimeter”. In: *Journal of Instrumentation* 3.02 (Feb. 2008), P02010–P02010. DOI: [10.1088/1748-0221/3/02/p02010](https://doi.org/10.1088/1748-0221/3/02/p02010). URL: <https://doi.org/10.1088/1748-0221/3/02/p02010> (cit. on p. 72).
- [93] ATLAS Collaboration. *ATLAS muon spectrometer: Technical Design Report*. Technical design report. ATLAS. Geneva: CERN, 1997. URL: <https://cds.cern.ch/record/331068> (cit. on p. 72).
- [94] ATLAS Collaboration. “Operation of the ATLAS trigger system in Run 2”. In: *Journal of Instrumentation* 15.10 (Oct. 2020), P10004–P10004. DOI: [10.1088/1748-0221/15/10/p10004](https://doi.org/10.1088/1748-0221/15/10/p10004). URL: <https://doi.org/10.1088/1748-0221/15/10/p10004> (cit. on pp. 74, 75).
- [95] Joao Pequeno. “Event Cross Section in a computer generated image of the ATLAS detector.” Mar. 2008. URL: <http://cds.cern.ch/record/1096081> (cit. on p. 76).

- [96] ATLAS Collaboration. “Performance of the ATLAS Track Reconstruction Algorithms in Dense Environments in LHC run 2. Performance of the ATLAS Track Reconstruction Algorithms in Dense Environments in LHC run 2”. In: *Eur. Phys. J. C* 77 (Apr. 2017), 673. 44 p. DOI: [10.1140/epjc/s10052-017-5225-7](https://doi.org/10.1140/epjc/s10052-017-5225-7). arXiv: [1704.07983](https://arxiv.org/abs/1704.07983). URL: <https://cds.cern.ch/record/2261156> (cit. on pp. 76, 78).
- [97] ATLAS Collaboration. “Performance of the ATLAS Inner Detector Track and Vertex Reconstruction in the High Pile-Up LHC Environment”. In: (Mar. 2012) (cit. on p. 76).
- [98] R. Frühwirth. “Application of Kalman filtering to track and vertex fitting”. In: *Nuclear Instruments and Methods in Physics Research Section A: Accelerators, Spectrometers, Detectors and Associated Equipment* 262.2 (1987), pp. 444–450. ISSN: 0168-9002. DOI: [https://doi.org/10.1016/0168-9002\(87\)90887-4](https://doi.org/10.1016/0168-9002(87)90887-4). URL: <https://www.sciencedirect.com/science/article/pii/0168900287908874> (cit. on p. 77).
- [99] ATLAS Collaboration. *Comparison of Run1 and Run2 impact parameter resolution*. URL: <https://atlas.web.cern.ch/Atlas/GROUPS/PHYSICS/PLOTS/IDTR-2015-007> (cit. on p. 78).
- [100] ATLAS Collaboration. *Performance of primary vertex reconstruction in proton-proton collisions at $\sqrt{s} = 7$ TeV in the ATLAS experiment*. Tech. rep. Geneva: CERN, July 2010. URL: <https://cds.cern.ch/record/1281344> (cit. on p. 78).
- [101] R. Frühwirth, W. Waltenberger, and P. Vanlaer. “Adaptive vertex fitting”. In: *J. Phys. G* 34 (2007), N343. DOI: [10.1088/0954-3899/34/12/N01](https://doi.org/10.1088/0954-3899/34/12/N01) (cit. on p. 79).
- [102] ATLAS Collaboration. *Vertex Reconstruction Performance of the ATLAS Detector at $\sqrt{s} = 13$ TeV*. Tech. rep. Geneva: CERN, July 2015. URL: <http://cds.cern.ch/record/2037717> (cit. on p. 79).
- [103] M. Aaboud, G. Aad, B. Abbott, et al. “Electron reconstruction and identification in the ATLAS experiment using the 2015 and 2016 LHC proton–proton collision data at $\sqrt{s} = 13$ TeV”. In: *The European Physical Journal C* 79.8 (Aug. 2019). ISSN: 1434-6052. DOI: [10.1140/epjc/s10052-019-7140-6](https://doi.org/10.1140/epjc/s10052-019-7140-6). URL: <http://dx.doi.org/10.1140/epjc/s10052-019-7140-6> (cit. on p. 80).
- [104] ATLAS Collaboration. “Measurement of the photon identification efficiencies with the ATLAS detector using LHC Run 2 data collected in 2015 and 2016”. In: *The European Physical Journal C* 79.3 (Mar. 2019). ISSN: 1434-6052. DOI: [10.1140/epjc/s10052-019-6650-6](https://doi.org/10.1140/epjc/s10052-019-6650-6). URL: <http://dx.doi.org/10.1140/epjc/s10052-019-6650-6> (cit. on p. 80).
- [105] *Electron efficiency measurements with the ATLAS detector using the 2015 LHC proton-proton collision data*. Tech. rep. Geneva: CERN, June 2016. URL: <https://cds.cern.ch/record/2157687> (cit. on pp. 80, 81).

- [106] W Lampl, S Laplace, D Lelas, et al. *Calorimeter Clustering Algorithms: Description and Performance*. Tech. rep. Geneva: CERN, Apr. 2008. URL: <https://cds.cern.ch/record/1099735> (cit. on p. 80).
- [107] *Photon identification in 2015 ATLAS data*. Tech. rep. Geneva: CERN, Aug. 2016. URL: <https://cds.cern.ch/record/2203125> (cit. on p. 81).
- [108] ATLAS Collaboration. “Muon reconstruction performance of the ATLAS detector in proton–proton collision data at $\sqrt{s}=13$ TeV. Muon reconstruction performance of the ATLAS detector in proton–proton collision data at $\sqrt{s}=13$ TeV”. In: *Eur. Phys. J. C* 76 (Mar. 2016), 292. 45 p. DOI: [10.1140/epjc/s10052-016-4120-y](https://doi.org/10.1140/epjc/s10052-016-4120-y). arXiv: [1603.05598](https://arxiv.org/abs/1603.05598). URL: <https://cds.cern.ch/record/2139897> (cit. on pp. 82, 83).
- [109] ATLAS Collaboration. “Topological cell clustering in the ATLAS calorimeters and its performance in LHC Run 1. Topological cell clustering in the ATLAS calorimeters and its performance in LHC Run 1”. In: *Eur. Phys. J. C* 77 (Mar. 2016), 490. 87 p. DOI: [10.1140/epjc/s10052-017-5004-5](https://doi.org/10.1140/epjc/s10052-017-5004-5). arXiv: [1603.02934](https://arxiv.org/abs/1603.02934). URL: <https://cds.cern.ch/record/2138166> (cit. on p. 84).
- [110] Matteo Cacciari, Gavin P Salam, and Gregory Soyez. “The anti-ktjet clustering algorithm”. In: *Journal of High Energy Physics* 2008.04 (Apr. 2008), pp. 063–063. ISSN: 1029-8479. DOI: [10.1088/1126-6708/2008/04/063](https://doi.org/10.1088/1126-6708/2008/04/063). URL: <http://dx.doi.org/10.1088/1126-6708/2008/04/063> (cit. on p. 84).
- [111] CMS Collaboration. *Jets at CMS and the determination of their energy scale*. URL: <https://cms.cern/news/jets-cms-and-determination-their-energy-scale> (cit. on p. 84).
- [112] Angela Barbaro Galtieri, Fabrizio Margaroli, and Igor Volobouev. “Precision measurements of the top quark mass from the Tevatron in the pre-LHC era”. In: *Reports on Progress in Physics* 75.5 (Apr. 2012), p. 056201. ISSN: 1361-6633. DOI: [10.1088/0034-4885/75/5/056201](https://doi.org/10.1088/0034-4885/75/5/056201). URL: <http://dx.doi.org/10.1088/0034-4885/75/5/056201> (cit. on p. 85).
- [113] Michela Paganini and. “Machine Learning Algorithms for b-Jet Tagging at the ATLAS Experiment”. In: *Journal of Physics: Conference Series* 1085 (Sept. 2018), p. 042031. DOI: [10.1088/1742-6596/1085/4/042031](https://doi.org/10.1088/1742-6596/1085/4/042031). URL: <https://doi.org/10.1088/1742-6596/1085/4/042031> (cit. on p. 86).
- [114] ATLAS Collaboration. *Secondary vertex finding for jet flavour identification with the ATLAS detector*. Tech. rep. Geneva: CERN, June 2017. URL: <http://cds.cern.ch/record/2270366> (cit. on p. 86).
- [115] *Commissioning of the ATLAS high-performance b-tagging algorithms in the 7 TeV collision data*. Tech. rep. Geneva: CERN, July 2011. URL: <https://cds.cern.ch/record/1369219> (cit. on p. 86).

- [116] *Impact parameter-based b-tagging algorithms in the 7 TeV collision data with the ATLAS detector: the TrackCounting and JetProb algorithms*. Tech. rep. Geneva: CERN, July 2010. URL: <https://cds.cern.ch/record/1277681> (cit. on p. 86).
- [117] *Identification of Jets Containing b-Hadrons with Recurrent Neural Networks at the ATLAS Experiment*. Tech. rep. Geneva: CERN, Mar. 2017. URL: <http://cds.cern.ch/record/2255226> (cit. on p. 86).
- [118] *Optimisation and performance studies of the ATLAS b-tagging algorithms for the 2017-18 LHC run*. Tech. rep. Geneva: CERN, July 2017. URL: <https://cds.cern.ch/record/2273281> (cit. on p. 87).
- [119] Andreas Höcker, Peter Speckmayer, Jörg Stelzer, et al. “TMVA: The Toolkit for Multivariate Data Analysis with ROOT”. In: (2008). DOI: [10.5170/CERN-2008-001.184](https://doi.org/10.5170/CERN-2008-001.184). URL: <https://cds.cern.ch/record/1099990> (cit. on p. 87).
- [120] *Calibration of light-flavour b-jet mistagging rates using ATLAS proton-proton collision data at $\sqrt{s} = 13$ TeV*. Tech. rep. Geneva: CERN, Apr. 2018. URL: <https://cds.cern.ch/record/2314418> (cit. on p. 87).
- [121] F. Chollet et al. *Keras*. URL: <https://keras.io> (cit. on p. 87).
- [122] The Theano Development Team et al. *Theano: A Python framework for fast computation of mathematical expressions*. 2016. arXiv: [1605.02688](https://arxiv.org/abs/1605.02688) [cs.SC] (cit. on p. 87).
- [123] Diederik P. Kingma and Jimmy Ba. *Adam: A Method for Stochastic Optimization*. 2017. arXiv: [1412.6980](https://arxiv.org/abs/1412.6980) [cs.LG] (cit. on p. 87).
- [124] ATLAS Collaboration. “ATLAS b-jet identification performance and efficiency measurement with $t\bar{t}$ events in pp collisions at $\sqrt{s} = 13$ TeV”. In: *Eur. Phys. J. C* 79 (July 2019), 970. 36 p. DOI: [10.1140/epjc/s10052-019-7450-8](https://doi.org/10.1140/epjc/s10052-019-7450-8). arXiv: [1907.05120](https://arxiv.org/abs/1907.05120). URL: <https://cds.cern.ch/record/2682119> (cit. on p. 88).
- [125] ATLAS Collaboration. “Jet energy scale measurements and their systematic uncertainties in proton-proton collisions at $\sqrt{s} = 13$ TeV with the ATLAS detector. Jet energy scale measurements and their systematic uncertainties in proton-proton collisions at $\sqrt{s} = 13$ TeV with the ATLAS detector”. In: *Phys. Rev. D* 96 (Mar. 2017), 072002. 36 p. DOI: [10.1103/PhysRevD.96.072002](https://doi.org/10.1103/PhysRevD.96.072002). arXiv: [1703.09665](https://arxiv.org/abs/1703.09665). URL: <https://cds.cern.ch/record/2257300> (cit. on p. 89).
- [126] ATLAS Collaboration. “Performance of missing transverse momentum reconstruction with the ATLAS detector using proton-proton collisions at $\sqrt{s} = 13$ TeV”. In: *Eur. Phys. J. C* 78 (Feb. 2018), 903. 66 p. DOI: [10.1140/epjc/s10052-018-6288-9](https://doi.org/10.1140/epjc/s10052-018-6288-9). arXiv: [1802.08168](https://arxiv.org/abs/1802.08168). URL: <https://cds.cern.ch/record/2305380> (cit. on p. 90).
- [127] I Bird, P Buncic, F Carminati, et al. *Update of the Computing Models of the WLCG and the LHC Experiments*. Tech. rep. Apr. 2014. URL: <https://cds.cern.ch/record/1695401> (cit. on p. 91).

- [128] John C. Collins, Davison E. Soper, and George F. Sterman. “Factorization of Hard Processes in QCD”. In: *Adv. Ser. Direct. High Energy Phys.* 5 (1989), pp. 1–91. DOI: [10.1142/9789814503266_0001](https://doi.org/10.1142/9789814503266_0001). arXiv: [hep-ph/0409313](https://arxiv.org/abs/hep-ph/0409313) (cit. on p. 92).
- [129] M Dobbs and J B Hansen. *The HepMC C++ Monte Carlo Event Record for High Energy Physics*. Tech. rep. Geneva: CERN, June 2000. URL: <https://cds.cern.ch/record/684090> (cit. on p. 92).
- [130] Stefano Frixione and Bryan R Webber. “Matching NLO QCD computations and parton shower simulations”. In: *Journal of High Energy Physics* 2002.06 (June 2002), pp. 029–029. DOI: [10.1088/1126-6708/2002/06/029](https://doi.org/10.1088/1126-6708/2002/06/029). URL: <https://doi.org/10.1088/1126-6708/2002/06/029> (cit. on p. 93).
- [131] Paolo Nason. “A New Method for Combining NLO QCD with Shower Monte Carlo Algorithms”. In: *Journal of High Energy Physics* 2004.11 (Nov. 2004), pp. 040–040. DOI: [10.1088/1126-6708/2004/11/040](https://doi.org/10.1088/1126-6708/2004/11/040). URL: <https://doi.org/10.1088/1126-6708/2004/11/040> (cit. on p. 93).
- [132] Stefano Frixione, Paolo Nason, and Carlo Oleari. “Matching NLO QCD computations with parton shower simulations: the POWHEG method”. In: *Journal of High Energy Physics* 2007.11 (Nov. 2007), pp. 070–070. DOI: [10.1088/1126-6708/2007/11/070](https://doi.org/10.1088/1126-6708/2007/11/070). URL: <https://doi.org/10.1088/1126-6708/2007/11/070> (cit. on p. 93).
- [133] Simone Alioli, Paolo Nason, Carlo Oleari, et al. “A general framework for implementing NLO calculations in shower Monte Carlo programs: the POWHEG BOX”. In: *Journal of High Energy Physics* 2010.6 (June 2010). ISSN: 1029-8479. DOI: [10.1007/jhep06\(2010\)043](https://doi.org/10.1007/jhep06(2010)043). URL: [http://dx.doi.org/10.1007/JHEP06\(2010\)043](http://dx.doi.org/10.1007/JHEP06(2010)043) (cit. on pp. 93, 153).
- [134] Stefan Hoeche, Frank Krauss, Marek Schonherr, et al. “QCD matrix elements + parton showers: The NLO case”. In: *JHEP* 04 (2013), p. 027. DOI: [10.1007/JHEP04\(2013\)027](https://doi.org/10.1007/JHEP04(2013)027). arXiv: [1207.5030](https://arxiv.org/abs/1207.5030) [[hep-ph](https://arxiv.org/abs/hep-ph)] (cit. on p. 93).
- [135] Stefano Catani, Frank Krauss, Bryan R Webber, et al. “QCD Matrix Elements + Parton Showers”. In: *Journal of High Energy Physics* 2001.11 (Nov. 2001), pp. 063–063. DOI: [10.1088/1126-6708/2001/11/063](https://doi.org/10.1088/1126-6708/2001/11/063). URL: <https://doi.org/10.1088/1126-6708/2001/11/063> (cit. on p. 93).
- [136] Torbjörn Sjöstrand, Stephen Mrenna, and Peter Skands. “PYTHIA 6.4 physics and manual”. In: *Journal of High Energy Physics* 2006.05 (May 2006), pp. 026–026. DOI: [10.1088/1126-6708/2006/05/026](https://doi.org/10.1088/1126-6708/2006/05/026). URL: <https://doi.org/10.1088/1126-6708/2006/05/026> (cit. on p. 93).

- [137] Torbjörn Sjöstrand, Stephen Mrenna, and Peter Skands. “A brief introduction to PYTHIA 8.1”. In: *Computer Physics Communications* 178.11 (2008), pp. 852–867. ISSN: 0010-4655. DOI: <https://doi.org/10.1016/j.cpc.2008.01.036>. URL: <https://www.sciencedirect.com/science/article/pii/S0010465508000441> (cit. on pp. 93, 152).
- [138] Manuel Bähr, Stefan Gieseke, Martyn A. Gigg, et al. “Herwig++ physics and manual”. In: *The European Physical Journal C* 58.4 (Nov. 2008), pp. 639–707. ISSN: 1434-6052. DOI: [10.1140/epjc/s10052-008-0798-9](https://doi.org/10.1140/epjc/s10052-008-0798-9). URL: <http://dx.doi.org/10.1140/epjc/s10052-008-0798-9> (cit. on p. 93).
- [139] Johannes Bellm, Stefan Gieseke, David Grellscheid, et al. “Herwig 7.0/Herwig++ 3.0 release note”. In: *The European Physical Journal C* 76.4 (Apr. 2016). ISSN: 1434-6052. DOI: [10.1140/epjc/s10052-016-4018-8](https://doi.org/10.1140/epjc/s10052-016-4018-8). URL: <http://dx.doi.org/10.1140/epjc/s10052-016-4018-8> (cit. on p. 93).
- [140] S. Agostinelli, J. Allison, K. Amako, et al. “Geant4—a simulation toolkit”. In: *Nuclear Instruments and Methods in Physics Research Section A: Accelerators, Spectrometers, Detectors and Associated Equipment* 506.3 (2003), pp. 250–303. ISSN: 0168-9002. DOI: [https://doi.org/10.1016/S0168-9002\(03\)01368-8](https://doi.org/10.1016/S0168-9002(03)01368-8). URL: <https://www.sciencedirect.com/science/article/pii/S0168900203013688> (cit. on pp. 93, 142).
- [141] W Lukas. *Fast Simulation for ATLAS: Atlfast-II and ISF*. Tech. rep. Geneva: CERN, June 2012. DOI: [10.1088/1742-6596/396/2/022031](https://doi.org/10.1088/1742-6596/396/2/022031). URL: <https://cds.cern.ch/record/1458503> (cit. on pp. 93, 94).
- [142] ATLAS Collaboration. “ATLAS pixel detector electronics and sensors”. In: *JINST* 3 (2008), P07007. DOI: [10.1088/1748-0221/3/07/P07007](https://doi.org/10.1088/1748-0221/3/07/P07007). URL: <https://cds.cern.ch/record/1119279> (cit. on pp. 95, 97, 100, 104).
- [143] B. Abbott, J. Albert, F. Alberti, et al. “Production and integration of the ATLAS Insertable B-Layer”. In: *Journal of Instrumentation* 13.05 (May 2018), T05008–T05008. ISSN: 1748-0221. DOI: [10.1088/1748-0221/13/05/t05008](https://doi.org/10.1088/1748-0221/13/05/t05008). URL: <http://dx.doi.org/10.1088/1748-0221/13/05/T05008> (cit. on pp. 95–97, 100–102).
- [144] M Garcia-Sciveres, D Arutinov, M Barbero, et al. *The FE-I4 Pixel Readout Integrated Circuit*. Tech. rep. Geneva: CERN, Jan. 2010. URL: <https://cds.cern.ch/record/1231359> (cit. on pp. 95, 108, 118, 119).
- [145] I. Peric, L. Blanquart, G. Comes, et al. “The FEI3 readout chip for the ATLAS pixel detector”. In: *Nucl. Instrum. Meth. A* 565 (2006). Ed. by J. Grosse-Knetter, H. Krueger, and N. Wermes, pp. 178–187. DOI: [10.1016/j.nima.2006.05.032](https://doi.org/10.1016/j.nima.2006.05.032) (cit. on pp. 95, 108).
- [146] Michael Beimforde. “Development of thin sensors and a novel interconnection technology for the upgrade of the ATLAS pixel system”. June 2010. URL: <https://cds.cern.ch/record/1511029> (cit. on p. 99).

- [147] G Lindström, M Ahmed, S Albergo, et al. “Radiation hard silicon detectors developments by the RD48 (ROSE) collaboration”. In: *Nuclear Instruments and Methods in Physics Research Section A: Accelerators, Spectrometers, Detectors and Associated Equipment* 466.2 (2001), pp. 308–326. ISSN: 0168-9002. DOI: [https://doi.org/10.1016/S0168-9002\(01\)00560-5](https://doi.org/10.1016/S0168-9002(01)00560-5). URL: <https://www.sciencedirect.com/science/article/pii/S0168900201005605> (cit. on p. 99).
- [148] Arturo Ayon, R Bayt, and Kenneth Breuer. “Deep reactive ion etching: A promising technology for micro- and nanosatellites”. In: *Smart Materials and Structures* 10 (Nov. 2001), p. 1135. DOI: [10.1088/0964-1726/10/6/302](https://doi.org/10.1088/0964-1726/10/6/302) (cit. on p. 101).
- [149] ATLAS Collaboration. “Development of radiation hard pixel modules employing planar n-in-p siliconsensors with active edges for the ATLAS detector at HL-LHC”. 2015. URL: <http://cds.cern.ch/record/2676574> (cit. on p. 102).
- [150] S.I. Parker, C.J. Kenney, and J. Segal. “3D — A proposed new architecture for solid-state radiation detectors”. In: *Nuclear Instruments and Methods in Physics Research Section A: Accelerators, Spectrometers, Detectors and Associated Equipment* 395.3 (1997), pp. 328–343. ISSN: 0168-9002. DOI: [https://doi.org/10.1016/S0168-9002\(97\)00694-3](https://doi.org/10.1016/S0168-9002(97)00694-3). URL: <https://www.sciencedirect.com/science/article/pii/S0168900297006943> (cit. on p. 101).
- [151] C. Da Via et al. “3D active edge silicon sensors: Device processing, yield and QA for the ATLAS-IBL production”. In: *Nucl. Instrum. Methods Phys. Res., A* 699 (2013), 18–21. 4 p. DOI: [10.1016/j.nima.2012.05.070](https://doi.org/10.1016/j.nima.2012.05.070). URL: <https://cds.cern.ch/record/1709857> (cit. on p. 101).
- [152] G. Pellegrini, M. Lozano, M. Ullán, et al. “First double-sided 3-D detectors fabricated at CNM-IMB”. In: *Nuclear Instruments and Methods in Physics Research Section A: Accelerators, Spectrometers, Detectors and Associated Equipment* 592.1 (2008), pp. 38–43. ISSN: 0168-9002. DOI: <https://doi.org/10.1016/j.nima.2008.03.119>. URL: <https://www.sciencedirect.com/science/article/pii/S0168900208004828> (cit. on p. 102).
- [153] Andrea Zoboli, Maurizio Boscardin, Luciano Bosisio, et al. “Double-Sided, Double-Type-Column 3-D Detectors: Design, Fabrication, and Technology Evaluation”. In: *IEEE Transactions on Nuclear Science* 55.5 (2008), pp. 2775–2784. DOI: [10.1109/TNS.2008.2002885](https://doi.org/10.1109/TNS.2008.2002885) (cit. on p. 102).
- [154] A Macchiolo, L Andricek, M Ellenburg, et al. “Thin n-in-p pixel sensors and the SLID-ICV vertical integration technology for the ATLAS upgrade at the HL-LHC”. In: *Nucl. Instrum. Methods Phys. Res., A* 731 (Oct. 2012), pp. 210–215. URL: <https://cds.cern.ch/record/1693128> (cit. on p. 103).

- [155] V Zivkovic, J-D Schipper, M Garcia-Sciveres, et al. “The FE-I4 pixel readout system-on-chip resubmission for the insertable B-Layer project”. In: *Journal of Instrumentation* 7.02 (Feb. 2012), pp. C02050–C02050. DOI: [10.1088/1748-0221/7/02/c02050](https://doi.org/10.1088/1748-0221/7/02/c02050). URL: <https://doi.org/10.1088/1748-0221/7/02/c02050> (cit. on p. 103).
- [156] M Backhaus. “Characterization of the FE-I4B pixel readout chip production run for the ATLAS Insertable B-layer upgrade”. In: *Journal of Instrumentation* 8.03 (Mar. 2013), pp. C03013–C03013. ISSN: 1748-0221. DOI: [10.1088/1748-0221/8/03/c03013](https://doi.org/10.1088/1748-0221/8/03/c03013). URL: <http://dx.doi.org/10.1088/1748-0221/8/03/c03013> (cit. on p. 103).
- [157] Marlon et al Barbero. “FE-I4 ATLAS pixel chip design”. In: *PoS VERTEX2009* (2009), p. 027. DOI: [10.22323/1.095.0027](https://doi.org/10.22323/1.095.0027) (cit. on p. 103).
- [158] M Karagounis. “Development of the ATLAS FE-I4 pixel readout IC for b-layer Upgrade and Super-LHC”. In: (2008). DOI: [10.5170/CERN-2008-008.70](https://doi.org/10.5170/CERN-2008-008.70). URL: <https://cds.cern.ch/record/1158505> (cit. on p. 104).
- [159] Michael Moll. “Radiation damage in silicon particle detectors: Microscopic defects and macroscopic properties”. PhD thesis. Hamburg U., 1999 (cit. on p. 106).
- [160] *A Leakage Current-based Measurement of the Radiation Damage in the ATLAS Pixel Detector*. Tech. rep. Geneva: CERN, Aug. 2014. URL: <https://cds.cern.ch/record/1752122> (cit. on p. 107).
- [161] Iseg Spezialelektronik GmbH. *High Voltage Power Supply EHQ F607n-E, Operators Manual*. URL: <https://iseg-hv.com> (cit. on p. 107).
- [162] K Lantsch et al. “The ATLAS Detector Control System”. In: *Journal of Physics: Conference Series* 396.1 (Dec. 2012), p. 012028. DOI: [10.1088/1742-6596/396/1/012028](https://doi.org/10.1088/1742-6596/396/1/012028). URL: <https://doi.org/10.1088/1742-6596/396/1/012028> (cit. on p. 107).
- [163] ATLAS Collaboration. “ATLAS Detector Control System Data Viewer”. In: *Conf. Proc.* C111010 (2011), MOPKN019. 4 p. URL: <https://cds.cern.ch/record/1564291> (cit. on p. 107).
- [164] ATLAS Collaboration. “The FEI3 readout chip for the ATLAS pixel detector”. In: *Nuclear Instruments and Methods in Physics Research Section A: Accelerators, Spectrometers, Detectors and Associated Equipment* 565.1 (2006), pp. 178–187. ISSN: 0168-9002. DOI: <https://doi.org/10.1016/j.nima.2006.05.032>. URL: <https://www.sciencedirect.com/science/article/pii/S0168900206007649> (cit. on p. 108).
- [165] CERN. *The HL-LHC project*. URL: <https://hilumilhc.web.cern.ch/content/hl-lhc-project> (cit. on p. 134).

- [166] Burkhard Schmidt. “The High-Luminosity upgrade of the LHC: Physics and Technology Challenges for the Accelerator and the Experiments”. In: *Journal of Physics: Conference Series* 706 (Apr. 2016), p. 022002. DOI: [10.1088/1742-6596/706/2/022002](https://doi.org/10.1088/1742-6596/706/2/022002). URL: <https://doi.org/10.1088/1742-6596/706/2/022002> (cit. on p. 135).
- [167] P. Ferracin et al. “The HL-LHC Low- β Quadrupole Magnet MQXF: From Short Models to Long Prototypes”. In: *IEEE Transactions on Applied Superconductivity* 29.5 (2019), pp. 1–9. DOI: [10.1109/TASC.2019.2895908](https://doi.org/10.1109/TASC.2019.2895908) (cit. on p. 135).
- [168] *Projections for measurements of Higgs boson cross sections, branching ratios, coupling parameters and mass with the ATLAS detector at the HL-LHC*. Tech. rep. Geneva: CERN, Dec. 2018. URL: <https://cds.cern.ch/record/2652762> (cit. on p. 135).
- [169] A. Liss and J. Nielsen. *Physics at a High-Luminosity LHC with ATLAS*. Tech. rep. Geneva: CERN, July 2013. arXiv: [1307.7292](https://arxiv.org/abs/1307.7292). URL: <https://cds.cern.ch/record/1564937> (cit. on p. 136).
- [170] Collaboration ATLAS. *Letter of Intent for the Phase-II Upgrade of the ATLAS Experiment*. Tech. rep. Geneva: CERN, Dec. 2012. URL: <https://cds.cern.ch/record/1502664> (cit. on p. 137).
- [171] ATLAS Collaboration. *Technical Proposal: A High-Granularity Timing Detector for the ATLAS Phase-II Upgrade*. Tech. rep. Geneva: CERN, June 2018. URL: <https://cds.cern.ch/record/2623663> (cit. on p. 137).
- [172] *Expected tracking and related performance with the updated ATLAS Inner Tracker layout at the High-Luminosity LHC*. Tech. rep. Geneva: CERN, July 2021. URL: <http://cds.cern.ch/record/2776651> (cit. on pp. 138, 139).
- [173] *Technical Design Report for the ATLAS Inner Tracker Strip Detector*. Tech. rep. Geneva: CERN, Apr. 2017. URL: <https://cds.cern.ch/record/2257755> (cit. on pp. 139, 140).
- [174] RD-53 Collaboration Home Page. URL: <http://rd53.web.cern.ch/> (cit. on p. 140).
- [175] *Technical Design Report for the ATLAS Inner Tracker Pixel Detector*. Tech. rep. Geneva: CERN, Sept. 2017. URL: <https://cds.cern.ch/record/2285585> (cit. on pp. 141, 142).
- [176] Maurice Garcia-Sciveres and Norbert Wermes. “A review of advances in pixel detectors for experiments with high rate and radiation”. In: *Reports on Progress in Physics* 81.6 (May 2018), p. 066101. ISSN: 1361-6633. DOI: [10.1088/1361-6633/aab064](https://doi.org/10.1088/1361-6633/aab064). URL: <http://dx.doi.org/10.1088/1361-6633/aab064> (cit. on p. 141).
- [177] Jacobus Willem van Hoorn. “Study and Development of a novel Silicon Pixel Detector for the Upgrade of the ALICE Inner Tracking System”. Oct. 2015. URL: <https://cds.cern.ch/record/2119197> (cit. on p. 142).

- [178] N. Sakai. “Naturalness in Supersymmetric Guts”. In: *Z. Phys. C* 11 (1981), p. 153. DOI: [10.1007/BF01573998](https://doi.org/10.1007/BF01573998) (cit. on p. 150).
- [179] Glennys R. Farrar and Pierre Fayet. “Phenomenology of the production, decay, and detection of new hadronic states associated with supersymmetry”. In: *Physics Letters B* 76.5 (1978), pp. 575–579. ISSN: 0370-2693. DOI: [https://doi.org/10.1016/0370-2693\(78\)90858-4](https://doi.org/10.1016/0370-2693(78)90858-4). URL: <https://www.sciencedirect.com/science/article/pii/0370269378908584> (cit. on p. 150).
- [180] Takeo Moroi. “Erratum: Muon anomalous magnetic dipole moment in the minimal supersymmetric standard model [Phys. Rev. D 53, 6565 (1996)]”. In: *Phys. Rev. D* 56 (7 Oct. 1997), pp. 4424–4424. DOI: [10.1103/PhysRevD.56.4424](https://doi.org/10.1103/PhysRevD.56.4424). URL: <https://link.aps.org/doi/10.1103/PhysRevD.56.4424> (cit. on p. 150).
- [181] Jonathan L. Feng and Takeo Moroi. “Supernatural supersymmetry: Phenomenological implications of anomaly-mediated supersymmetry breaking”. In: *Phys. Rev. D* 61 (9 Mar. 2000), p. 095004. DOI: [10.1103/PhysRevD.61.095004](https://doi.org/10.1103/PhysRevD.61.095004). URL: <https://link.aps.org/doi/10.1103/PhysRevD.61.095004> (cit. on p. 150).
- [182] G. Aad, B. Abbott, D.C. Abbott, et al. “ATLAS data quality operations and performance for 2015–2018 data-taking”. In: *Journal of Instrumentation* 15.04 (Apr. 2020), P04003–P04003. ISSN: 1748-0221. DOI: [10.1088/1748-0221/15/04/p04003](https://doi.org/10.1088/1748-0221/15/04/p04003). URL: <http://dx.doi.org/10.1088/1748-0221/15/04/P04003> (cit. on p. 152).
- [183] Richard D. Ball, Valerio Bertone, Stefano Carrazza, et al. “Parton distributions with LHC data”. In: *Nuclear Physics B* 867.2 (Feb. 2013), pp. 244–289. ISSN: 0550-3213. DOI: [10.1016/j.nuclphysb.2012.10.003](https://doi.org/10.1016/j.nuclphysb.2012.10.003). URL: <http://dx.doi.org/10.1016/j.nuclphysb.2012.10.003> (cit. on pp. 152, 153).
- [184] *The Pythia 8 A3 tune description of ATLAS minimum bias and inelastic measurements incorporating the Donnachie-Landshoff diffractive model*. Tech. rep. Geneva: CERN, Aug. 2016. URL: <https://cds.cern.ch/record/2206965> (cit. on p. 152).
- [185] J. Alwall, R. Frederix, S. Frixione, et al. “The automated computation of tree-level and next-to-leading order differential cross sections, and their matching to parton shower simulations”. In: *Journal of High Energy Physics* 2014.7 (July 2014). ISSN: 1029-8479. DOI: [10.1007/jhep07\(2014\)079](https://doi.org/10.1007/jhep07(2014)079). URL: [http://dx.doi.org/10.1007/JHEP07\(2014\)079](http://dx.doi.org/10.1007/JHEP07(2014)079) (cit. on p. 152).
- [186] *ATLAS Pythia 8 tunes to 7 TeV data*. Tech. rep. Geneva: CERN, Nov. 2014. URL: <https://cds.cern.ch/record/1966419> (cit. on p. 152).

- [187] Jonathan Debove, Benjamin Fuks, and Michael Klasen. “Threshold resummation for gaugino pair production at hadron colliders”. In: *Nuclear Physics B* 842.1 (Jan. 2011), pp. 51–85. ISSN: 0550-3213. DOI: [10.1016/j.nuclphysb.2010.08.016](https://doi.org/10.1016/j.nuclphysb.2010.08.016). URL: <http://dx.doi.org/10.1016/j.nuclphysb.2010.08.016> (cit. on p. 153).
- [188] Benjamin Fuks, Michael Klasen, David R. Lamprea, et al. “Gaugino production in proton-proton collisions at a center-of-mass energy of 8 TeV”. In: *Journal of High Energy Physics* 2012.10 (Oct. 2012). ISSN: 1029-8479. DOI: [10.1007/jhep10\(2012\)081](https://doi.org/10.1007/jhep10(2012)081). URL: [http://dx.doi.org/10.1007/JHEP10\(2012\)081](http://dx.doi.org/10.1007/JHEP10(2012)081) (cit. on p. 153).
- [189] Benjamin Fuks, Michael Klasen, David R. Lamprea, et al. “Precision predictions for electroweak superpartner production at hadron colliders with Resummino”. In: *The European Physical Journal C* 73.7 (July 2013). ISSN: 1434-6052. DOI: [10.1140/epjc/s10052-013-2480-0](https://doi.org/10.1140/epjc/s10052-013-2480-0). URL: <http://dx.doi.org/10.1140/epjc/s10052-013-2480-0> (cit. on p. 153).
- [190] J. Fiaschi and M. Klasen. “Neutralino-chargino pair production at NLO+NLL with resummation-improved parton density functions for LHC Run II”. In: *Physical Review D* 98.5 (Sept. 2018). ISSN: 2470-0029. DOI: [10.1103/physrevd.98.055014](https://doi.org/10.1103/physrevd.98.055014). URL: <http://dx.doi.org/10.1103/PhysRevD.98.055014> (cit. on p. 153).
- [191] Christoph Borschensky, Michael Krämer, Anna Kulesza, et al. “Squark and gluino production cross sections in pp collisions at $\sqrt{s} = 13, 14, 33$ and 100 TeV”. In: *The European Physical Journal C* 74.12 (Dec. 2014). ISSN: 1434-6052. DOI: [10.1140/epjc/s10052-014-3174-y](https://doi.org/10.1140/epjc/s10052-014-3174-y). URL: <http://dx.doi.org/10.1140/epjc/s10052-014-3174-y> (cit. on p. 153).
- [192] Michał Czakon and Alexander Mitov. “Top++: A program for the calculation of the top-pair cross-section at hadron colliders”. In: *Computer Physics Communications* 185.11 (Nov. 2014), pp. 2930–2938. ISSN: 0010-4655. DOI: [10.1016/j.cpc.2014.06.021](https://doi.org/10.1016/j.cpc.2014.06.021). URL: <http://dx.doi.org/10.1016/j.cpc.2014.06.021> (cit. on p. 153).
- [193] M. Aliev, H. Lacker, U. Langenfeld, et al. “HATHOR – HAdronic Top and Heavy quarks crOss section calculator”. In: *Computer Physics Communications* 182.4 (Apr. 2011), pp. 1034–1046. ISSN: 0010-4655. DOI: [10.1016/j.cpc.2010.12.040](https://doi.org/10.1016/j.cpc.2010.12.040). URL: <http://dx.doi.org/10.1016/j.cpc.2010.12.040> (cit. on p. 153).
- [194] T Gleisberg, S Höche, F Krauss, et al. “Event generation with SHERPA 1.1”. In: *Journal of High Energy Physics* 2009.02 (Feb. 2009), pp. 007–007. ISSN: 1029-8479. DOI: [10.1088/1126-6708/2009/02/007](https://doi.org/10.1088/1126-6708/2009/02/007). URL: <http://dx.doi.org/10.1088/1126-6708/2009/02/007> (cit. on p. 153).

- [195] Charalampos Anastasiou, Lance Dixon, Kirill Melnikov, et al. “High-precision QCD at hadron colliders: Electroweak gauge boson rapidity distributions at next-to-next-to leading order”. In: *Physical Review D* 69.9 (May 2004). ISSN: 1550-2368. DOI: [10.1103/physrevd.69.094008](https://doi.org/10.1103/physrevd.69.094008). URL: <http://dx.doi.org/10.1103/PhysRevD.69.094008> (cit. on p. 153).
- [196] ATLAS Collaboration. “Measurement of the Z/γ boson transverse momentum distribution in pp collisions at $\sqrt{s} = 7$ TeV with the ATLAS detector”. In: *Journal of High Energy Physics* 2014.9 (Sept. 2014). ISSN: 1029-8479. DOI: [10.1007/jhep09\(2014\)145](https://doi.org/10.1007/jhep09(2014)145). URL: [http://dx.doi.org/10.1007/JHEP09\(2014\)145](http://dx.doi.org/10.1007/JHEP09(2014)145) (cit. on p. 153).
- [197] Pavel M. Nadolsky, Hung-Liang Lai, Qing-Hong Cao, et al. “Implications of CTEQ global analysis for collider observables”. In: *Physical Review D* 78.1 (July 2008). ISSN: 1550-2368. DOI: [10.1103/physrevd.78.013004](https://doi.org/10.1103/physrevd.78.013004). URL: <http://dx.doi.org/10.1103/PhysRevD.78.013004> (cit. on p. 153).
- [198] David J. Lange. “The EvtGen particle decay simulation package”. In: *Nuclear Instruments and Methods in Physics Research Section A: Accelerators, Spectrometers, Detectors and Associated Equipment* 462.1 (2001), pp. 152–155. ISSN: 0168-9002. DOI: [https://doi.org/10.1016/S0168-9002\(01\)00089-4](https://doi.org/10.1016/S0168-9002(01)00089-4) (cit. on p. 153).
- [199] ATLAS Collaboration. “Electron and photon performance measurements with the ATLAS detector using the 2015–2017 LHC proton-proton collision data”. In: *Journal of Instrumentation* 14.12 (Dec. 2019), P12006–P12006. ISSN: 1748-0221. DOI: [10.1088/1748-0221/14/12/p12006](https://doi.org/10.1088/1748-0221/14/12/p12006). URL: <http://dx.doi.org/10.1088/1748-0221/14/12/P12006> (cit. on p. 154).
- [200] ATLAS Collaboration. “Muon reconstruction performance of the ATLAS detector in proton–proton collision data at $\sqrt{s} = 13$ TeV”. In: *The European Physical Journal C* 76.5 (May 2016). ISSN: 1434-6052. DOI: [10.1140/epjc/s10052-016-4120-y](https://doi.org/10.1140/epjc/s10052-016-4120-y). URL: <http://dx.doi.org/10.1140/epjc/s10052-016-4120-y> (cit. on p. 154).
- [201] *Tagging and suppression of pileup jets with the ATLAS detector*. Tech. rep. Geneva: CERN, May 2014. URL: <https://cds.cern.ch/record/1700870> (cit. on p. 155).
- [202] Masahiro Yamatani. “Boosted Jets; identifying highly boosted W, Z, top, Higgs and more”. In: (May 2019). URL: <https://cds.cern.ch/record/2676523> (cit. on p. 155).
- [203] *Boosted hadronic vector boson and top quark tagging with ATLAS using Run 2 data*. Tech. rep. All figures including auxiliary figures are available at <https://atlas.web.cern.ch/Atlas/PHYS-PUB-2020-017>. Geneva: CERN, July 2020. URL: <http://cds.cern.ch/record/2724149> (cit. on p. 155).

- [204] Duccio Pappadopulo, Andrea Thamm, Riccardo Torre, et al. “Heavy vector triplets: bridging theory and data”. In: *Journal of High Energy Physics* 2014.9 (Sept. 2014). ISSN: 1029-8479. DOI: [10.1007/jhep09\(2014\)060](https://doi.org/10.1007/jhep09(2014)060). URL: [http://dx.doi.org/10.1007/JHEP09\(2014\)060](http://dx.doi.org/10.1007/JHEP09(2014)060) (cit. on p. 155).
- [205] Andrew J. Larkoski, Ian Mould, and Duff Neill. “Power counting to better jet observables”. In: *Journal of High Energy Physics* 2014.12 (Dec. 2014). ISSN: 1029-8479. DOI: [10.1007/jhep12\(2014\)009](https://doi.org/10.1007/jhep12(2014)009). URL: [http://dx.doi.org/10.1007/JHEP12\(2014\)009](http://dx.doi.org/10.1007/JHEP12(2014)009) (cit. on p. 155).
- [206] M. Aaboud, G. Aad, B. Abbott, et al. “Performance of top-quark and W -boson tagging with ATLAS in Run 2 of the LHC”. In: *The European Physical Journal C* 79.5 (Apr. 2019). ISSN: 1434-6052. DOI: [10.1140/epjc/s10052-019-6847-8](https://doi.org/10.1140/epjc/s10052-019-6847-8). URL: <http://dx.doi.org/10.1140/epjc/s10052-019-6847-8> (cit. on p. 155).
- [207] G. Aad, B. Abbott, D. C. Abbott, et al. “Identification of boosted Higgs bosons decaying into b-quark pairs with the ATLAS detector at 13

TeV

- ”. In: *The European Physical Journal C* 79.10 (Oct. 2019). ISSN: 1434-6052. DOI: [10.1140/epjc/s10052-019-7335-x](https://doi.org/10.1140/epjc/s10052-019-7335-x). URL: <http://dx.doi.org/10.1140/epjc/s10052-019-7335-x> (cit. on p. 155).
- [208] D Adams, C Anastopoulos, A Andreazza, et al. *Recommendations of the Physics Objects and Analysis Harmonisation Study Groups 2014*. Tech. rep. Geneva: CERN, July 2014. URL: <https://cds.cern.ch/record/1743654> (cit. on p. 156).
- [209] Matteo Cacciari, Gavin P Salam, and Gregory Soyez. “The catchment area of jets”. In: *Journal of High Energy Physics* 2008.04 (Apr. 2008), pp. 005–005. DOI: [10.1088/1126-6708/2008/04/005](https://doi.org/10.1088/1126-6708/2008/04/005). URL: <https://doi.org/10.1088/1126-6708/2008/04/005> (cit. on p. 157).
- [210] N. Hartmann. URL: <https://gitlab.com/nikoladze/ahoi> (cit. on p. 162).
- [211] M. Baak, G.J. Besjes, D. Côte, et al. “HistFitter software framework for statistical data analysis”. In: *Eur. Phys. J. C* 75 (Oct. 2014), 153. 38 p. DOI: [10.1140/epjc/s10052-015-3327-7](https://doi.org/10.1140/epjc/s10052-015-3327-7). arXiv: [1410.1280](https://arxiv.org/abs/1410.1280). URL: <http://cds.cern.ch/record/1953093> (cit. on p. 162).
- [212] Richard D. Ball, Valerio Bertone, Stefano Carrazza, et al. “Parton distributions for the LHC run II”. In: *Journal of High Energy Physics* 2015.4 (Apr. 2015). ISSN: 1029-8479. DOI: [10.1007/jhep04\(2015\)040](https://doi.org/10.1007/jhep04(2015)040). URL: [http://dx.doi.org/10.1007/JHEP04\(2015\)040](http://dx.doi.org/10.1007/JHEP04(2015)040) (cit. on p. 174).

- [213] A L Read. “Presentation of search results: theCLstechnique”. In: *Journal of Physics G: Nuclear and Particle Physics* 28.10 (Sept. 2002), pp. 2693–2704. DOI: [10.1088/0954-3899/28/10/313](https://doi.org/10.1088/0954-3899/28/10/313). URL: <https://doi.org/10.1088/0954-3899/28/10/313> (cit. on p. 176).